THE RELATIONSHIP BETWEEN VOID RATIO AND SHEAR WAVE VELOCITY OF GOLD TAILINGS

HSIN-PEI NICOL CHANG

A dissertation submitted in partial fulfillment of the requirement for the degree of

MASTER OF ENGINEERING (GEOTECHNICAL ENGINEERING)

In the

FACULTY OF ENGINEERING, BUILD ENVIROMENT AND
INFORMATION TECHNOLOGY

UNIVERSITY OF PRETORIA

October 2004

DISSERTATION SUMMARY

THE RELATIONSHIP BETWEEN VOID RATIO AND SHEAR WAVE VELOCITY OF GOLD TAILINGS

HSIN-PEI NICOL CHANG

Supervisor:	Professor G. Heymann
Department:	Civil and Biosystems Engineering
University:	University of Pretoria
Degree:	Master of Engineering (Geotechnical Engineering)

South Africa, as one of the world's largest gold producing countries, also generates large amounts of tailings. These tailings are disposed in tailings dams, which pose great threat to the environment in the case of failure, in particular, liquefaction. In order to evaluate the potential of liquefaction, the void ratio of the tailings is required and is often impossible to obtain. Seismic methods allow an indirect method to estimate void ratio of in situ deposits of which tailings are examples of.

Currently, the use of seismic methods to estimate void ratio of tailings rely on shear wave velocity – void ratio relationships derived for sands. It is thus uncertain whether this relationship holds for gold tailings, which is classified as a sandy silt or silt.

The measurement of shear wave velocity of tailings is done in the laboratory using a triaxial apparatus modified to accommodate bender element. Shear wave velocities are measured using wide square pulses and continuous sinusoidal waves.

The results show that there is a near linear relationship between void ratio and shear wave velocity normalized against effective stress. The position of this relationship lies below the previously published results for sands. Shear wave velocity of gold tailings is more sensitive to changes in effective stress than changes in void ratio or over-consolidation ratio. Furthermore, using phase sensitive detection of continuous waves, we can conclude that shear wave velocity of gold tailings is also frequency dependent.

Key words: Shear wave velocity; void ratio; bender elements; gold tailings; seismic methods; liquefaction; silts.

ACKNOWLEDGEMENT

I wish to express my appreciation to the following persons who made this dissertation possible:

- Professor G Heymann, my supervisor for his guidance and support.
- Mr. J van Staden for his help and support in the laboratory.
- Mr. H Booysens and Mr. J Peens for their assistance with instrumentation.
- Mr. F Windell for his help with downloading data.
- Professor J. Coetzee, Mr A.J. Botha and Mr A.N. Hall of Microscopy for their help with the electron micrographs and microanalysis.

TABLE OF CONTENTS

LIST OF FIGURES

LIST OF TABLES

LIST OF SYMBOLS

a	Real number.
b	Complex number.
B	Relative response of the Biot medium.
e	Void ratio.
f	Wave frequency.
F	Relative response of the forced harmonic oscillator.
FC_{th}	Threshold fines content.
G_{max}	Small strain shear stiffness.
G_S	Specific gravity of soil particles.
L	Distance between sender and receiver bender element.
L_E	Effective travel distance of shear wave.
M	Mass of sample.
M_{Solid}	Mass of solids in a sample.
n	Index number of the complex number set
N	Total number of data points taken.
q’	Effective deviatoric stress.
p’	Mean normal effective stress.
Pa	Atmospheric pressure.
S_B	Subsystem response of Biot medium.
S_F	Subsystem response of forced harmonic oscillator.
t	Travel time of shear wave from sender to receiver bender.
T	Period of the wave.

V	Volume of sample.
V_{Solid}	Volume of solids in the sample.
V_V	Volume of voids in the sample.
V_S	Shear wave velocity.
Vs(n)	Normalized shear wave velocity (against effective stress).
w	Moisture content.
ε	Axial strain.
ε_x ε_y ε_z	Axial strain in the x, y, and z direction.
θ	Phase angle.
γ	Unit weight of soil.
λ	Wave length.
ρ_w	Density of water.
σ'_v	Effective vertical stress.
τ	Time shift of two signals used in cross correlation.

CHAPTER 1

INTRODUCTION

1.1 BACKGROUND

The design process is an important part of any engineering project. The design process not only encompasses the technical and environmental aspects, but also the financial aspects of the project. This includes the risks that are to be encountered during the lifespan of the project.

South Africa is a country renowned for its vast deposit of mineral resources, one of which is gold. South Africa, as one of the world's largest gold producing countries, deliver about 25% of the of the world's annual gold production. The by-product, after the gold extraction process, is large amounts of fine-grained crushed rock. These fine grained materials are transported via mixture with water to tailings dams for disposal. These tailings dams are often tens of meters high, and pose a great threat to the environment in case of failure. In order to successfully manage a mining project, the risks regarding all mine facilities should be quantified. One of the main risks that face a tailings dam during its lifespan is that risk of liquefaction.

The Bafokeng platinum mine's tailings impoundment failed as a result of overtopping (Jennings 1979). During a large storm, the high rate of precipitation caused a rapid rise in the phreatic surface and the water overflowed the walls of the tailings impoundment. The overflow caused a breach in the wall of the impoundment, through which approximately 3 million cubic meters of tailings slurry flowed, killing 13 people in the process. At a distance of 4 km from the breach, the tailings had spread 800m with a depth of 10m. Failure of the Merriespruit gold tailings dam in 1994 was similar in many respects to the Bafokeng failure, which occurred as a result of overtopping after a large storm. The overtopping caused a breach in the embankment wall. Approximately half a million cubic meters of tailings slurry flowed through the breach, destroying 80 houses, severely damaging 200 others and killing 17 people in the nearby Merriespruit village (Blight 1997). Both of these are well known examples of tailings dam failure due to liquefaction.

The term liquefaction is often associated with the consequences of dynamic loading such as earthquakes or explosions. The concern when discussing the Bafokeng and Merriespruit tailings mine failures is not with dynamic loading, but with a phenomenon known as static liquefaction. Failures due to liquefactions results from a sudden loss of shear strength, which can be triggered by slope instability, a rise in phreatic surface, rapid application of surface loading or sudden loss of confining stress such as embankment failure (Papageorgiou et al., 1999).

Undrained behavior of soil under monotonic loading can generally be characterized by two extreme types of response; Dilation and contraction. Dilation leads to a decrease in pore pressure and thus increases in effective stress while contraction involves an increase in pore pressure and a decrease in effective stress. When the shear strength approaches zero, the soil begins to flow, or liquefy. The contractive or dilative behavior of a soil under loading is a function of the state of the soil (void ratio, mean effective stress and deviator stress).

The state of soil in most natural deposits can be easily estimated by acquiring undisturbed samples. The difficulty in estimating the state of mine tailings arises from the inability to obtain undisturbed samples of the tailings material, especially below the water table. The stress conditions can be estimated with relative ease, but in situ density or void ratio cannot easily be estimated. Although undisturbed samples can be obtained using ground freezing techniques, and the void ratio thereby obtained, the method is expensive and unsuitable for South African conditions.

There have been many attempts to relate shear wave velocity, void ratio and the effective confining stresses of a soil using the resonant column and bender elements. (Hardin and Richart 1963; Rosler 1979; Yu and Richart 1984; De Alba et al. 1984, Stokoe et al. 1985, Robertson et al. 1995). These results show that a unique relationship exists between the shear wave velocity and void ratio at a certain effective confining stress, for a particular soil.

With the introduction of in situ seismic methods like the continuous surface wave method, spectral analysis of surface waves and seismic cone penetration test, the use of seismic methods to obtain void ratio is gaining popularity. Although many authors have derived the shear wave velocity-void ratio relationship for sands of different origins, no relationship has been published for silts, of which tailings are examples of. Seismic methods used in tailings material currently rely on shear wave velocity-void ratio relationships derived mainly for sands. Since shear wave velocity is largely a function of the stiffness, the void ratios of silts derived from shear wave velocity-void ratio relationships for sands are therefore doubtful.

1.2 OBJECTIVE OF STUDY

The motivation for conducting this study is to generate a relationship between shear wave velocity and void ratio under a range of stress conditions for gold tailings material obtained from a tailings dam in the Free State gold fields. Using this relationship, the void ratio of gold tailings, which could not be estimated before, can now be obtained directly from in situ measurements of shear wave velocity. With the in situ state of the tailings deposit known, the behavior of the deposit can be predicted with regards to liquefaction and the risk can be quantified.

1.3 SCOPE OF STUDY

In order to have a better understanding of the problem, a literature study was conducted which included the several topics. These topics included the concept of liquefaction and the liquefaction resistance, the development and use of the seismic methods, and the relationships between shear wave velocity and void ratio that have been published by various authors. In order to proceed with the experimental stage, the topic of bender element testing within a triaxial apparatus was investigated. The data obtained from the experimental stage were analyzed in conjunction with knowledge of shear wave velocity analysis, frequency analysis and the Fast Fourier Transform (FFT). Finally, a short study was conducted regarding the properties of the soil to be used in the research.

1.4 METHODOLOGY

A hypothesis was set up that states: **a relationship exists between shear wave velocity and void ratio for gold tailings**. In order to validate this hypothesis, a thorough literature study was conducted in order to acquire the necessary knowledge regarding the research. The shear wave velocity of the gold tailings was measured under various void ratios and stress conditions in a triaxial apparatus which was modified to accommodate bender elements. The data was then analyzed and the results discussed. Conclusions were then made keeping in mind the hypothesis.

1.5 ORGANIZATION OF REPORT

The dissertation is divided into 7 chapters, and a brief description of the contents of each chapter is given below. Firstly, the dissertation starts with an Introduction in Chapter 1. This chapter entails a description of the background of the research. Chapter 1 is followed by a Literature study in Chapter 2, which contains all information regarding the research gathered prior to commencing the experimental stage. Chapter 3 consists of information regarding the experimental section, and is named the Test Methodology chapter. All the data obtained are analyzed and shown in Chapter 4, the Analysis chapter. The Analysis chapter is followed by Chapter 5, the Discussion chapter, in which the results obtained in Chapter 4 are discussed. All conclusions made regarding the research can be found in the Conclusion chapter in Chapter 6. Chapter 7, the Reference chapter, contains all sources of information used in this research.

All results and calculations are attached in appendices together with all additional information. *Appendix A* contains the electron micrographs taken and the microanalysis done with the soil specimen used in this research. A step by step guide for bender element development is attached in *Appendix B*. The data recorded for each triaxial test from which void ratio can be determined is shown in *Appendix C*, while all input and output traces obtained using the first arrivals method are given in *Appendix D*. Spreadsheet calculations for phase sensitive detection of continuous waves are attached in *Appendix E*. *Appendix F* contains A4 size graphs of data generated and shown in the Discussion chapter.

CHAPTER 2

LITERATURE STUDY

2.1 BACKGROUND

Management of tailings facilities is extremely important as far as the profitability of a mine is concerned. One of the most important aspects in tailings risk assessment is the liquefaction potential of the facility. In order to assess the liquefaction potential, the state of the tailings material is required, ie. void ratio and effective confining stress. As it is impossible to obtain undisturbed samples of the tailings material from below the water table, the in situ void ratios of tailings are often unknown.

With the development of triaxial local strain instrumentation (Burland and Symes, 1982; Clayton and Khatrush, 1986; Tatsuoka, 1988), the accuracy of strain measurements has significantly improved. Clayton and Heymann (2001) verified that soils with varying stiffness all show a linear stress-strain response up to a strain of 0.002%. This suggests that seismic methods, which operate at the elastic range, can be used to obtain meaningful parameters for the deposit.

The dependency of shear wave velocity on void ratio and stress condition has been shown by many previous authors (Hardin and Richart, 1963; Rosler, 1979; Yu and Richart, 1984; Stokoe et al., 1985). With the development of geotechnical seismic methods such as the seismic cone, designers now have an indirect method from which various engineering parameters of natural or artificial soil deposits can be estimated. This includes indirectly obtaining the void ratio from tailings deposits, which was previously not possible.

The hypothesis was set up that **a relationship exists between shear wave velocity and void ratio for gold tailings**. This chapter presents the literature study undertaken to acquire the necessary knowledge in order to validate the hypothesis.

2.2 LIQUEFACTION

The behavior of soil under undrained loading can generally be categorized by two types of response, dilation and contraction, which can be demonstrated by the marble analogy in *figure 1*. When densely packed soil particles are loaded, the particles tend to move over each other, causing a tendency to increase in void spaces. This behavior is known as dilation, as seen in *figure 1a.* In undrained conditions, water cannot be expelled or sucked into the soil mass. Thus a tendency to increase the void spaces lead to a decrease in pore pressure and an increase in effective stress. On the other hand, loose material exhibit contractive behavior under loading. Under undrained conditions, the tendency to decrease the void spaces, as shown in *figure 1b,* result in an increase in pore pressure and a decrease in effective stress.

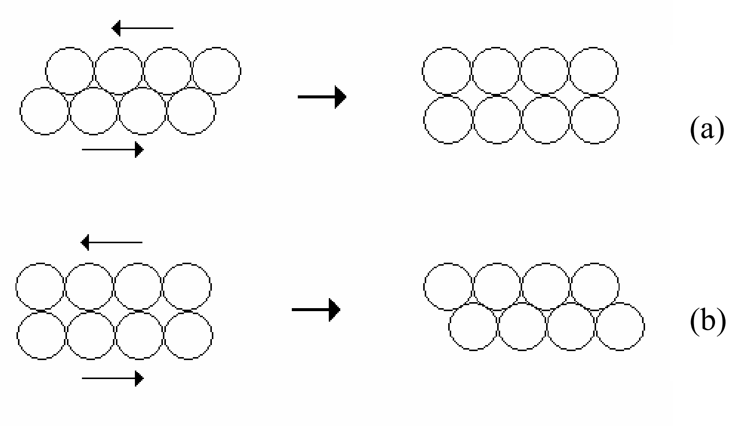

Figure 1. Marble analogy for dilation and contraction.

The behavior of soil under loading can also be demonstrated by the shear stress vs mean normal effective stress and stress vs strain graphs shown in *figure 2* below (Cubrinovski and Ishihara, 2000). Dense material with low void ratio shows strain hardening response and an increasing shear stress is required to induce shear strain until eventually the steady state is reached. This type of soil behavior is associated with dilation or strain hardening, as shown by the 'no flow' line in *figure 2*. If the void ratio of the soil is somewhat higher, then strain softening (contraction) is followed by strain hardening (dilation) in which the soil recovers its strength and restores stability. In this case, the flow deformation takes place over a limited range until dilative behavior is initiated. This type of response is also known as limited liquefaction, as is shown by the 'limited flow' line in *figure 2*. Material with high void ratio shows fully contractive behavior where following the peak stress the material strain softens until the steady state is reached at large strains. This strain softening phase of the response resembling flow behavior is known as liquefaction. This type of behavior is demonstrated by the 'flow' line in *figure 2*.

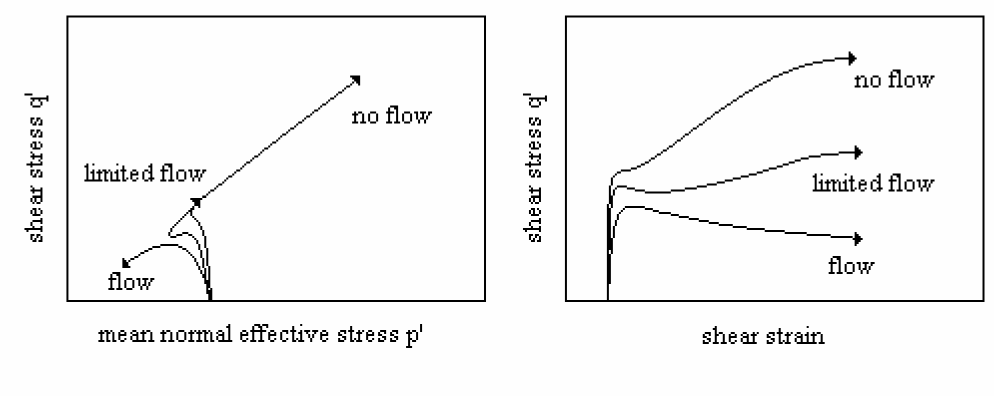

Figure 2. Soil behavior under loading (Cubrinovski and Ishihara, 2000).

Liquefaction can be defined as:

> *a phenomenon wherein a mass of soil loses a large percentage of its shear resistance, when subjected to monotonic, cyclic or shock loading, and flows in a manner resembling a liquid until the shear stresses acting on the mass are as low as the reduced shear resistance (Castro et al. 1982).*

Liquefaction involves a loss of strength or a sudden loss of equilibrium of slopes. This sudden loss of strength and equilibrium will result in the soil mass flowing like a liquid until the steady state is reached. Early works by Casagrande (1938), Geuze (1948), Koppejan et al. (1948) have shown that the potential for liquefaction for fine sands is sensitive to the void ratio and postulated that liquefaction can only occur above a certain critical void ratio.

Casagrande and his co-workers developed the critical void ratio concept into a formalized design procedure (Castro 1969, 1975; Poulos 1971, 1981; Casagrande 1975; Castro et al. 1977). This approach to design is termed the 'steady state' method which is a limiting equilibrium method developed for partially liquefiable soils. The essence of the steady state method is the concept of 'steady state of deformation', which has been defined by Poulos (1981):

> *The steady state of deformation for any mass of particles is that state in which the mass is constantly deforming at constant volume, constant normal effective stress, constant shear stress and constant velocity. The steady state of deformation is achieved only after all particle orientation*

> *has reached a statistically steady state and after all particle breakage, if any, is completed, so that the shear stress needed to continue deformation and the velocity of deformation remains the same.*

The steady state of deformation can therefore be considered as state of plastic flow at constant velocity. Been et al. (1991) have shown that the steady state and the critical state, which is a boundary of elastic behavior for soil, are in fact the same condition.

The steady state line defines the relationship between void ratio and the mean effective stress and forms the boundary between contractive and dilative behavior. In situ soils at a void ratio above the steady state line will strain soften and liquefy, whilst a void ratio below this line will result in strain hardening (dilation). Material lying above but very close to the steady state line will show strain softening followed by strain hardening. These behaviors are shown in *figure 3.*

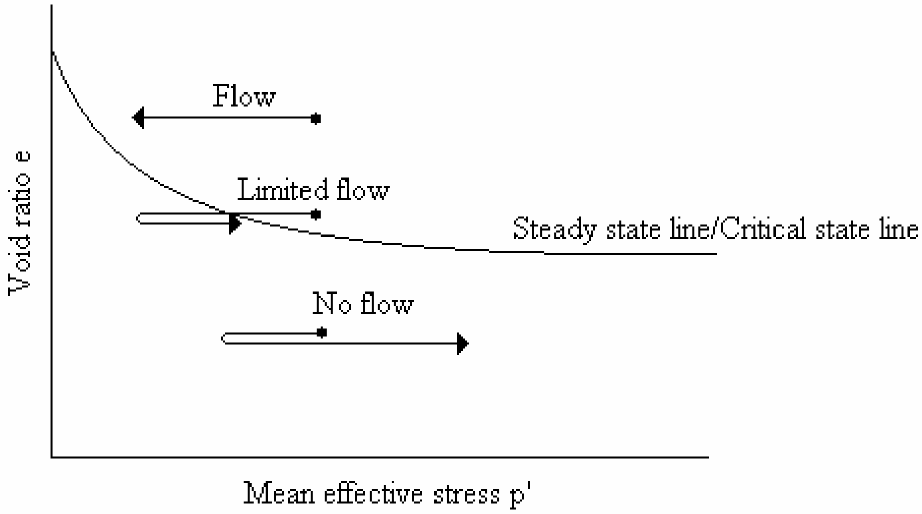

Figure 3. Flow behavior in the e-p’ plane at various void ratios (Cubrinovski and Ishihara, 2000)

The position of the steady state line is independent of sample setup procedure, soil fabric, stress path followed to reach the steady state condition, strain rate, consolidation stresses prior to shear or the mode of loading, as shown by Sladen et al. (1985), Ishihara (1993), Robertson and Fear (1995). The steady state line is however influenced by particle size distribution, particle shape and fines content, with the fines content being by far the most dominating factor. Various researches have shown that a change in the fines content of a sample results in a change in the position of the steady state line and its susceptibility to liquefaction (Sladen et al., 1985; Pitman et al., 1994; Lade and Yamamuro, 1997 and Thevanayagan, 1998). Papageorgiou et al. (1999) have shown that for Merriespruit gold tailings, a change in fines content from 20 percent to 60 percent can dramatically alter the position of the steady state line.

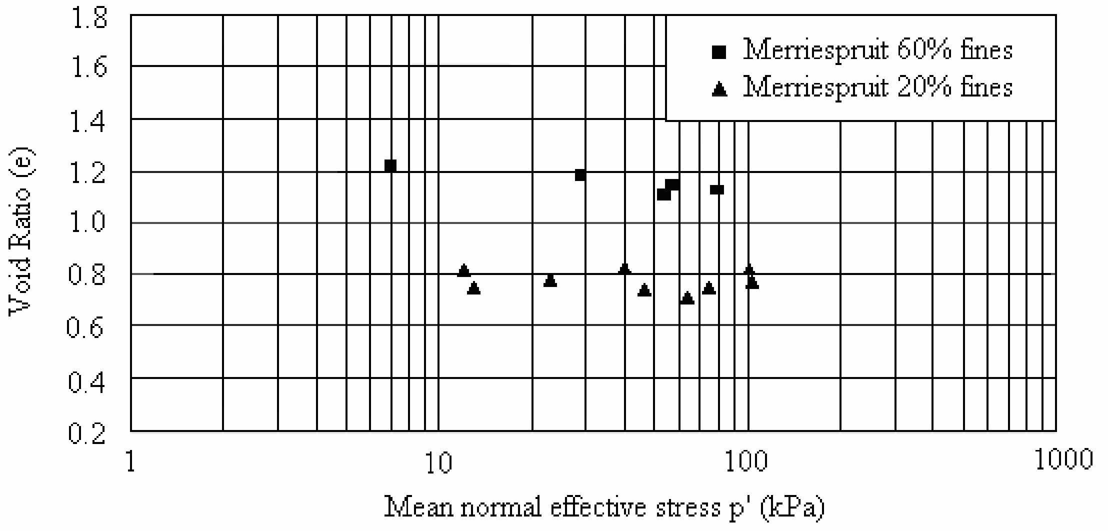

Figure 4. Steady state diagram for Merriespruit gold tailings (Papageorgiou et al., 1999)

Liquefaction has been shown to occur in a variety of geological materials such as sensitive clays, residual soils and cohesionless soils (Sasitharan et al., 1993). However, liquefaction of saturated deposits of loose cohesionless soils is by far the most common.

There are a few criterions required for liquefaction to take place. Firstly, a large portion of the material must exist in a liquefiable state ie. having a stress and void ratio condition above the steady state line. Secondly, a triggering mechanism in the form of undrained loading must take place. This undrained loading can be caused either by cyclic loading such as earthquakes, blasting and pile driving or a sudden static loading such as rapid construction or oversteepening of a slope. Ekersley (1990) performed laboratory model tests and showed that flow failure could be initiated under drained conditions when a slope was wetted by allowing the phreatic surface to slowly rise.

2.3 SEISMIC METHODS

The first ground seismic exploration dates back to 1845, when Mallet experimented with artificial earthquakes in an attempt to measure seismic velocities. The development of seismic methods in geotechnical engineering as a means of testing originated from the field of geophysics. Seismic methods have been used extensively in petroleum exploration, in ground water mapping as well as in measurement of depth of bedrock for major civil engineering projects such as the construction of large buildings, dams, highways and harbours (Flinn, Robinson and Treitel, 1967).

The use of seismic methods in geotechnical engineering was introduced by Terzaghi (1943) and Hvorslev (1949) in as early as the 1940's. They compiled work carried out primarily in Germany in the 1930s, which uses continuous mechanical vibration as a source of energy.

Seismic waves generated by a source can produce four types of waves, namely compression waves, shear waves, Rayleigh waves and Love waves. Compression waves are longitudinal body waves in which the particle motions are in the same direction as the wave propagation. Compression waves are also the fastest of all mechanical wave types. Compression waves can be propagated through both the soil skeleton as well as through water. In water, compression waves travel at a velocity of around 1500m/s. Shear waves are transverse body waves in which the particle motions are perpendicular to the wave direction of wave propagation. Since water does not exhibit shear stiffness, shear waves can only travel through the soil skeleton at a velocity of around 70% of the compression wave velocity in the same medium. One of the properties of shear wave that have often been used in seismic testing is the reversibility of the shear waves. This property enables researchers to distinguish shear waves from other waves.

Rayleigh waves and Love waves, on the other hand, are surface waves which exhibit complex particle motion. Rayleigh waves travel at a velocity of around 91% to 95% of the shear wave velocity, but attenuates slower then all other waves. On impact, two thirds of the energy produces Rayleigh waves. Love waves are not generated to a significant degree by surface sources, and are not often used in seismic investigations.

With the introduction of triaxial local strain instrumentation, the accuracy of strain, and thus stiffness measurements have notably improved (Burland and Symes, 1982; Clayton and Khatrush, 1986; Tatsuoka, 1988). Heymann (2001) showed that soil exhibit linear stress strain response at very small strains using highly accurate local strain instrumentation calibrated against an interferometer. Clayton and Heymann (2001) further showed that this linear stress strain response exist up to a strain of 0.002% for geomaterials with widely varying stiffnesses, ranging from soft clays to weak rocks. This has great significance in terms of the applicability of seismic methods. Seismic waves, which are believed to operate within this linear elastic range, can now be used to indirectly obtain meaningful engineering parameters. As a result, the use of seismic techniques to obtain various parameters for design purposes is gaining popularity. In situ seismic methods can be used to obtain design parameters with relative ease and cost effectiveness, without disturbance of the soil.

Seismic methods rely on the differences in velocity of elastic waves through different geological or man-made materials. Measurement of the time interval between the generation of the wave and its reception at vibration detectors enables the velocity of the elastic wave through various soil deposits to be determined. In situ seismic methods can be divided into two main categories, namely surface wave tests and body wave tests. A body wave test involves waves propagating within the depth of the ground (compression wave and shear wave), while surface wave tests entail waves travelling alone the surface of the ground (Rayleigh wave and Love wave). Different in situ seismic tests are listed below.

Surface wave tests

- Continuous surface wave test
- Spectral analysis of surface wave test

Body wave tests

- Cross-hole test
- Down-hole test
- Up-hole test
- Seismic cone test
- Seismic reflection test
- Seismic refraction test
- Seismic tomography

Apart from the in situ tests, shear wave velocity can be determined in the laboratory using two tests, namely resonant column test (Hardin and Richart, 1963; Hardin and Drnevich, 1972) and bender element tests (Shirley and Hampton, 1978; Shirley, 1978; Dyvic and Madshus, 1985). Both these tests are body wave tests. While resonant column tests require expensive resonant column apparatus, bender element tests can be produced at relatively low costs. For this reason the popularity of bender element testing has increased as a way of laboratory seismic testing.

Although seismic tests were initially used to obtain various stiffness parameters (Matthews, Hope and Clayton, 1997), the method is being exploited to relate wave velocity with other engineering parameters such as coefficient of earth pressure at rest, k_o (Fioravante et al., 1998), void ratio (Robertson and Fear, 1995). Other applications of seismic methods are obtaining Poisson's ratio (Abbiss, 1981), evaluate in situ and specimen anisotropy (Sully and Campanella, 1995; Pennington et al., 2001), simulate dynamically loaded foundations (Degrande and Pyl, 2002), evaluate sample disturbance (Sasitharan et al., 1993; Dasari and Bolton, 1998) and estimate liquefaction potential (De Albe et al., 1984; Ishihara and Cubrinovski, 2000).

2.4 SHEAR WAVE VELOCITY AND VOID RATIO

Shear wave velocity is dependent primarily on the void ratio, the effective confining stresses, and the intrinsic characteristics of the soil (Hardin and Richart; 1963, Hardin and Drnevich, 1972). Unless significant grain crushing occurs, the intrinsic characteristics of the soil do not change with changes in void ratio and effective confining stress. Thus in many uncemented, cohesionless soils, shear wave velocity can be regarded as a fundamental parameter. Hence, there is an increasing interest in using shear wave velocity to define the state (void ratio, and effective confining stress) of a soil, since shear wave velocity can be measured both in situ and in the laboratory.

Resonant column results are used extensively to relate shear wave velocity to void ratio and the effective confining stresses in the soil (Hardin and Richart, 1963; Rosler, 1979; Yu and Richart, 1984; Stokoe et al., 1985). The results obtained by Hardin and Richart (1963) for sands of various gradings are shown in *figure 5*.

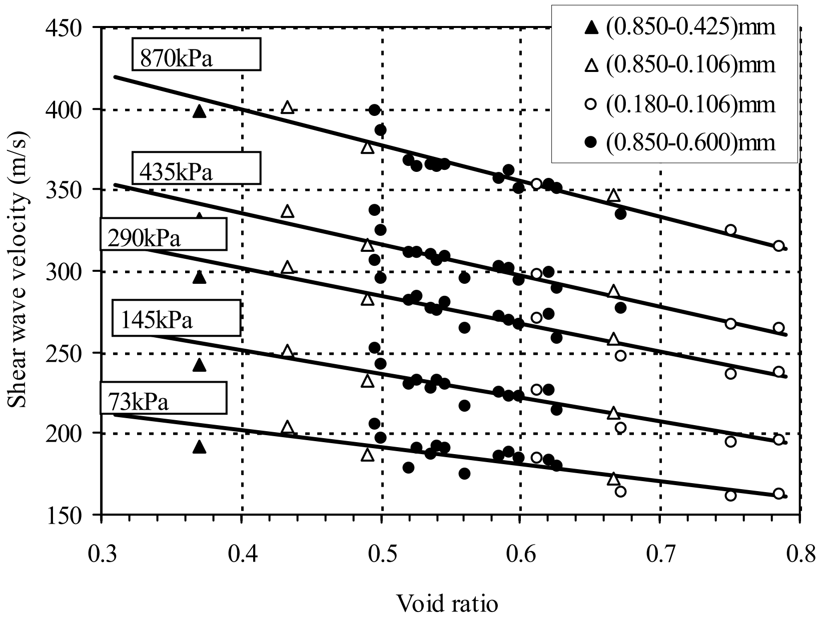

Figure 5. Graph of shear wave velocity vs void ratio for sands of various gradings at various stresses (Hardin and Richart, 1963).

To account for the influence of the varying stress conditions, the shear wave velocity can be normalized using *equation 1*, proposed by Sykora (1987) and Robertson et al. (1992):

$$Vs(n) = Vs\,(Pa/\sigma'_v)^{0.25}$$ **Eq.** (1)

where Vs(n) is normalized shear wave velocity, Vs is shear wave velocity, Pa is atmospheric pressure (usually 100 kPa), and σ'_v is the major principle effective stress. The graph of normalized shear wave velocity against void ratio is shown in *figure 6*. From *figure 6,* it is clear that as shear wave velocity is normalized against effective stress, the data points and thus the relationships shown in *figure 5* collapses onto one single relationship.

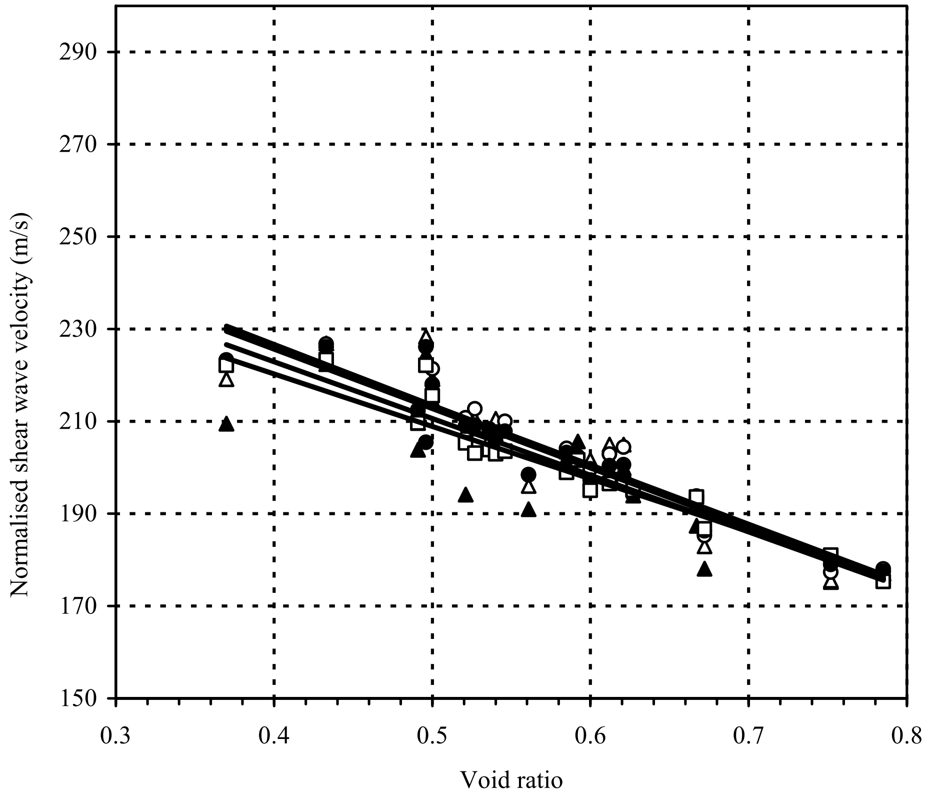

Figure 6. Graph of normalized shear wave velocity vs void ratio (Hardin and Richart, 1963).

Figure 7 below shows the relationship between normalized shear wave velocity and void ratio for a wide range of freshly deposited uncemented sand samples in the laboratory (Robertson and Fear, 1995). These results show that a definite relationship exists between shear wave velocity and void ratio under a certain confining stress.

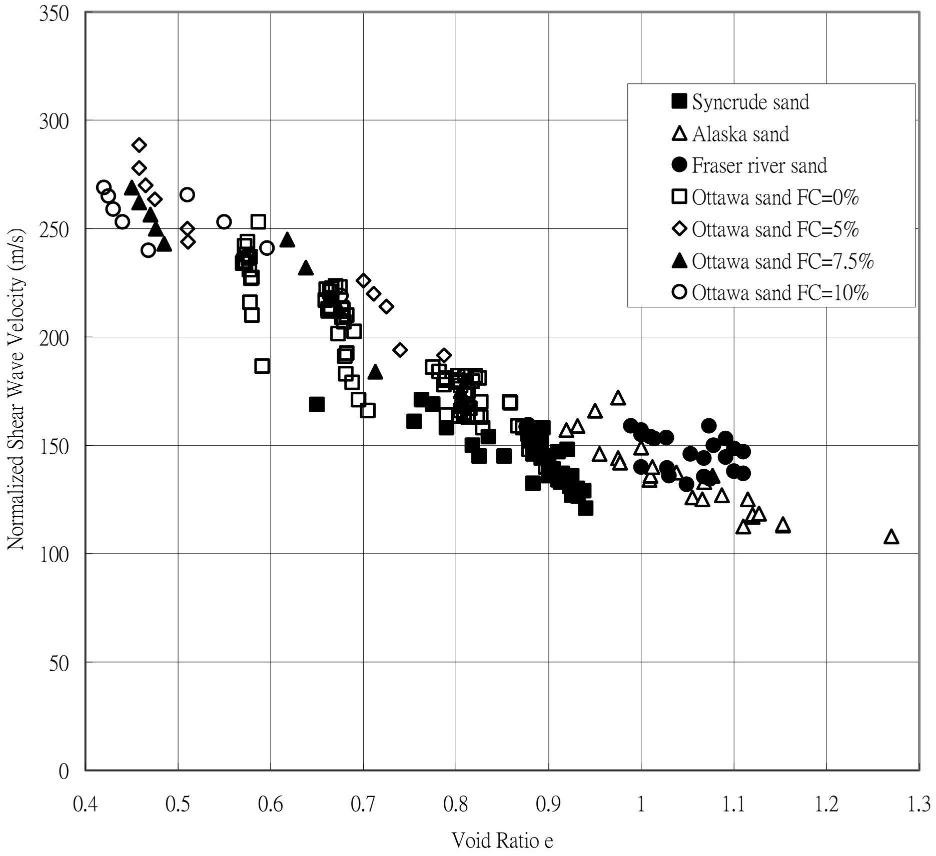

Figure 7. Void ratio against normalized shear wave velocity for various sands (Robertson and Fear, 1995).

According to *figure 7,* there is a clear relationship between shear wave velocity and void ratio. The relationship is valid for sands of different properties obtained from various sources. The question in mind now is whether silt, and gold tailings in particular, show similar relationship between shear wave velocity and void ratio.

A hypothesis was established that **a relationship exists between shear wave velocity and void ratio for gold tailings**, which is essentially a silt.

2.5 BENDER ELEMENT TESTING AND SHEAR WAVE VELOCITY

Bender elements were developed by Shirley and Hampton (1977) as part of a program to measure in situ acoustic parameters of sediments. A bender element consists of two thin piezoelectric ceramic plates rigidly bonded together along their lengths. Piezoelectric ceramics are high impedance materials that undergo a volume change in response to a driving voltage. When the two rigidly bonded plates are driven 180º out of phase, one plate extends while the other shortens causing the composite element to bend, as seen exaggerated in *figure 8.*

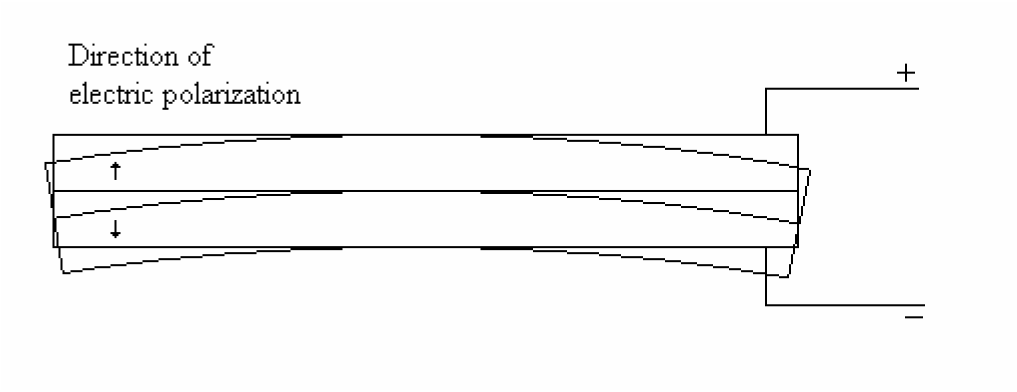

Figure 8. Schematic representation of the mechanism of a piezoceramic bender element.

Conversely, any movement detected by the composite bender element will induce a pulse, which can be measured as a potential difference.

If the bender element is embedded in a medium, mechanical motion will be transferred from the element to the particles in the medium so that the particle motion will be perpendicular to the length dimension of the element. If the medium in which the element is embedded exhibits some kind of rigidity, the shearing motion will be propagated as a shear wave with the direction of propagation perpendicular to the particular motion (i.e. parallel to the length of the element). Conversely, only small amounts of energy will be propagated perpendicular to the element length, since the particle motions cancel in two directions perpendicular to the bender length. Therefore, the result is a shear wave propagating in the directions parallel to the element.

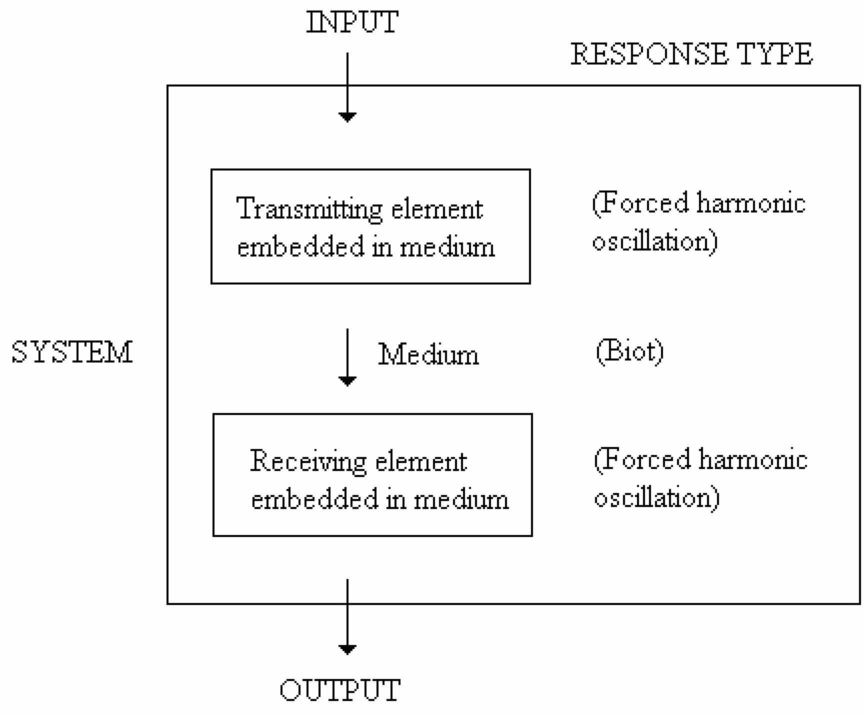

Figure 9. Propagation of signal through a system containing two harmonic oscillators (bender elements) and a Biot medium (soil specimen) (Blewett et al., 2000).

The response of the soil specimen to waves generated by a bender element and received by a second bender element can be envisaged as in *figure 9.* An electrical waveform is applied to the driving bender element, which is embedded in the soil medium. This can be regarded as damped, forced harmonic oscillator (Santamarina and Fam, 1997). The shear wave then propagates into and through the soil medium, which responds to shear waves in a manner described by Biot (1956a, 1956b). This subsystem response can be named S_B. The shear wave energy then arrives at the receiving bender element which again behaves as a damped harmonic oscillator in the soil. The response of the two bender elements can be incorporated into a single subsystem, S_F, since the two are practically identical. The response of the two subsystems, S_F and S_B can be combined as in *equation 2* to form the response of the bender element - system as a whole, which is labelled S.

$$S = FS_FBS_B \qquad \textbf{Eq.}\ (2)$$

where F and B are the relative response of the forced harmonic oscillator and Biot subsystems.

In order to measure the shear wave velocity of a material, a generator and a receiver element is required at both ends of the sample. The shear wave generated by the function generator will be detected by the receiver and the output can be digitally recorded or displayed on an oscilloscope. Using the time lag between the generated and the received pulse and the distance the shear wave travelled, the shear wave velocity can be calculated. Bender element systems can be utilized in most laboratory apparatus, but are particular versatile when used in triaxial tests as described by Dyvik

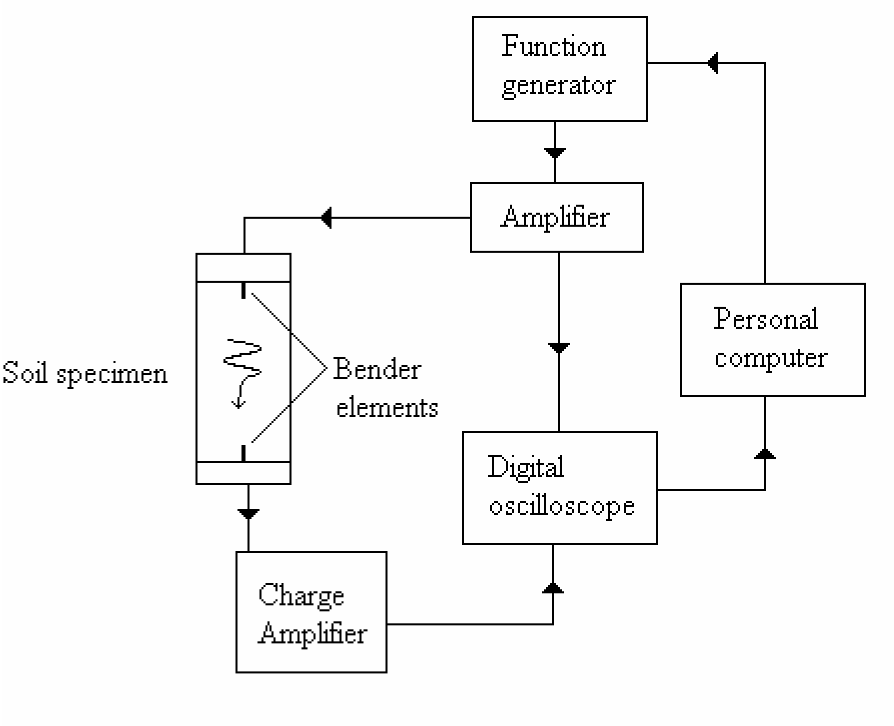

Figure 10. Simple bender element system.

and Madshus (1985). They also reported excellent agreement between bender element and resonant column results. *Figure 10* shows an example of simple bender element system.

It should be emphasized that, since bender elements are high impedance devices, it is necessary to waterproof the element when used, for example, in saturated material.

To obtain shear wave velocity, both the effective length between the benders, L, and the travel time from the sender to the receiving bender, t, are required. Travel length L can be taken as the distance between the tips of the generator and receiving benders based on the results obtained using samples of different length (Viggiani and Atkinson, 1995). Since L can be measured with relative ease and accuracy, the error in the shear wave velocity would mainly be caused by errors in travel time determination. Various methods have been used to determine travel time and the methods can be divided into two categories: time of flight techniques and phase sensitive detection techniques. The main difference between the two categories is that the time of flight technique uses single pulse, while phase sensitive detection technique uses continuous waves. Both methods have their benefits and problems, which are discussed below.

2.5.1 Time of flight techniques

As mentioned earlier, the time of flight techniques use a single pulse as the driving signal. Initially, single square excitations have been used, as seen in *figure 11 (a)*. Many authors have commented on the difficulty in identifying the exact time of

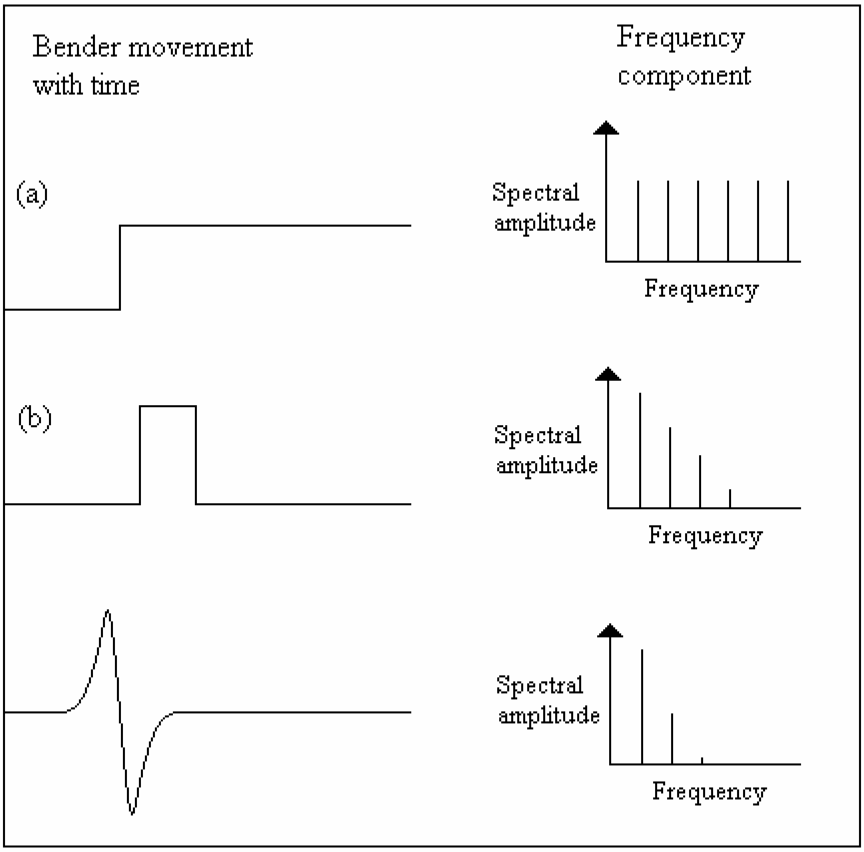

Figure 11. Frequency component in driving waveforms.

arrival of the shear wave (Dyvik and Madshus, 1985; Brignoli et al., 1996; Viggiani and Atkinson, 1995). Thus Viggiani and Atkinson (1995) suggested the use of a single-shot sinusoidal excitation pulse, shown in *figure 11 (c),* to aid in identifying points of similarity between the input and output waveform. This indeed leads to significant improvements over the square pulse excitations shown in *figure 11 (a)* and *(b).* In order to determine the travel time, many analysis methods have been used by various authors as discussed below.

Travel time to first direct arrival of output signal.

Travel time of the shear wave can be estimated as the time between the start of the voltage pulse input to the transmitting bender and the first deflection in the output signal from the receiving bender. The difficulty in this method arises in identifying an unambiguous first arrival in the output signal. The output signals are often obscured

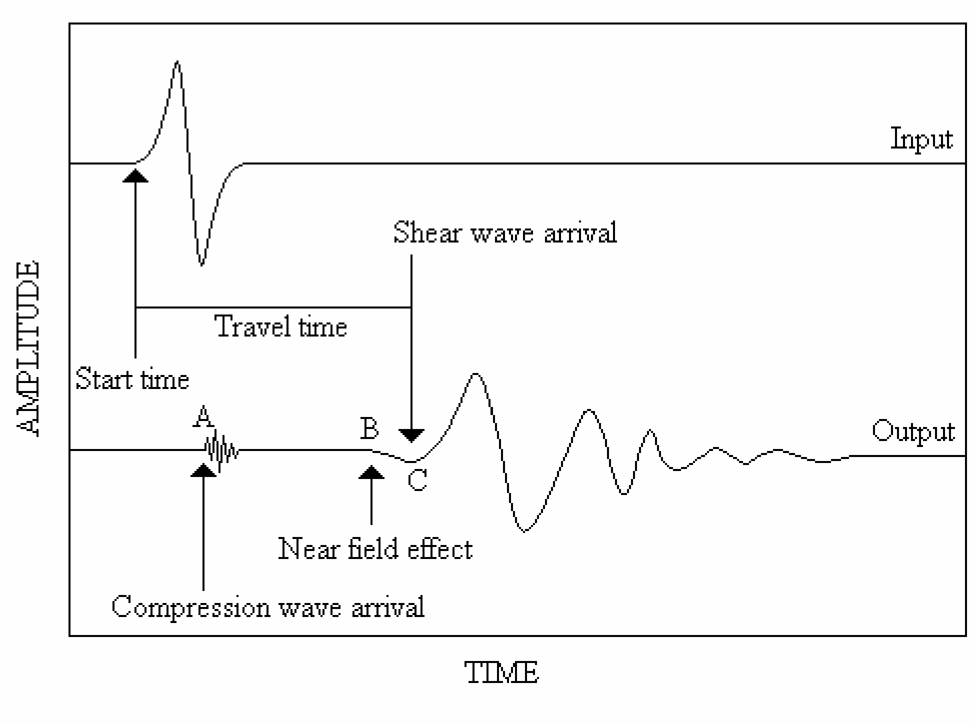

Figure 12. Typical bender element signals.

by near-field effects, which can lead to erroneous shear wave velocity calculations. (Brignoli and Gotti, 1992; Viggiani and Atkinson, 1995; Jovicic et al., 1996). A typical bender output is shown in *figure 12*. The shear wave arrival is preceded by earlier and much lower intensity waves, as indicated by point A, which is in fact a compression wave through the fluid-soil system.

The initial downwards movement just before the shear wave, indicated by point B, shows the arrival of the near field component. This near field component will be discussed in detail later in the chapter. The arrival of the shear wave is defined as the first intense signal arrival, indicated by point C, combined with the correct polarity for the transmitter input. Travel time is calculated as the time difference between the beginning of the input pulse and the arrival of the shear wave as discussed above. Using *figure 12,* the travel time is the time difference between 'start time' and 'shear wave arrival'.

Travel time between characteristic points of input and output signals.

Travel time of the shear wave can be taken as the time between two corresponding characteristic points in the single sinusoidal input signal and the output signals. The most commonly used characteristic points are the first peak, first trough, or the zero crossing of the input and output signals. It has been found that the received signal experience a gentle spread while traveling through the sample. Because of this spread, it can be expected that the travel time measured from the first peak yields the closest value to the correct arrival of the shear wave.

Travel time by cross correlation of input and output signals.

Travel time of the shear wave can be taken as the time shift that produces the peak correlation between a single sinusoidal input signal and the output signals. This method is arguably the method which produces the most accurate shear wave velocity results since this method eliminates the ambiguity from visual estimations of other methods. The cross-correlation of two signals, *a* and *b* can be defined as:

$$CC(\tau) = \lim_{T \to \infty} \frac{1}{T} \int_{-T/2}^{T/2} a(t) b(t+\tau) dt$$

Eq. (3)

where T is the total time length of the signal, and τ is the time shift between the two signals.

2.5.2 Phase sensitive detection

Phase-sensitive detection is a widely used standard instrumentation technique which involves the use of continuous waves (Blair and Sydenham, 1975). A signal is generated at a particular frequency, and the change in phase angle (phase difference) between the driving and the received wave can be determined. The relationship between the change in phase angle and travel time can be determined by:

$$dt = \frac{d\theta}{360 f}$$

Eq. (4)

where dt is the travel time in seconds, $d\theta$ is the change in phase angle in degrees, and f is the frequency of the driving wave in hertz. Depending upon the drive frequency used, small changes in time can result in multiple revolutions of the phase angle and the technique is therefore extremely sensitive.

In an ideal scenario, the driving wave propagates through the medium and completely received by the receiving element and thus the frequency of the received wave is exactly the same as the frequency of the driving wave. In practice, this is not the case. The original signal is unavoidably combined with some noise before arriving at the final recording device. Although the signal is now a mixture of many frequencies, usually only the part of the signal at the original frequency is of interest. In this case, FFT analysis, which will be discussed in section 2.7 can be used to obtain the frequency and phase angle of the frequency with the highest spectral amplitude, which is the original wave.

Blewett et al. (1999) showed that phase sensitive detection technique using continuous waves has a few benefits over conventional time of flight techniques. Firstly, since noise levels are inversely proportional to frequency, the use of high frequency sinusoidal wave input significantly reduces the level of noise in the received signal. Furthermore, the use of continuous waves eliminates the ambiguity of selecting characteristic points of the input and output waves by visual inspection. The use of continuous waves also eliminates the potential problem of grouped velocity dispersion component, which will be discussed in section 2.6.1, as the element is driven by a single continuous frequency component. The results obtained from their tests showed that there is no significant difference (less than three percent) in shear wave velocity obtained from the two analysis methods at axial strain of below two percent.

2.6 POTENTIAL PROBLEMS OF BENDER ELEMENT TESTING.

The problems associated with bender element testing can be categorized into three groups: Problems associated with time of flight techniques, problems associated with phase sensitive detection and problems associated with bender element testing in general.

2.6.1 Problems associated with time of flight techniques.

There are many reasons why the received pulse may be distorted, and in the laboratory, some of these effects are magnified due to the scale of the specimen size.

Near field effects

The term near field effects is used frequently to describe the initial deflection just prior to the arrival of the shear wave. There is no clear definition for this phenomenon, but many authors have suggested explanations. One of the more understandable explanations has been given by Sanchez-Salinero et al. (1986), when they evaluated the assumptions made by the different methods for interpreting travel time in tests like down-hole or cross-hole shear wave velocity tests. Their analytical solutions showed that body waves generated by a point source in a 3-D elastic medium spread in a spherical manner. During wave propagation, coupling between waves that exhibites the same particle motion but propagate at different velocities and attenuate at different rates was shown to affect the results. The coupling of these waves was shown to obscure the first direct arrival of the shear waves and affected the travel time calculated characteristic peaks or cross-correlation at locations near the source.

Near-field effect in bender element tests is recognized by previous investigators (Brignoli and Gotti, 1992; Viggiani and Atkinson, 1995; Jovicic et al., 1996), with reference made to the findings of Sanchez-Salinero et al. (1986). Near-field effects are potentially more complicated in a triaxial specimen than in the unbounded 3-D space considered by Sanchez-Salinero (1986). As a pulse moves farther from the transmitter it develops a more uniform wave front, but it is unknown how far the near field extends. It can affect a large proportion of the sample length. To minimize near-field effects, the ratio L/λ should be kept between 6 and 9. (Sanchez-Salinero, 1986; Brignoli and Gotti, 1992; Jovicic et al., 1996). For lower values of L/λ, there's an initial downward deflection of the trace before the shear wave arrives, representing the near-field component. At higher L/λ ratios, the near-field component is almost absent. The value of L/λ, and hence the influence of near-field effects depend not only on the frequency of the signal but also on wave velocity. For a given frequency this effect will be greater in stiffer materials.

Grouped velocity distortion

Any practical pulse comprises a range of frequencies, as can be seen in *figure 11*. These varying frequencies give rise to the possibility of distortion simply due to the natural propagation by and within physical subsystems possessing a non-uniform response to each frequency component (Santamarina and Fam 1997). Although the use of single-shot sinusoidal driving voltage proved to be an improvement over square pulses, significant distortions may still occur. The use of a single frequency continuous driving waves as proposed by Blewett et al. (1999) eliminates this problem.

2.6.2 Problems associated with phase sensitive detection.

Shear wave velocity and frequency

Blewett et al. (2000) have shown that within a triaxial cell, the system displays a frequency dependent velocity response. The form of the velocity response suggests roughly equivalent importance for the two subsystem types, S_F and S_B, and requires the Biot response S_B to be at a lower frequency than the embedded element response, S_F. *Figure 13* represents results of triaxial test done at 50 kPa effective stress.

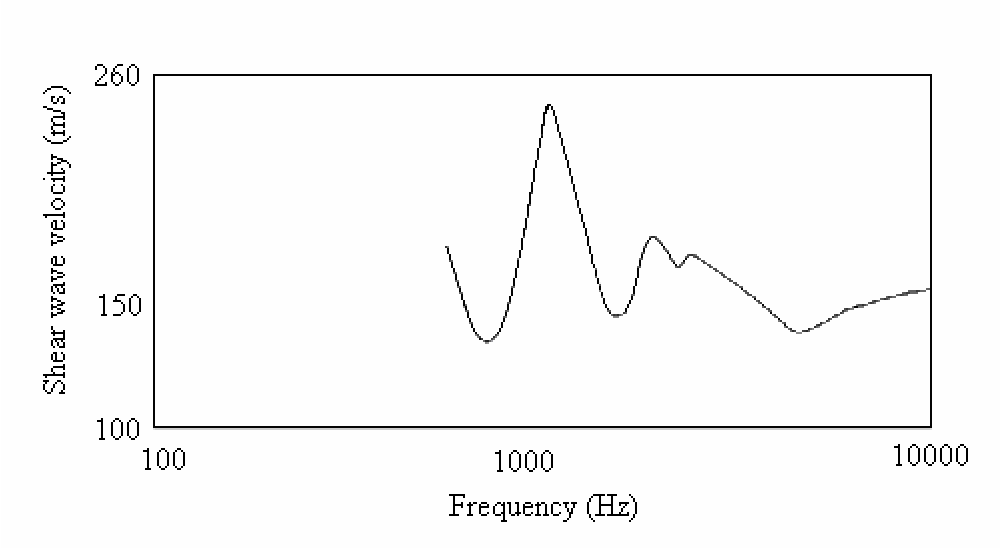

Figure 13. Variation of shear wave velocity with frequency (Blewett et al. 2000).

Other results obtained from various confining pressures shown that an increase in confining pressure on the sample reduces the difference between the maximum and minimum velocity values (Blewett et al. 2000).

2.6.3 Problems associated with bender element testing in general

Time or phase lag

The transfer functions relating the physical wave forms to the measured electrical signals introduce significant phase or time lags that are different at the transmitting and receiving benders. The time lag of the system as a whole can be measured by putting bender elements for generating and detecting waves in direct contact with each other. This calibration method was originally proposed by Dyvik and Madshus (1985), who found a nil time lag for small bender transducers. This method was later used by others (e.g. Brignoli and Gotti, 1992; Gajo et al., 1997), who found a time lag of 5 μs and 2.8 μs for larger benders.

Wave interference and reflection at rigid boundaries

Arulnathan et al. (1998) preformed bender elements tests to investigate how the interference of incident and reflected waves at rigid boundaries can affect the determination of travel time. The transmitter and receiver caps are assumed to be perfectly rigid boundaries and finite elements analyses were done. The results of the finite elements model shows that the correct travel time can be obtained when the ratio of bender separation L to wave length λ is more than or equal to 1/4. In other words the wave length λ must be less than or equal to 4L, or that there must be at least a quarter wave within the sample separation L. As L/λ decreases below 1/4, travel times are progressively underestimated, and hence shear wave velocity overestimated.

Although there are many errors and uncertainties associated with bender element testing, the technique has nevertheless gained popularity in the recent years. Dyvik and Madshus (1985) found that the G_{max} (and thus shear wave velocity) obtained from resonant column device and bender element tests were in excellent agreement. Not only has the technique been used to investigate small strain stiffness of soils, many authors have found various applications for the use of bender elements e.g. sample disturbance (Sasitharan et al., 1993; Dasari and Bolton, 1998), anisotropy of G_{max}

(Pennington et al., 1997), and liquefaction potential (De Alba et al., 1984).

2.7 FAST FOURIER TRANSFORM (FFT)

Phase results can be analyzed using the Fast Fourier Transform, which yields the phase angle and spectral amplitude of all frequencies smaller than half the logging frequency.

Signals are assumed to be composed of a number (perhaps an infinite number) of (co)-sinusoidal components at various frequencies, each having a given amplitude and initial phase. A typical sinusoidal component with amplitude A, initial phase θ and circular frequency *f* is illustrated in *figure 14 (a)* below. *Figure 14 (b)* illustrates another representation of the same sinusoidal component, this time as the vector sum

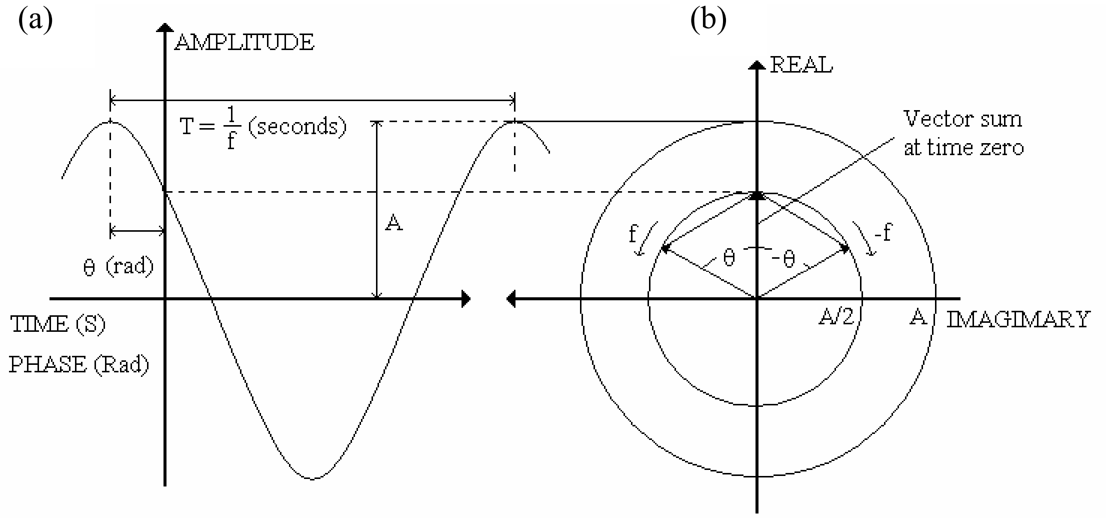

Figure 14. Interpretation of a co-sinusoidal wave (Randell, 1987).

of two counter-rotating vectors, each with amplitude A/2. One has initial phase angle θ and rotates with frequency *f* while the other has initial phase angle –θ and rotates with frequency –*f*.

FFT converts the data from the time domain into data in the frequency domain shown in *figure 15*. FFT results are represented by complex numbers, and each complex number represents the state of the wave at a certain frequency.

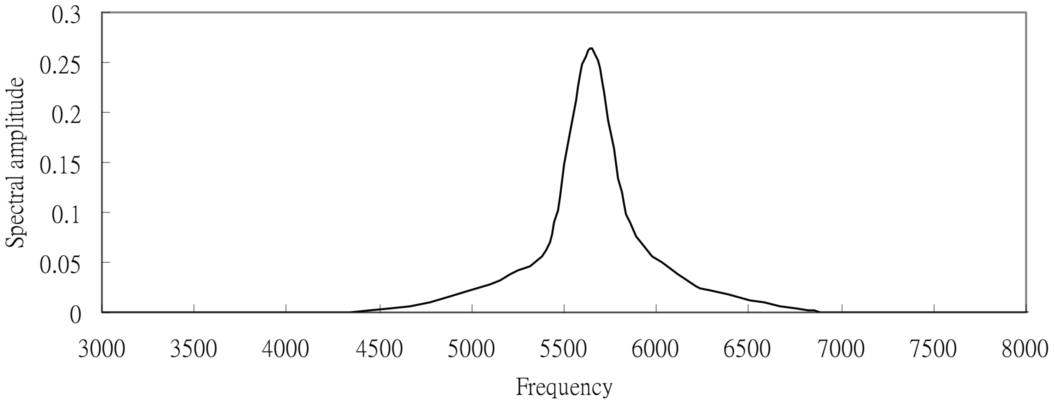

Figure 15. Wave expressed in the frequency domain.

For a certain complex number a + *j*b, the spectral amplitude can be calculated using *equation 5:*

$$A = \sqrt{(a)^2 + (b)^2}$$

Eq. (5)

and the phase angle θ at each frequency can be calculated by using *equation*

$$\theta = \tan^{-1}\left(\frac{b}{a}\right)$$

Eq. (6)

The frequency *f* to which the complex numbers correspond can be calculated using *equation 7*:

$$f = \frac{n}{N\Delta t} \qquad \textbf{Eq. } (7)$$

where Δt is the time interval at which the wave is sampled, N is the total number of samples taken, and n is the index number of the complex number set ($0 < n < N$).

Thus at each frequency a corresponding amplitude and a phase angle can be determined. The dominant frequency is indicated by the frequency with the maximum spectral amplitude and phase angle corresponding to this maximum amplitude is used to determine the phase difference. A FFT must be done on both input and output waves to obtain the corresponding θ_{in} and θ_{out} so the phase difference $\Delta\theta$ can be calculated. Since *equation 6* only yields a phase angle from -90° to 90°, it is necessary to plot the complex number on a real-imaginary graph. From the graph, the real phase difference can be seen and the corresponding number of $\pi/2$'s can be added. Consider position A in *figure 16*, for a negative real value and a positive imaginary value, a phase angle calculation with the (equation above) might yield a value of – 45°, but it is in fact 90° + 45°.

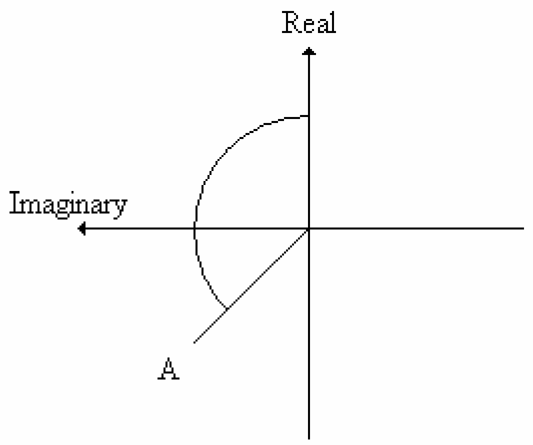

Figure 16. Phase angle expressed as a complex number.

2.8 GOLD TAILINGS MATERIAL PROPERTIES

The gold tailings used in this research originated from the Free State gold fields. The Free State gold fields are part of the gold deposit lying in an oval area approximately 42 000 km² in Gauteng, North-West Province and the Freestate Province. The sediments of the deposit originated from the surrounding Archian granite-greenstone terrains and were laid down between 2.7 and 3 billion years ago. Detrital particles in the deposit underwent low grade metamorphism which led to re-crystallization, forming gold.

The gold extraction processes used are generally similar. Rocks containing gold minerals are retrieved and crushed into rock powder, from which gold is extracted. Following the extraction of gold, the rock powder water mixture, known as tailings, are transported to tailings dams in the form of slurry for disposal. Vermeulen (2001) showed that the mineralogy of the gold tailings delivery slurry can be summarized as:

- 75% Quartz
- 10% Muscovite
- 5% Pyrophyllite
- 5% Illite
- Traces of Clinochlore, Kaolinite and Pyrite.

Tailing material has been categorized into tailings sands, which consist of highly angular to sub-rounded bulky but flattened particles larger than 63 μm and tailings slimes smaller than 63 μm, which contain thin plate-like particles as well as some silt sized particles similar to the sands (Vermeulen, 2001).

Gold tailings can classified as a low to high plasticity rock flour with a specific gravity Gs of around 2.75 Mg/m^3. It has also been shown that tailings has no cohesion and an effective angle of internal friction, independent of grading, density, overconsolidation and effective stress level, of 34° (Vermeulen, 2001).

CHAPTER 3

TEST METHODOLOGY

3.1 BACKGROUND

The hypothesis states that **a clear relationship exists between shear wave velocity and void ratio for gold tailings** under a range of stress conditions. In order to validate the hypothesis, a testing strategy was set up to which the testing procedures were strictly followed. This chapter describes the testing strategy used, the test procedures, the experimental system setup and calibration, some properties of the material used, and the procedures for sample preparation and bender element testing.

3.2 TESTING STRATEGY

The testing strategy used during this project was to test samples of gold tailings in a triaxial apparatus modified to accommodate bender elements. Shear wave velocity measurements were made at known stress conditions and void ratios

The initial aim was to use the first arrivals method in conjunction with phase sensitive detection of continuous waves. The first arrivals, although obscured by near field effects, could be used first to obtain a rough estimate of the shear wave velocity. Having a rough indication of the shear wave velocity, phase sensitive detection could then be used to determine the actual shear wave velocity.

In order for the method to be valid, an assumption had to be made that shear wave velocity is independent of the driving frequency, which is not true. From the literature study, Blewett et al. (2000) showed that shear wave velocity is frequency dependent under the same stress and void ratio conditions within a triaxial specimen. This implied that pulse generated response could yield different results as the output response generated from continuous waves. On the basis of this knowledge, the investigation was then simplified to use the first arrivals method to estimate the shear wave velocity, with the near field component shown as error ranges of the shear wave velocity.

To generate data for the first arrivals method, a square pulse, similar to *figure 7(a)*, was used. Although the response of a square pulse is most affected by near field effects, it is the simplest wave form to generate. To generate more complicated waveforms such as a sinusoidal pulse similar to *figure 7(c)*, a programmable signal generator would be required. Three sets of first arrivals data were taken so the data could be stacked. Since noise is random, stacking the received data reduced the noise and thus increased the quality of the results.

In addition to square pulse data, continuous wave data was taken to validate the frequency dependency of shear wave velocity within a triaxial specimen.

Samples were prepared at specific target void ratio. It was not clear what the magnitude of collapse would be during the flushing process, thus in order to cover the range of void ratios required, various target void ratio were used. From *figure 3* it is clear that the limits of void ratios sand specimens prepared in the laboratory are between 0.4 and 1.1. In this experiment, the choice of target void ratios ranged from 0.6 to 1.3. After the flushing and saturation process, the range of void ratios achieved ranged between 0.578 and 0.828.

3.3 TESTING PROCEDURE

After the sample was prepared at the target void ratio, the sample was flushed to remove any air trapped within the specimen. Full saturation was achieved by applying a back pressure of between 400 and 500 kPa, yielding a minimum B-value of 0.96.

Each specimen was taken through various consolidation stages with effective stress increments of 25, 50, 100, 200, 400 kPa and then swelled through the same effective stress increments. This would amount to 9 effective stress increment data sets. During each consolidation and swelling stages, the volume change of the sample was measured using a burette volume gauge. This allowed the void ratio to be determined at any time during the test.

At each consolidation or swelling stage, the shear wave velocity was determined. For the time of flight measurements, three readings were taken using a square wave at a frequency of approximately 0.02 kHz. A square wave propagating at low frequency has the same effect as a single pulse if the frequency of the square wave is low enough so that before the next pulse, the energy from the previous pulse has already attenuated.

For phase sensitive measurements, shear wave data was taken for a frequency range of 1 kHz to 15 kHz at approximately 50 Hz increments. For this part of the experiment, continuous sinusoidal waves would be used.

3.4 EXPERIMENTAL SYSTEM SETUP

The instrumentation used was similar to that illustrated by Dyvik and Madshus (1985), but was augmented to improve the quality of the received signal and the means of interpretation. The test system setup is shown in *figure 17* below:

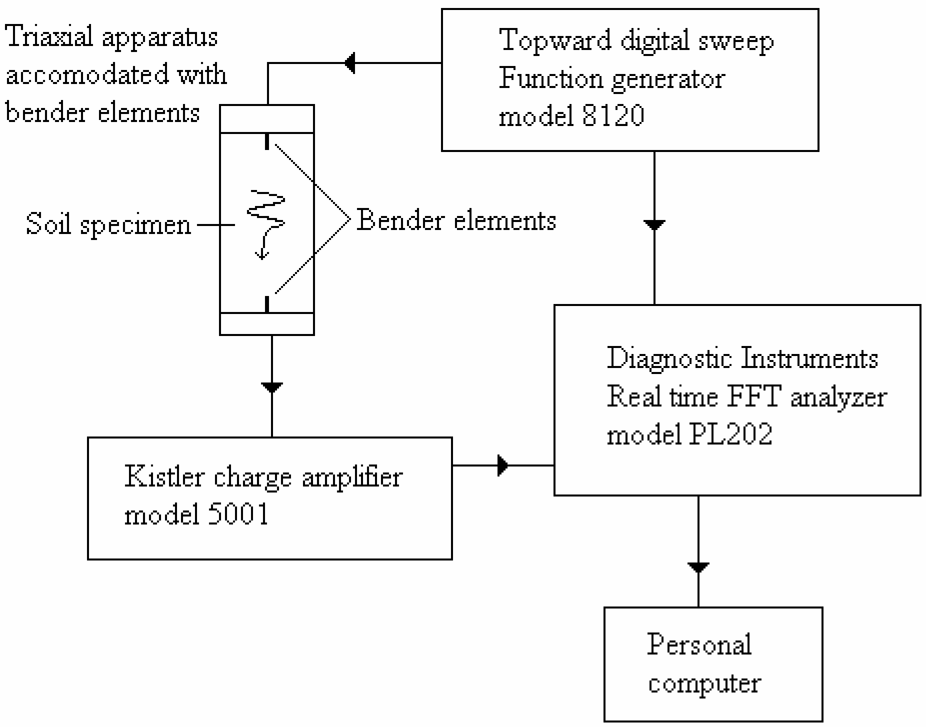

Figure 17. Instrumentation setup.

3.4.1 Signal Generator

The use of sinusoidal waves of various forms have been reported by various authors (Jovičić et al., 1996; Pennington et al., 1997). In order to generate these complex wave forms, a programmable digital function generator would be required. In this research, the methods made use of square pulses and continuous sinusoidal waves and thus a less sophisticated function generator could be used. The function generator was a Topward Digital Sweep Function Generator Model 8120 which allowed continuous square and sinusoidal waves to be generated at the required frequencies.

3.4.2 Charge Amplifier

Bender elements are piezo-ceramic based transducers and are therefore essentially charge rather than current-driven devices. Charge-driven devices perform best when matched with appropriate signal receiver equipment. Output signals have traditionally been connected directly to an oscilloscope for viewing or to PC for storage in digital format. In this research, a Kistler 5001 charge amplifier interfacing between the receiving bender and the FFT analyser was used. This provided a significantly lower load on the receiver bender. With this configuration, received signals were of greater amplitude and thus more accurate travel time results can be determined.

3.4.3 Bender elements

The piezoceramic elements used were Bi-morph elements obtained from RS components with a cantilever action vibrating at 10µm peak to peak. The elements were of dimensions 14.9mm x 1.55 mm x 0.65mm. One of the most important aspects associated with the use of bender elements is the waterproofing of the elements, since piezo-ceramics are high impedance devices that may short when coming in contact with moisture. Many attempts were made with various dipping techniques to waterproof the element without success. A technique was then developed to encapsulate the bender in epoxy. The volume of epoxy was significantly larger then the bender and after the epoxy had hardened, and the mould was removed, the excess

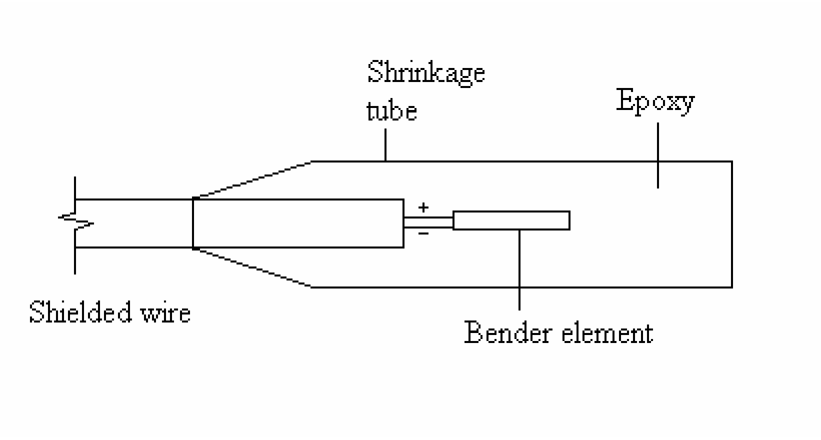

Figure 18. Bender element encapsulation.

epoxy was ground off using a miniature grinder. This technique proved simple and effective. The layout of the bender encapsulation is shown in *figure 18*.

The encapsulated elements were then placed within the pre-drilled holes in the top cap and the base pedestal of the triaxial cell. The fixed end of the bender was embedded into the hole by injecting epoxy into the hole using a syringe and needle. It was important to ensure that no air was trapped within the epoxy, as this could weaken the epoxy. The system is shown in *figure 19* below.

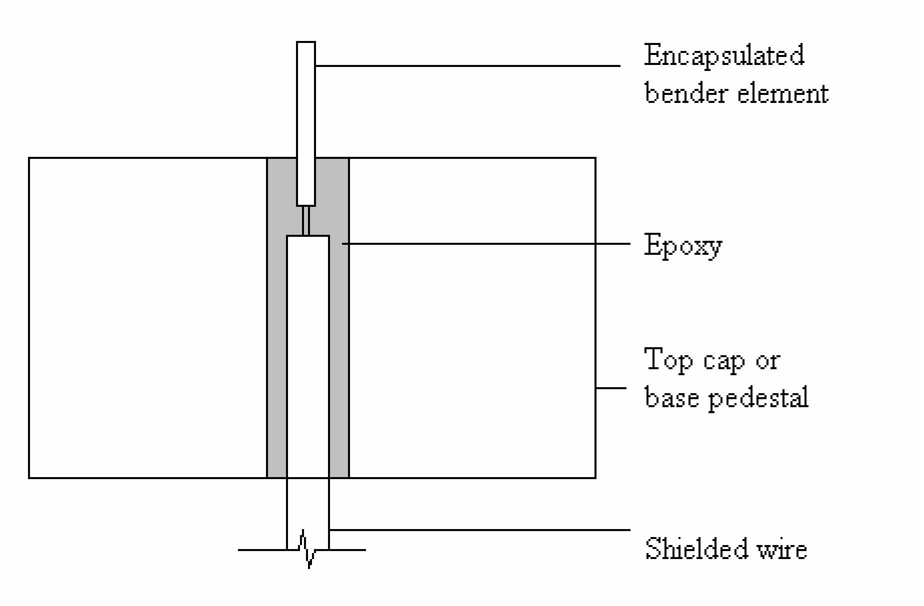

Figure 19. Layout of bender within top cap or base pedestal.

The stiffness of the sealant used for the encapsulating of the element was also important. If the stiffness of the sealant used was too low, the element will vibrate within the sealant layer without any movement transferred to the soil particles. On the other hand, if the stiffness of the sealant was too high, it would minimize the movement of the element to the extent that the signal could not be detected. Cracking would also occur at the base of the element if the sealant was too brittle.

Both these situations were encountered during the investigation. The element was encapsulated with an extremely stiff epoxy, which restricted the movement of the element completely. A polyurethane sealant was also evaluated as a sealant. In this case, the sealant was too soft to transfer any movement from the element to the soil.

The epoxy used was an araldite epoxy obtained from Hitech Polymers. The epoxy consisted of the resin (LY5052) and a hardener (HY5052) mixed in 500 : 190 ratio. The epoxy hardened in approximately 90 minutes and obtained full strength in 24 hours.

After the encapsulation process had been completed, , the top cap bender had a dimension of 2.5 mm x 1.83 mm, protruding 9.9 mm from the top cap, and the bottom bender had a dimension of 2.75 mm x 2.05 mm and a protrusion of 11.5mm from the base pedestal.

Shielded wires were used to minimize noise interfering with the signal. Wires for the base pedestal and the top cap both exited the cell from below the pedestal. The bottom wire exited through a predrilled hole in the centre and the top cap wire exited through a specially designed plug. A top view of the base pedestal and an enlarged view of the plug are shown in *figure 20* below.

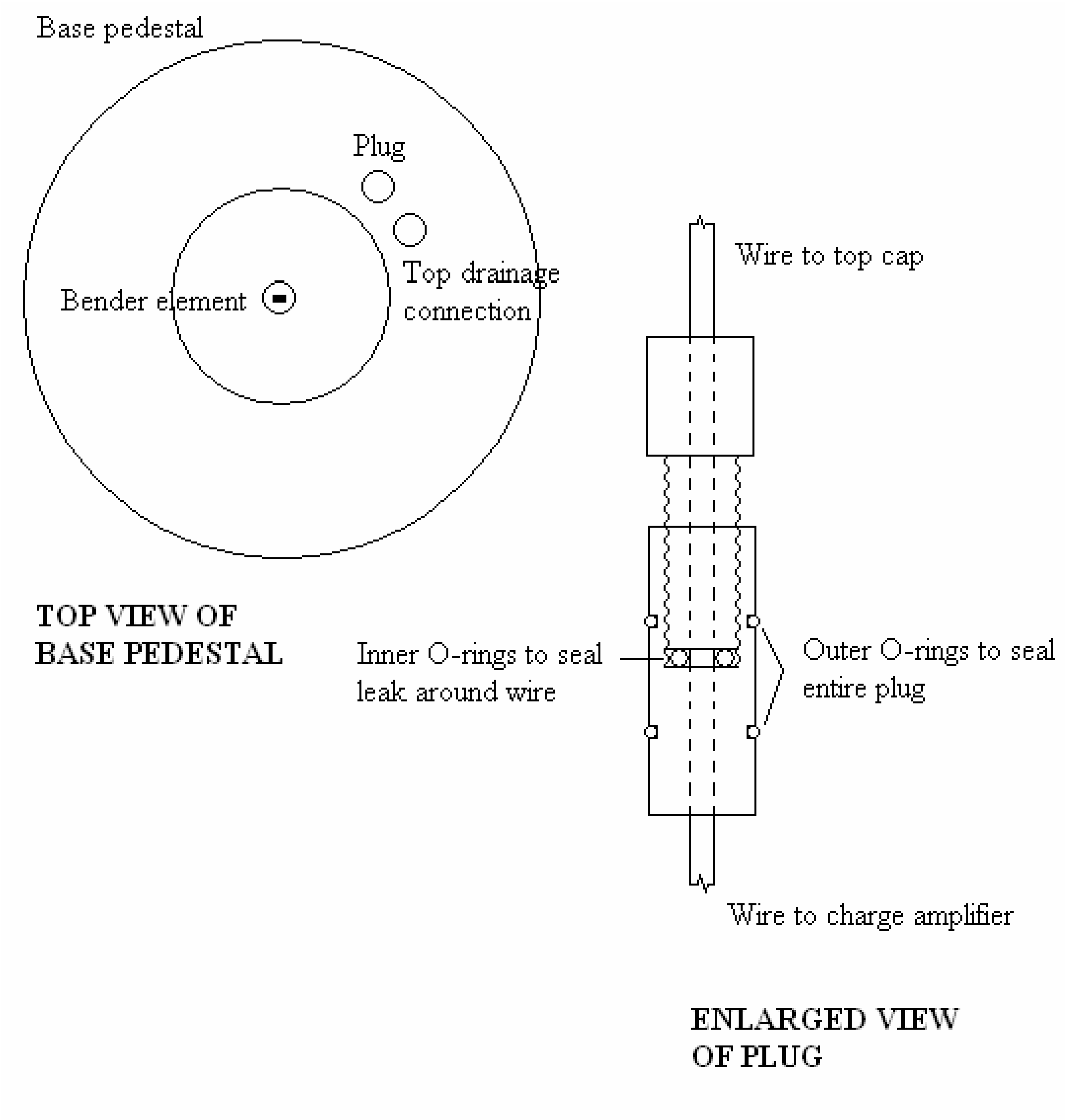

Figure 20. Top view of base pedestal and enlarged plug design.

One of the problems associated with using bender elements within saturated soil specimens is earthing of the system. When working within a triaxial cell, the metal parts of the cell and the triaxial apparatus can also act as an antenna and receive the surrounding noise. It was thus important that the triaxial apparatus was earthed in some way. In this investigation, the earthing was done by connecting the negative terminal of the receiver bender to any metal part of the triaxial apparatus. In this way, the whole system would be referenced against the same earth. Improper earthing resulted in the received signal not showing any phase change upon a change in driving frequency. This implied that the received signal did not result from the mechanical shear wave, but from some other form of wave energy captured by the receiving bender.

A schematic representation of the bender element development process is attached in *Appendix B*.

3.4.4 Data acquisition system

Both input and output data was fed into the Diagnostic Instruments PL202 Real Time FFT Analyser and recorded. The data was later downloaded and stored in a personnel computer from which all analysis were done.

3.4.5 Pressure system

Two water pressure systems were used to supply pressure to the triaxial system. Back pressure was provided by a compressor which yielded a maximum pressure of 500 to 600 kPa. The readout unit for this pressure system was a Bourdon tube pressure gauge. The cell pressure was provided by a GDS pressure controller with a resolution of 1 kPa and a maximum pressure of 3 MPa. Pore pressure was measured by a Gems Pressure transducer GS4200. The GDS offered the benefit of volume change measurements, which enabled sample volume change to be estimated during initial flushing stages. *Figure 21* above illustrates the setup for the triaxial test.

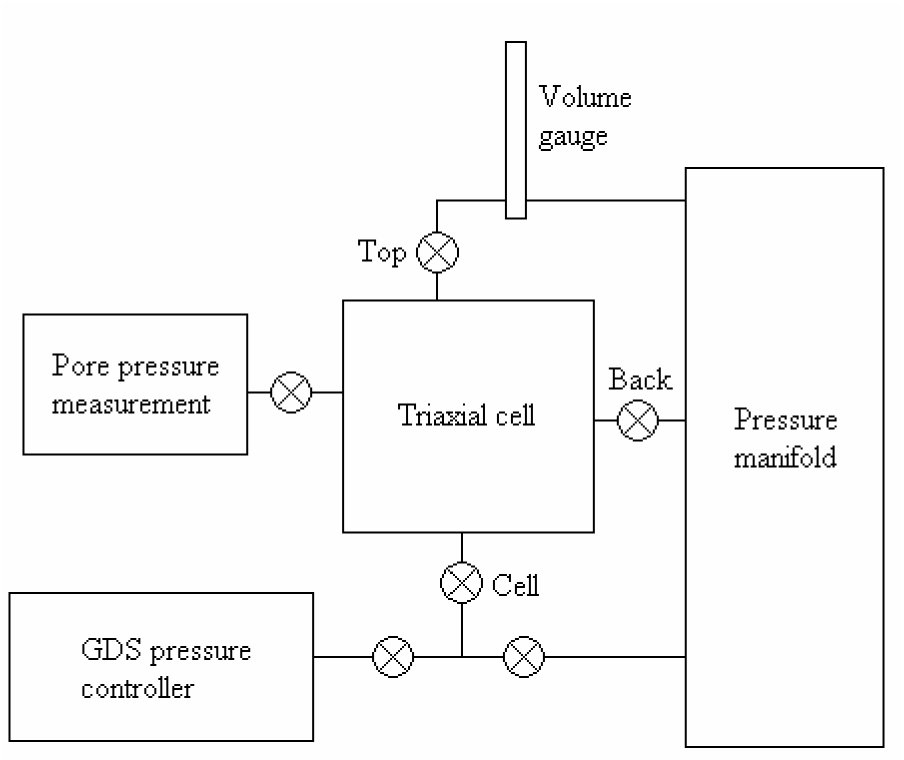

Figure 21. Pressure system layout.

3.5 SYSTEM CALIBRATION

Calibration of the test equipment was done against a Budenberg dead weight calibration system. The pore pressure system was first calibrated against the Budenberg system and included the pore pressure transducer and the readout unit. The

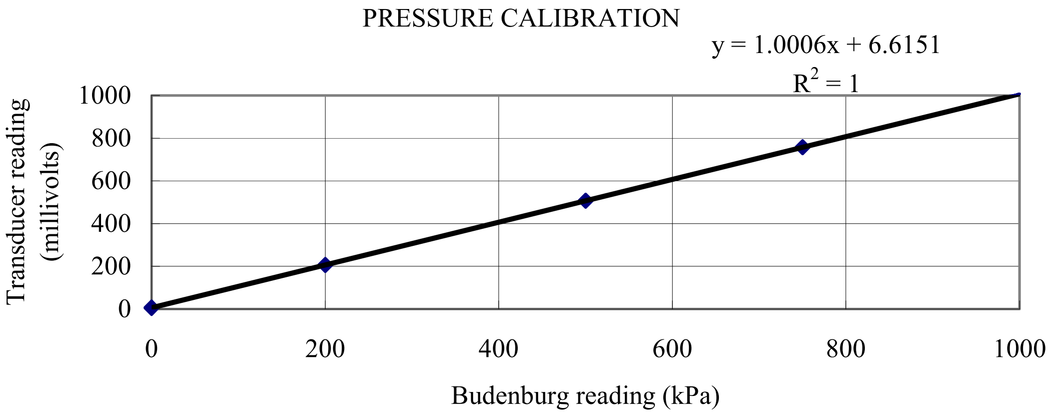

Figure 22. Calibration result of pore pressure transducer against the Budenberg dead weight calibration system.

calibration result showed that during loading and unloading, the system exhibited no hysteresis. There was however a 7 kPa offset, which was accounted for during the test. The GDS and the bourdon tube pressure gauge were then calibrated against the pore pressure system. Both showed no or little deviation from the true pressure.

From the literature study, many authors have reported on the time delay of the bender element system. They reported time delays in the range of 0 to 5 microseconds. During this study, the time delay of the bender element system was completely ignored, as the delay would produce shear wave velocity errors of less then 0.1%.

3.6 GOLD TAILINGS

The gold tailings used could be described as a grey sandy silt with a specific gravity, Gs, of 2.7, which was determined by a commercial soil testing laboratory. In order to

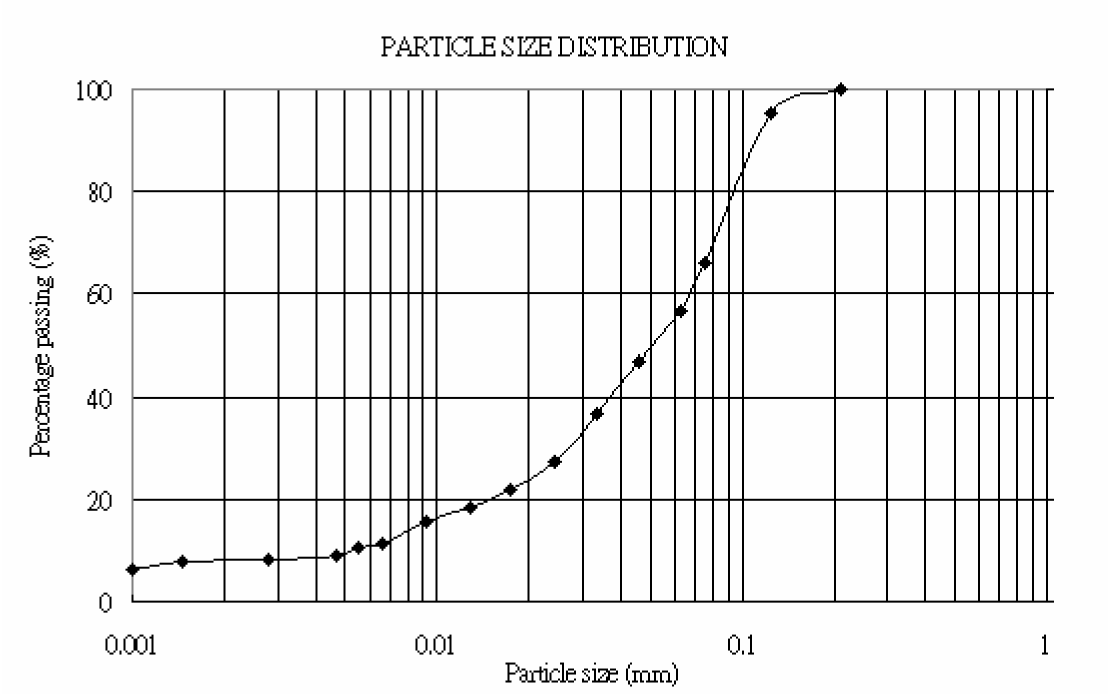

Figure 23. Particle size distribution of gold tailings specimen.

produce a particle size distribution curve for the sample, a sieve analysis (according to TMH procedures) and a hydrometer test (according to BS and ASTM procedures) was done. The sieve analysis indicated the size distributions for coarser particles (particles > 0.75 μm) while the particle size distribution for fines (particles < 0.75 μm) was obtained from the hydrometer test. The particle size distribution result is shown in *figure 23*.

Since the amount of fines could significantly alter the position of the steady state line, and thus the soils susceptibility to liquefaction, it was possible that fines content could also influence the shear wave velocity. According to Thevanayagam et al. (2002), there is a certain threshold fines content, FC_{th}, which defines the soil's response to shear behavior for the same global void ratio. With fines content above FC_{th}, the coarse grained particles becomes dispersed within the fines and the shear behavior is dominated by the fines. Below this FC_{th}, the shear behavior of the soil is dominated by the coarse grained particles. From the particle size distribution, it could be deduced that the fines content for the sample used was approximately 65 % with clay fraction (platy particles passing 0.002mm sieve) of approximately 13 % of the entire sample. This implied that, according to the intergranular matrix diagram classification (Thevanayagam et al., 2000), the shear behavior of this tailings would be dominated by the fines with coarse-grained particles acting as a reinforcing element.

Electron micrographs were taken of the various fractions of the specimen to obtain some indication of the shape and surface texture of the soil particles. These micrographs are attached in *appendix A*. The micrographs of the entire sample show that the sample consisted of larger angular particles (tailings sands) as well as finer platy particles (tailings slimes) clinging to the larger particles. Tailings sands further consisted of smooth surfaced, angular to flat grains with some rough surfaced, more rounded grains. Tailings slimes, on the other hand, consisted generally of platy particles with some silt sized, bulky particles which had similar texture to the smooth surfaced sands.

During the microscopy session, microanalysis of the sample was also done to analyze the constituent elements in the particles. *Table 1* below shows the various material fractions with its composite elements and the percentage by weight for each element. These microanalysis results are also attached in *Appendix A.*

	Constituent element in percentage by weight (Error) for:		
Element	Material retained on 150 µm sieve	Material retained on 75 µm sieve	Material fines (<75 µm)
Aluminum (Al)	2.16 (± 0.20)	0.26 (± 0.15)	6.01 (± 0.32)
Silicon (Si)	97.84 (± 1.01)	99.74 (± 0.90)	63.79 (± 0.72)
Iron (Fe)			17.34 (± 1.30)
Potassium (K)			2.79 (± 0.23)
Sulfur (S)			10.07 (± 0.74)

Table 1. The constituent elements of each material fraction with its proportion (by weight) in the sample.

This is in agreement with the findings of Vermeulen (2001) for gold tailings originating from the same region, who found similar percentages for the various elements in the different fractions.

3.7 SAMPLE PREPARATION AND TRIAXIAL TESTING

Sample preparation played a very important part of this research in order to obtain samples at various initial void ratios. The moist tamping technique was used for all samples preparation. Gold tailings material was well mixed, air-dried and left in a sealed container. All samples were prepared from the same material obtained randomly from the container. About 1kg of material was removed from the container and placed into a smaller container to be ready for test the following day. The moisture content of the material was tested and the required moisture was added to a preferred working moisture content of 10 - 15 percent. Materials prepared the same way and under the same conditions ensure that samples were consistent in terms of the preparation method. This consistency eliminated any differences in the result due to different sample preparation techniques.

All tests were preformed on samples of size 50 mm x 100 mm. The required void ratio was obtained from the moisture content and the dry unit weight of the material from the following equation:

$$e = Gs(1+w)\frac{\gamma w}{M/V} - 1 \qquad \textbf{Eq. } (8)$$

where γ and γ_w are unit weight of the soil and unit weight of water respectively, *w* is the moisture content in the material, *Gs* is the specific gravity of the soil, M is the sample mass and V the sample volume. In this case, the total sample mass was back calculated from a target void ratio, assuming an ideal sample with the same volume as the split mould. Once the target void ratio was determined, the total sample mass was divided into 5 equal masses and compacted in 5 layers of 20mm in a split mould. This ensured that the density was uniform throughout the entire sample.

After the sample had been built, it was placed onto the bottom porous disk. The sample dimensions were measured by a vernier caliper and the sample weight by a digital scale accurate to two decimal places. Both the dimension and weight measurements were done including the bottom porous disk. The weight and mass of the disk were then taken into account.

Once the sample was measured and weighed, the latex membrane and the top porous stone were placed onto the specimen. Porous stones used were copper porous disks with predrilled holes to accommodate the bender elements. Finally the top cap was

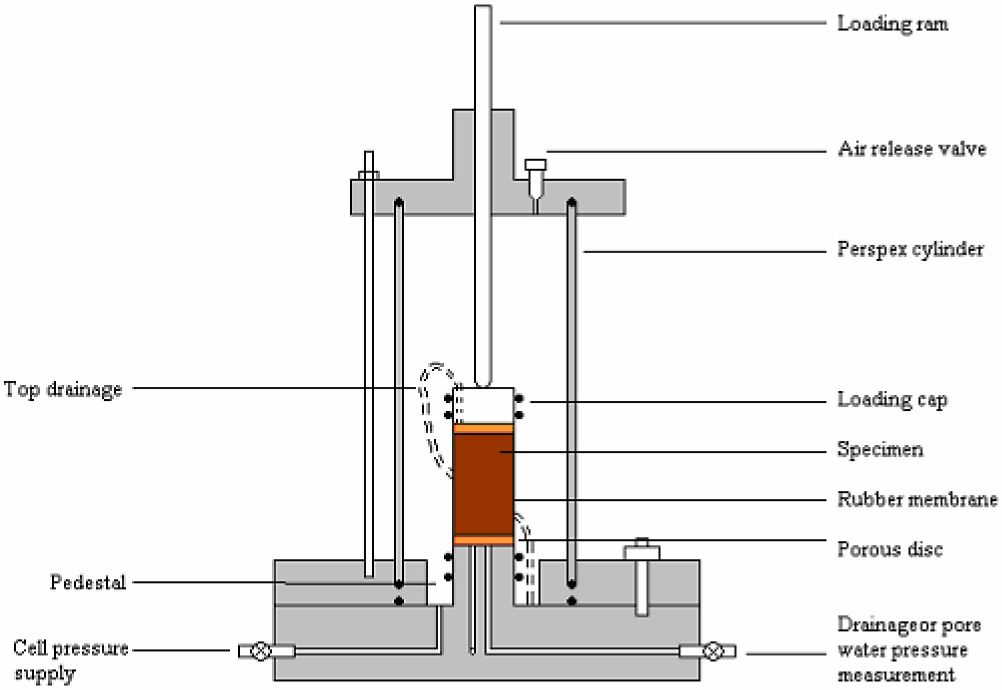

Figure 24. A schematic illustration of the Wykeham Farrance triaxial apparatus

placed onto the specimen and the latex membrane sealed with O-rings. After the sample was placed on the triaxial apparatus, the perspex cell was fitted. The triaxial apparatus used was a Wykeham Farrance triaxial apparatus, with the main features illustrated in *figure 24.*

A moisture sample was then taken to determine the initial moisture content at which the sample was built. The moisture sample was weighed, oven dried for approximately 24 hours, cooled to room temperature and weighed again to determine the moisture content.

Cell water was allowed to flow under a small head of about 16 kPa from the de-airator into the triaxial chamber until filled. During this stage the air relief valve at the top of the triaxial cell was kept open. Once water flushed out the air relief valve, the cell valve was closed, after which the air relief valve was closed. The cell valve to the de-airator was then closed and the cell valve to the GDS pressure controller opened. The pressure in the cell was now controlled by the GDS pressure controller, which was set to 25 kPa.

One of the potential difficulties during saturation was the possibility of collapse of the material. Any volume change would alter the void ratio, and this must be taken into account. Collapse was observed to occur upon wetting of the material during the initial flushing process. To approximate the magnitude of collapse, the volume change of the GDS controller were recorded during the flushing process. This volume change took into account the sample collapse, as well as secondary effects such as the reduction in the volume of the air bubbles in the cell, any cell deformation as well as any minor volume changes in the system. It was argued that the secondary effects would be small compared to the volume change of the sample due to collapse during flushing. The volumetric changes induced during flushing were thus accounted for during the analysis process. The volume of collapse was taken as the volume change during the first opening of the back valve (begin flushing) and close of the top valve (begin of saturation).

During the flushing process, de-aired water was allowed to flow from the de-airator through the back valve, through the sample, and out the top valve. The process took a few days, during which all possible collapse was assumed to have taken place. The change in volume in the GDS pressure controller was assumed to be the change in volume of the sample due to collapse.

After the specimen was flushed in the triaxial cell, it was saturated using a maximum back pressure of 400 kPa until the B value was above 0.95, at which point the sample was assumed to be fully saturated. During saturation, the cell pressure was always kept 15 kPa higher than the back pressure.

The consolidation process took place at mean effective stresses of 25, 50, 100, 200 and 400 kPa. The use of the GDS pressure controller yielded problems during the consolidation process due to its slow response to pressure changes. The cell pressure dropped immediately when the back pressure (top) valve was opened to begin consolidation. The conventional pressure system allowed a much higher flow rate, thus restoring the required cell pressure almost immediately. The GDS pressure controller had a much lower flow rate and thus the time required to restore the original cell pressure was much longer. This implied that the cell pressure during consolidation would not be constant and would yield consolidation conditions that did not adhere to classical consolidation theory. For this investigation therefore, the consolidation process was simplified to only recording volume change data. A volume gauge reading was taken prior to consolidation. The sample was then consolidated to the required effective stress by increasing the cell pressure and consolidating against a back pressure of 400 kPa. A final volume gauge reading was then taken after the sample had consolidated for a few hours. When no more volume changes could be observed, the shear wave data was taken, keeping the top drainage valve open.

Shear wave data was taken at effective stresses of 25, 50, 100, 200, and 400 kPa using square pulses. Following consolidation, the sample was taken through stages of swelling, again at effective stresses of 200, 100, 50 and 25 kPa. Shear wave data was again taken at each stress in the same manner as during consolidation.

No triaxial shear was conducted during this research, and thus after the last swelling stage was completed, the top valve was closed to prevent any further changes in the void ratio of the sample. The pore pressure at this point would remain at 400 kPa. The cell pressure was then released and the cell fluid and the perspex cell removed. Since the top valve remained closed, the sample remained intact even after the cell pressure was removed.

Before the sample was removed from the pedestal, dimensions were taken to determine the final void ratio. After the final dimensions of the sample were measured, the top cap and the porous disk were removed carefully to prevent any moisture or soil loss. The sample was then removed from the pedestal and weighed. Finally, the moisture content of the sample was determined. This final moisture content provided an additional means of determining the final void ratio.

CHAPTER 4

ANALYSIS

4.1 BACKGROUND

In order to establish a relationship between void ratio and shear wave velocity, both these parameters have to be taken into consideration. This chapter provides the analyzed void ratio and shear wave velocity results, as well as the methods of analysis from which the results were obtained.

4.2 VOID RATIO ANALYSIS

One of the problems that Papageorgiou et al. (1999) encountered working with Merriespruit tailings was the collapse behavior of tailings material upon wetting. This is caused by the plate-like particles being held together by suction pressures when moist, but upon wetting, the suction pressures are lost, resulting in a decrease in volume. The volume change measured by the GDS pressure controller was assumed to be the same as the volume of collapse. The volume change during saturation was assumed to be zero, in other words, it was assumed that any water entering the specimen during saturation would displace or dissolve some air and the specimen volume would remain the same. Volume changes during consolidation and swelling were measured by means of the volume gauge. The initial volume was determined from the average specimen height and diameter measured. Using the initial moisture content, w, and initial specimen weight, M, the mass of solids could be determined via *equation 9:*

$$M_{solid} = \frac{M}{(w+1)} \qquad \textbf{Eq.}\ (9)$$

where M_{solid} is the mass of solid particles within the specimen. With the mass of solids known, the volume of the solids, V_{solid}, could be determined from *equation 10:*

$$V_{solid} = \frac{M_{solid}}{Gs\rho_w} \qquad \textbf{Eq.}\ (10)$$

where Gs is the specific gravity of the soil particles and ρ_w is the density of water. In this investigation, Gs was 2.7 Mg/m³ and ρ_w was 1 Mg/m³. Using the solid volume, V_{solid}, and the initial specimen volume, V, the volume of voids, V_v, could be determined. The void ratio of a specimen could be calculated as:

$$e = \frac{V_v}{V_{solid}} \qquad \textbf{Eq.}\ (11)$$

where e is void ratio, V_v is the volume of voids. The volume changes during consolidation or swelling were used to determine the void ratio at the various consolidation or swelling stages.

A back analysis was also done to estimate the uncertainty range for the void ratio calculations. Since the specimens were not sheared, the final volumes could be determined. The back analysis used the final volume of the specimen, and assuming that no soil particles were lost during the test. In other words, the volume of solids remained the same throughout the test and thus the void ratios could be determined for the various consolidation and swelling stages.

4.3 SHEAR WAVE VELOCITY ANALYSIS

Input and output data was sampled at 256 samples per channel within 2.45 ms. In other words, data was sampled at 104.5 kHz per channel. Output data could be divided into two groups, square pulse data used for first arrivals, and continuous sinusoidal wave data used for phase sensitive detection.

4.3.1 Signal interpretation

For a typical input pulse shown in *figure 25* below, the first arrivals data from various test specimens showed the initial upward near field component followed by the shear wave arrival in the opposite direction of the driving pulse. It was found that when the orientation of the one of the benders was reversed, the polarity of the received signal would also reverse as expected.

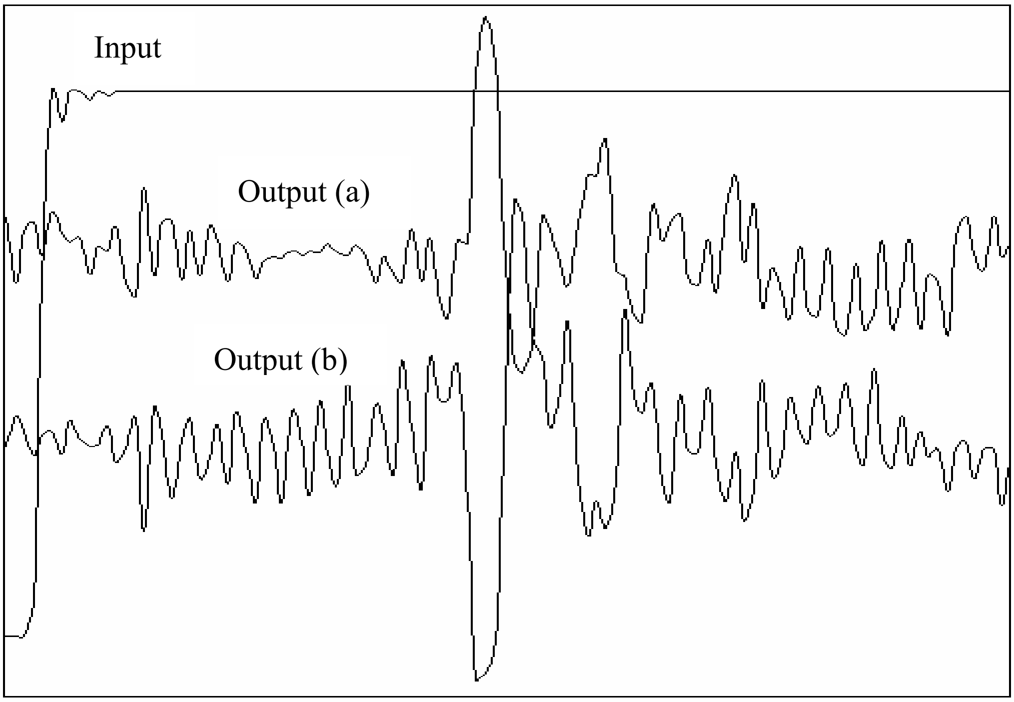

Figure 25. Typical received signal with reversed polarity for square wave input.

This would affect the first arrivals results as well as phase sensitive detection outcomes. When the polarity of the signal was reversed, the arrival of the shear wave would be in the opposite direction as driving pulse, as shown by *figure 25* signal *(b)*.

In the same condition, the phase difference should be determined as the difference between an input peak and an output trough. Similarly, when the first peak of the received signal is in same direction as the driving pulse, as shown in *figure 25 signal (*a*)*, the phase difference is the peak to peak difference.

4.3.2 Analysis method: first arrivals

The velocity of shear wave propagating through a medium could be determined from *equation 12:*

$$Vs = L_E/t \qquad \textbf{Eq.}\ (12)$$

where Vs is shear wave velocity, L_E is the effective distance of wave propagation and *t* is the time in which the distance was covered. In the case of shear wave velocity propagating within a triaxial specimen, L_E, the distance of wave propagation was taken as the tip to tip distance between the two generator and receiver bender elements (Viggiani and Atkinson, 1995). The change in travel distance during consolidation and swelling was also taken into account. Since the specimen was loaded in isotropic conditions within the triaxial cell, it was assumed that the axial strain in each direction was the same. In other words, the volumetric strain $\Delta V/V$ could be defined as:

$$\frac{\Delta V}{V} = (1+\varepsilon_x)(1+\varepsilon_y)(1+\varepsilon_z) - 1$$ **Eq.** (13)

where $\varepsilon_x = \varepsilon_y = \varepsilon_z = \varepsilon$. The effective travel distance, L_E, could then be determined by *equation 14:*

$$L_E = L\ (1 - \varepsilon)$$ **Eq.** (14)

where L is the initial specimen height less the bender lengths.

To determine the time of wave propagation was not simple, since the received waves were usually obscured by near field effects, as discussed in the previous chapters.

In order for the analysis to be consistent, the arrival of the shear wave was taken as the first peak. This technique is similar to that used by Dyvik and Madshus (1985), Jovičić et al. (1996), Brignoli et al. (1996). The start of the first deflection was taken as the arrival of the near field components. The shear wave velocity will be shown with the near field component as uncertainty ranges.

4.3.3 Analysis method: phase sensitive detection

For phase sensitive detection of the continuous wave analysis, two peaks would be visually identified for both the input and the output wave, and one trough for the output waves would also be obtained in the same manner. The frequency associated with the continuous wave would be calculated from *equation 15:*

$$f = \frac{1}{T}$$ **Eq.** (15)

where f is the frequency and T is the period.

The peaks and troughs would also be used to determine the phase difference between the input and output waves. From the phase difference, the shear wave velocity was determined for each number of wave lengths from 0 to 10, taking into account the change in travel distance as a result of the change in volume due to consolidation or swelling.

Figure 26 shows a typical continuous wave result, with schematic indications about how the peak to peak and the peak to trough phase differences were determined. An indication of whether to use peak to peak or peak to trough phase difference was the direction of the shear wave arrival in comparison with the driving pulse. If the shear

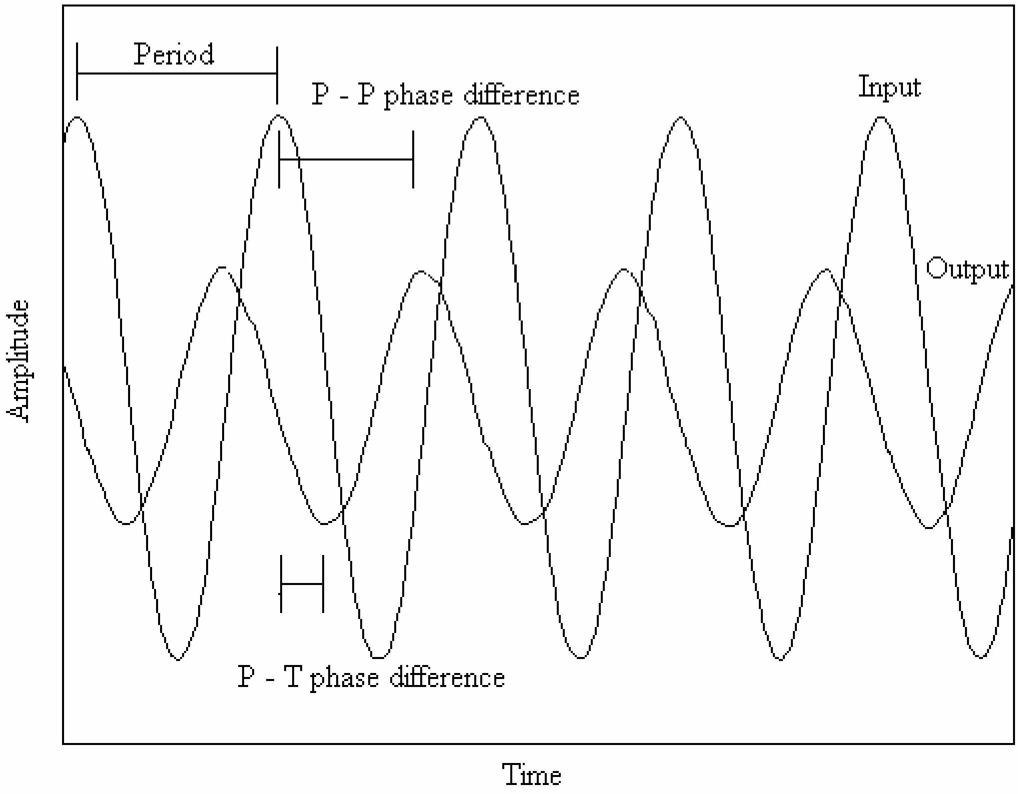

Figure 26. Typical continuous wave result.

wave peak was in the same direction as the driving square wave, then peak to peak phase difference was used and if the shear wave peak was in the opposite direction as the driving square wave, then peak to trough phase difference was used.

4.4 VOID RATIO ANALYSIS RESULTS

The void ratios obtained from the various specimens ranged between 0.47 and 0.87. The differences in void ratio determined from the forward and back analyses ranged from 0.002 to 0.07 with an average of 0.032. Uncertainties in the 6 data sets ranged from 0.2 to 7.9 percent. A summary of void ratios for various samples at various consolidation or swelling stages are shown in the tables below. All worksheets and spreadsheets used in the void ratio calculations are attached in *Appendix C*.

SPECIMEN 06			**Range**	
			Forward	Back
	Change	Volume	Void ratio	Void ratio
	(mm³)	(mm³)		
Initial volume		196595	0.716	0.714
Flushing	5741	190854	0.665	0.664
Saturation	0	190854	0.665	0.664
Consolidation 25 kPa	300	190554	0.663	0.661
Consolidation 50 kPa	750	189804	0.656	0.655
Consolidation 100 kPa	2350	187454	0.636	0.634
Consolidation 200 kPa	3000	184454	0.610	0.608
Consolidation 400 kPa	3900	180554	0.576	0.574
Swell 200 kPa	500	181054	0.580	0.578
Swell 100 kPa	400	181454	0.583	0.582
Swell 50 kPa	600	182054	0.589	0.587
Swell 25 kPa	600	182654	0.594	0.592

Table 2. Void ratio calculations for specimen 06.

SPECIMEN 08			**Range**	
			Forward	Back
	Change	Volume	Void ratio	Void ratio
	(mm^3)	(mm^3)		
Initial volume		198181	0.744	0.685
Flushing	12296	185885	0.636	0.577
Saturation	0	185885	0.636	0.577
Consolidation 25 kPa	300	185585	0.633	0.574
Consolidation 50 kPa	1050	184535	0.624	0.565
Consolidation 100 kPa	3250	181285	0.595	0.537
Consolidation 200 kPa	3550	177735	0.564	0.505
Consolidation 400 kPa	3600	174135	0.532	0.474
Swell 200 kPa	600	174735	0.538	0.479
Swell 100 kPa	450	175185	0.542	0.483
Swell 50 kPa	500	175685	0.546	0.487
Swell 25 kPa	500	176185	0.55	0.492

Table 3. Void ratio calculations for specimen 08.

SPECIMEN 10			**Range**	
			Forward	Back
	Change	Volume	Void ratio	Void ratio
	(mm^3)	(mm^3)		
Initial volume		196153	1.108	1.178
Flushing	31163	164990	0.773	0.844
Saturation	0	164990	0.773	0.844
Consolidation 25 kPa	500	164490	0.767	0.838
Consolidation 50 kPa	2650	161840	0.739	0.810
Consolidation 100 kPa	3550	158290	0.701	0.772
Consolidation 200 kPa	3400	154890	0.664	0.735
Consolidation 400 kPa	3350	151540	0.628	0.699
Swell 200 kPa	450	151990	0.633	0.704
Swell 100 kPa	450	152440	0.638	0.709
Swell 50 kPa	600	153040	0.644	0.715
Swell 25 kPa	700	153740	0.652	0.723

Table 4. Void ratio calculations for specimen 10.

SPECIMEN 12			**Range**	
			Forward	Back
	Change	Volume	Void ratio	Void ratio
	(mm³)	(mm³)		
Initial volume		196388	0.617	0.626
Flushing	4800	191588	0.578	0.586
Saturation	0	191588	0.578	0.586
Consolidation 25 kPa	2050	189538	0.561	0.570
Consolidation 50 kPa	400	189138	0.558	0.566
Consolidation 100 kPa	1500	187638	0.545	0.554
Consolidation 200 kPa	2300	185338	0.526	0.535
Consolidation 400 kPa	2800	182538	0.503	0.512
Swell 200 kPa	600	183138	0.508	0.517
Swell 100 kPa	550	183688	0.513	0.521
Swell 50 kPa	550	184238	0.517	0.526
Swell 25 kPa	550	184788	0.522	0.530

Table 5. Void ratio calculations for specimen 12.

SPECIMEN 14			**Range**	
			Forward	Back
	Change	Volume	Void raio	Void ratio
	(mm³)	(mm³)		
Initial volume		196153	1.341	1.312
Flushing	43000	153153	0.828	0.799
Saturation	0	153153	0.828	0.799
Consolidation 25 kPa	200	152953	0.826	0.796
Consolidation 50 kPa	800	152153	0.816	0.787
Consolidation 100 kPa	2600	149553	0.785	0.756
Consolidation 200 kPa	3100	146453	0.748	0.719
Consolidation 400 kPa	3400	143053	0.708	0.678
Swell 200 kPa	400	143453	0.712	0.683
Swell 100 kPa	400	143853	0.717	0.688
Swell 50 kPa	400	144253	0.722	0.693
Swell 25 kPa	500	144753	0.728	0.699

Table 6. Void ratio calculations for specimen 14.

SPECIMEN 08 C			**Range**	
			Forward	Back
	Change	Volume	Void raio	Void ratio
	(mm^3)	(mm^3)		
Initial volume		197461	0.845	0.823
Flushing	10224	187237	0.749	0.728
Saturation	0	187237	0.749	0.728
Consolidation 25 kPa	300	186937	0.747	0.725
Consolidation 50 kPa	1200	185737	0.735	0.714
Consolidation 100 kPa	3300	182437	0.705	0.683
Consolidation 200 kPa	3400	179037	0.673	0.651
Consolidation 400 kPa	4600	174437	0.630	0.608
Swell 200 kPa	400	174837	0.634	0.612
Swell 100 kPa	500	175337	0.638	0.616
Swell 50 kPa	600	175937	0.644	0.622
Swell 25 kPa	600	176537	0.649	0.628

Table 7. Void ratio calculations for specimen 08C.

4.5 SHEAR WAVE VELOCITY ANALYSIS RESULTS

As discussed previously, the shear wave velocity was determined using two different techniques, namely first arrivals using square pulses and phase sensitive detection using continuous sinusoidal waves at various frequencies. The results for both methods are discussed in this section.

4.5.1 Signal quality

The amplitude of input waves was in the order of 10 volts peak to peak while the amplitude of output waves varied between 5-300 µV peak to peak for varying frequencies. Signal to noise ratio for the output waves, which was also dependent on the drive frequency, were found to vary between 1 and 70. For the phase sensitive detection results obtained using continuous waves, output amplitude was also frequency and system dependent. This is discussed later in the Discussions chapter.

4.5.2 Shear wave velocity from first arrivals method

Shear wave velocity results were determined using the first arrivals method for various consolidation and swelling stages, taking into account the change in wave travel distance due to change in volume during consolidation or swelling.

SAMPLE 06			Travel	Min	Max	
	Change	Volume	Distance	Velocity	Velocity	Diff
	(mm³)	(mm³)	(mm)	(m/s)	(m/s)	(%)
Initial volume		196595	78.5			
Flushing	5741	190854	77.8			
Saturation	0	190854	77.8			
Consolidation 25 kPa	300	190554	77.7	91	100	9%
Consolidation 50 kPa	7540	189804	77.6	109	125	15%
Consolidation 100 kPa	2350	187454	77.3	134	152	13%
Consolidation 200 kPa	3000	184454	76.9	164	183	12%
Consolidation 400 kPa	3900	180554	76.4	212	230	8%
Swell 200 kPa	500	181054	76.5	179	197	10%
Swell 100 kPa	400	181454	76.6	140	154	10%
Swell 50 kPa	600	182054	76.6	114	127	11%
Swell 25 kPa	600	182654	76.7	93	96	13%

Table 8. Shear wave velocity for specimen 06.

SAMPLE 08			Travel	Min	Max	
	Change	Volume	Distance	Velocity	Velocity	Diff
	(mm³)	(mm³)	(mm)	(m/s)	(m/s)	(%)
Initial volume		198181	78.7			
Flushing	12296	185885	77.1			
Saturation	0	185885	77.1			
Consolidation 25 kPa	300	185585	77.0	82	91	11%
Consolidation 50 kPa	1050	184535	76.9	103	111	8%
Consolidation 100 kPa	3250	181285	76.5	125	146	17%
Consolidation 200 kPa	3550	177735	76.0	158	185	17%
Consolidation 400 kPa	3600	174135	75.6	216	252	17%
Swell 200 kPa	600	174735	75.7	168	176	5%
Swell 100 kPa	450	175185	75.7	140	151	8%
Swell 50 kPa	500	175685	75.8	113	133	18%
Swell 25 kPa	500	176185	75.8	96	97	1%

Table 9. Shear wave velocity for specimen 08.

SAMPLE 10			Travel	Min	Max	
	Change	Volume	Distance	Velocity	Velocity	Diff
	(mm³)	(mm³)	(mm)	(m/s)	(m/s)	(%)
Initial volume		196153	78.5			
Flushing	31163	164990	74.5			
Saturation	0	164990	74.5			
Consolidation 25 kPa	500	164490	74.5	76	85	12%
Consolidation 50 kPa	2650	161840	74.2	98	110	12%
Consolidation 100 kPa	3550	158290	73.7	123	134	9%
Consolidation 200 kPa	3400	154890	73.3	160	170	7%
Consolidation 400 kPa	3350	151540	73.0	192	214	11%
Swell 200 kPa	450	151990	73.0	159	174	9%
Swell 100 kPa	450	152440	73.1	129	141	9%
Swell 50 kPa	600	153040	73.1	106	112	6%
Swell 25 kPa	700	153740	73.2	91	104	14%

Table 10. Shear wave velocity for specimen 10.

SAMPLE 12			Travel	Min	Max	
	Change	Volume	Distance	Velocity	Velocity	Diff
	(mm³)	(mm³)	(mm)	(m/s)	(m/s)	(%)
Initial volume		196366	78.3			
Flushing	4800	191588	77.7			
Saturation	0	191588	77.7			
Consolidation 25 kPa	2050	189538	77.4	91	96	5%
Consolidation 50 kPa	400	189138	77.4	105	117	11%
Consolidation 100 kPa	1500	187638	77.2	131	139	6%
Consolidation 200 kPa	2300	185338	76.9	164	179	9%
Consolidation 400 kPa	2800	182538	76.5	204	224	10%
Swell 200 kPa	600	183138	76.6	171	179	5%
Swell 100 kPa	550	183688	76.7	140	154	2%
Swell 50 kPa	550	184238	76.8	122	130	7%
Swell 25 kPa	550	184788	76.8	96	108	13%

Table 11. Shear wave velocity for specimen 12.

SAMPLE 14			Travel	Min	Max	
	Change	Volume	Distance	Velocity	Velocity	Diff
	(mm³)	(mm³)	(mm)	(m/s)	(m/s)	(%)
Initial volume		196153	78.4			
Flushing	43000	153153	73.0			
Saturation	0	153153	73.0			
Consolidation 25 kPa	200	152953	73.0	82	86	5%
Consolidation 50 kPa	800	152153	72.9	102	108	6%
Consolidation 100 kPa	2600	149553	72.6	126	140	11%
Consolidation 200 kPa	3100	146453	72.2	161	176	9%
Consolidation 400 kPa	3400	143053	71.8	198	222	12%
Swell 200 kPa	400	143453	71.9	167	181	8%
Swell 100 kPa	400	143853	71.9	139	154	11%
Swell 50 kPa	400	144253	72.0	113	119	5%
Swell 25 kPa	500	144753	72.0	94	100	6%

Table 12. Shear wave velocity for specimen 14.

SAMPLE 08C			Travel	Min	Max	
	Change	Volume	Distance	Velocity	Velocity	Diff
	(mm³)	(mm³)	(mm)	(m/s)	(m/s)	(%)
Initial volume		1967461	78.6			
Flushing	10222	187237	77.2			
Saturation	0	187237	77.2			
Consolidation 25 kPa	300	186937	77.2	81	91	12%
Consolidation 50 kPa	1200	185737	77.0	99	105	6%
Consolidation 100 kPa	3300	182437	76.6	121	129	7%
Consolidation 200 kPa	3400	179037	76.2	153	166	8%
Consolidation 400 kPa	4600	174437	75.6	198	221	6%
Swell 200 kPa	400	174837	75.7	165	165	0%
Swell 100 kPa	500	175337	75.7	136	149	10%
Swell 50 kPa	600	175937	75.8			
Swell 25 kPa	600	176537	75.9	90	90	0%

Table 13. Shear wave velocity for specimen 08 C.

Specimen 06, 08 and 10 used generating and receiving bender of lengths 10mm and 11.6mm respectively. The initial travel distance was determined by subtracting the combined bender lengths from the specimen height. The change in travel distance during consolidation and swelling were calculated using *equations 13 and 14.* A new set of benders, with lengths 11.6mm and 9.95mm were used for specimens 12, 14 and 08C. The travel distance was calculated using the new bender lengths. The shear wave velocities are shown in the tables above.

The minimum shear wave velocity was determined from the first peak of the received wave, which indicated the arrival of the shear wave. The maximum shear wave velocity was determined from the first deflection of the received wave, which indicated the arrival of the shear wave component.

Spreadsheets were used in order to calculate the shear wave results. These spreadsheets are attached in *Appendix D.* It should be noted that the amplitude for the received wave (the right hand scale) could not be used as an indication of the amplitude of the received wave, as the amplitude was sometimes reversed or increased in order to aid the stacking process. This did not affect the shear wave velocity results, since wave velocity was determined using the time information and not amplitude information.

The uncertainty of the shear wave results ranged from 0 to 19%. This is in agreement with the findings of Ricketts et al. (1996), who suggested that under average circumstances, the shear wave velocity of a geomaterial can be estimated to within 10 – 20%.

4.5.3 Shear wave velocity from phase sensitive detection

Continuous wave data obtained from sample 08C were used to determine the shear wave velocity by phase sensitive detection. An example of the spreadsheets used to calculate the shear wave velocity is shown in *table 14* and *15* on the following pages.

After the frequency and phase difference had been calculated from the peak and trough values, the shear wave velocity was determined for each number of wave lengths. This is shown in *table 14* on the following page. From this spreadsheet, the actual shear wave velocity with its number of wavelengths must be identified. For example, for file 104, the shear wave velocities corresponding to 0, 1 and 2 wavelengths were 3700, 229 and 118 m/s respectively. From the time of flight information, it was known that the shear wave velocity was around 229 m/s, and not

3700 or 118 m/s. This technique therefore allowed the number of full wavelengths within the sample to be determined.

The initial intent was to use a frequency range of between 0 and 15 kHz, since Blewett et al. (2000) found the largest shear wave velocity variation at approximately 1 kHz. During the test, it was noticed that at low frequencies, the output signals were too small to be detected by the FFT analyser. The lowest frequency at which the output signal was visible was approximately 3 kHz.

After the first shear wave velocity was identified at 3.23 kHz, the shear wave velocity for the following files were identified as the value closest to the previous shear wave velocity value. It was assumed that shear wave velocity would not change dramatically within the frequency increment of 50 Hz.

For each frequency, the amplitude of the output signal was also determined. This was obtained from the difference between an arbitrary peak and trough of the output signal. The spreadsheet used in analysing continuous wave velocities is attached in *Appendix E*.

4.6 CONCLUSION

This chapter presented the analyzed results from the experimental phase of the project. These results are discussed in the next chapter. From the discussions, insight can be gained into the behaviour of the material.

CHAPTER 5

DISCUSSION

5.1 BACKGROUND

Using a bender element system within a triaxial apparatus, the shear wave velocity of gold tailings could be measured and from these shear wave velocity results obtained at various void ratios, numerous conclusions could be made.

This chapter presents the discussions of the results obtained during this research. From these discussions, important conclusions will be drawn. Discussion topics include the output signal interpretation, the collapse behavior of the gold tailings material, the void ratio – shear wave velocity relationship and the shear wave velocity – frequency relationship.

5.2 SHEAR WAVE INTERPRETATION

The interpretation of shear wave signals has been the topic under question. The question most debated was the identification of the first arrivals of the received signal. The arrival was often preceded by a near field component which obscured the point of first arrivals of the shear wave. As discussed in section 2.5.1, various types of pulses, ranging from square pulse to single sinusoidal pulse, were used by various authors to obtain the best signal. They concluded that a single sinusoidal pulse yields the best output, while a wide square pulse containing an infinite frequency range yields a signal with the strongest near field and grouped velocity dispersion component.

Although the single sinusoidal pulse and even a narrow square pulse can produce signals of much better quality than the wide square pulse, more sophisticated signal generators are required. In this research, the wide square pulse was used, since this pulse could be generated with any signal generator.

The use of wide square pulses would imply a strong near field component preceding the initial deflection indicating the shear wave. *Figure 27* shows an example of the shear wave result taken from sample 14 at an effective stress of 100 kPa after consolidation. The received wave showed an initial downwards deflection (points a to b), followed by a stronger peak in the opposite direction (point c). Since the benders were installed 180° out of phase, the peak which indicated the arrival of the shear wave would also be 180° out of phase. This implied that the section from the first deflection downwards (point a) to the first peak (point b) indicated the near field component. The arrival of the shear wave was thus taken as the first peak in the same direction as the input pulse at (point b). Similarly, the phase differences for phase sensitive detection were therefore determined using the peak to trough values and not the conventional peak to peak values.

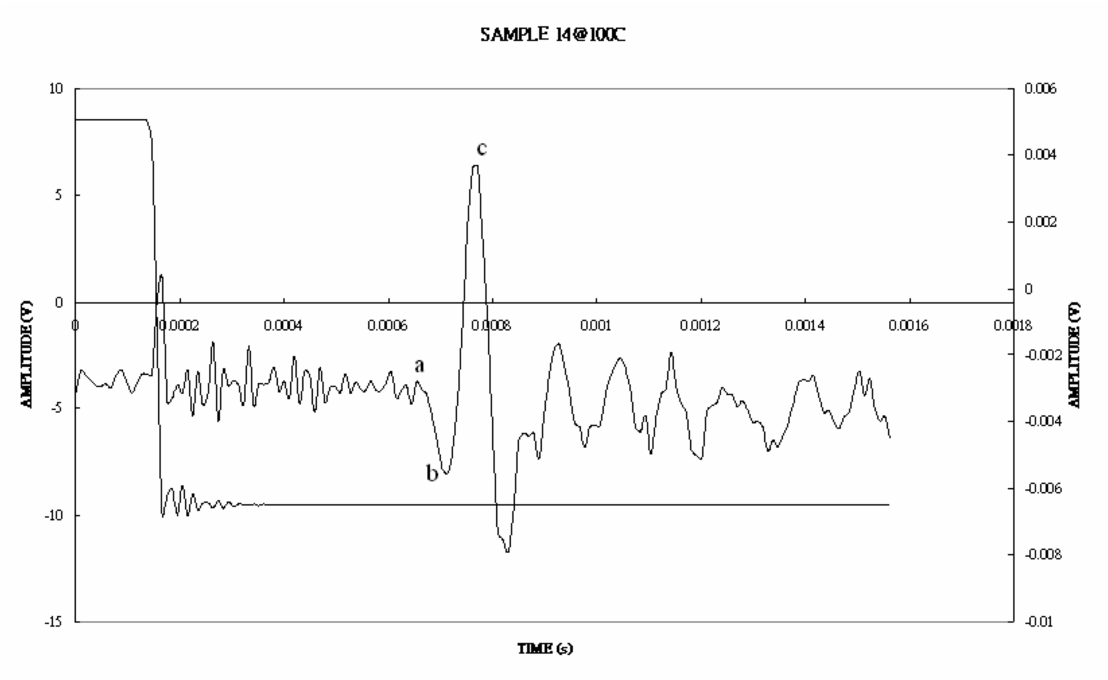

Figure 27. Shear wave result of sample 14 at 100 kPa effective stress consolidation.

Although near field effects seemed to be a potential problem in bender element testing, this does not seem to be the case when dealing with in situ seismic testing. Most engineers working with continuous surface wave testing (CSW) ignore the effect of the near field component. In situ CSW tests usually use maximum frequencies of 50 or 60 Hz. For the receiver to operate outside the near field, the receivers would have to be placed a few meters away from the source. An impractically large energy source would also be required to generate sufficient energy to travel to the geophones. In practice, receivers are simply placed within 2 or 3 meters of the source, which is well inside the near field. Even with the knowledge of this potential deficiency, many researchers continue with CSW testing, with good outcomes and results. The extent of the influence of near field effects in seismic testing is thus questionable.

In numerous samples, the reversibility of the shear wave was demonstrated, as exemplified by *figure 28*. The figure shows two output traces exactly 180° out of

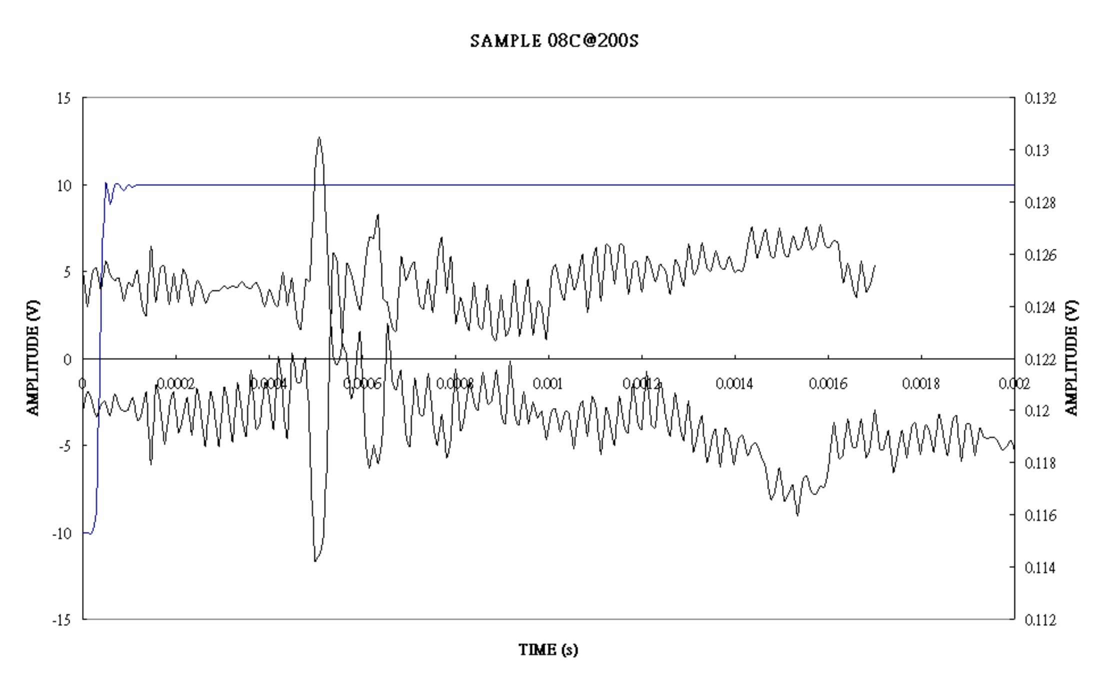

Figure 28. Results from sample 08C at 200 kPa effective stress swelling. Reversibility of the shear wave clearly demonstrated.

phase (ignoring the random noise), which were produced by two opposite square pulses, of which only one is shown. From the reversibility of the output waves, one can be confident that the received signal was in fact a shear wave.

The initial intent was to use FFT to analyze the frequency content of the output continuous waves. During the testing, it was found that the resolution of the data was sufficient for visual inspection and that FFT would not yield better phase results. With a maximum of 256 data points which the recording device could record, the resolution of the frequency after FFT would only be 400 Hz. This was not sufficient for this application. Thus it was decided that visual identification of peaks would be used instead of FFT.

5.3 COLLAPSE BEHAVIOR OF GOLD TAILINGS

During the investigation, it was difficult to obtain a high void ratio after flushing had taken place. The electron micrographs taken of the sample particles show that the material was dominated by angular, bulky particles with some (approximately 13 %) finer, platy particles. This could possibly explain why the specimen could not sustain higher void ratios after flushing. On contact with water, the specimen loses the shear strength when the coarser, angular particles slide into a denser state. If more fines were present, the fines could act as fillers and keep the system stable.

From the works of Papageorgiou et al. (1999), it was noticed that tailings material exhibit collapse behavior to some extent upon wetting. This collapse behavior could be seen with the gold tailings material used in this research. As mentioned before, the volume of collapse was determined from the volume change of the GDS pressure controller. Potential errors may include cavitations of air bubbles, cell deformation as well as any minor volume changes in the system. Despite these potential errors, the void ratios obtained from the forward and backward calculations show relatively little difference. The estimated volume of collapse for the six samples is shown in the *figure 29*.

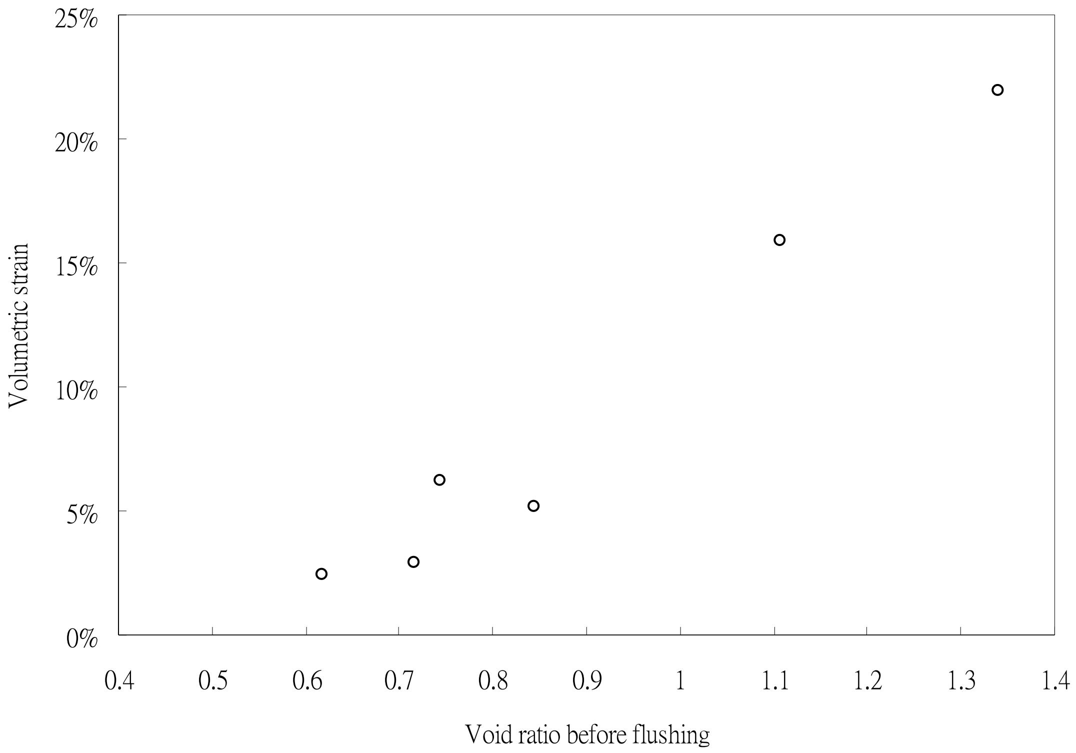

Figure 29. Volume strain due to collapse plotted against target void ratio.

From *figure 29*, it is clear that the volume of collapse is dependent upon the void ratio or density of the material. Samples at a higher void ratio show more collapse then samples at lower void ratios.

5.4 VOID RATIO – SHEAR WAVE VELOCITY RELATIONSHIP

From the graph of normalized shear wave velocity vs. void ratio compiled by Robertson and Fear (1995) (*figure 7*), it was clear that a relationship exist between normalized shear wave velocity and void ratio for sands. A similar relationship was derived by Hardin and Richart (1963) using the resonant column. Both relationships show extreme sensitivity to the effective confining stresses, while Robertson and Fear results also showed that this relationship is independent of the material type. The question which comes to mind, which forms the basis of the hypothesis, was whether a similar relationship holds for silts, of which gold tailings are examples of.

In this section, the shear wave velocity data and the corresponding void ratio values will be shown on various graphs. From these graphs, knowledge regarding the behavior of shear wave propagation in gold tailings can be derived.

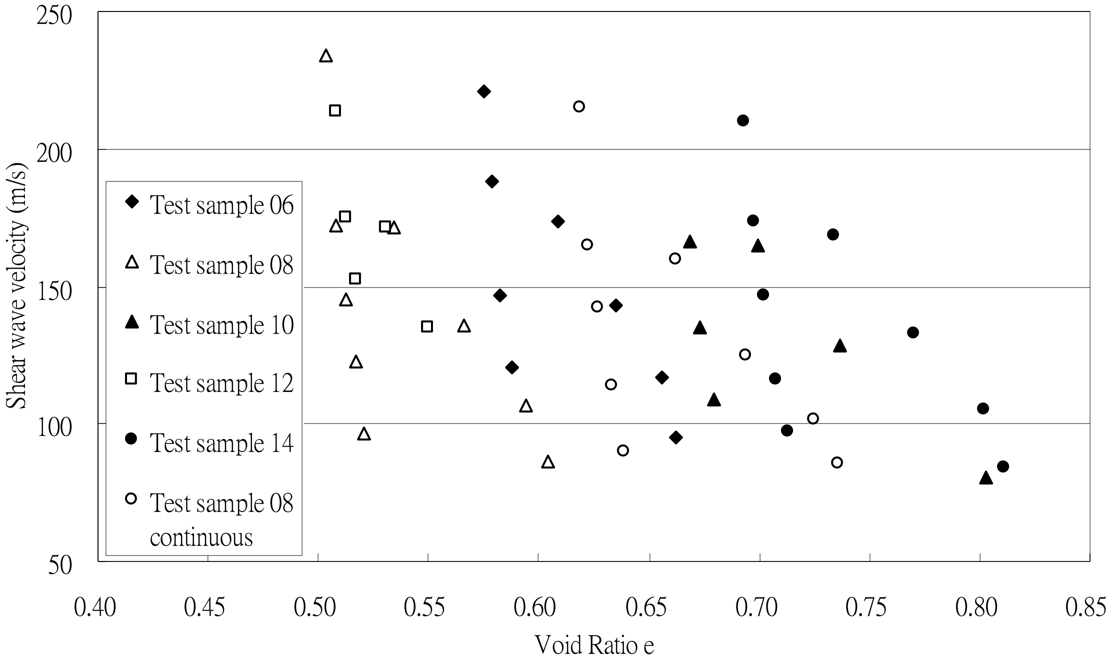

Figure 30. Graph of shear wave velocity against void ratio for various samples.

Figure 30 shows the shear wave velocity vs void ratio results obtained from 6 samples of the same gold tailings material, built at various target void ratios. The results for each sample exhibits two legs, which forms the paths followed during consolidation and swelling. The flatter path of each sample indicates consolidation, while the steeper path shows swelling. It is clear that although the samples were built at very different void ratios, the shear wave velocity seems to be very similar, ranging between approximately 80 m/s and 240 m/s. It should be mentioned that if the shear wave velocity could not be determined for a particular data point, due to for instance a poor signal; the data point was ignored and left out from all figures and analyses.

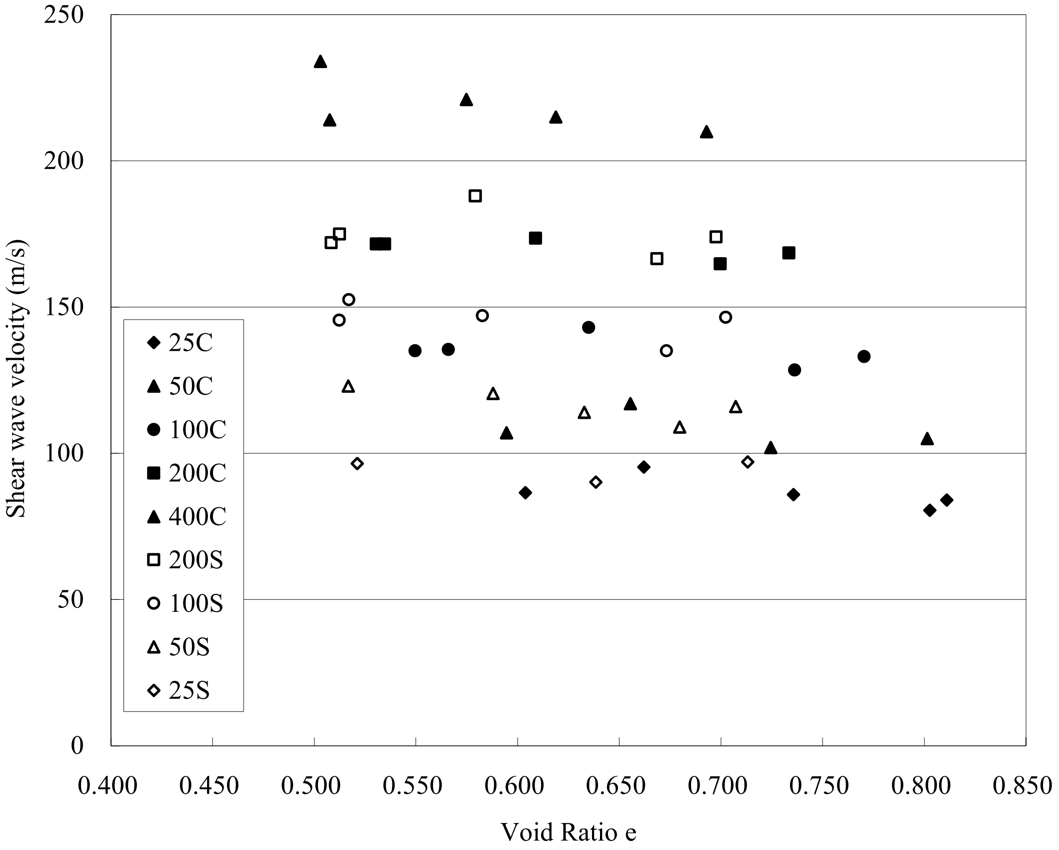

Figure 31. Shear wave velocity vs void ratio plot for various effective stresses.

The results can also be plotted by grouping the data points which have the same effective stress. This is shown in *figure 31,* with full data points being consolidation points and empty data points being swelling points. The legends show the mean effective stress in kPa and the postscripts indicate consolidation (c) or swelling (s). From *figure 31,* it can be seen that firstly, the shear wave velocity is insensitive to the overconsolidation ratio, as the consolidation and swelling data points fall on the same line, for each effective stress increment. Furthermore, it can be seen that there is a relationship between shear wave velocity and void ratio for each effective stress increment. This relationship is further made apparent in *figure 32,* which shows the same shear wave velocity vs void ratio plot, but with trend lines added to each data set. From the trend lines, the relationship between shear wave velocity and void ratio can

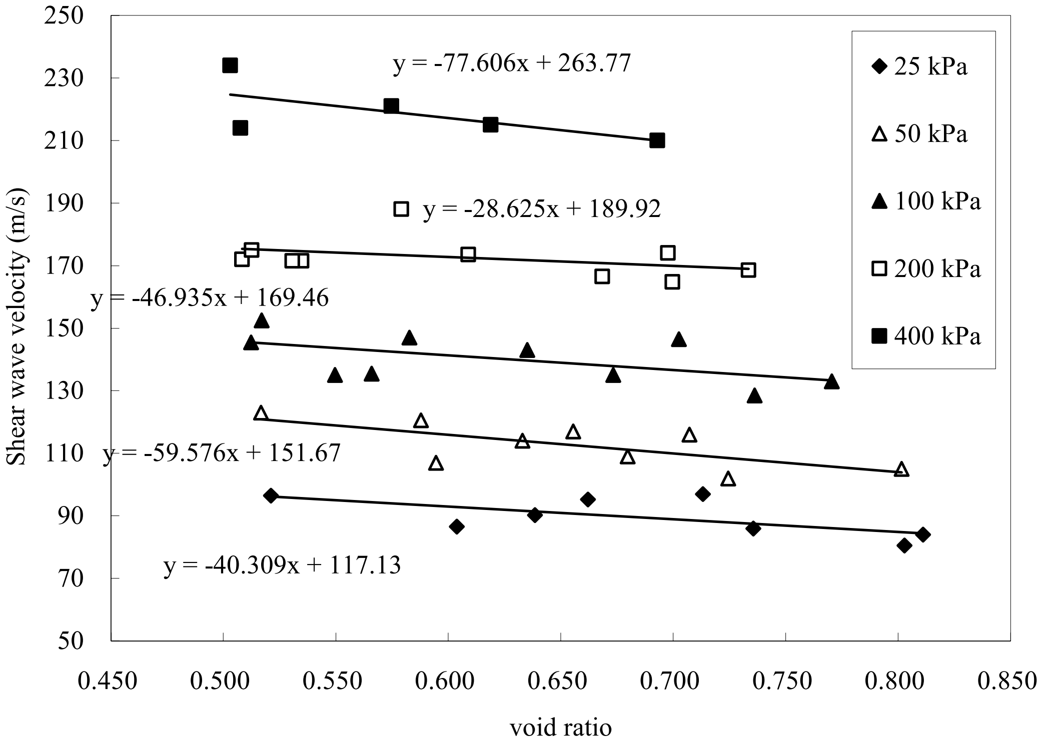

Figure 32. Shear wave velocity vs void ratio graph for various effective stress increments, adding trend lines.

be estimated. The relationships show that a change in void ratio of 0.1 can result in a change in shear wave velocity of between 5 and 8 m/s. From the trend lines, it can also be seen that as the effective stress increases, so does the slope of the relationship. This is consistent with the results obtained by Hardin and Richart using a resonant column (1963).

During the analysis of the result, it was found that the equation used for normalizing shear wave velocity against pressure, *equation 1*, did not yield the best normalization for shear wave velocity determined from gold tailing. Referring back to the normalization equation, *equation 1*; $Vs(n) = Vs\ (Pa / \sigma_v')^{0.25}$, it was found that

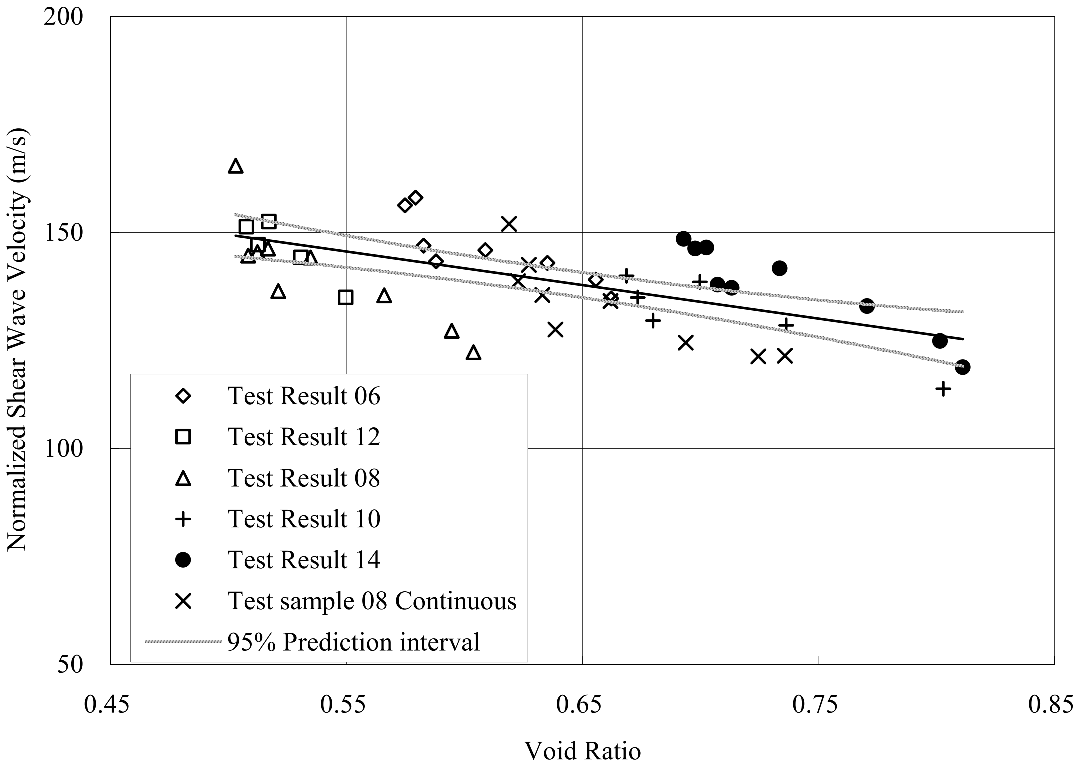

Figure 33. Shear wave velocity being normalized with a factor of 0.28. Including the 95% (solid line) and 80% (dotted line) confidence intervals.

instead of the power value of 0.25, which is used by most authors in their normalization, a power of 0.28 yielded the best regression results. But to avoid confusion and to be consistent with other publications, a power value of 0.25 was used in shear wave normalization in this research. It should be noted that the use of 0.25 instead of 0.28 only made a small difference in terms of the normalized shear wave velocity. After the normalization, the results yield *figure 33.* Included in *figure 33* are the 95% confidence intervals. From this figure, it can be seen that after being normalized, there is a clear relationship between shear wave velocity and void ratio.

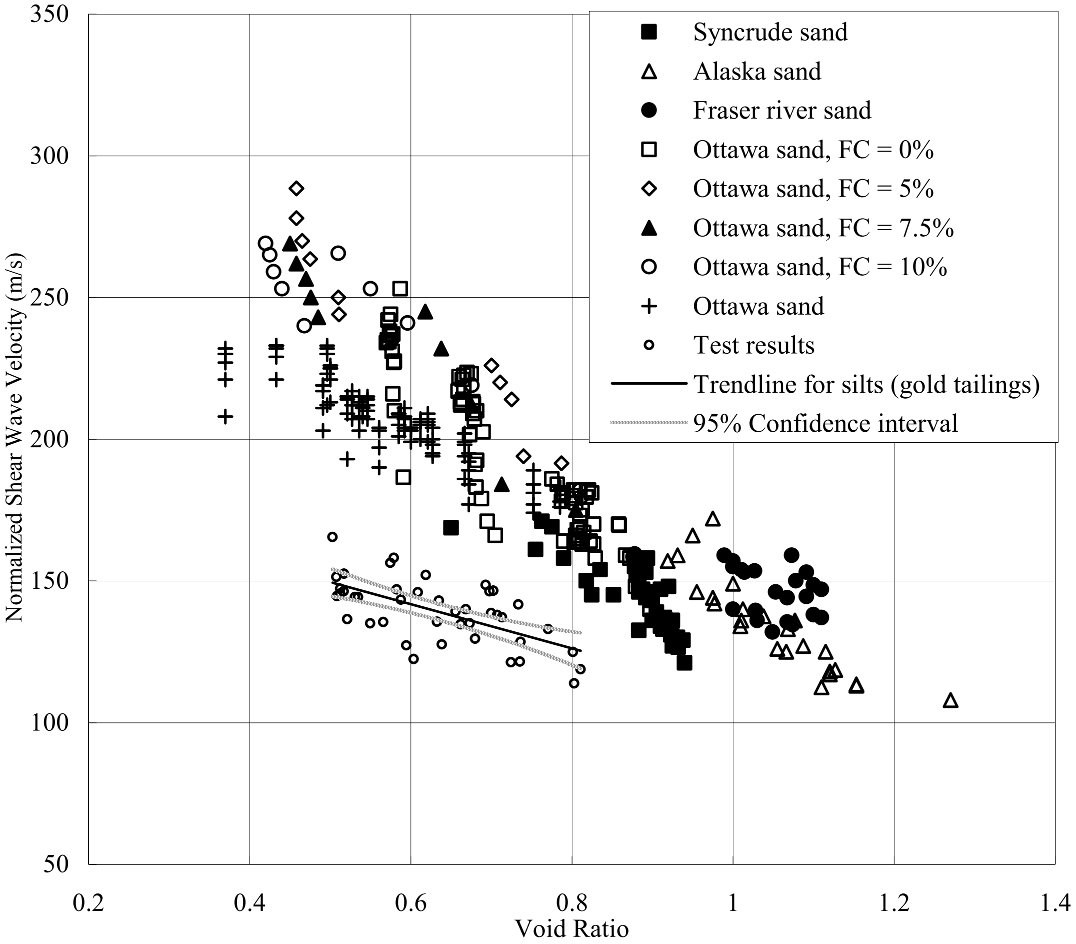

Figure 34. Results obtained in this research imposed on previous results from Robertson and Fear (1995).

Having established the relationship between normalized shear wave velocity against void ratio, it is necessary to compare this relationship to that observed by Robertson and Fear (1995). *Figure 34* shows the normalized results compiled by Robertson and Fear (1995) for sands in larger data points and the results for gold tailings obtained during this research in the smaller data points.

Figure 35 shows the test results in solid square data points plotted on the same graph as the results of Hardin and Richart (1963) for granular materials obtained using the resonant column.

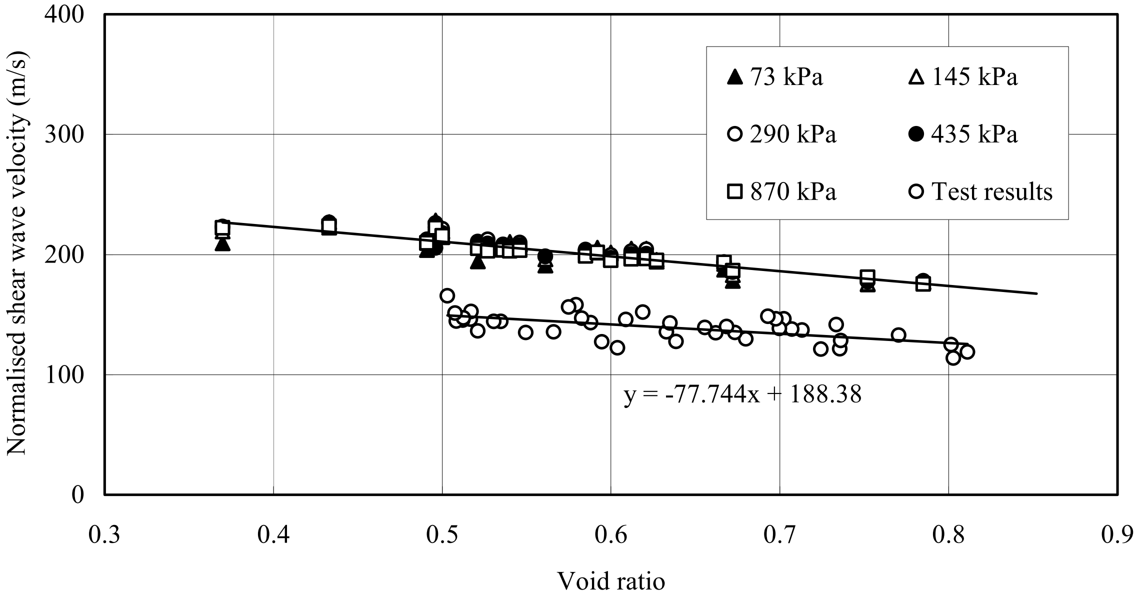

Figure 35. Normalized shear wave velocity imposed on results of Hardin and Richart (1963).

An equation for a least-squares power function regression was derived for all the data points obtained for this research. The equation is shown below:

$$V_s(n) = 117.51e^{-0.355}$$

Although a slightly better R-squared value can be obtained using a straight line regression, the relationship should in fact be some kind of exponential or power function with shear wave velocity values for zero void ratio identical to that of solid particles. For practical purposes, the data points could be approximated by the following straight line equation:

$$V_s(n) = -77.744e + 188.38 \qquad \textbf{Eq.}\ (16)$$

Differentiating *equation 16* yielded:

$$\frac{dV_s(n)}{de} = -77.744$$

This shows the low sensitivity of void ratio to a change in normalized shear wave velocity. A 0.1 change in void ratio only produces a 7.8 m/s change in normalized shear wave velocity. This has some implications for the application of the results from this research, especially when using in situ shear wave velocity measurements to estimate in situ void ratio of gold tailings deposits. Ricketts 1996 suggested that shear wave velocity can only be estimated with an accuracy of 20 percent. This level of uncertainty, coupled with the low sensitivity of the void ratio to a change in normalized shear wave velocity, imply that the relationship shown in figure x (eq xx) should only be used as a guideline and not for exact void ratio determinations. The relationship nevertheless provides a simple and cost effective method to estimate in situ void ratio for gold tailings deposits.

From *figure 34* and *35*, it can be seen that the normalized shear wave velocity vs. void ratio relationship of gold tailings falls below the relationship complied by Robertson and Fear (1995) and Hardin and Richart (1963), and has a smaller gradient. This is not entirely surprising, since the data from Robertson and Fear and Hardin and Richart were derived from natural sands, and sands containing small amounts of fines (≤ 10 %). As discussed in chapter 2, the shear wave velocity may be sensitive to the fines content. According to the intergranular matrix diagram classification proposed by Thevanayagam (2002), the shear behavior of materials used in Robertson and Fear's (1995) compilation will be dominated by the coarse grains. In the case of gold tailings test material, with a fines content of around 65%, the coarse grains will be immersed in the fines with the shear behavior dominated by the fines. From the scanning electron micrographs taken from the tailings mix, it was evident that the fines contain rotund particles as well as platy particles. It is thus questionable whether the response of the soil to small strain behavior is dominated by platy particles alone, the rotund particles or a combination of both.

The stiffness of this conglomerate of platy and rotund particles is significantly lower than the solid particles, and thus with the shear behavior of tailings dominated by fines, the shear wave velocity of tailings should theoretically be lower than values for sands or sands with some fines content below FC_{th}.

The results can also be plotted with shear wave velocity on the y-axis and effective stress on the x-axis, as shown in *figure 36* below. This shows the sensitivity of shear wave velocity to the changes in effective stress. Comparing *figure 32* and *figure 36*, it is clear that shear wave velocity for gold tailings is much more sensitive to the changes in effective stress than to changes in void ratio. In fact, the effect of change in void ratio was so minimal that an attempt to normalize shear wave velocity against void ratio only marginally improved the error in the regression equation.

Using a power function regression of the data points in *figure 36* yields:

$$Vs = 32.11(p')^{0.3189} \qquad \textbf{Eq.}\ (17)$$

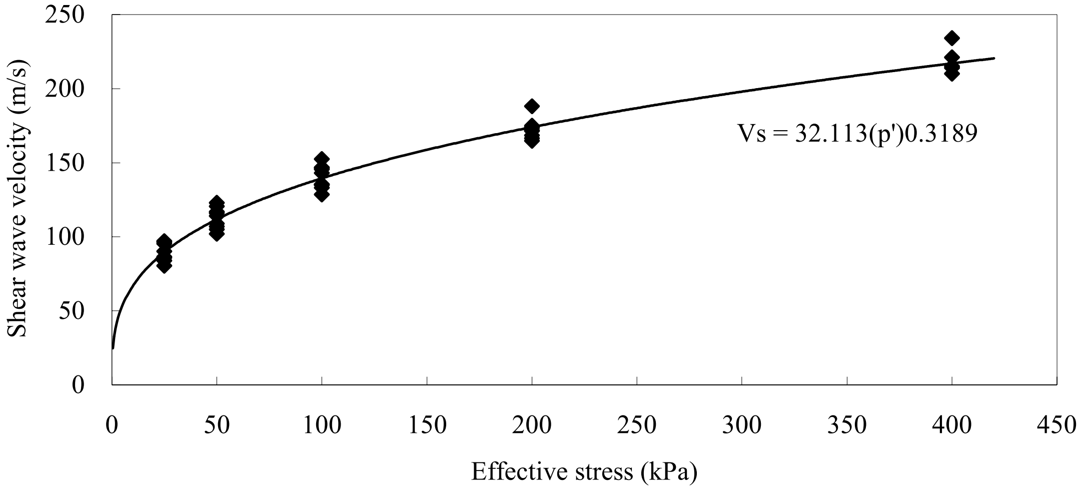

Figure 36. Graph of shear wave velocity against effective stress.

5.5 SHEAR WAVE VELOCITY WITH FREQUENCY

The second part of the results analysis deals with the results obtained from phase sensitive detection using continuous waves. Shear wave velocity had been shown to be a function of the frequency (Blewett et al., 2000). From the results of Blewett et al. (2000), the shear wave velocity could vary as much as a factor of two. Using continuous waves, the changes in shear wave velocity could be seen with changing frequency. From the results obtained at 400 kPa effective stress, a shear wave velocity vs frequency graph was generated as shown in *figure 37*. Empty squares (left axis) indicate shear wave velocity measurements while solid squares indicate output signal amplitude (right axis). From *figure 37*, it can be seen that for an increasing frequency, the shear wave velocity initially decreases rapidly to a minimum at 6.5 kHz, and then remains constant at frequencies in excess of 6.5 kHz. This is consistent with the findings of Blewett et al. (2000). Their results show a peak shear wave velocity at a frequency of around 1 kHz. As mentioned in the previous chapter, the continuous wave measurements for this research were taken where output signals were of significant quality to allow interpretation. Below around 3 kHz, the output was weak and the peaks could not be clearly identified.

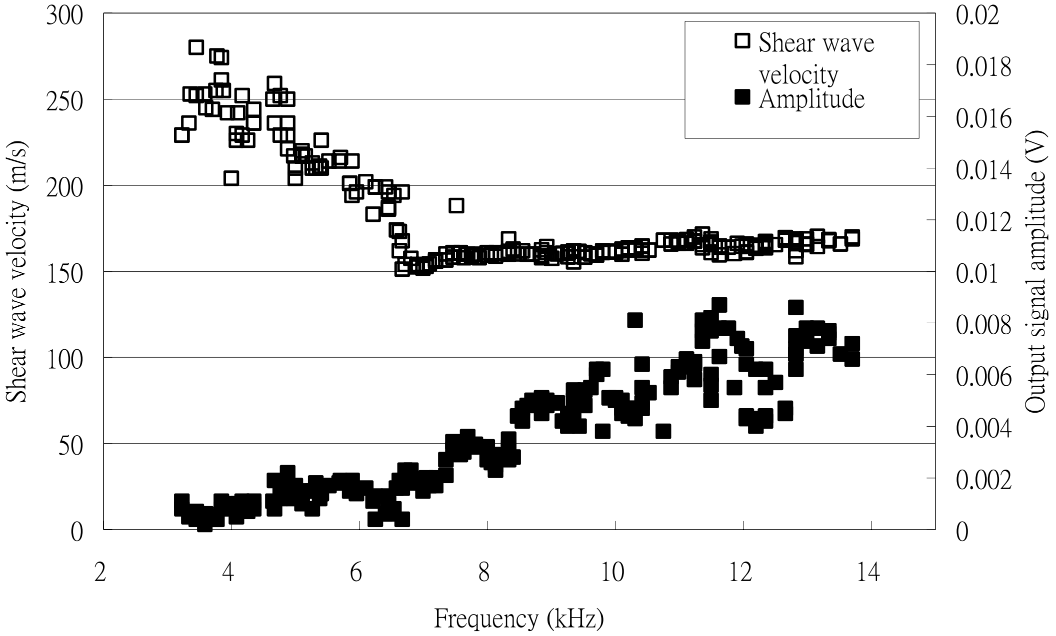

Figure 37. Graph of shear wave velocity and output signal amplitude against frequency.

CHAPTER 6

CONCLUSION

6.1 CONCLUSIONS FROM THE LITERATURE STUDY

- From *figure 7* of the literature study chapter, it is evident that there is a relationship between normalized shear wave velocity and void ratio for sands. This relationship encompasses different types of sands, some of which included small percentages of fines.

- It is evident from *figure 5* that a relationship exists between shear wave velocity and void ratio under constant stress conditions.

6.2 CONCLUSIONS MADE DURING THE RESEARCH PROGRAM

- Cost effective bender elements can be successfully constructed using a method developed by the author using epoxy encapsulation and a hand held grinder.

- In order to generate high quality signals, the shielding of wires and connections of the entire bender element system is important. The addition of a charge amplifier also improves the output signal.

- The arrival of the shear wave can be taken as the first peak of the output signal. The assumption is made that the initial deflection of the output signal is in fact the arrival of the near field component.

- Reversibility of the output signal verifies the reversal property of the shear wave.

- The shear wave velocity of gold tailings is insensitive to overconsolidation ratio.

- The shear wave velocity for gold tailings is significantly more sensitive to the effective stress applied than the void ratio of the material.

- The use of 0.28 instead of 0.25 in the normalization equation (*equation 1)* yields a slightly better shear wave velocity normalization against pressure for gold tailings.

- The void ratio vs normalized shear wave velocity relationship for gold tailings is consistent with the void ratio vs normalized shear wave velocity relationship for sands as published by Hardin and Richart (1963) and Robertson and Fear (1995). The e - Vs(n) relationship for gold tailings lies below the e – Vs(n) relationship for sands and has a flatter gradient.

- The shear wave velocity of gold tailings is sensitive to the frequency. At lower frequencies, the shear wave velocity is higher.

6.3 FINAL CONCLUSION

The hypothesis states that there exists a relationship between shear wave velocity and void ratio for gold tailings. From the results obtained in this research, the hypothesis is accepted. It was demonstrated that a relationship exists between shear wave velocity and void ratio under a range of effective stress conditions. The normalized shear wave velocity - void ratio relationship for gold tailings is positioned below similar relationship compiled by Hardin and Richart (1963) and Robertson and Fear (1995) for sands and sands with small amounts of fines.

CHAPTER 7

REFERENCE

- Abbiss, C.P. 1981. Shear wave measurements of the elasticity of the ground. *Géotechnique,* **31**(1): 91-104.

- Arulnathan, R., Boulanger, R.W. and Reimer, M.F. 1998. Analysis of Bender Element Tests. *Geotechnical Testing Journal,* **21**(2): 120-131.

- Been, K., Jefferies, M.G., and Hachey, J. 1991. The critical state of sands. *Géotechnique,* **41**(3): 365-381.

- Biot, M.A. 1956a. Theory of propagation of elastic waves in a fluid-saturated porous solid. I. Low frequency range. *Journal of the Acoustic society of America*, **28**(168): 168-178.

- Biot, M.A. 1956a. Theory of propagation of elastic waves in a fluid-saturated porous solid. II. Higher frequency range. *Journal of the Acoustic society of America*, **28**(168): 179-191.

- Blair, D.P. and Sydenham, P.H. 1975. Phase sensitive detection as a means to recover signals buried in noise. *Journal of Physics E,* **8**: 621-627.

- Blewett, J., Blewett, I.J. and Woodward, P.K. 1999. Measurement of Shear Wave Velocity using Phase-Sensitive Detection Technique. *Canadian Geotechnical Journal,* **36**: 934-939.

- Blewett, J., Blewett, I.J. and Woodward, P.K. 2000. Phase and amplitude responses associated with the measurement of shear wave velocity in sand by bender elements. *Canadian Geotechnical Journal,* **37**: 1348-1357.

- Blight, G.E. 1997. Destructive mudflows as a Consequence of Tailings Dyke Failures. *Proceedings of the Institute of Civil Engineers*, **125**: 9-18.

- Brignoli, E. and Gotti, M. 1992. Misure della velocita di onde elastiche di taglio in laboratorio con I'impiego di trasduttori piezoelettriei. *Riv. Ital. Geotec.,* **26**(1): 5-16.

- Brignoli, E., Gotti, M. and Stokoe, K.H. 1996. Measurement of Shear Waves in Laboratory Specimens by means of Piezoelectric Transducers. *Geotechnical Testing Journal,* **19**(4): 384-397.

- Burland, J.B. and Symes, M. 1982. A simple axial displacement gauge for use in the triaxial apparatus. *Géotechnique*, **32**(1): 62-65.

- Casagrande, A. 1938. The shearing resistance of soils and its relation to the stability of earth dam. *Proceedings, Soils and Foundation Conference of the U.S. Engineers Department.*

- Casagrande, A. 1975. Liquefaction and cyclic deformation of sands, a critical review. *5th Pan American Conference, Soil Mechanics and Foundation Engineering*, Buenos Aires, Argentina, **5**: 79-113.

- Castro, G. 1969. *Liquefaction of Sands.* PhD thesis. Harvard Soil Mechanics Series, No.81, Harvard University, Cambridge, MA.

- Castro, G. 1975. Liquefaction and Cyclic Deformation of Sands. *Journal of*

Geotechnical Engineering Division, ASCE, **101**(GT6): 551-569.

- Castro, G. and Poulos, S.J. 1977. Factors affecting liquefaction and cyclic mobility. *Journal of the Geotechnical Engineering*, ASCE, **103**(GT6): 501-516.

- Castro, G., Enos, J.L., France, J.W., and Poulos, S.J. 1982. Liquefaction Induced by Cyclic Loading. Report to National Science Foundation, Washington, DC, No. NSF/CEE-82018.

- Clayton, C.R.I. and Heymann, G. 2001. The stiffness of geomaterials at very small strains. *Géotechnique*, **51**(3): 245-256.

- Clayton, C.R.I. and Khatrush, S.A. 1986. A new device for measuring local axial strains on triaxial specimens. *Géotechnique*, **36**(4): 593-597.

- Dasari, G.R. and Bolton, M.D. 1998. Comparison of field and laboratory stiffness of Gault Clay. *Pre-failure deformation behavior of geomaterials*: 345-352.

- De Alba, P., Baldwin, K., Janoo, V., Roe, G. and Celikkol, B. 1984. Elastic-Wave Velocities and Liquefaction Potential. *Geotechnical Testing Journal*, **7**(2): 77-87.

- Degrande, G. and Pyl, L. 2002. Determination of the dynamic soil characteristics with the SASW method at the site of Cit'e universitaire in Paris. Report BMW-2002-08, Department of Civil Engineering, Katholieke Universiteit Leuven.

- Dyvik, R. and Madshus, C. 1985. Lab measurement of G_{max} using bender elements. *Advances in the art of testing soil under cyclic conditions,* Edited by V. Khosla. New York: ASCE: 186-196.

- Eckersley, D. 1990. Instrumented laboratory flow slides. *Géotechnique*, **40**: 489-502.

- Flinn, E.A., Robinson, E.A. and Treitel, S. 1967. Special issue in the MIT geophysical report, *Geophysics,* **18**: 271-288.

- Fioravante, V., Jamiolkowski, D., Lo Presti, D.C.F., Manfredini, G. and Pedroni, S. 1998. Assessment of the coefficient of earth pressure at rest from shear wave velocity measurements. *Géotechnique,* **48**(5): 657-666.

- Gajo, A., Fedel, A. and Mongiovi, L. 1997. Experimental analysis of the effects of fluid-solid coupling on the velocity of elastic waves in saturated porous media. *Géotechnique,* **47**(5): 993-1008.

- Geuze, E.C.W.A. 1948. Critical density of some Dutch sands. *Proceedings, Second International Conference on Soil Mechanics and Foundation Engineering,* Rotterdam, Holland.

- Hardin, B.O. and Richart, F.E. Jr. 1963. Elastic Wave Velocity in Granular Soils. *Journal of Soil Mechanics and Foundation Division,* ASCE, **89**(1): 33-65.

- Hardin, B.O.and Drnevich, V.P. 1972. Shear modulus and damping of soils:

measurements and parameter effects. *Journal of Soil Mechanic and Foundation Division*, ASCE, **98**(6): 603-624.

- Head, K.H. 1992. *Manual of Soil Laboratory Testing 2nd Edition,* Pentech Press Limited, London: 218-228.

- Heymann, G. 2001. Seismic Surface Wave Method to Measure Soil Stiffness Profiles. *SAICE Geotechnical Division: Seminar on Ground improvement,* Johannesburg, South Africa.

- Hvorslev, M.J. 1949. *Subsurface exploration and sampling of soils for civil engineering purpose.* Waterways Experimental Station, Vicksburg, USA.

- Ishihara, K. 1993. Liquefaction and flow failure during earthquakes. *Géotechnique*, **46**(3): 529-546.

- Ishihara, K. and Cubrinovski, M. 2000. Flow potential of sandy soils. *Soils and Foundations*, Japanese Society of Soil Mechanics and Foundation Engineering, **40**(4): 103-120.

- Jennings, J.E. 1979. The Failure of Slimes Dams at Bafokeng: Mechanisms of Failure and Associated Design Considerations. *Civil Engineers in South Africa*, **21**(6): 135-141.

- Joviĉić, M., Coop, R. and Simić, M. 1996. Objective criteria for determining G_{max} from bender element Tests. *Géotechnique*, **46**(2): 357-362.

- Koppejan, A.W., van Wamelen, B.M. and Weinberg, L.J.H. 1948. Coastal landslides in the Dutch province of Zealand. *Proceedings, Second International Conference on Soil Mechanics and Foundation Engineering*, Rotterdam, Holland: 89-96.

- Matthews, M.C., Hope, V.S. and Clayton, C.R.I. 1996. The use of surface waves in the determination of ground stiffness profiles. *Proceedings, Institute of Civil Engineers, Geotechnical Engineering*: 84-95.

- National Institute for Transportation and Road Research. 1982. Technical Methods for Highways: Standard methods of testing road construction material. South Africa, CSIR.

- Papageorgiou, G.P., Fourie, A.B., and Sechet, B. 1999. Static Liquefaction of Merriespruit gold tailings. *Proceedings, 12th Regional Conference for Africa on Soil Mechanics and Geotechnical Engineering*, Durban, South Africa: 61-72.

- Pennington, D.S., Nash, D.F.T. and Lings, M.L. 1997. Anisotropy of Go Shear Stiffness in Gault Clay. *Géotechnique,* **47**(3): 391-398.

- Pitman, T.D., Robertson, P.K. and Sego, D.C. 1994. Influence of fines on the collapse of loose sands. *Canadian Geotechnical Journal,* **31**: 728-736.

- Poulos, S.J. 1971. The stress-strain curves of soils. Unpublished Monograph, Geotechnical Engineers Inc., Winchester, MA.

- Poulos, S.J. 1981. The steady state of deformation. *Journal of the Geotechnical Engineering Divisoin*, ASCE, **107**(GT5): 553-562.

- Randell, R.B. 1987. *Frequency Analysis 3rd Edition,* Bruel and Kjaer, Denmark.

- Ricketts, G.A., Smith, J. and Skipp, B.O. 1996. Confidence in seismic characterization of the ground. *Advances in site investigation practice,* Thomas Telford, London.

- Robertson, P.K., Woeler, D.J. and Finn, W.D. 1992. Seismic cone penetration test for evaluating liquefaction potential under cyclic loading. *Canadian Geotechnical Journal,* **29**: 686-695.

- Robertson, P.K. and Fear, C.E. 1995. Application of CPT to Evaluate Liquefaction Potential. *CPT '95,* Linkoping, **3**: 57-79, Swedish Geotechnical Society.

- Robertson, P.K., Sasitharan, S., Cunning, J.C., and Sego, D.C. 1995. Shear wave velocity to evaluate in-situ state of Ottawa sand. *Journal of Geotechnical Engineering Division,* ASCE, **121**(3): 262-273.

- Rosler, S.K. 1979. Anisotropic Shear Wave Modulus due to Stress Anisotropy. *Journal of Geotechnical Engineering Division,* ASCE, **105**(7): 871-880.

- Sanchez-Salinero, I., Roesset, J.M. and Stokoe, K.H. 1986. Analytical Studies of Body Wave propagation and Attenuation. Report GR 86-15, University of Texas, Austin.

- Santamarina, J.C. and Fam, M.A. 1997. Interpretation of bender element tests (discussion). *Géotechnique*, **47**(4): 873-877.

- Sasitharan, S., Robertson, P.K. and Sego, D.C. and Morgenstern, N.R. 1993. Collapse Behavior of Sands. *Canadian Geotechnical Journal,* **30**: 569-577.

- Shirley, D.J. 1978. An improved shear wave transducer. *Journal of the Acoustic Society of America*, **63**(5): 1643-1645.

- Shirley, D.J. and Hampton, L.D. 1978. Shear Wave Measurement in Laboratory Sediments. *Journal of the Acoustic Society of America*, **63**(2): 601-613.

- Sladen, J.A., Hollander, R.D.D. and Krahn, J. 1985. The Liquefaction of Sands, a Collapse Surface Approach. *Canadian Geotechnical Journal*, **22**: 564-578.

- Stokoe, K.H., Lee, H.H.S. and Knox, D.P. 1985. Shear moduli measurements under true triaxial stresses. *Proceedings, Advances in the art of testing soils under cyclic conditions,* ASCE, New York: 166-185.

- Sully, J.P. and Campanella, R.G. 1995. Evaluation of in situ anisotropy from crosshole and downhole shear wave velocity measurements. *Géotechnique,* **45**(2): 267-282.

- Sykora, D.W. 1987. Creation of a data base of seismic shear wave velocities for correlation analysis. *Geotech. Lab. Misc. Paper GL-87-26*, US Army Engineer Waterways Experimental Station, Vicksburg, MS.

- Tatsuoka, F. 1988. Some recent developments in triaxial testing systems for cohesionless soils. *Advanced Triaxial Testing of Soils and Rocks*, ASTM STP 977, American Society for Testing and Materials: 7-67.

- Thevanayagan, S. 1998. Effects of fines and confining stress on undrained shear strength of silty sands. *Journal of Geotechnical and Environmental Engineering*, **124**(6): 479-491.

- Terzaghi, K. 1943. *Theoretical soil mechanics.* Wiley, New York.

- Vermeulen, N.J. 2001. The Composition and State of Gold Tailings. PhD thesis, University of Pretoria, RSA.

- Viggiani, G. and Atkinson, J.H. 1995. Interpretation of Bender Element Tests. *Géotechnique*, **45**(1): 149-154.

- Yamamuro, J.A. and Lade, P.V. 1997. Effects of non-plastic fines on the static liquefaction of sands. *Canadian Geotechnical Journal*, **34**: 918-928.

- Yu, P., and Richart, F.E. Jr. 1984. Stress Ratio Effect on Shear Modulus of Dry Sands. *Journal of the Acoustic Society of America*, ASCE, **110**(3): 331-341.

APPENDIX A

SCANNING ELECTRON MICROGRAPHS AND QUANTITATIVE ANALYSIS OF SOIL SPECIMEN

Material retained on 150 μm sieve.

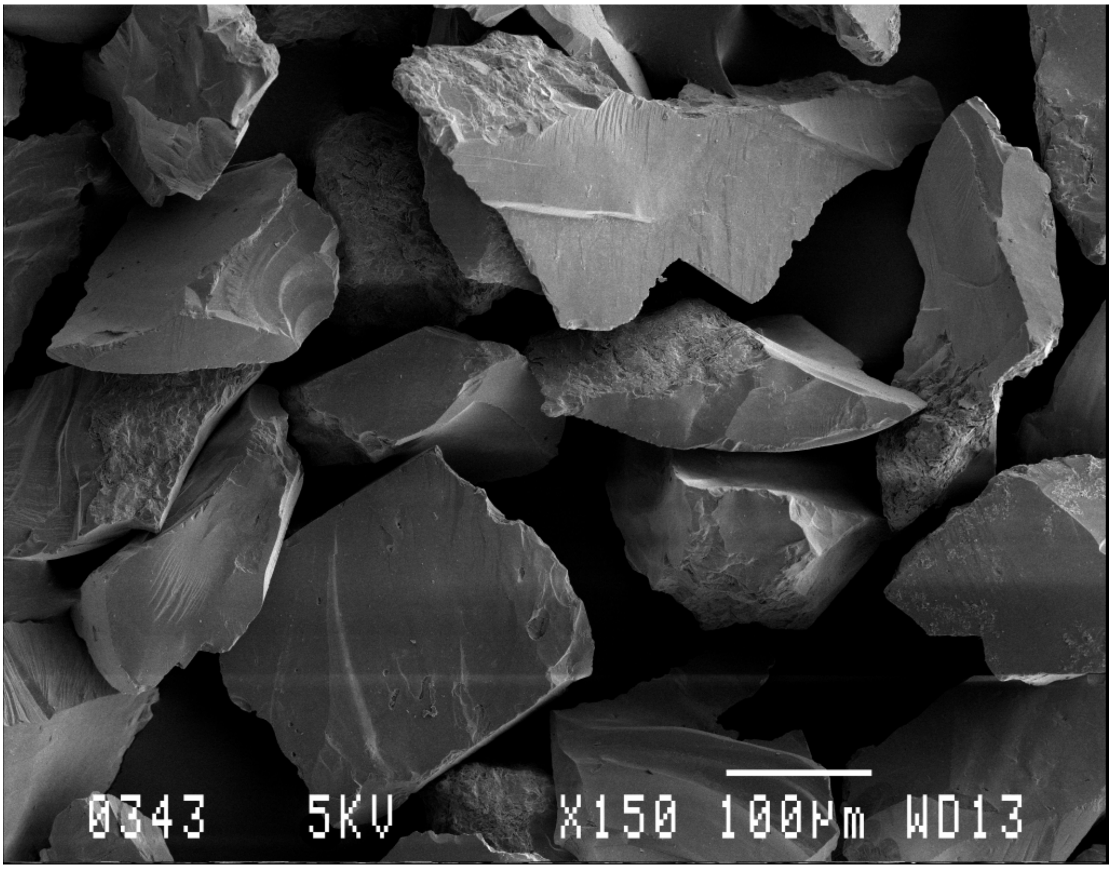

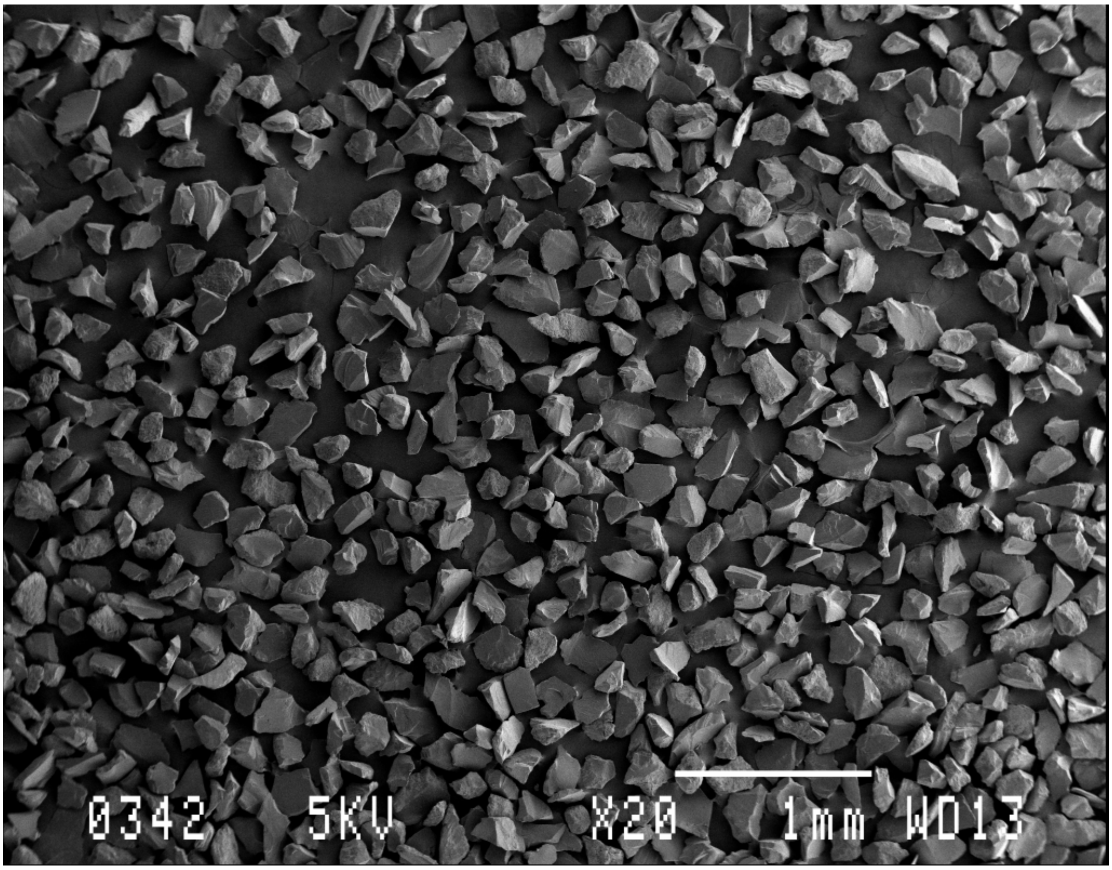

Material retained on 75 μm sieve.

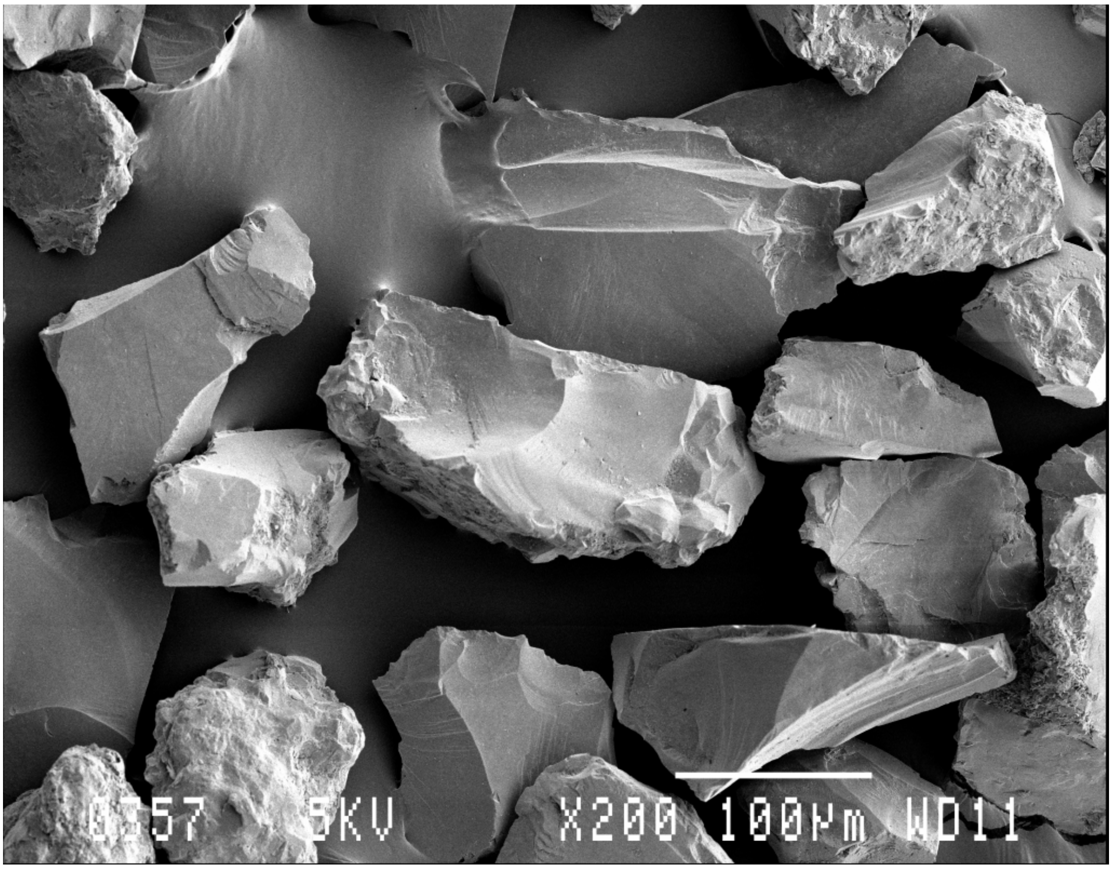

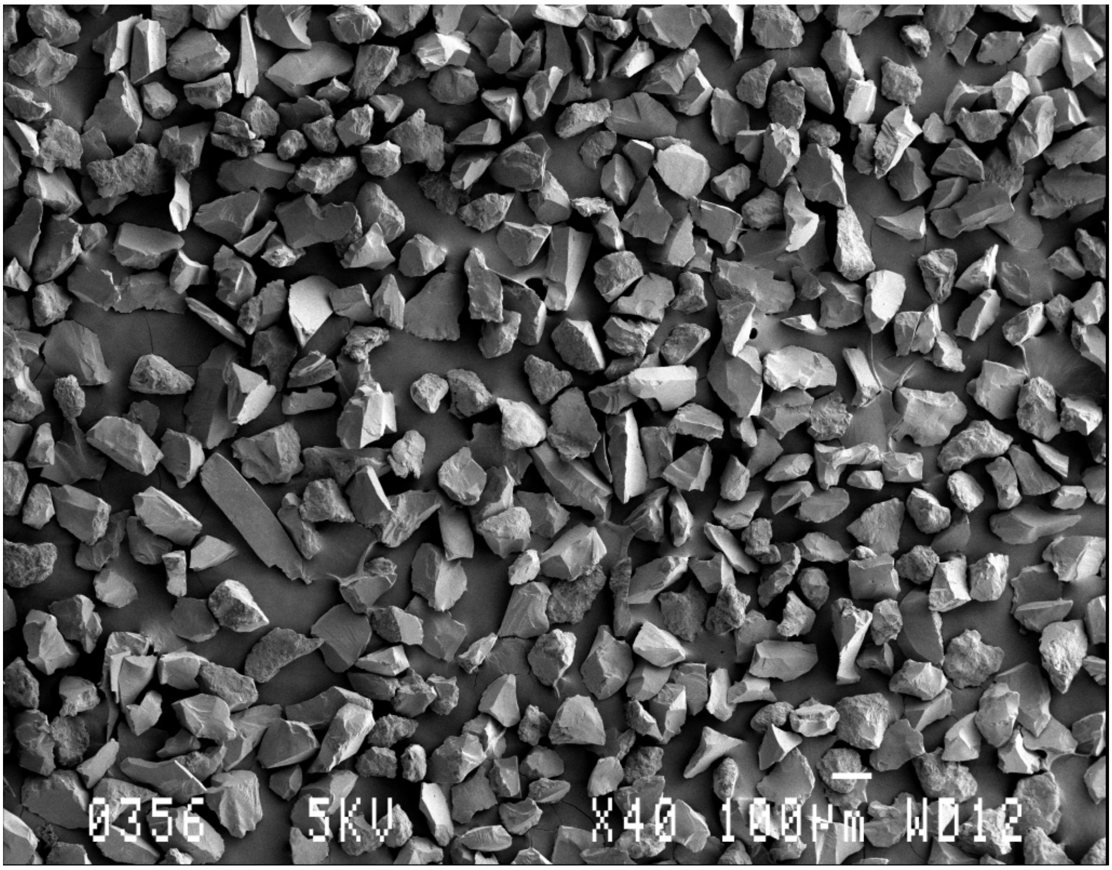

Fines (material passing 75 μm sieve).

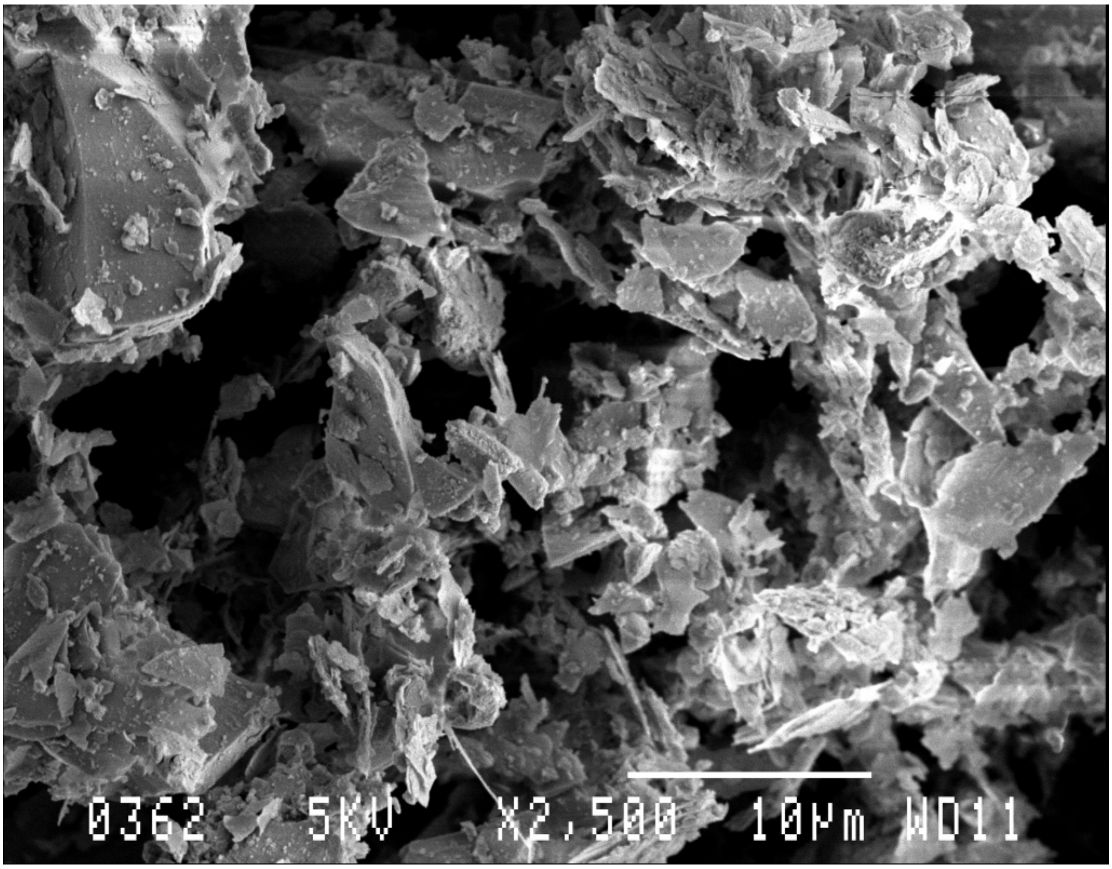

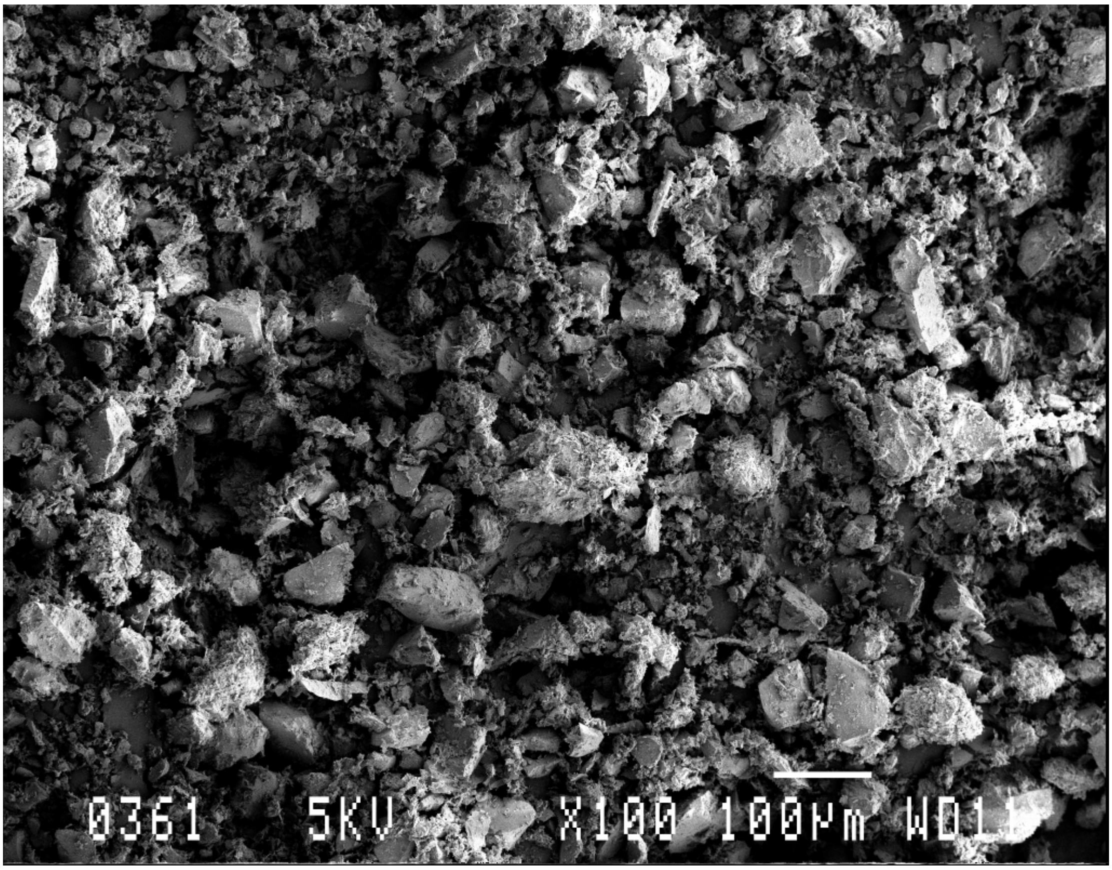

Sample material (including fine and coarse particles).

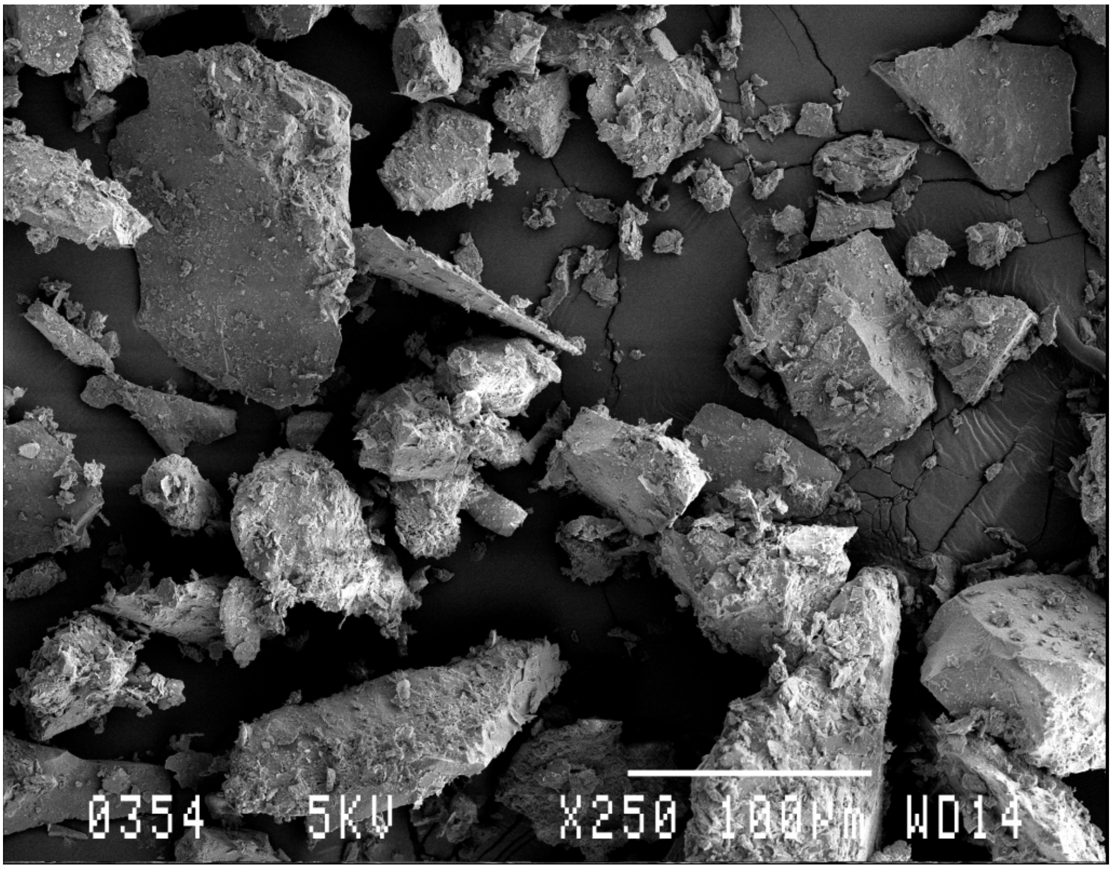

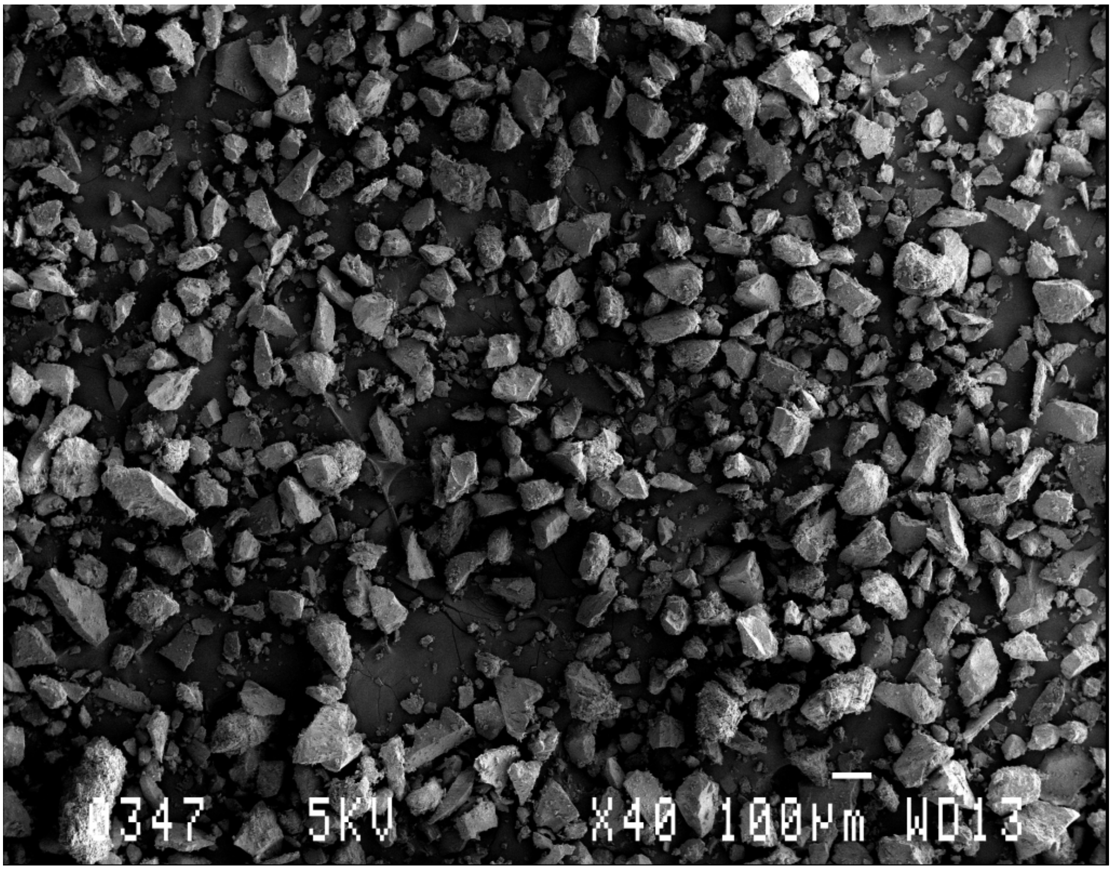

Sample retained on 150 µm sieve-A

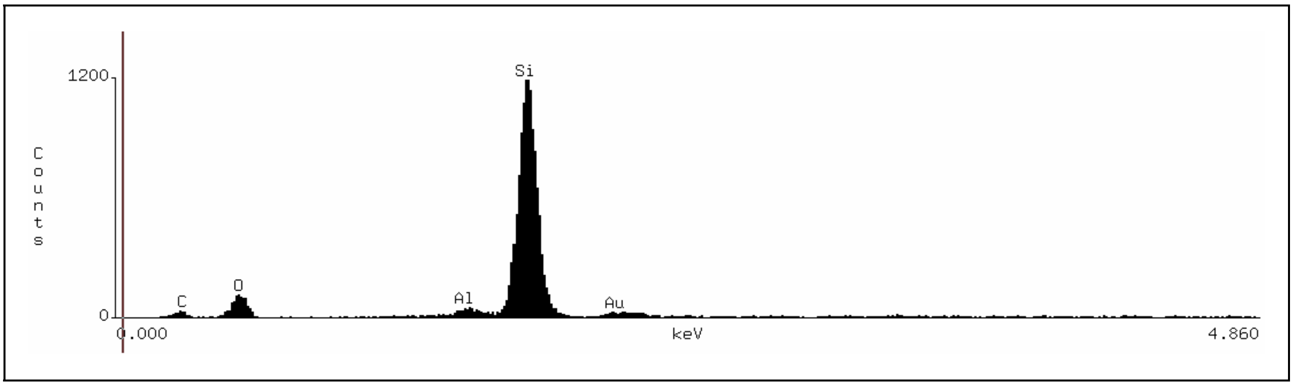

Sample retained on 150 µm sieve-B

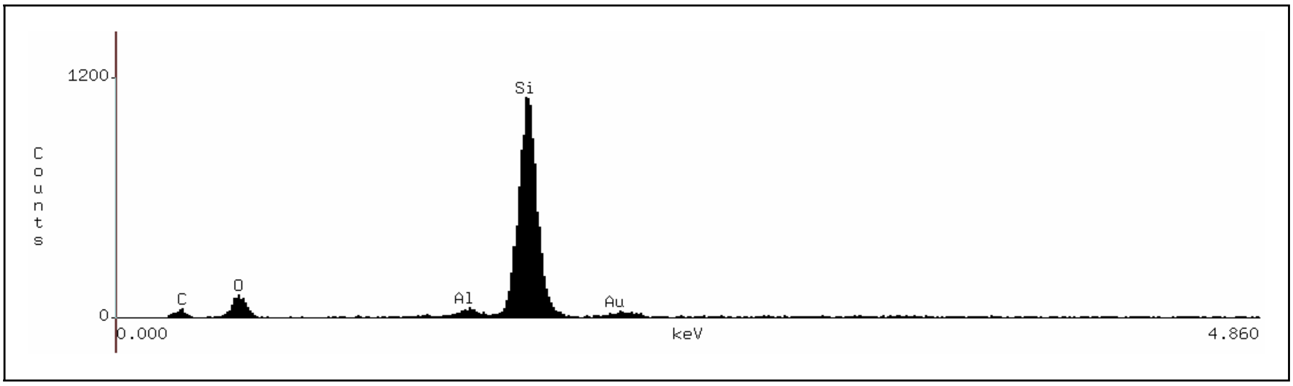

Quantitative Analysis

	Sample 150A chi-sqd 1.05 live time 100 s Acc. Voltage 20 KeV Take off angle 35 ° Dead time 11.993					Sample 150B chi-sqd 1.14 live time 100 s Acc. Voltage 20 KeV Take off angle 35 ° Dead time 11.781				
Element	k-ratio (calc)	ZAF	Atom %	Element wt %	wt % error	k-ratio (calc)	ZAF	Atom %	Element wt %	wt % error
Al-k	0.0211	1.024	2.25	2.16	± 0.20	0.0215	1.024	2.29	2.20	± 0.20
Si-k	0.9472	1.033	97.75	97.84	± 1.01	0.0946	1.034	97.71	97.80	± 1.05
Total			100.0	100.0				100.0	100.0	

Sample retained on 75 µm sieve-A

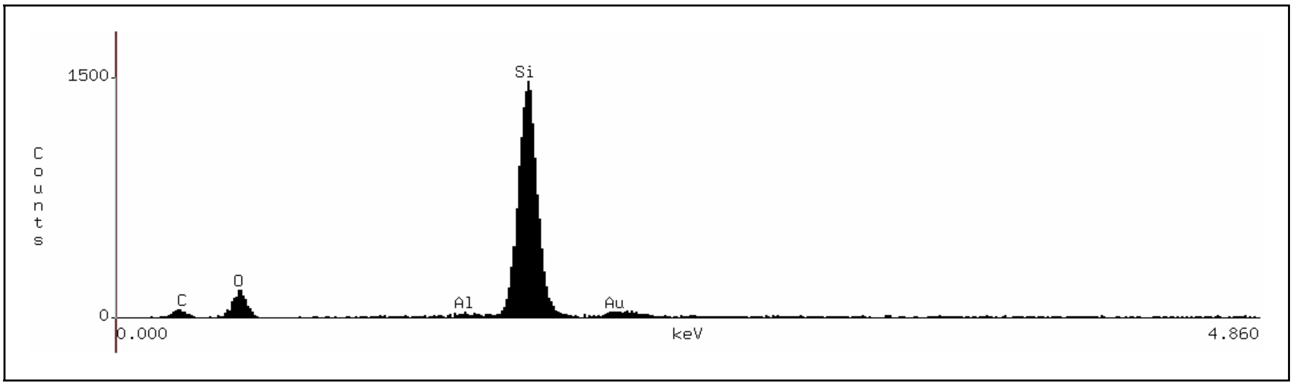

Sample retained on 75 µm sieve-B

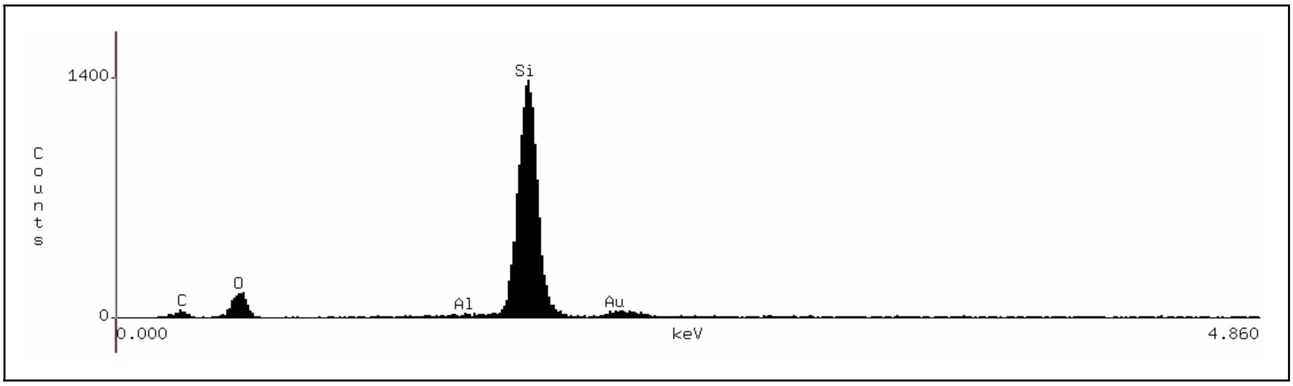

Quantitative Analysis

	Sample 75A					Sample 75B				
	chi-sqd	0.87				chi-sqd	1.19			
	live time	100 s				live time	100 s			
	Acc. Voltage	20 KeV				Acc. Voltage	20 KeV			
	Take off angle	35 °				Take off angle	35 °			
	Dead time	11.561				Dead time	11.957			
Element	k-ratio	ZAF	Atom	Element	wt %	k-ratio	ZAF	Atom	Element	wt %
	(calc)		%	wt %	error	(calc)		%	wt %	error
Al-k	0.0026	1.019	0.27	0.26	± 0.15	0.0048	1.019	0.51	0.49	± 0.15
Si-k	0.9935	1.004	99.73	99.74	± 0.90	0.8978	1.007	99.49	99.51	± 0.89
Total			100.0	100.0				100.0	100.0	

Fines-A

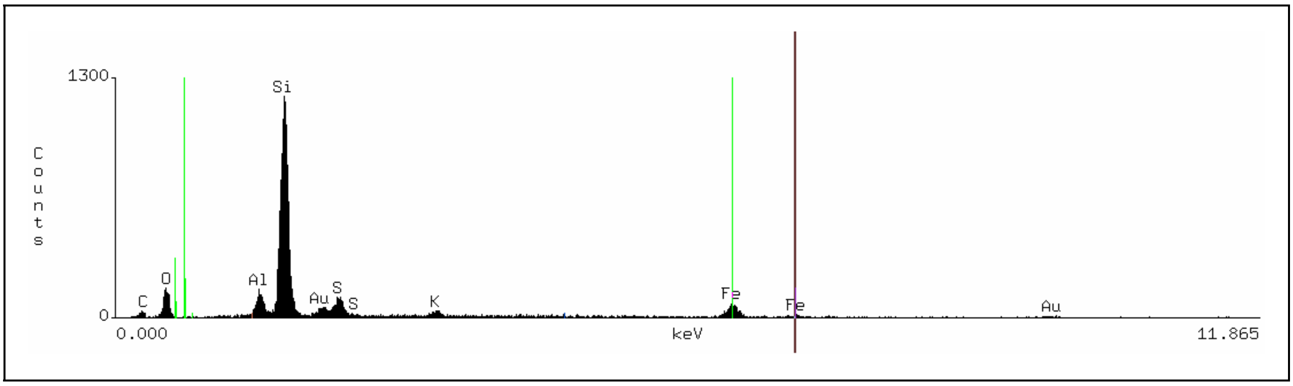

Fines-B

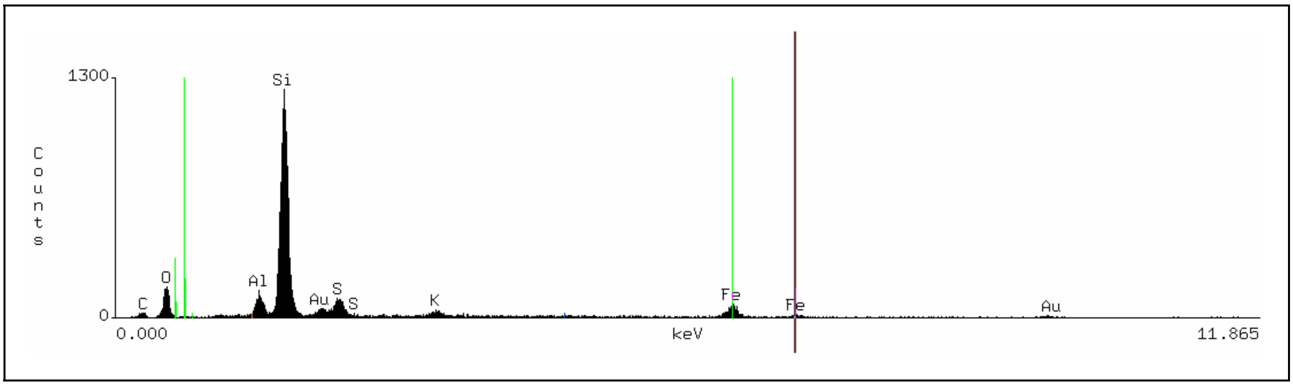

Quantitative Analysis

	Fines-A chi-sqd 1.16 live time 100 s Acc. Voltage 20 KeV Take off angle 35 ° Dead time 11.543					Fines-B chi-sqd 1.04 live time 100 s Acc. Voltage 20 KeV Take off angle 35 ° Dead time 11.738				
Element	k-ratio	ZAF	Atom	Element	wt %	k-ratio	ZAF	Atom	Element	wt %
	(calc)		%	wt %	error	(calc)		%	wt %	error
Al-k	0.0443	1.358	6.98	6.01	± 0.32	0.0409	1.332	6.29	5.45	± 0.20
Si-k	0.4984	1.280	71.20	63.79	± 0.72	0.5185	1.255	72.10	65.08	± 0.71
Fe-k	0.1539	1.127	9.74	17.34	± 0.30	0.1381	1.13	8.70	15.61	± 0.30
K -k	0.0207	1.343	2.23	2.79	± 0.23	0.0225	1.35	2.42	3.04	± 0.45
S -k	0.0574	1.755	9.85	10.07	± 0.74	0.0615	1.785	10.50	10.82	± 0.73
Total			100.0	100.0				100.0	100.0	

APPENDIX B

SCHEMATIC BENDER ELEMENT DEVELOPMENT PROCEDURE

STEP 1: SURFACE PREPARATION

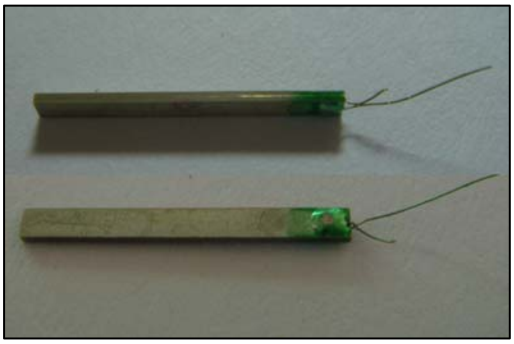

Before anything could be done on the element, the insulation paint was removed from the surface of the bender element. The paint or any grease or dirt on the surface of the bender element would prevent the epoxy adhering to the element and creates a weaker region. The epoxy coat could crack under continuous vibration and water pressure. The element was dipped in acetone momentarily to remove the green insulation paint. The element was then wiped clean.

STEP 2: ATTACHING ELEMENT TO WIRE

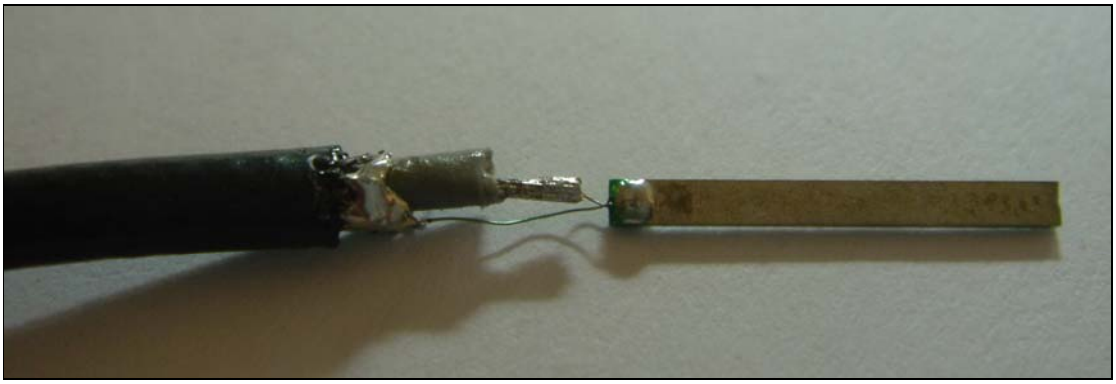

After the element surface had been prepared, the two lead wires from the element were connected to wire that could carry the signal from the element to the instrumentation. Shielded wires were used to reduce environmental noise. The one lead from the element was soldered to the center wire and the other lead was soldered to the outer shield of the wire.

STEP 3: INSTALLING SHRINGAKE TUBE

The shrinkage tube was then put onto the bender element wiring. The back end of the tube was shrunk onto the wire with a heat gun. It was important to leave enough space for the epoxy to cover the entire soldered part.

STEP 4: FILLING OF SHRINKAGE TUBE WITH EPOXY

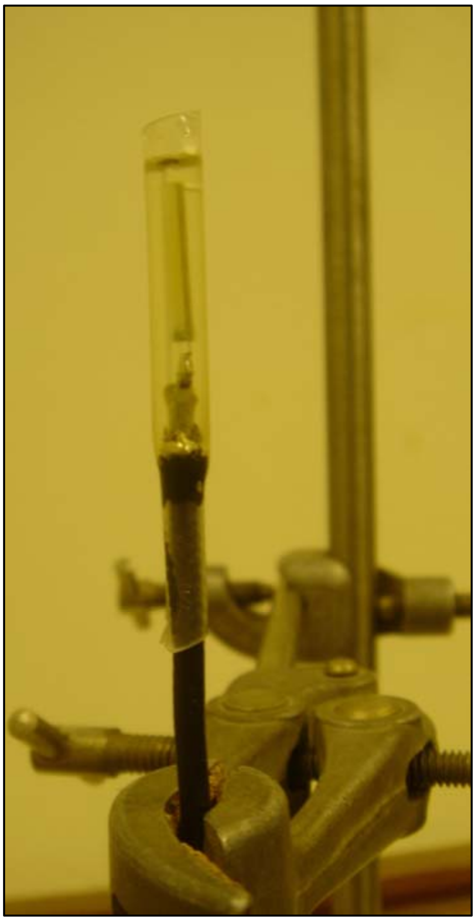

With the aid of a stand, the bender element was fixed in an upright position to be immersed in epoxy. The epoxy was injected into the cavity with the aid of a syringe and needle. It was important that no air bubbles were trapped within the epoxy, since any air would produce a weak spot within the epoxy coating. The bubbles could be removed with the needle, but care must be taken to ensure that the tube was not damaged. After all the air was removed, the epoxy was left to cure. This took a maximum of 2 days. During this period, it was important to ensure that the bender element did not touch the tube, as this would also produce weaknesses within the epoxy coat.

STEP 5: REMOVE SHRINKAGE TUBING

After the epoxy had fully hardened, the shrinkage tubing could be removed. The tube could be easily removed with a side cutter.

STEP 6: SHAPING THE ELEMENT

When the tubing was removed, the hardened epoxy took the form of the tube, which was cylindrical. A miniature grinder was used to shape the round epoxy coating into the shape of the element. If the coat was too thick, the element would only vibrate at very small amplitudes or not vibrate at all. The aim was to produce a thin layer of epoxy coating the bender element without the coat being too thin to crack under vibration and pressure, but at the same time not damage the bender or grind through the epoxy, as this would defeat the aim of the epoxy coat.

STEP 7: SEALING THE BACK END OF THE CAP

When the bender was to be installed into the top cap or the base, the back end of the cap must be sealed to prevent epoxy from leaking out under gravity. This was done using plumbers tape. When the injection of the epoxy was complete, the plumbers tape was left on.

STEP 8: ALIGNING THE BENDER ELEMENT

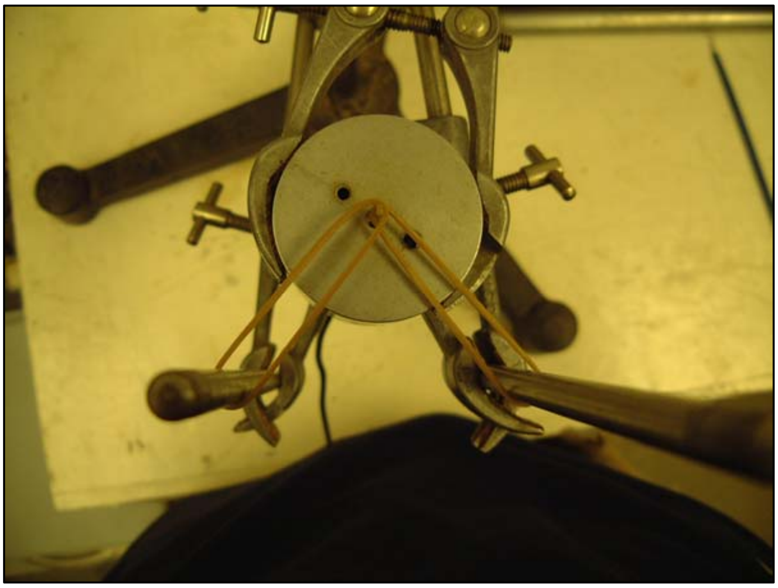

The alignment of the bender relative to the caps was also important. A perfectly vertical bender would generate the most energy in the preferred direction, as well as reduce wave reflections from the membrane. The bender was placed within the cap which was fixed vertically with a stand. The wire exiting the bottom of the cap was also fixed, as the wire could slip out under gravity. The epoxy was injected into the predrilled hole, again with a syringe and needle. It was again important that air bubbles were removed, as bubbles could create weaknesses within the epoxy. When mixing the epoxy, care should be taken not

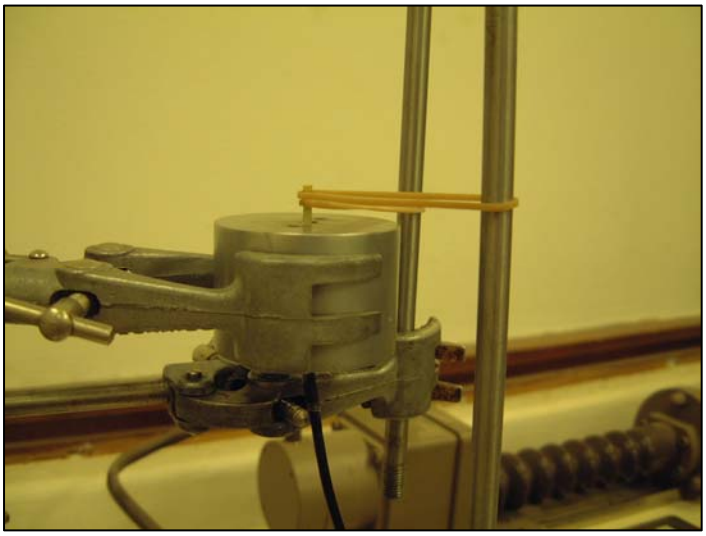

to mix too vigorously, as minor air bubbles would be introduced into the epoxy.

The bender was held in a vertical position with elastic bands in both directions. A top view of the setup is shown in the first figure above, while the figure directly above shows a side view of the setup. The epoxy was allowed to harden for a maximum of 2 days.

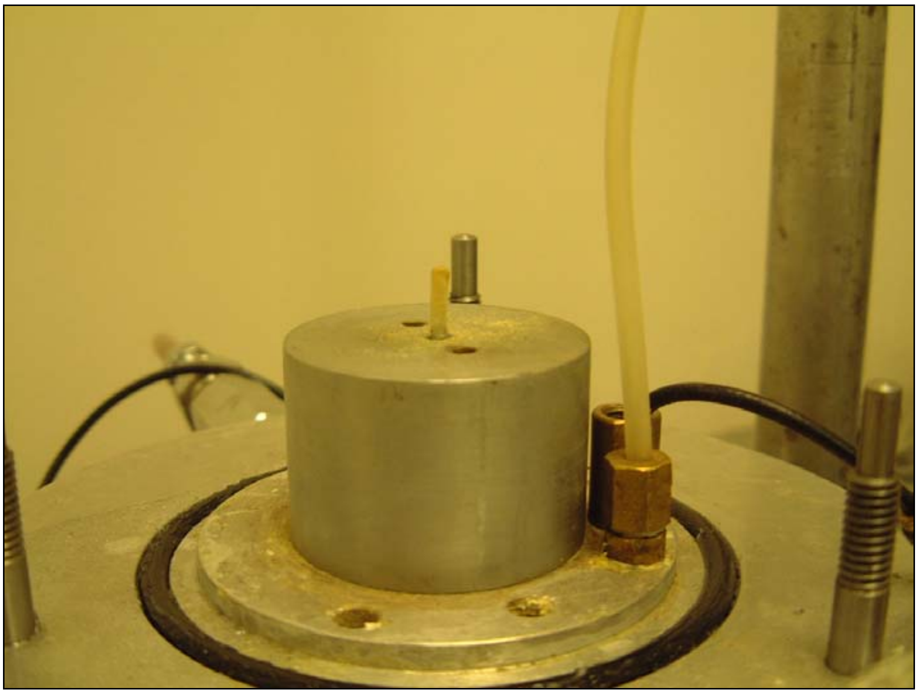

The figure above shows the finished base pedestal. The figure also shows the position of the top drainage as well as the position of the exit plug for the top cap wire. The plug prevented the cell water from escaping through the hole. The base wire exited through the bottom, which would not leak because of the presence of the O rings.

The figure below shows the complete bender element setup including the finished top cap.

APPENDIX D

SHEAR WAVE VELOCITY RESULTS DETERMINED USING FIRST ARRIVALS METHOD

Summary of signal interpretation

File name	Arrival time	File name	Arrival time
0625C	9.28E-04	1225C	Signal unclear
0650C	8.30E-04	1250C	Signal unclear
06100C	8.20E-04	12100C	9.57E-04
06200C	5.66E-04	12200C	7.13E-04
06400C	7.03E-04	12400C	1.01E-03
06200S	6.15E-04	12200S	1.22E-03
06100S	8.11E-04	12100S	7.81E-04
0650S	8.11E-04	1250S	Signal unclear
0625S	Signal unclear	1225S	Signal unclear
0825C	1.84E-03	1425C	1.06E-03
0850C	1.04E-03	1450C	8.98E-04
08100C	1.59E-03	14100C	7.13E-04
08200C	1.26E-03	14200C	7.62E-04
08400C	1.83E-03	14400C	5.57E-04
08200S	1.91E-03	14200S	5.76E-04
08100S	1.95E-03	14100S	7.81E-04
0850S	1.72E-03	1450S	7.13E-04
0825S	1.29E-03	1425S	1.07E-03
1025C	2.58E-03	08C25C	1.08E-03
1050C	Signal unclear	08C50C	1.04E-03
10100C	1.34E-03	08C100C	8.40E-04
10200C	1.02E-03	08C200C	5.86E-04
10400C	Signal unclear	08C400C	6.84E-04
10200S	5.66E-04	08C200S	4.79E-04
10100S	1.29E-03	08C100S	6.54E-04
1050S	1.71E-03	08C50S	1.25E-03
1025S	Signal unclear	08C25S	9.08E-04

SAMPLE 06

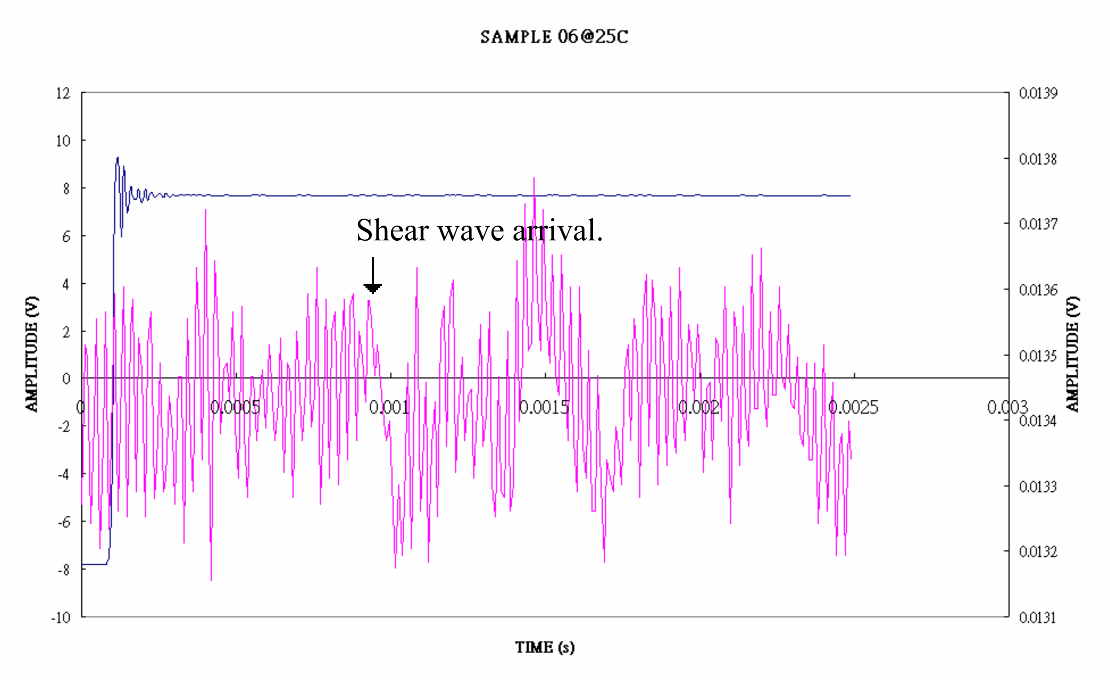
SAMPLE 06@25C
Shear wave arrival.
AMPLITUDE (V)
12
10
8
6
4
2
0
-2
-4
-6
-8
-10
0
0.0005
0.001
0.0015
0.002
0.0025
0.003
TIME (s)
0.0139
0.0138
0.0137
0.0136
0.0135
0.0134
0.0133
0.0132
0.0131
AMPLITUDE (V)

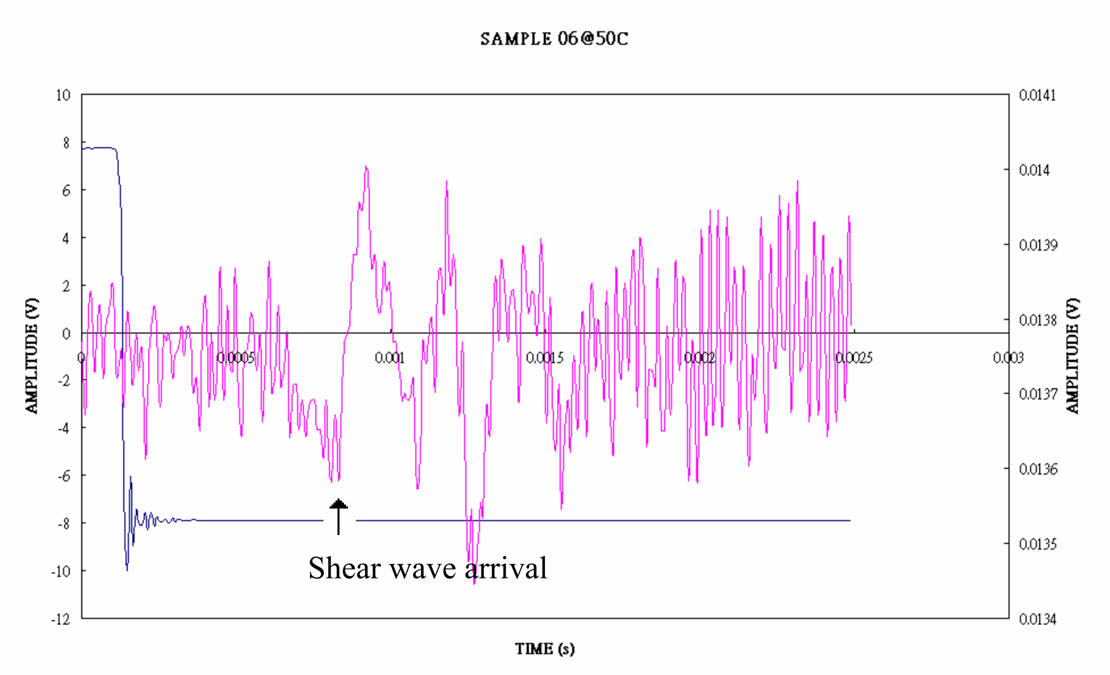
SAMPLE 06@50C
Shear wave arrival
AMPLITUDE (V)
10
8
6
4
2
0
-2
-4
-6
-8
-10
-12
0
0.0005
0.001
0.0015
0.002
0.0025
0.003
TIME (s)
0.0141
0.014
0.0139
0.0138
0.0137
0.0136
0.0135
0.0134
AMPLITUDE (V)

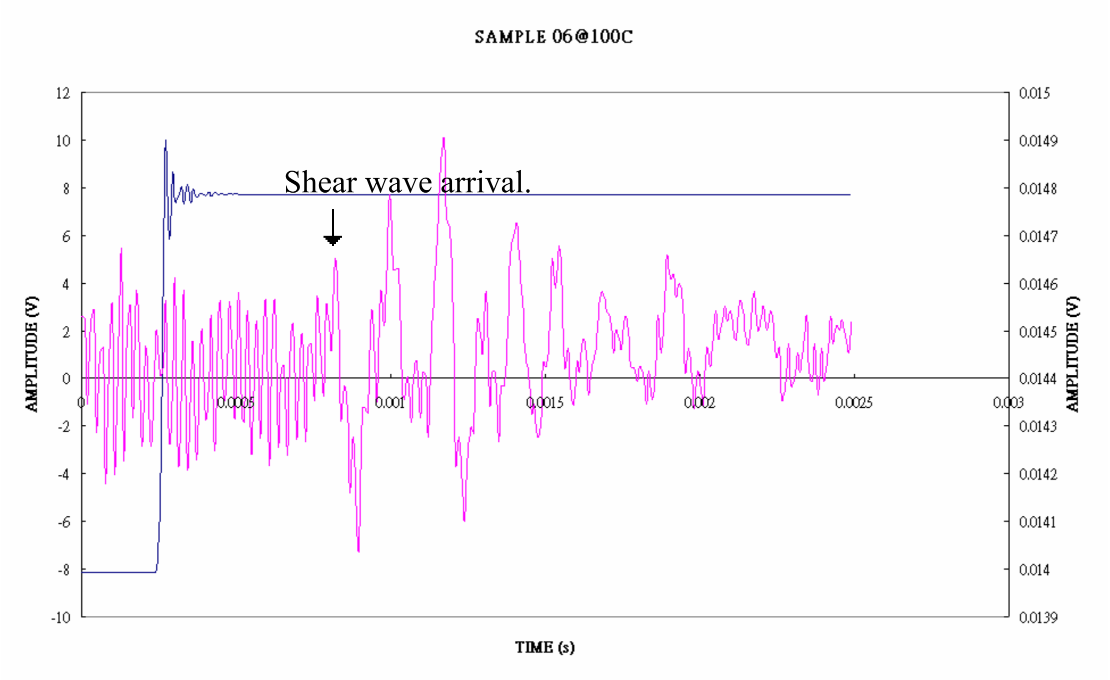
SAMPLE 06@100C
Shear wave arrival.
AMPLITUDE (V)
12
10
8
6
4
2
0
-2
-4
-6
-8
-10
0
0.0005
0.001
0.0015
0.002
0.0025
0.003
TIME (s)
AMPLITUDE (V)
0.015
0.0149
0.0148
0.0147
0.0146
0.0145
0.0144
0.0143
0.0142
0.0141
0.014
0.0139

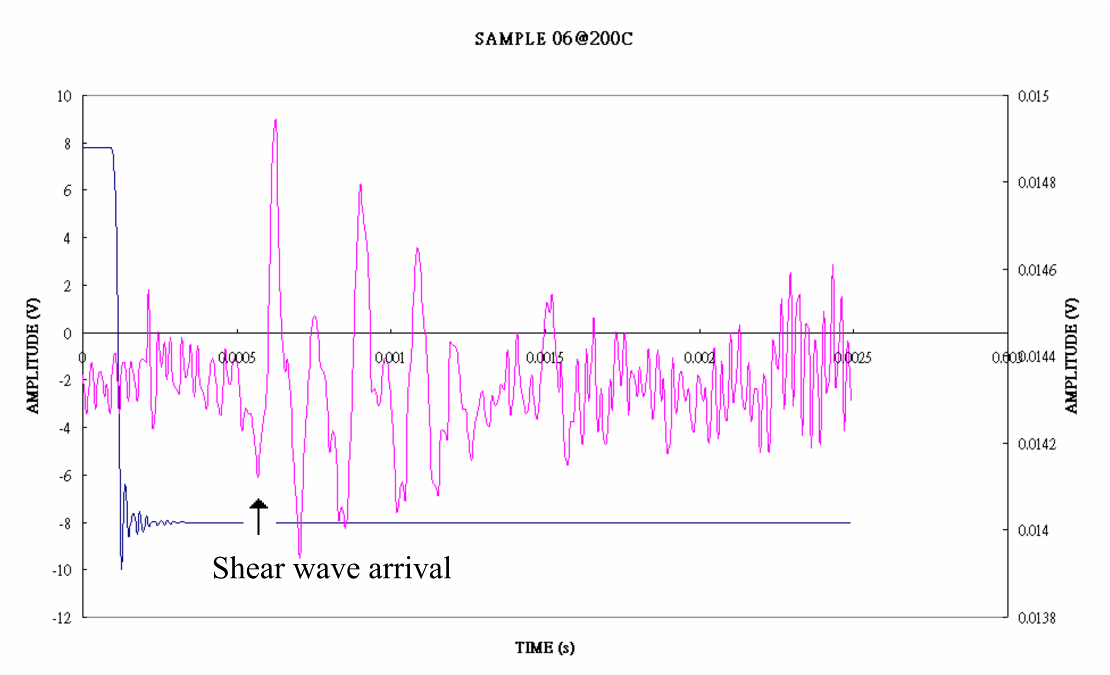
SAMPLE 06@200C
Shear wave arrival
AMPLITUDE (V)
10
8
6
4
2
0
-2
-4
-6
-8
-10
-12
0
0.0005
0.001
0.0015
0.002
0.0025
0.003
TIME (s)
AMPLITUDE (V)
0.015
0.0148
0.0146
0.0144
0.0142
0.014
0.0138

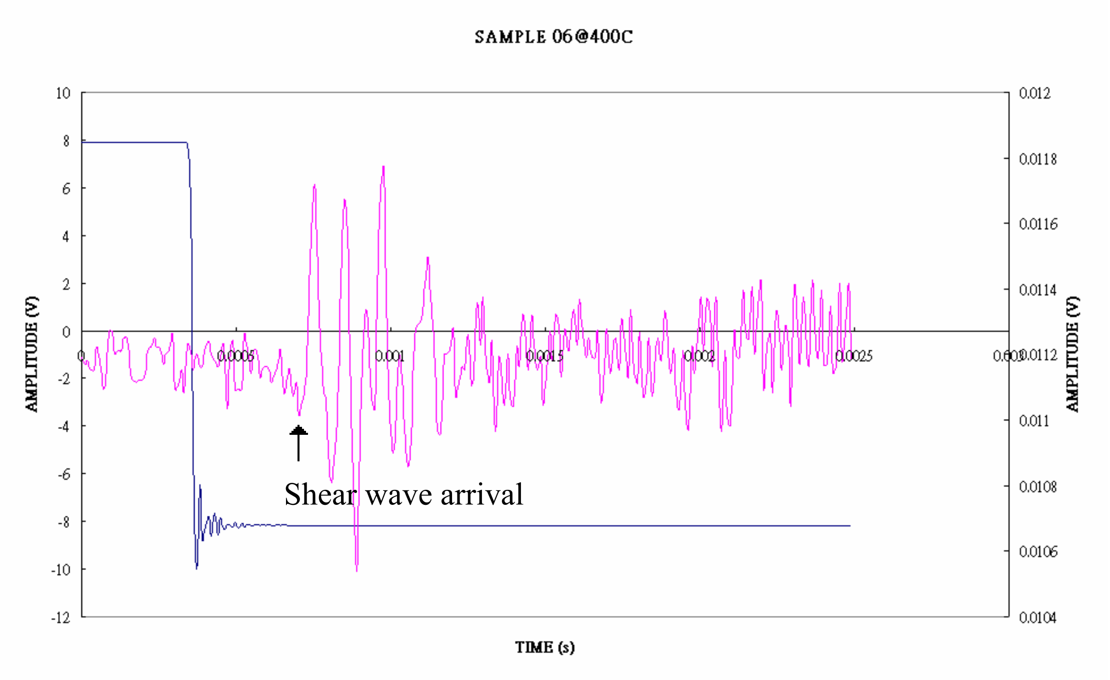
SAMPLE 06@400C
AMPLITUDE (V)
10
8
6
4
2
0
-2
-4
-6
-8
-10
-12
0
0.0005
0.001
0.0015
0.002
0.0025
0.003
0.012
0.0118
0.0116
0.0114
0.0112
0.011
0.0108
0.0106
0.0104
Shear wave arrival
TIME (s)

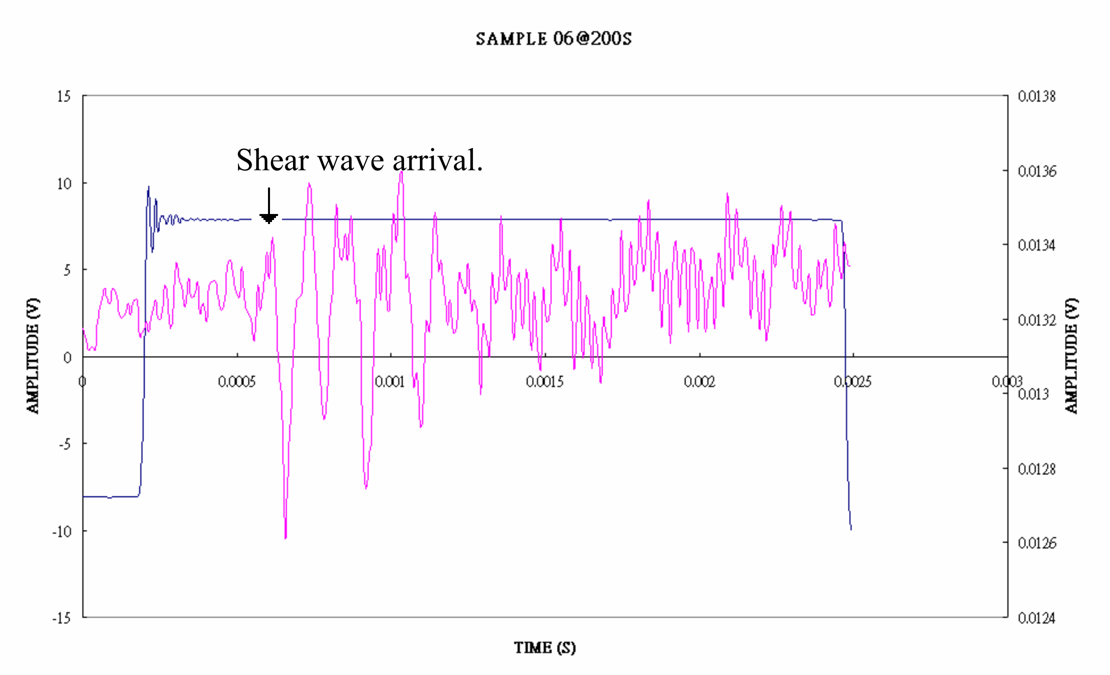
SAMPLE 06@200S
AMPLITUDE (V)
15
10
5
0
-5
-10
-15
0
0.0005
0.001
0.0015
0.002
0.0025
0.003
0.0138
0.0136
0.0134
0.0132
0.013
0.0128
0.0126
0.0124
Shear wave arrival.
TIME (S)

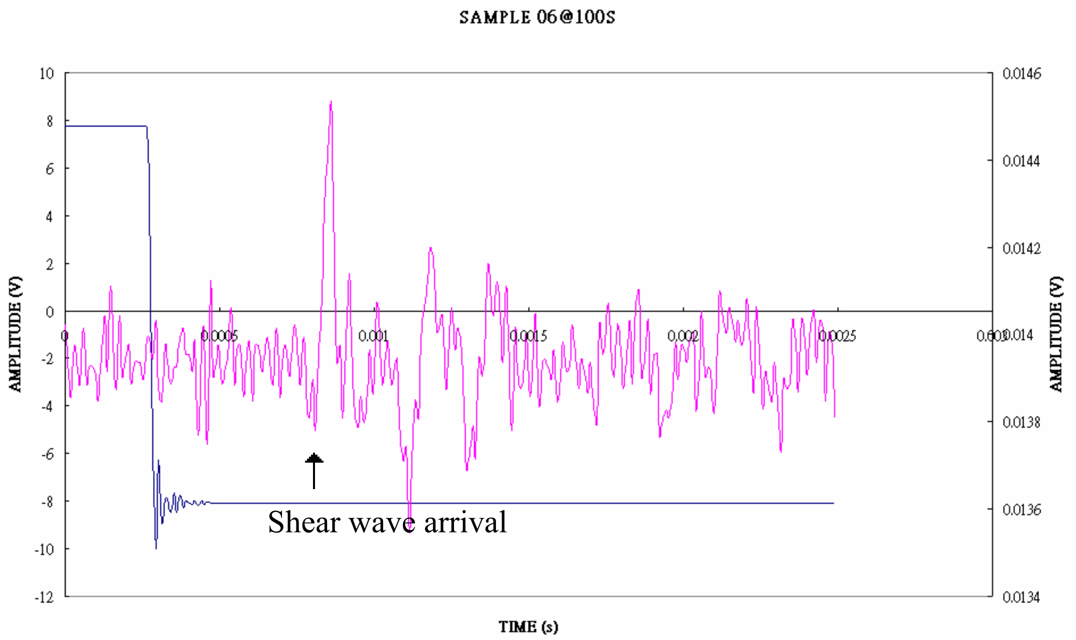

Shear wave arrival

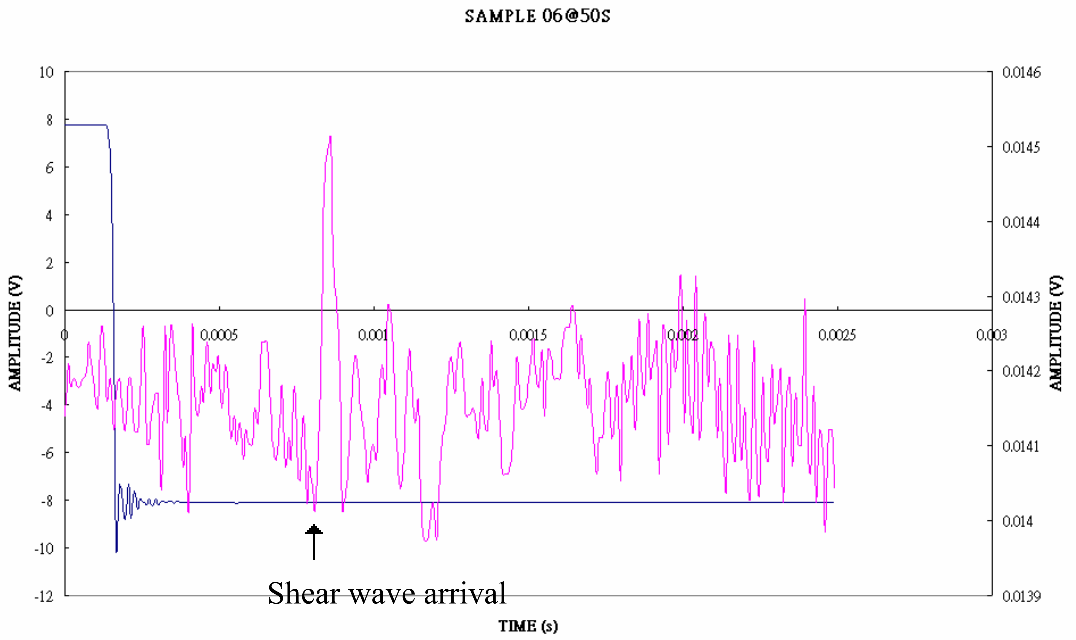

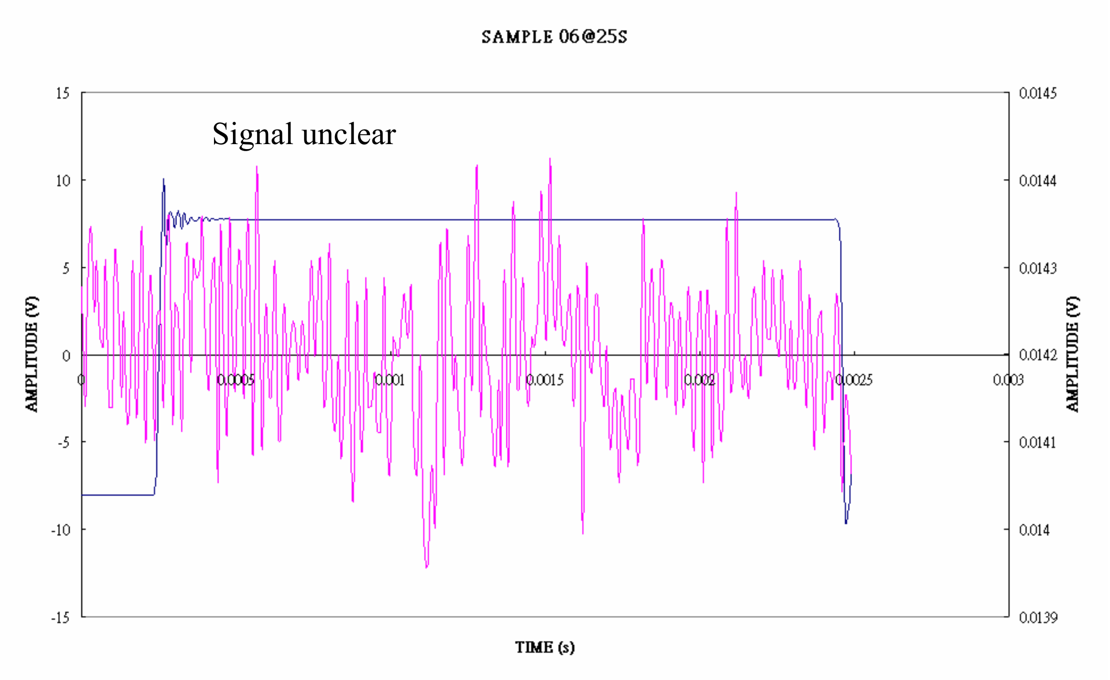
SAMPLE 06@25S
Signal unclear
AMPLITUDE (V)
15
10
5
0
-5
-10
-15
0
0.0005
0.001
0.0015
0.002
0.0025
0.003
TIME (s)
AMPLITUDE (V)
0.0145
0.0144
0.0143
0.0142
0.0141
0.014
0.0139

SAMPLE 08

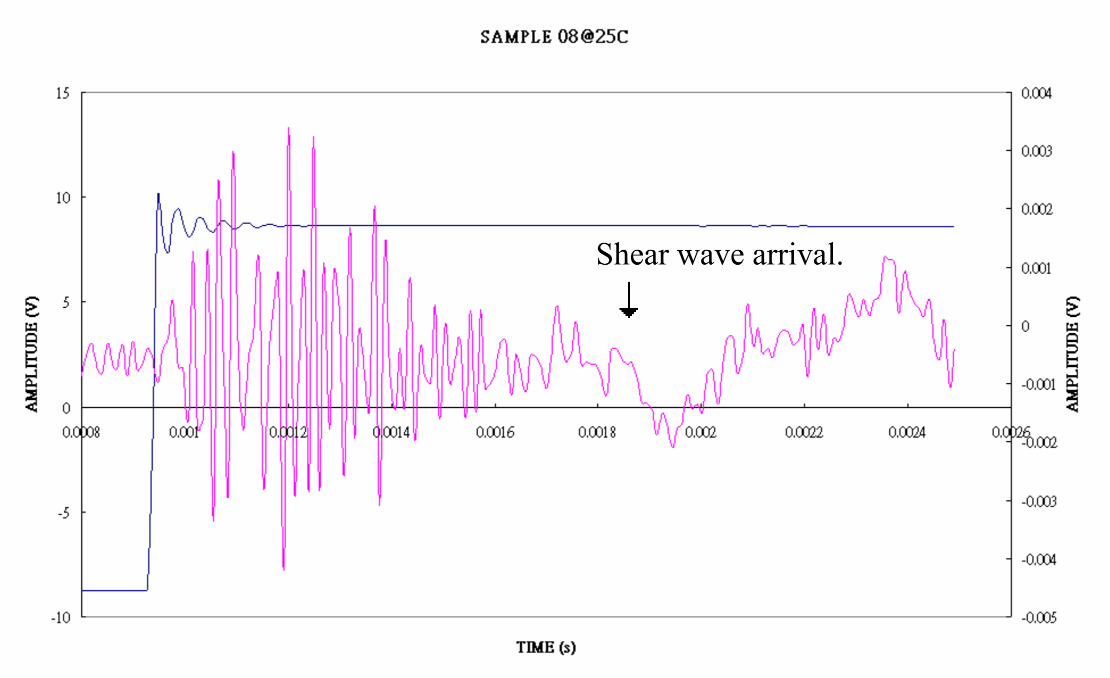
SAMPLE 08@25C
Shear wave arrival.
AMPLITUDE (V)
15
10
5
0
-5
-10
0.0008
0.001
0.0012
0.0014
0.0016
0.0018
0.002
0.0022
0.0024
0.0026
TIME (s)
AMPLITUDE (V)
0.004
0.003
0.002
0.001
0
-0.001
-0.002
-0.003
-0.004
-0.005

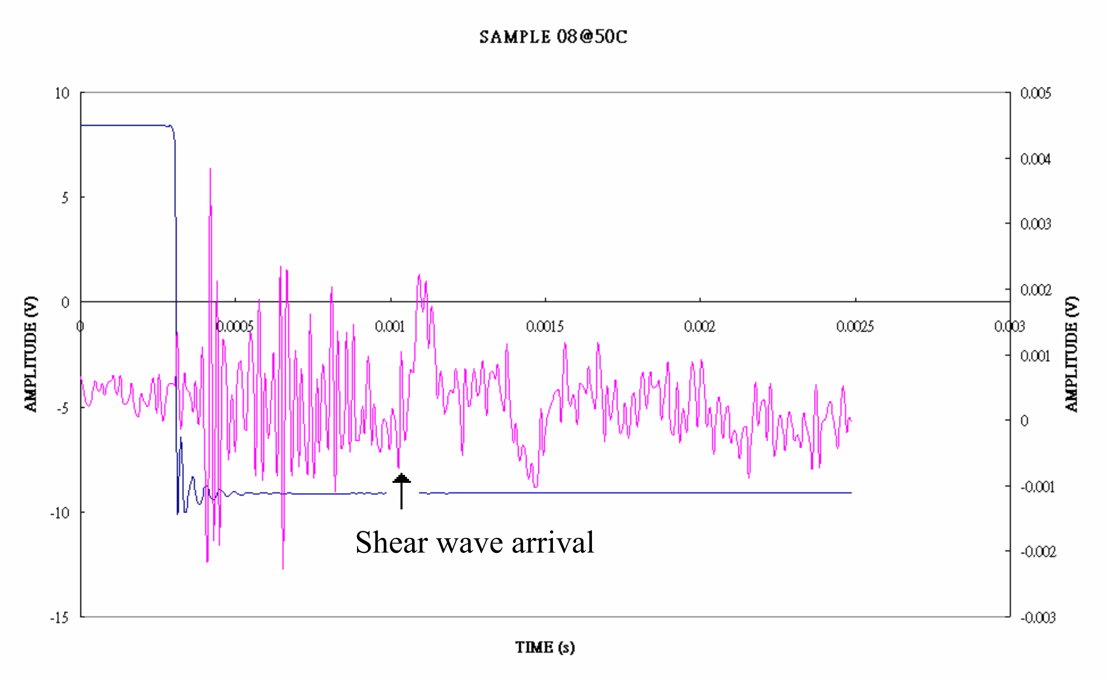
SAMPLE 08@50C
10
5
0
-5
-10
-15
0.005
0.004
0.003
0.002
0.001
0
-0.001
-0.002
-0.003
0
0.0005
0.001
0.0015
0.002
0.0025
0.003
AMPLITUDE (V)
AMPLITUDE (V)
TIME (s)
Shear wave arrival

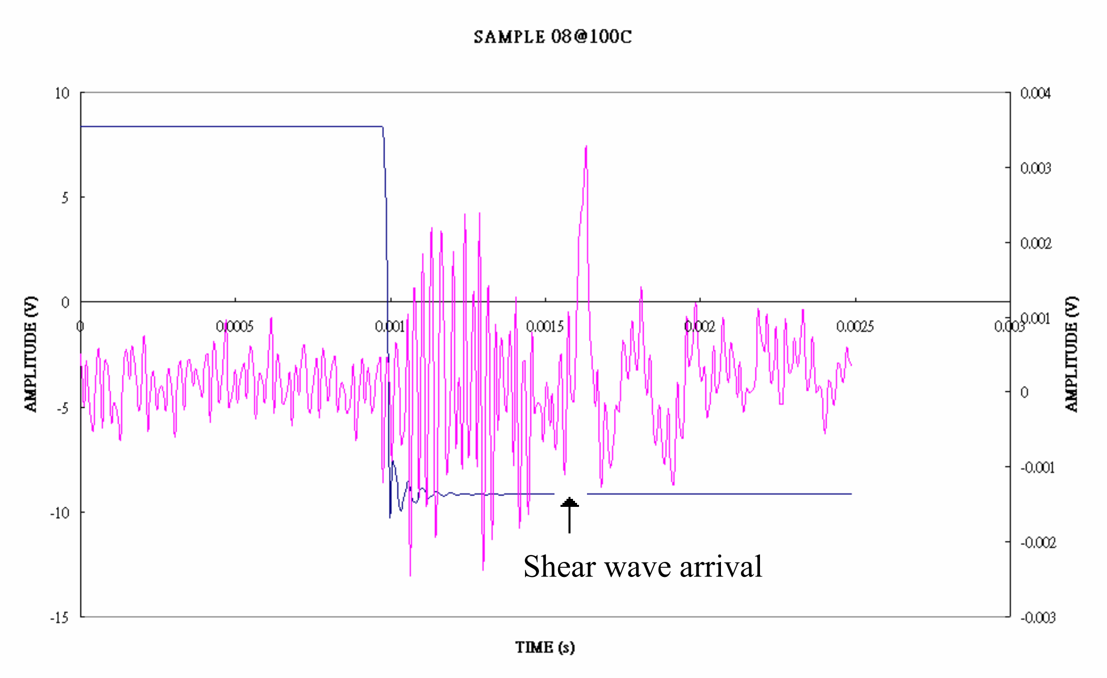
SAMPLE 08@100C
10
5
0
-5
-10
-15
0.004
0.003
0.002
0.001
0
-0.001
-0.002
-0.003
0
0.0005
0.001
0.0015
0.002
0.0025
0.003
AMPLITUDE (V)
AMPLITUDE (V)
TIME (s)
Shear wave arrival

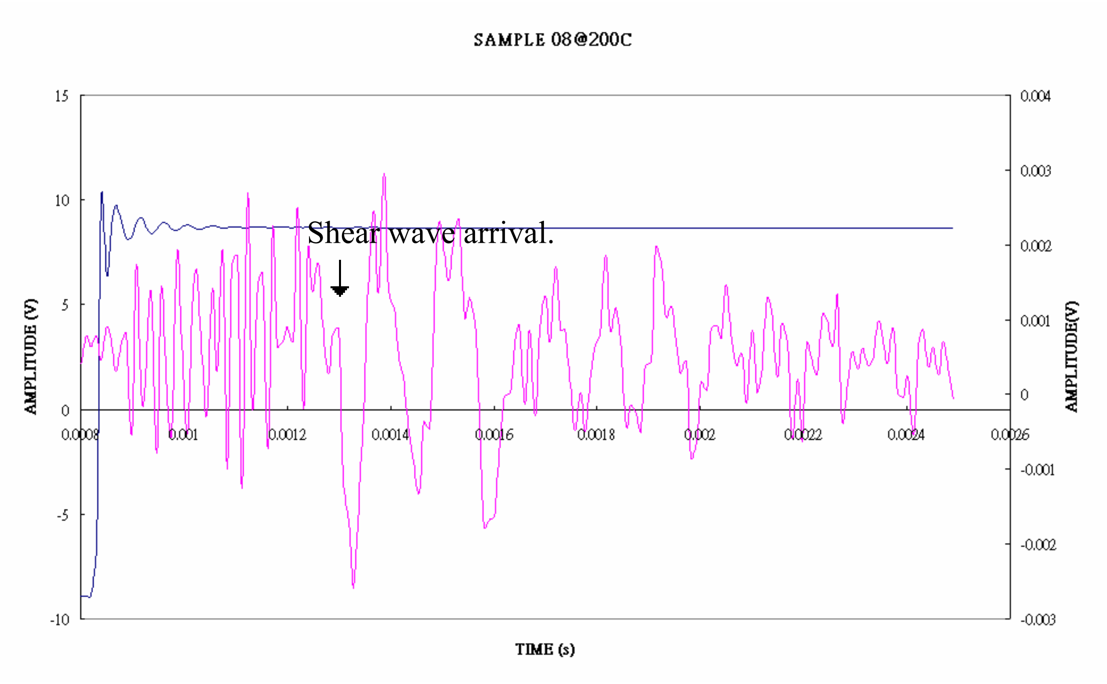
SAMPLE 08@200C
Shear wave arrival.
AMPLITUDE (V)
AMPLITUDE(V)
TIME (s)
15
10
5
0
-5
-10
0.004
0.003
0.002
0.001
0
-0.001
-0.002
-0.003
0.0008
0.001
0.0012
0.0014
0.0016
0.0018
0.002
0.0022
0.0024
0.0026

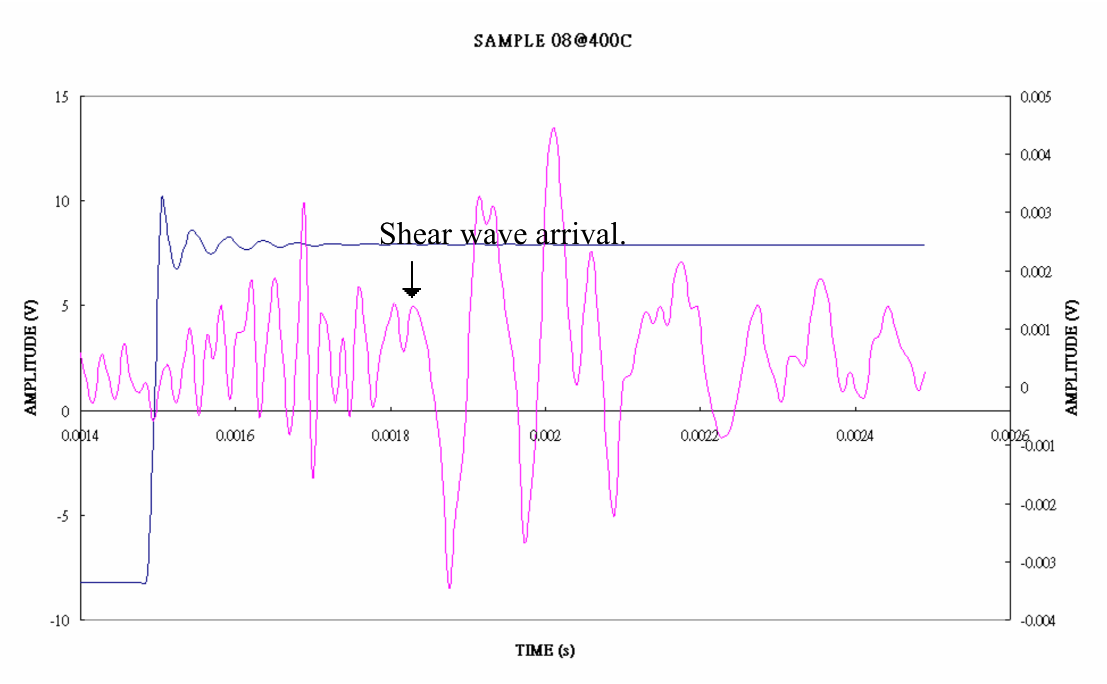
SAMPLE 08@400C
Shear wave arrival.
AMPLITUDE (V)
AMPLITUDE (V)
TIME (s)
15
10
5
0
-5
-10
0.005
0.004
0.003
0.002
0.001
0
-0.001
-0.002
-0.003
-0.004
0.0014
0.0016
0.0018
0.002
0.0022
0.0024
0.0026

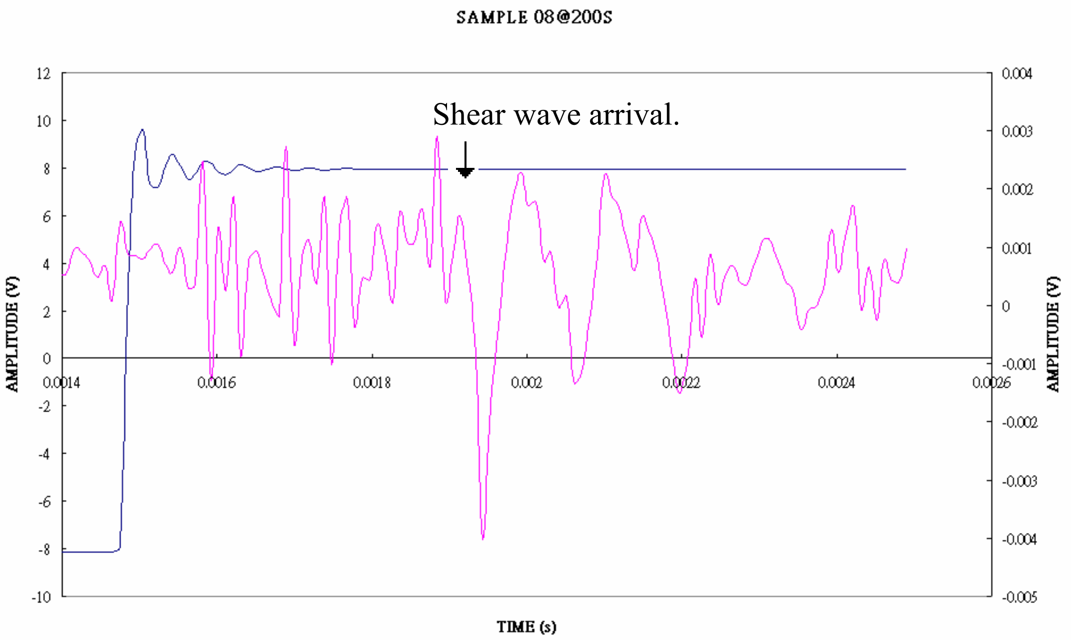
SAMPLE 08@200S
Shear wave arrival.
12
10
8
6
4
2
0
-2
-4
-6
-8
-10
0.0014
0.0016
0.0018
0.002
0.0022
0.0024
0.0026
0.004
0.003
0.002
0.001
0
-0.001
-0.002
-0.003
-0.004
-0.005
AMPLITUDE (V)
AMPLITUDE (V)
TIME (s)

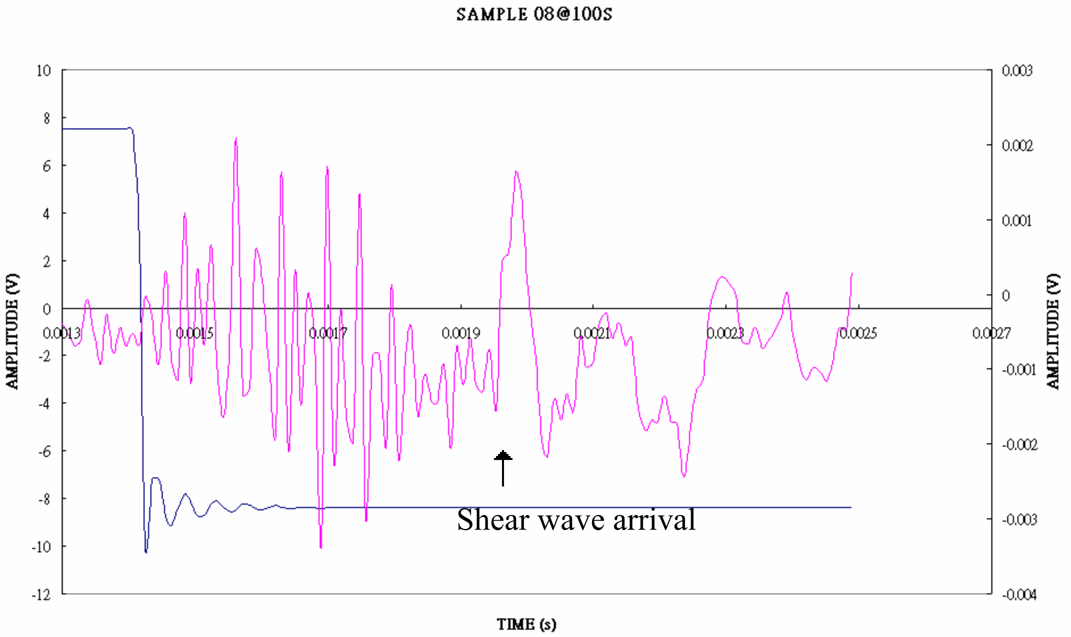
SAMPLE 08@100S
Shear wave arrival
10
8
6
4
2
0
-2
-4
-6
-8
-10
-12
0.0013
0.0015
0.0017
0.0019
0.0021
0.0023
0.0025
0.0027
0.003
0.002
0.001
0
-0.001
-0.002
-0.003
-0.004
AMPLITUDE (V)
AMPLITUDE (V)
TIME (s)

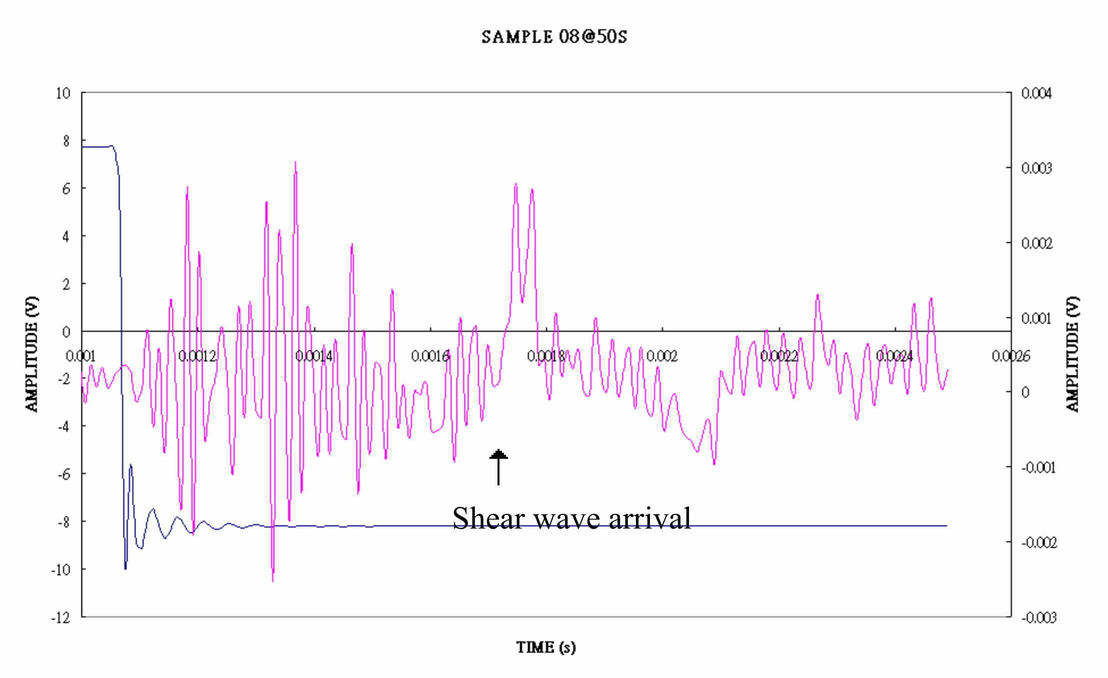
SAMPLE 08@50S
AMPLITUDE (V)
10
8
6
4
2
0
-2
-4
-6
-8
-10
-12
0.001
0.0012
0.0014
0.0016
0.0018
0.002
0.0022
0.0024
0.0026
TIME (s)
AMPLITUDE (V)
0.004
0.003
0.002
0.001
0
-0.001
-0.002
-0.003
Shear wave arrival

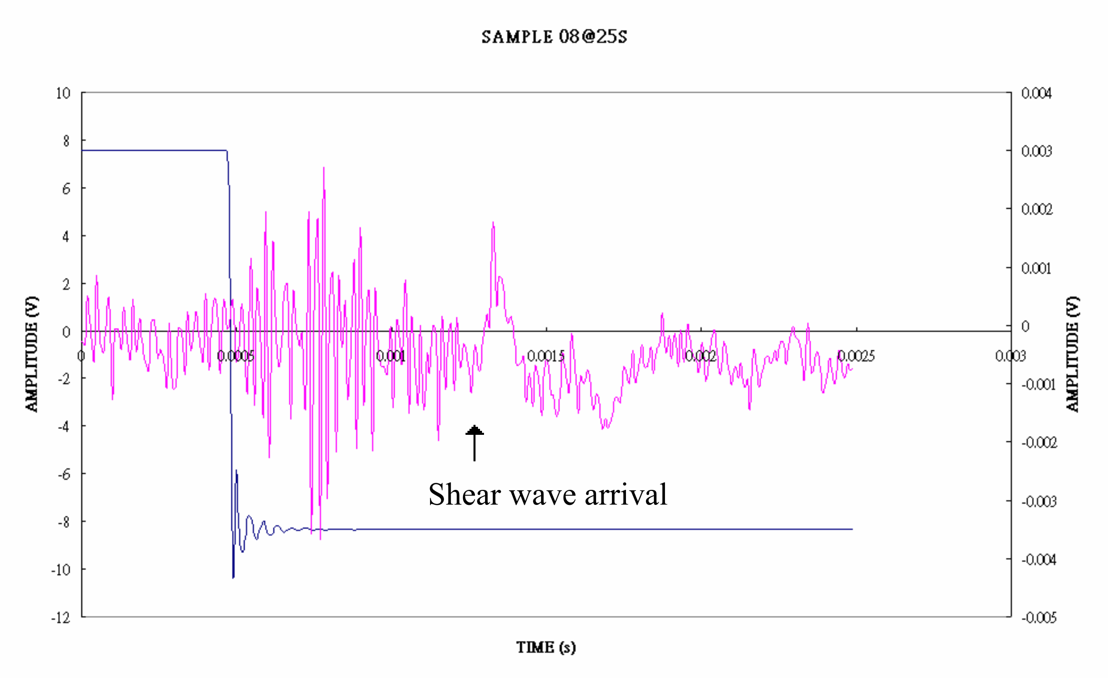
SAMPLE 08@25S
AMPLITUDE (V)
10
8
6
4
2
0
-2
-4
-6
-8
-10
-12
0
0.0005
0.001
0.0015
0.002
0.0025
0.003
TIME (s)
AMPLITUDE (V)
0.004
0.003
0.002
0.001
0
-0.001
-0.002
-0.003
-0.004
-0.005
Shear wave arrival

SAMPLE 10

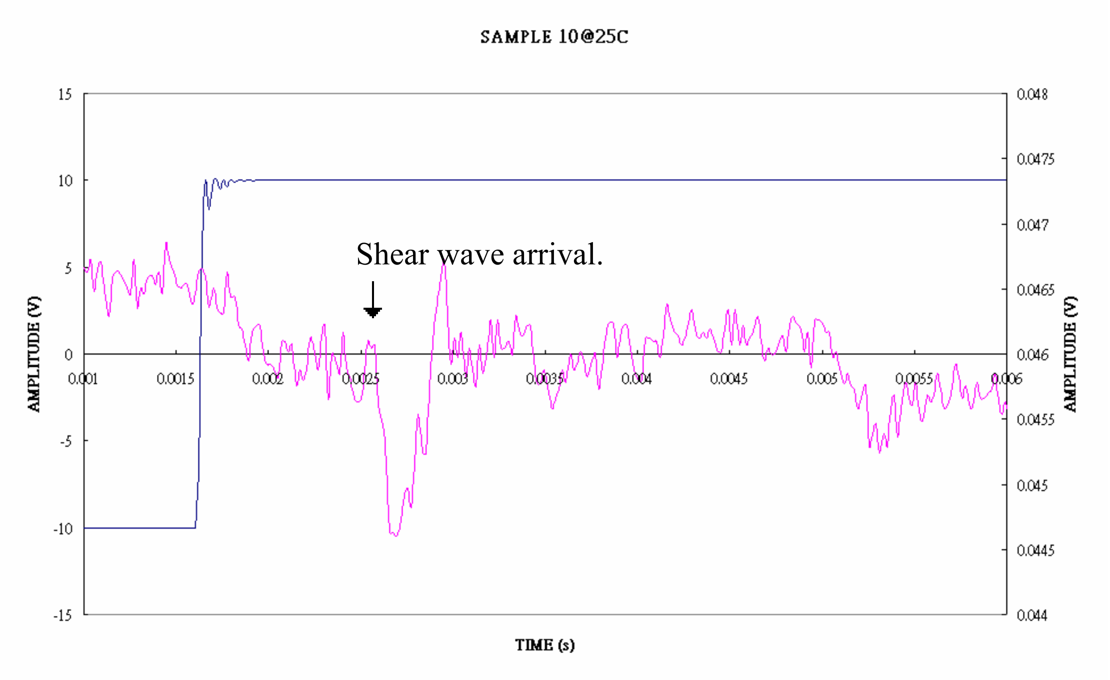
SAMPLE 10@25C
15
10
5
0
-5
-10
-15
AMPLITUDE (V)
0.001
0.0015
0.002
0.0025
0.003
0.0035
0.004
0.0045
0.005
0.0055
0.006
TIME (s)
0.048
0.0475
0.047
0.0465
0.046
0.0455
0.045
0.0445
0.044
AMPLITUDE (V)
Shear wave arrival.

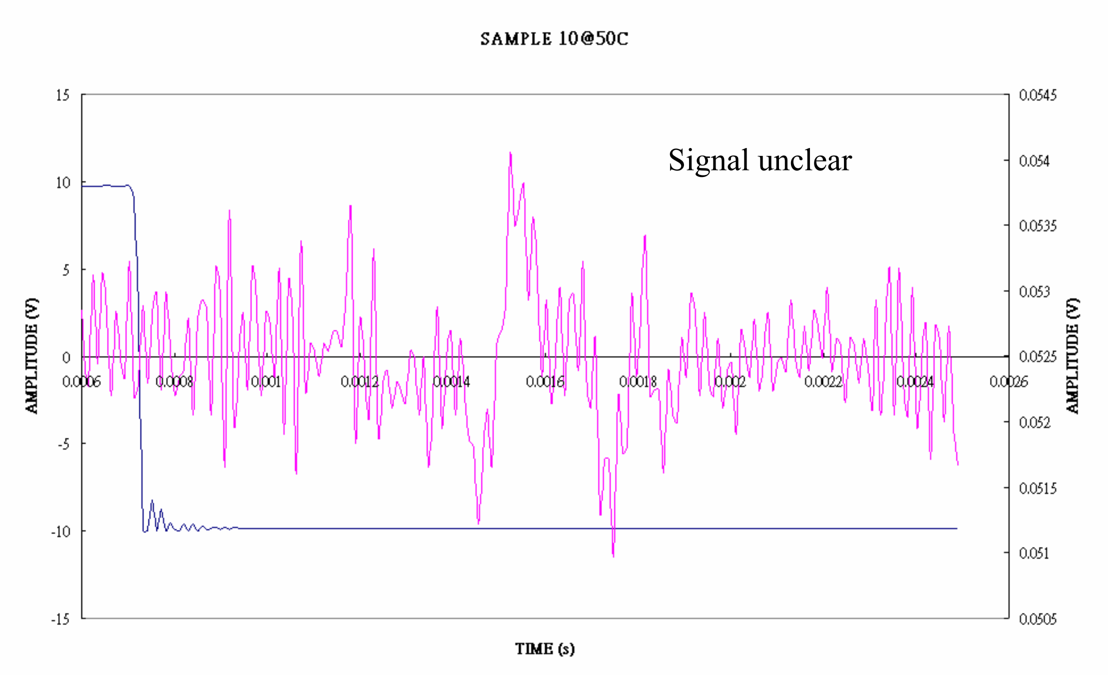
SAMPLE 10@50C
15
10
5
0
-5
-10
-15
AMPLITUDE (V)
0.0006
0.0008
0.001
0.0012
0.0014
0.0016
0.0018
0.002
0.0022
0.0024
0.0026
TIME (s)
0.0545
0.054
0.0535
0.053
0.0525
0.052
0.0515
0.051
0.0505
AMPLITUDE (V)
Signal unclear

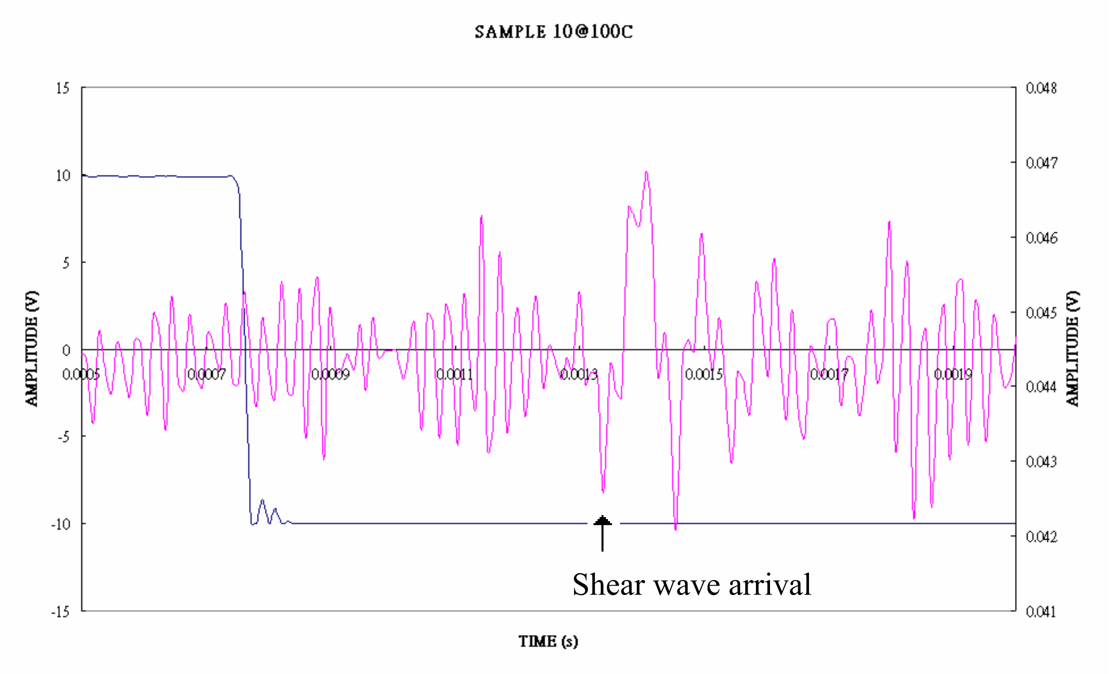
SAMPLE 10@100C
15
10
5
0
-5
-10
-15
AMPLITUDE (V)
0.048
0.047
0.046
0.045
0.044
0.043
0.042
0.041
AMPLITUDE (V)
0.0005
0.0007
0.0009
0.0011
0.0013
0.0015
0.0017
0.0019
Shear wave arrival
TIME (s)

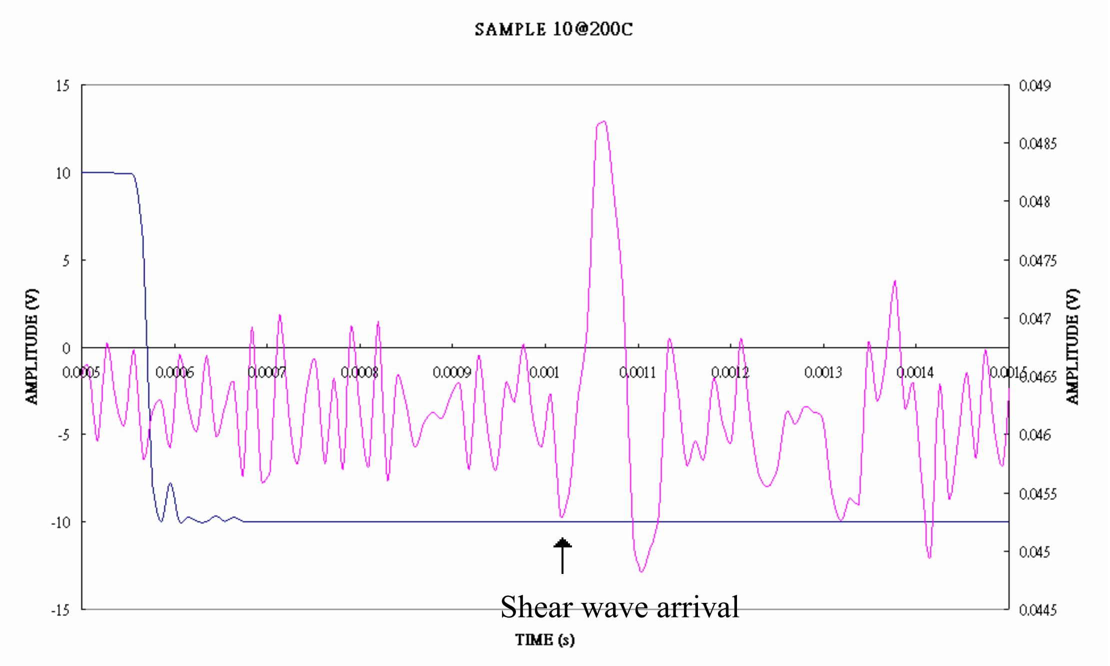
SAMPLE 10@200C
15
10
5
0
-5
-10
-15
AMPLITUDE (V)
0.049
0.0485
0.048
0.0475
0.047
0.0465
0.046
0.0455
0.045
0.0445
AMPLITUDE (V)
0.0005
0.0006
0.0007
0.0008
0.0009
0.001
0.0011
0.0012
0.0013
0.0014
0.0015
Shear wave arrival
TIME (s)

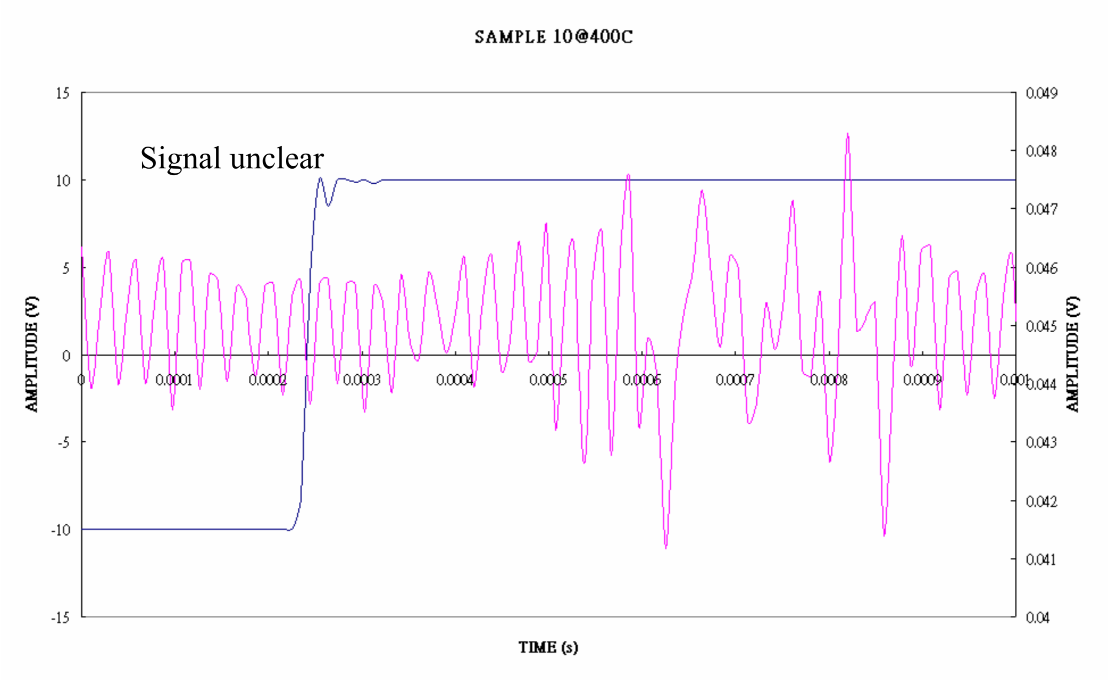
SAMPLE 10@400C
Signal unclear
AMPLITUDE (V)
15
10
5
0
-5
-10
-15
0
0.0001
0.0002
0.0003
0.0004
0.0005
0.0006
0.0007
0.0008
0.0009
0.001
TIME (s)
AMPLITUDE (V)
0.049
0.048
0.047
0.046
0.045
0.044
0.043
0.042
0.041
0.04

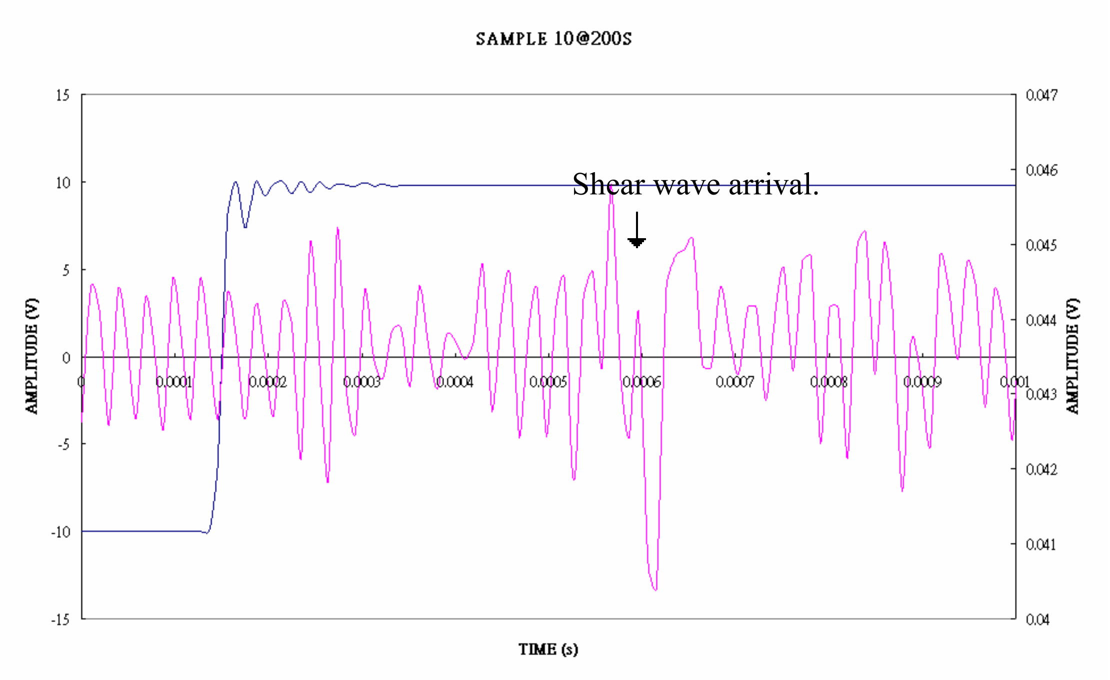
SAMPLE 10@200S
Shear wave arrival.
AMPLITUDE (V)
15
10
5
0
-5
-10
-15
0
0.0001
0.0002
0.0003
0.0004
0.0005
0.0006
0.0007
0.0008
0.0009
0.001
TIME (s)
AMPLITUDE (V)
0.047
0.046
0.045
0.044
0.043
0.042
0.041
0.04

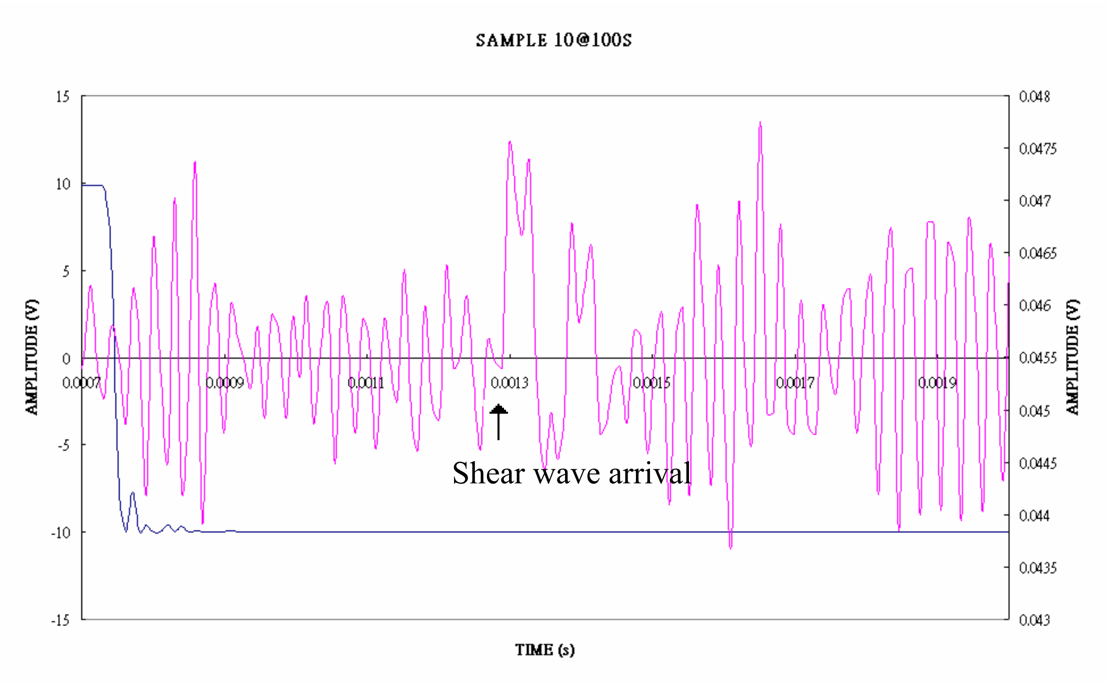
SAMPLE 10@100S

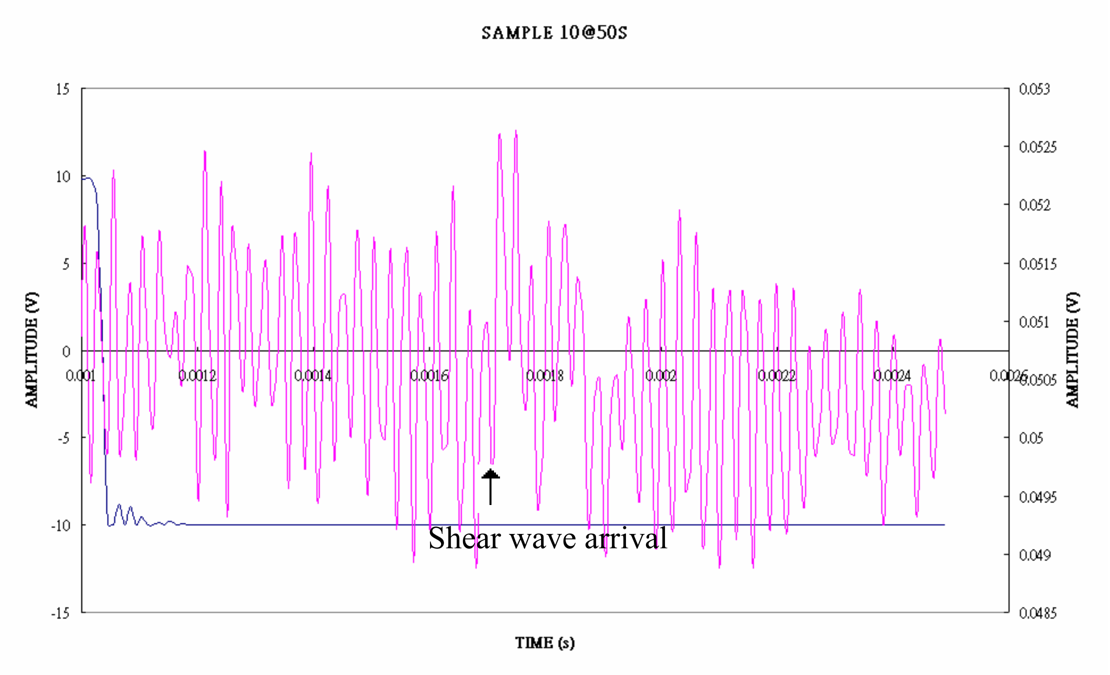
SAMPLE 10@50S

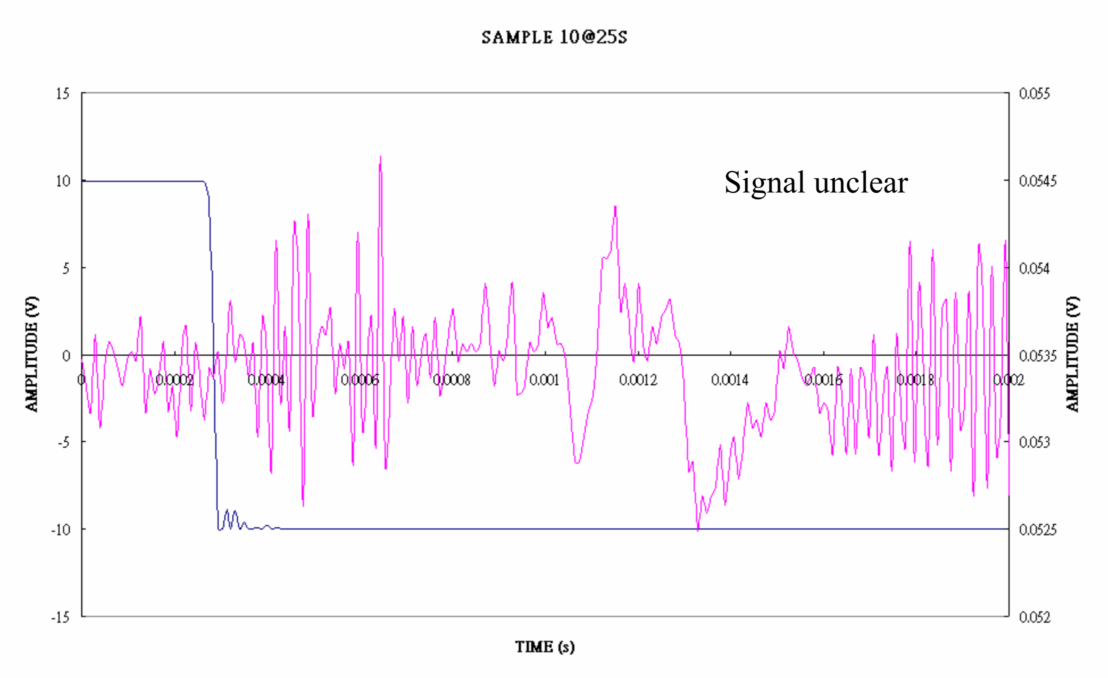
SAMPLE 10@25S
Signal unclear
AMPLITUDE (V)
15
10
5
0
-5
-10
-15
0.055
0.0545
0.054
0.0535
0.053
0.0525
0.052
0
0.0002
0.0004
0.0006
0.0008
0.001
0.0012
0.0014
0.0016
0.0018
0.002
TIME (s)

SAMPLE 12

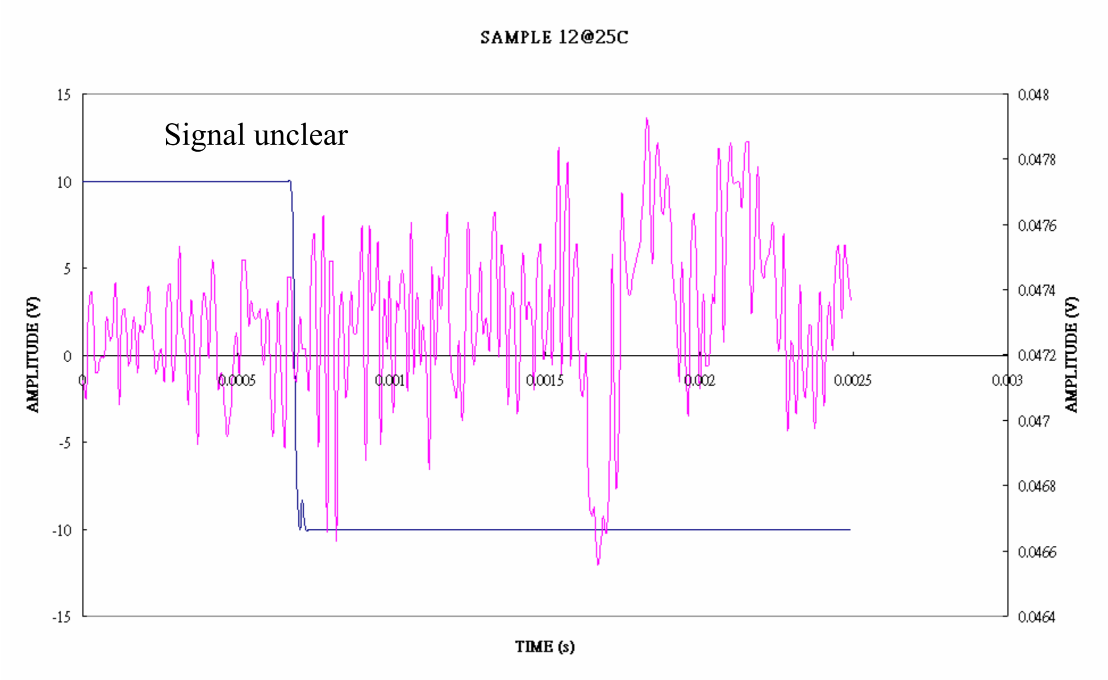
SAMPLE 12@25C
Signal unclear
AMPLITUDE (V)
15
10
5
0
-5
-10
-15
0.048
0.0478
0.0476
0.0474
0.0472
0.047
0.0468
0.0466
0.0464
0
0.0005
0.001
0.0015
0.002
0.0025
0.003
TIME (s)

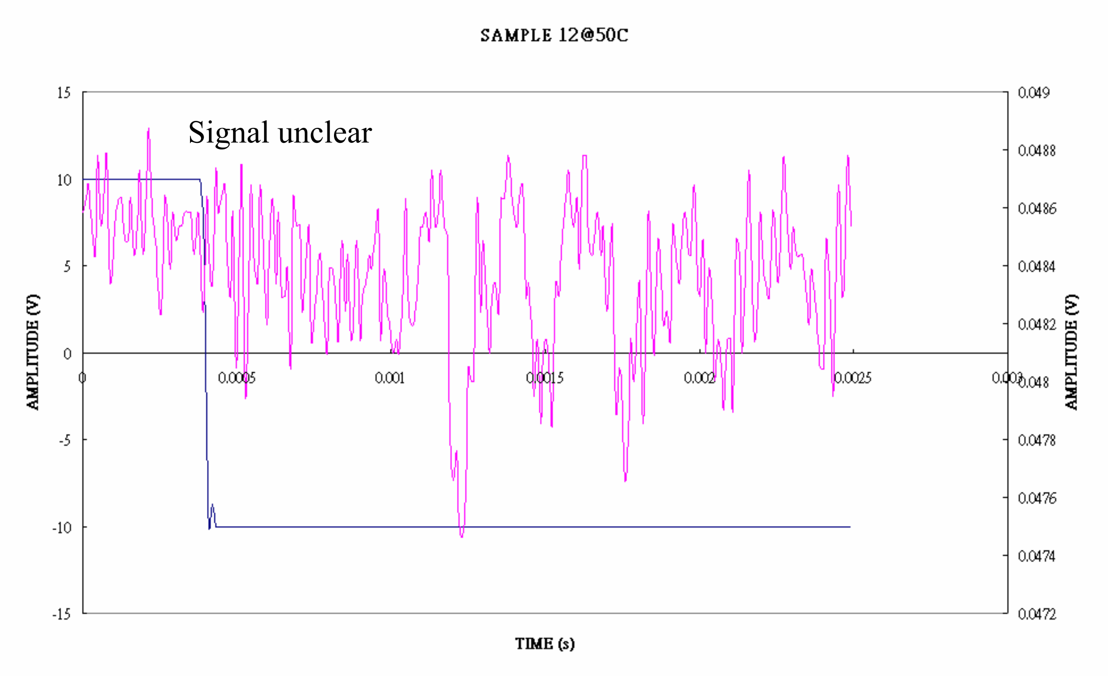
SAMPLE 12@50C
Signal unclear
AMPLITUDE (V)
15
10
5
0
-5
-10
-15
0
0.0005
0.001
0.0015
0.002
0.0025
0.003
TIME (s)
AMPLITUDE (V)
0.049
0.0488
0.0486
0.0484
0.0482
0.048
0.0478
0.0476
0.0474
0.0472

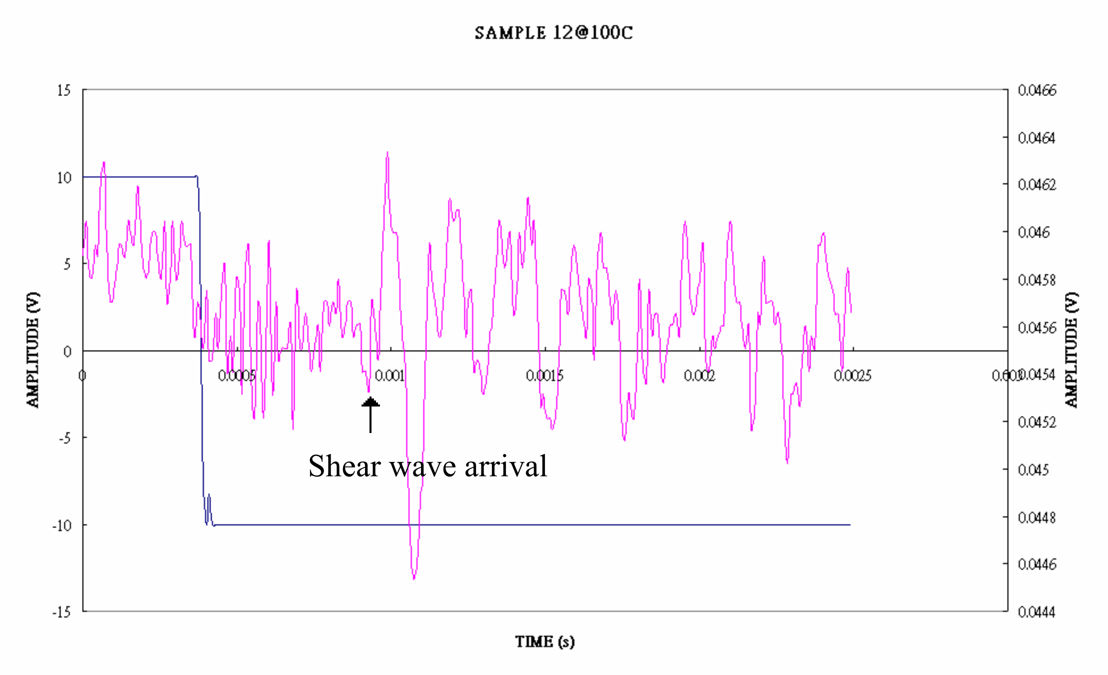
SAMPLE 12@100C
Shear wave arrival
AMPLITUDE (V)
15
10
5
0
-5
-10
-15
0
0.0005
0.001
0.0015
0.002
0.0025
0.003
TIME (s)
AMPLITUDE (V)
0.0466
0.0464
0.0462
0.046
0.0458
0.0456
0.0454
0.0452
0.045
0.0448
0.0446
0.0444

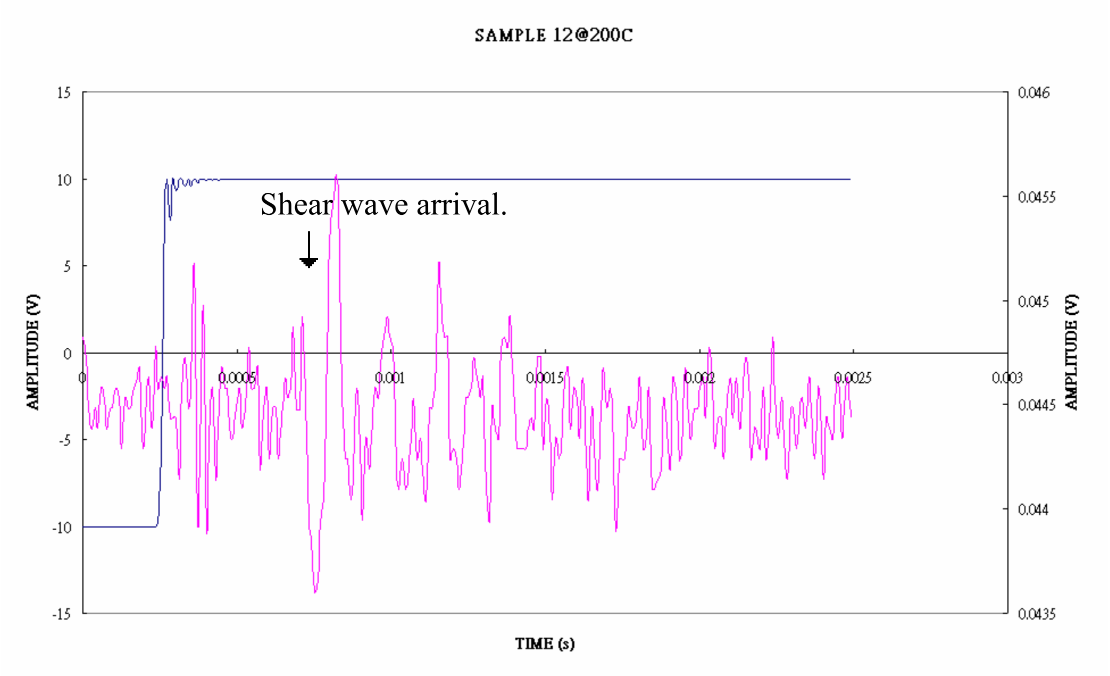
SAMPLE 12@200C
Shear wave arrival.
AMPLITUDE (V)
15
10
5
0
-5
-10
-15
0
0.0005
0.001
0.0015
0.002
0.0025
0.003
0.046
0.0455
0.045
0.0445
0.044
0.0435
AMPLITUDE (V)
TIME (s)

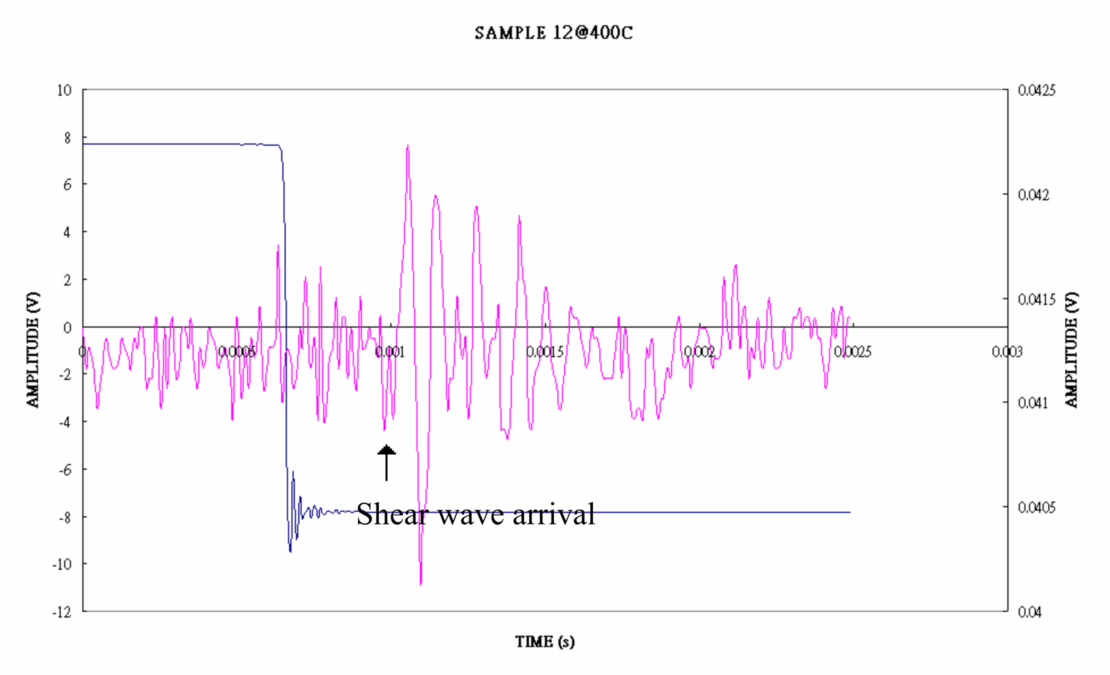
SAMPLE 12@400C
AMPLITUDE (V)
10
8
6
4
2
0
-2
-4
-6
-8
-10
-12
0
0.0005
0.001
0.0015
0.002
0.0025
0.003
Shear wave arrival
0.0425
0.042
0.0415
0.041
0.0405
0.04
AMPLITUDE (V)
TIME (s)

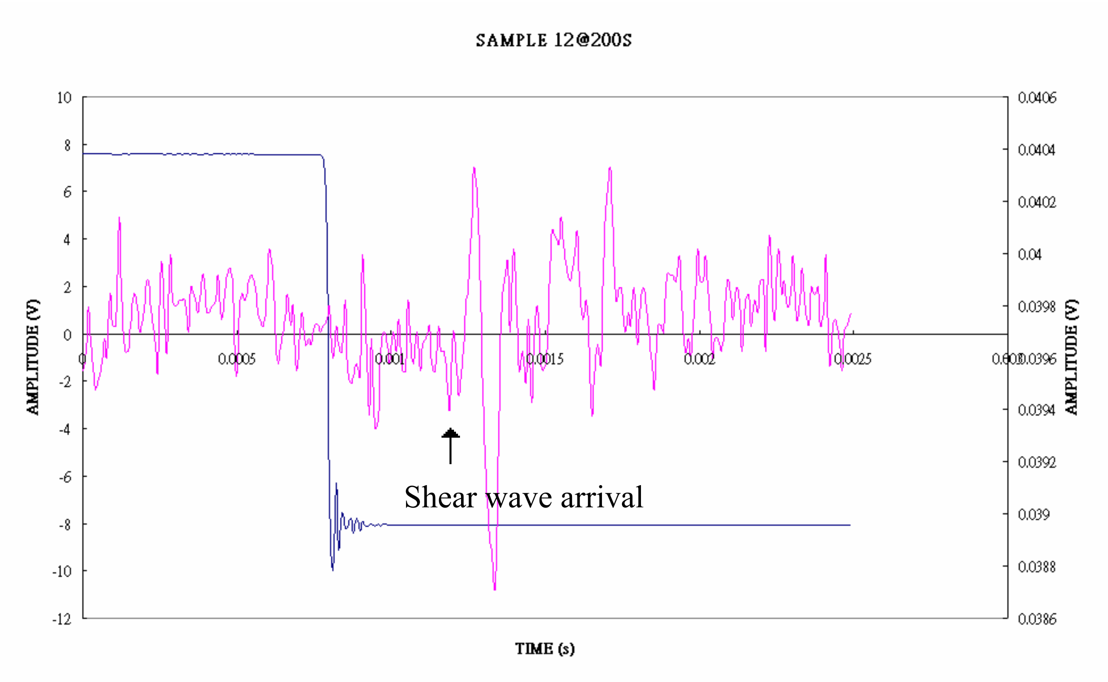
SAMPLE 12@200S
10
8
6
4
2
0
-2
-4
-6
-8
-10
-12
AMPLITUDE (V)
0
0.0005
0.001
0.0015
0.002
0.0025
0.003
0.0406
0.0404
0.0402
0.04
0.0398
0.0396
0.0394
0.0392
0.039
0.0388
0.0386
AMPLITUDE (V)
Shear wave arrival
TIME (s)

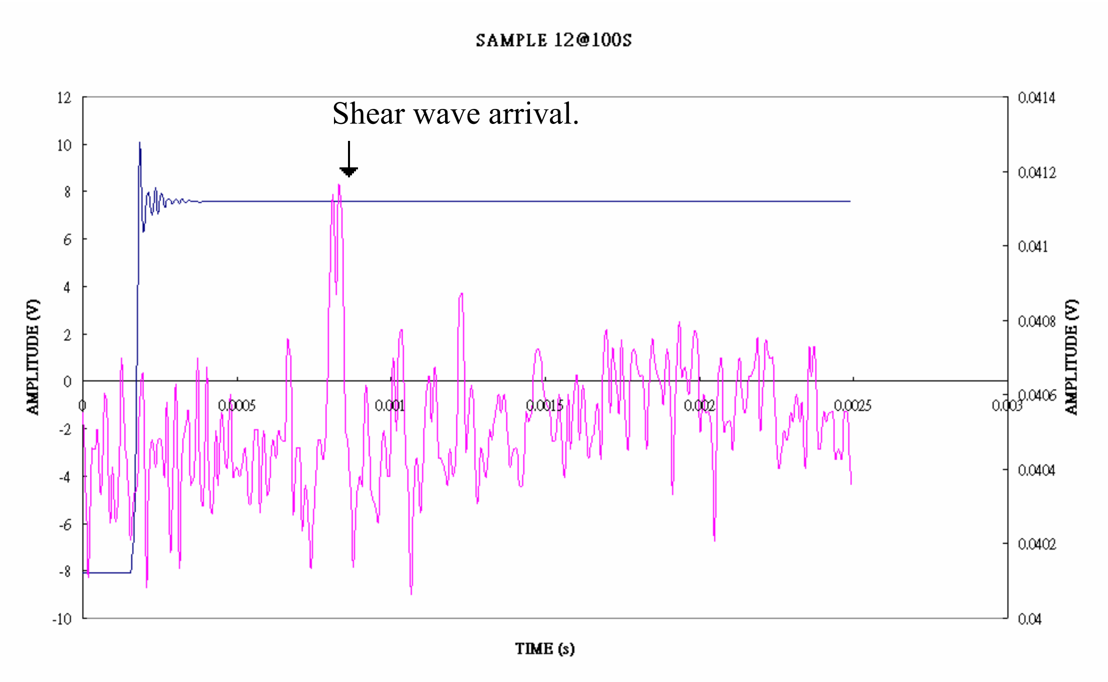
SAMPLE 12@100S
12
10
8
6
4
2
0
-2
-4
-6
-8
-10
AMPLITUDE (V)
0
0.0005
0.001
0.0015
0.002
0.0025
0.003
0.0414
0.0412
0.041
0.0408
0.0406
0.0404
0.0402
0.04
AMPLITUDE (V)
Shear wave arrival.
TIME (s)

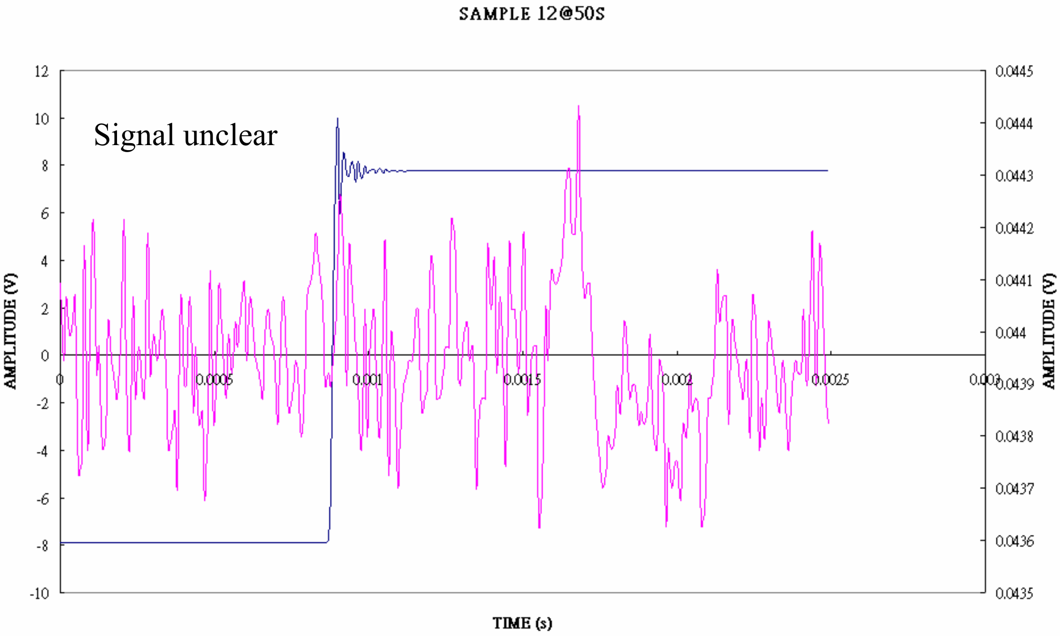
SAMPLE 12@50S
Signal unclear
AMPLITUDE (V)
12
10
8
6
4
2
0
-2
-4
-6
-8
-10
0
0.0005
0.001
0.0015
0.002
0.0025
0.003
TIME (s)
AMPLITUDE (V)
0.0445
0.0444
0.0443
0.0442
0.0441
0.044
0.0439
0.0438
0.0437
0.0436
0.0435

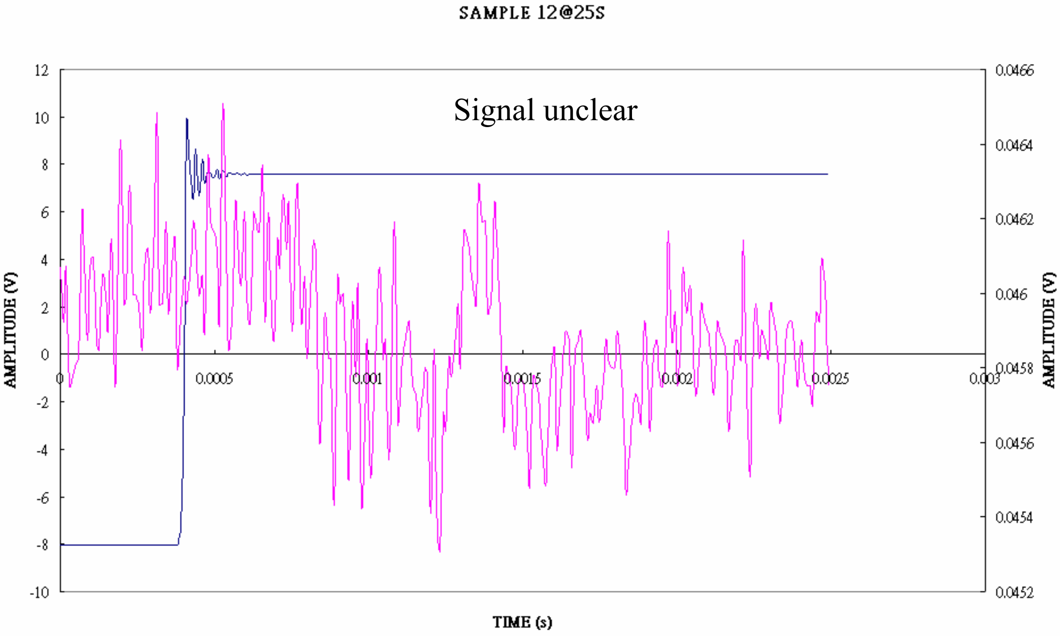
SAMPLE 12@25S
Signal unclear
AMPLITUDE (V)
12
10
8
6
4
2
0
-2
-4
-6
-8
-10
0
0.0005
0.001
0.0015
0.002
0.0025
0.003
TIME (s)
AMPLITUDE (V)
0.0466
0.0464
0.0462
0.046
0.0458
0.0456
0.0454
0.0452

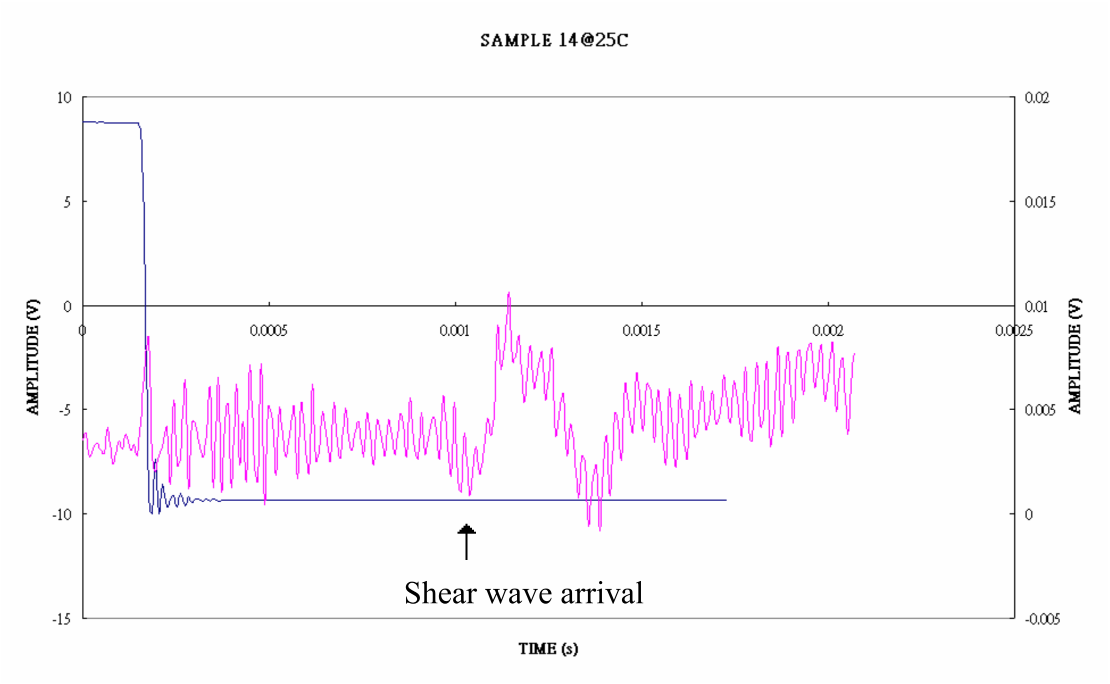
SAMPLE 14@25C
10
5
0
-5
-10
-15
0.02
0.015
0.01
0.005
0
-0.005
0
0.0005
0.001
0.0015
0.002
0.0025
AMPLITUDE (V)
AMPLITUDE (V)
Shear wave arrival
TIME (s)

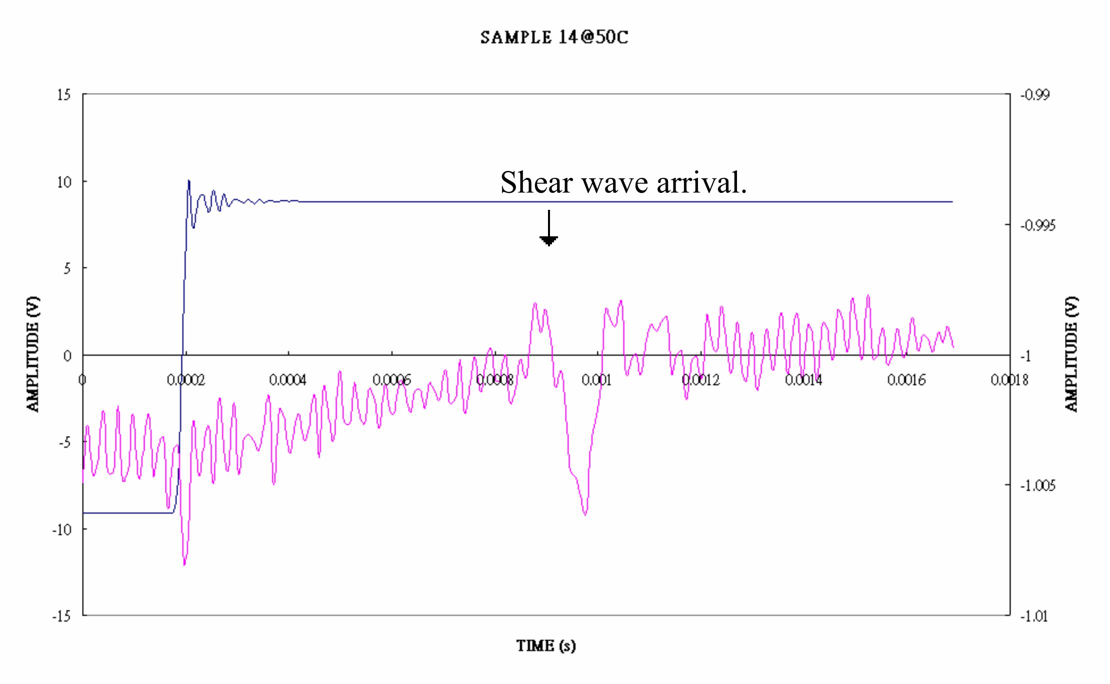
SAMPLE 14@50C
15
10
5
0
-5
-10
-15
-0.99
-0.995
-1
-1.005
-1.01
0
0.0002
0.0004
0.0006
0.0008
0.001
0.0012
0.0014
0.0016
0.0018
AMPLITUDE (V)
AMPLITUDE (V)
Shear wave arrival.
TIME (s)

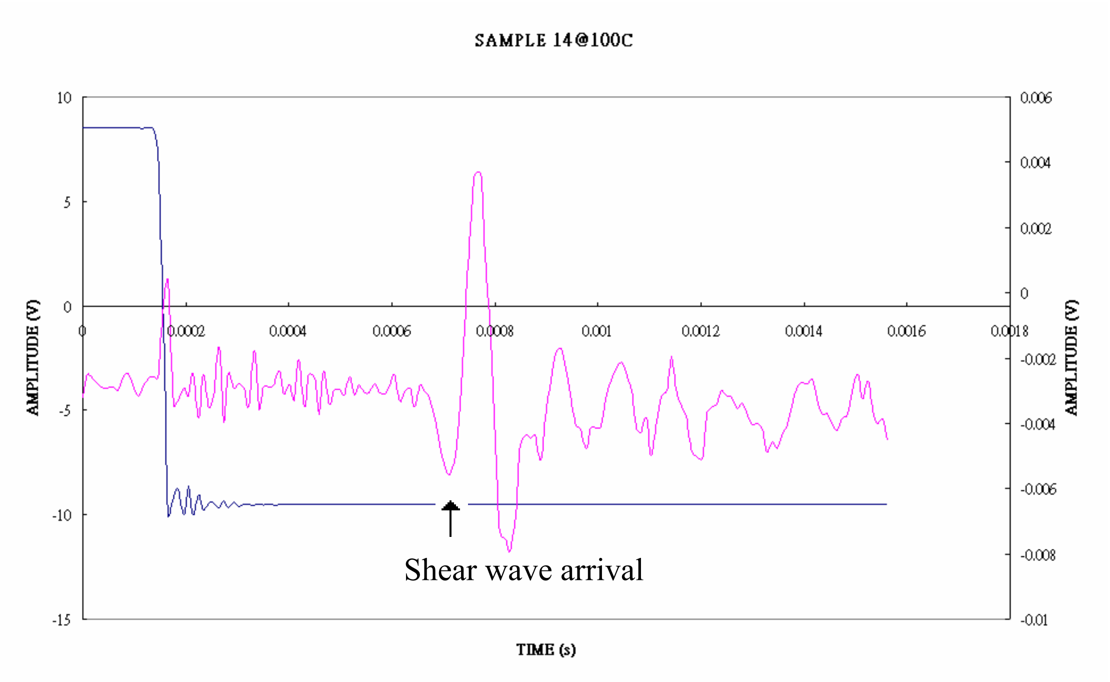
SAMPLE 14@100C
10
5
0
-5
-10
-15
AMPLITUDE (V)
0.006
0.004
0.002
0
-0.002
-0.004
-0.006
-0.008
-0.01
AMPLITUDE (V)
0
0.0002
0.0004
0.0006
0.0008
0.001
0.0012
0.0014
0.0016
0.0018
Shear wave arrival
TIME (s)

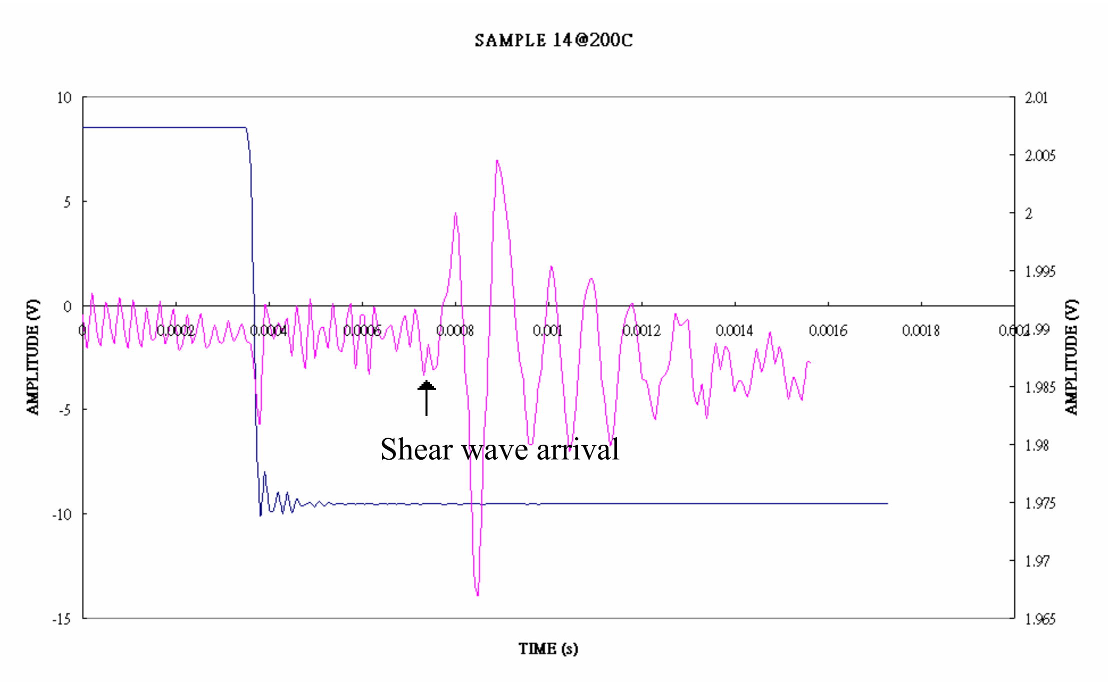
SAMPLE 14@200C
10
5
0
-5
-10
-15
AMPLITUDE (V)
2.01
2.005
2
1.995
1.99
1.985
1.98
1.975
1.97
1.965
AMPLITUDE (V)
0
0.0002
0.0004
0.0006
0.0008
0.001
0.0012
0.0014
0.0016
0.0018
0.002
Shear wave arrival
TIME (s)

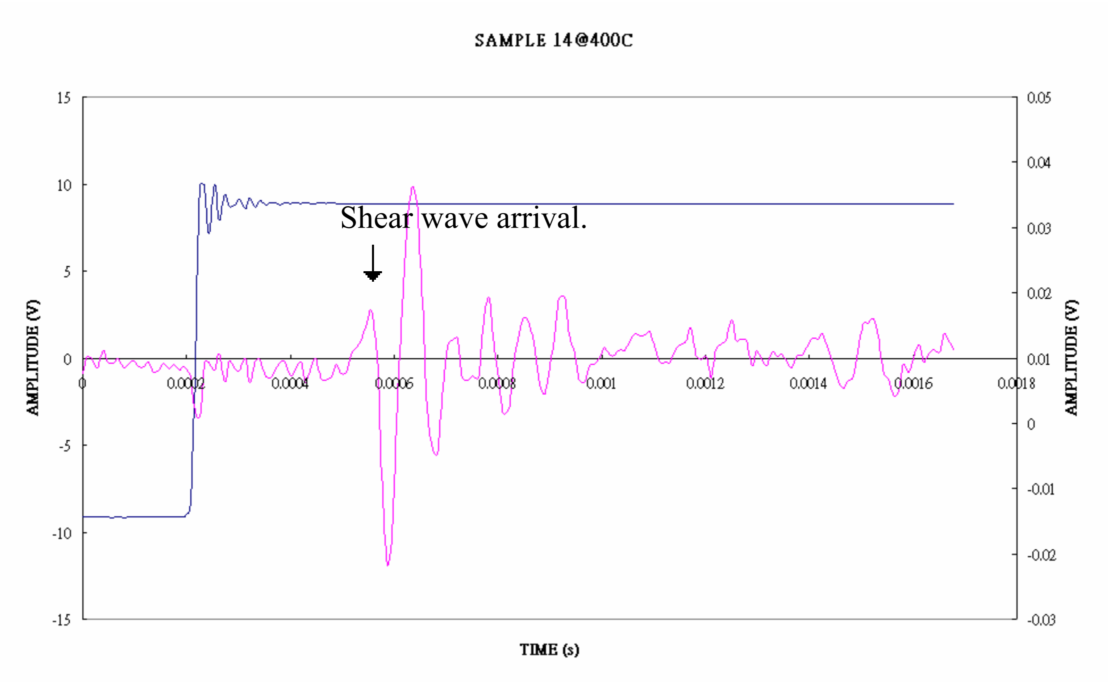
SAMPLE 14@400C
Shear wave arrival.
AMPLITUDE (V)
15
10
5
0
-5
-10
-15
0
0.0002
0.0004
0.0006
0.0008
0.001
0.0012
0.0014
0.0016
0.0018
TIME (s)
AMPLITUDE (V)
0.05
0.04
0.03
0.02
0.01
0
-0.01
-0.02
-0.03

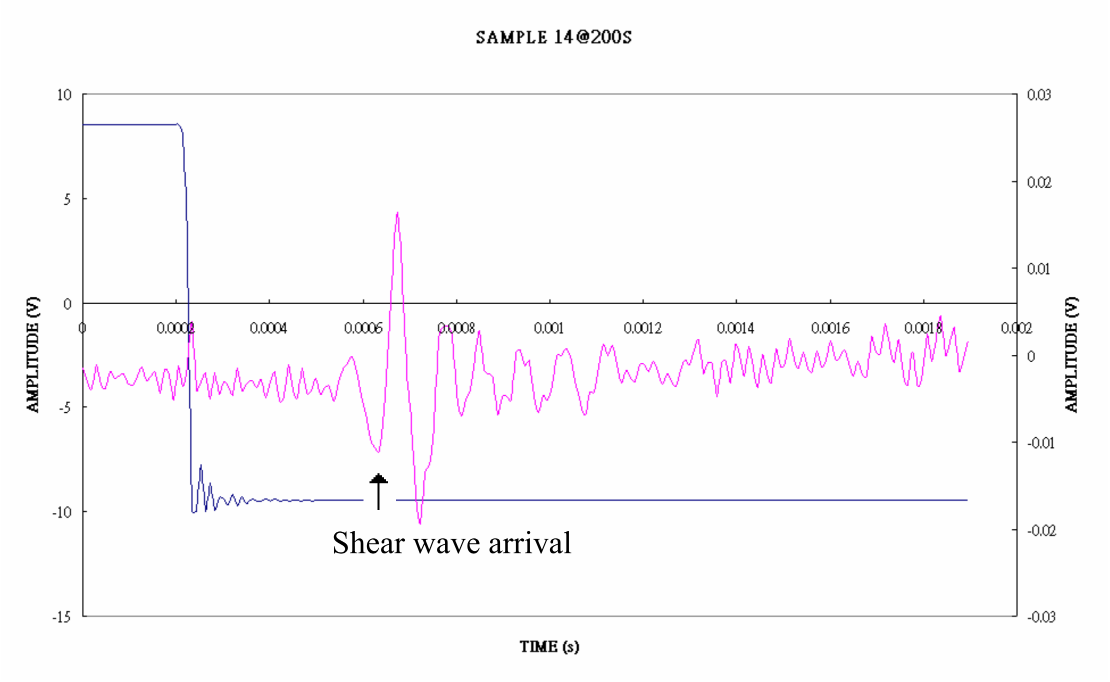
SAMPLE 14@200S
AMPLITUDE (V)
10
5
0
-5
-10
-15
0
0.0002
0.0004
0.0006
0.0008
0.001
0.0012
0.0014
0.0016
0.0018
0.002
Shear wave arrival
TIME (s)
AMPLITUDE (V)
0.03
0.02
0.01
0
-0.01
-0.02
-0.03

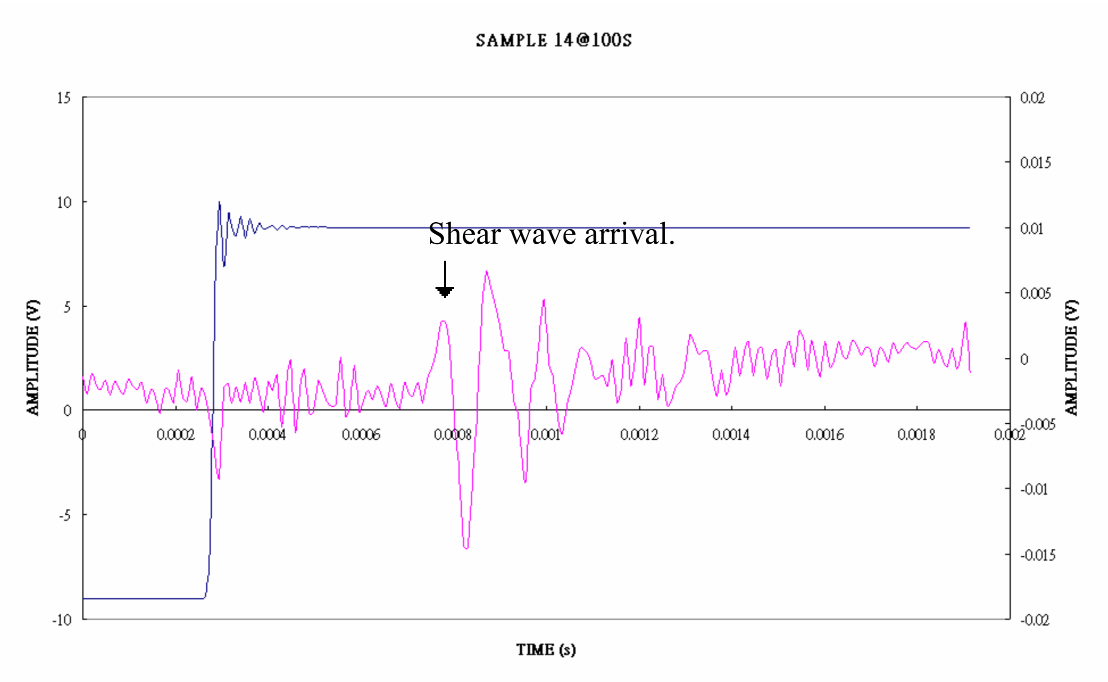
SAMPLE 14@100S
Shear wave arrival.
AMPLITUDE (V)
15
10
5
0
-5
-10
0
0.0002
0.0004
0.0006
0.0008
0.001
0.0012
0.0014
0.0016
0.0018
0.002
0.02
0.015
0.01
0.005
0
-0.005
-0.01
-0.015
-0.02
AMPLITUDE (V)
TIME (s)

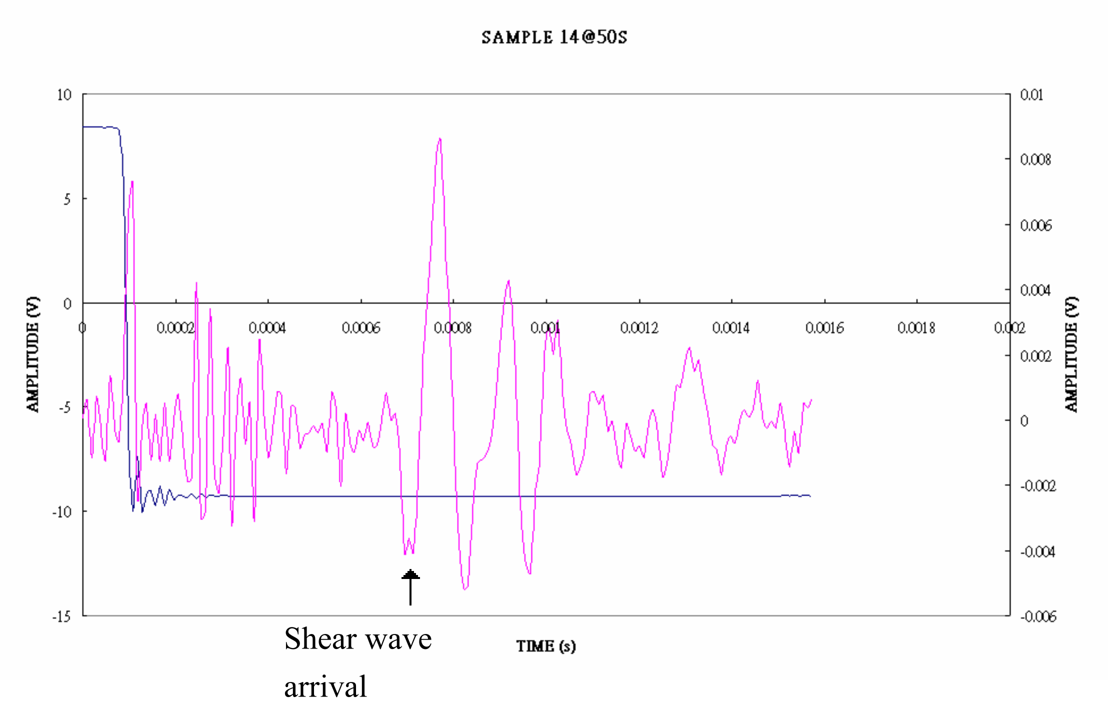
SAMPLE 14@50S
AMPLITUDE (V)
10
5
0
-5
-10
-15
0
0.0002
0.0004
0.0006
0.0008
0.001
0.0012
0.0014
0.0016
0.0018
0.002
0.01
0.008
0.006
0.004
0.002
0
-0.002
-0.004
-0.006
AMPLITUDE (V)
Shear wave arrival
TIME (s)

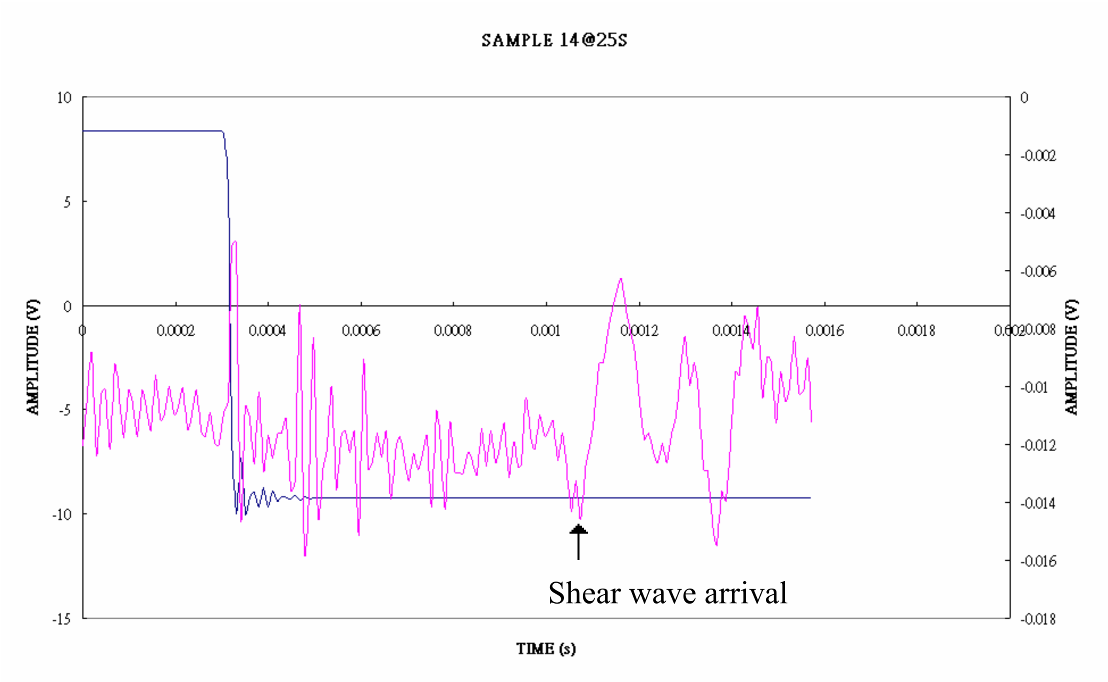
SAMPLE 14@25S
AMPLITUDE (V)
10
5
0
-5
-10
-15
0
0.0002
0.0004
0.0006
0.0008
0.001
0.0012
0.0014
0.0016
0.0018
0.002
-0.002
-0.004
-0.006
-0.008
-0.01
-0.012
-0.014
-0.016
-0.018
AMPLITUDE (V)
Shear wave arrival
TIME (s)

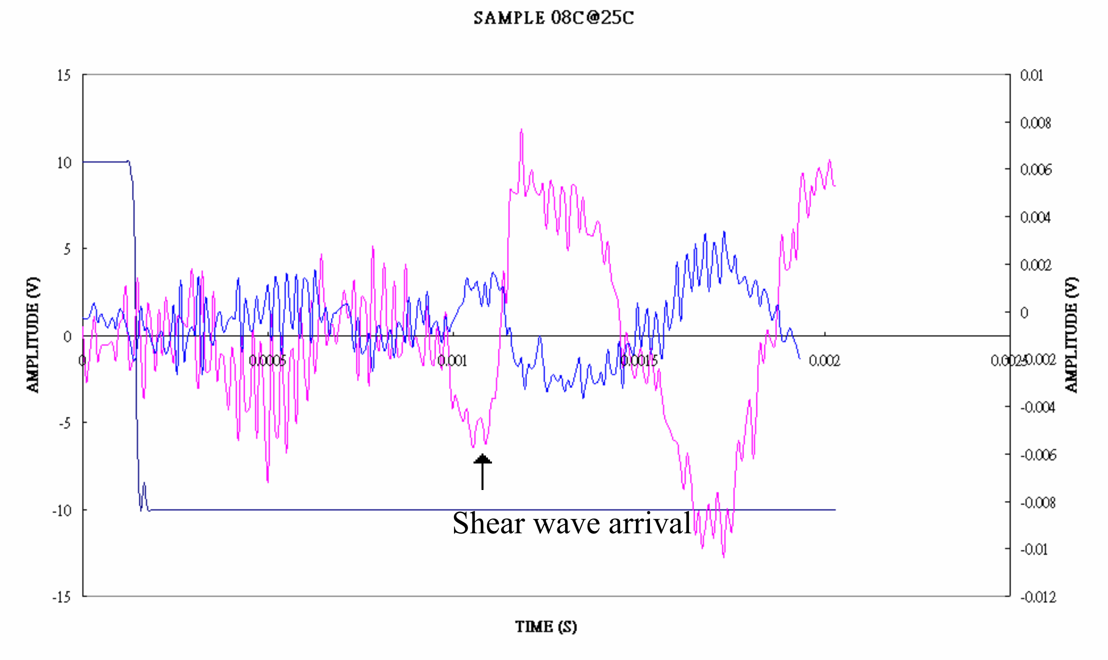
SAMPLE 08C@25C
AMPLITUDE (V)
15
10
5
0
-5
-10
-15
0
0.0005
0.001
0.0015
0.002
0.0025
0.01
0.008
0.006
0.004
0.002
0
-0.002
-0.004
-0.006
-0.008
-0.01
-0.012
AMPLITUDE (V)
Shear wave arrival
TIME (S)

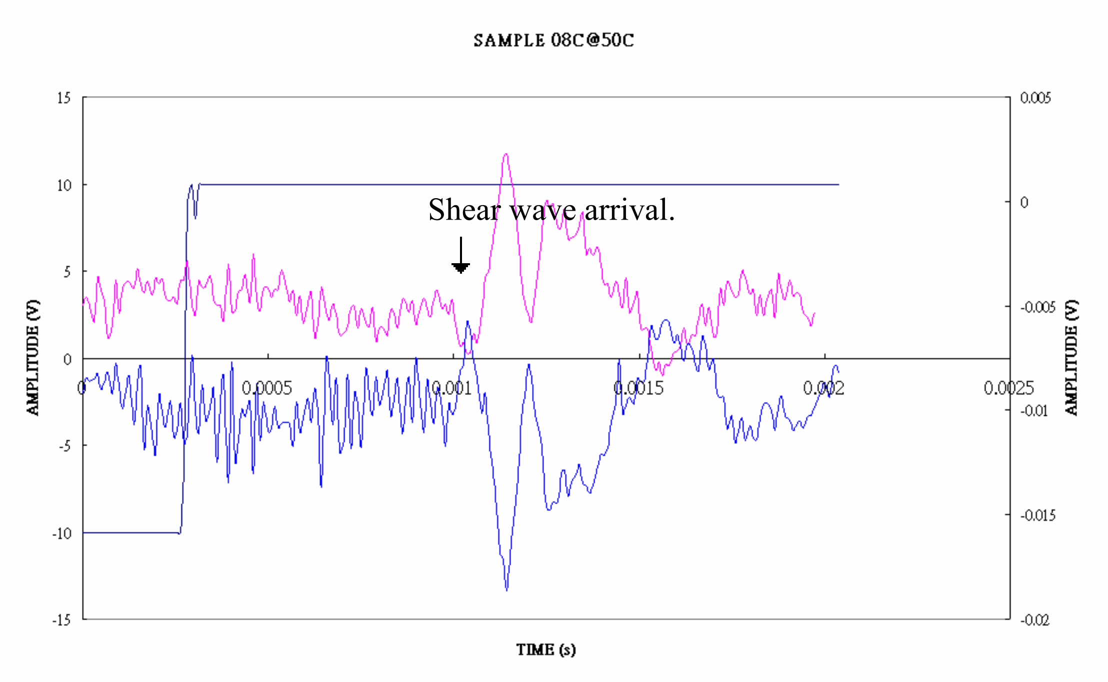
SAMPLE 08C@50C
AMPLITUDE (V)
15
10
5
0
-5
-10
-15
0
0.0005
0.001
0.0015
0.002
0.0025
TIME (s)
AMPLITUDE (V)
0.005
0
-0.005
-0.01
-0.015
-0.02
Shear wave arrival.

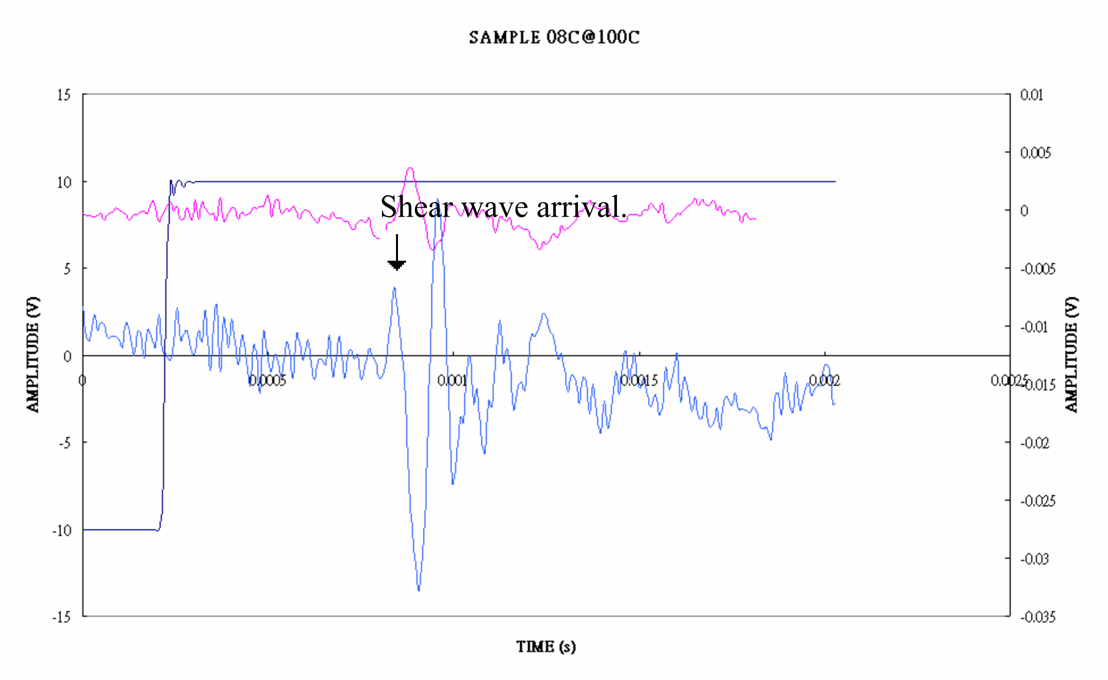
SAMPLE 08C@100C
AMPLITUDE (V)
15
10
5
0
-5
-10
-15
0
0.0005
0.001
0.0015
0.002
0.0025
TIME (s)
AMPLITUDE (V)
0.01
0.005
0
-0.005
-0.01
-0.015
-0.02
-0.025
-0.03
-0.035
Shear wave arrival.

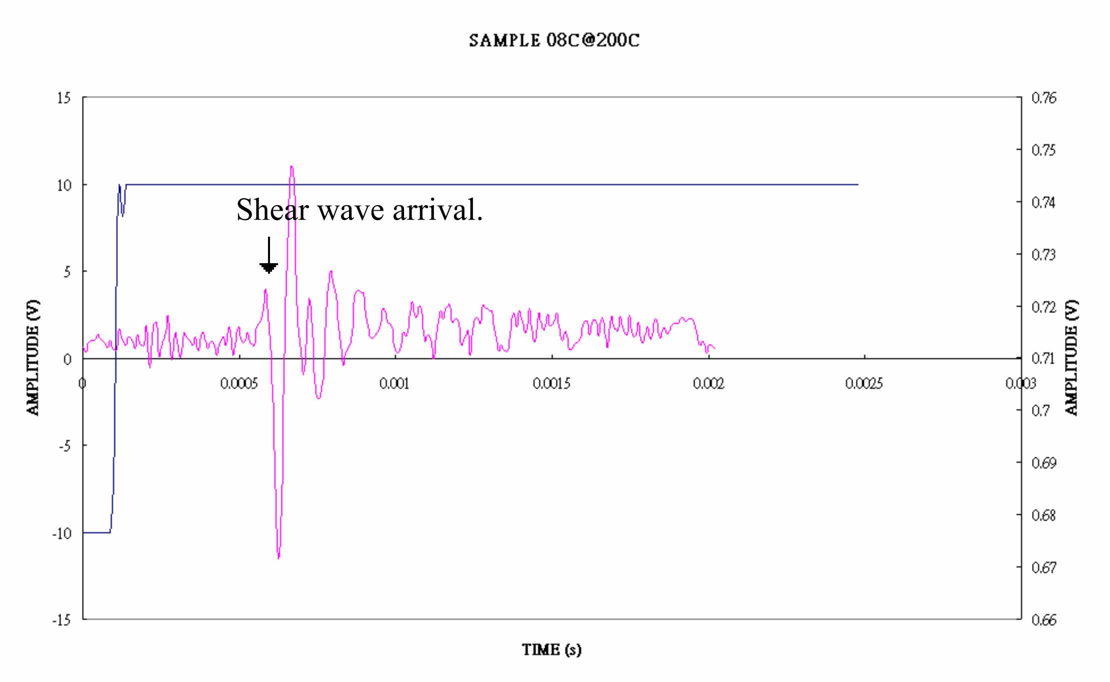
SAMPLE 08C@200C
Shear wave arrival.
15
10
5
0
-5
-10
-15
0.76
0.75
0.74
0.73
0.72
0.71
0.7
0.69
0.68
0.67
0.66
0
0.0005
0.001
0.0015
0.002
0.0025
0.003
AMPLITUDE (V)
AMPLITUDE (V)
TIME (s)

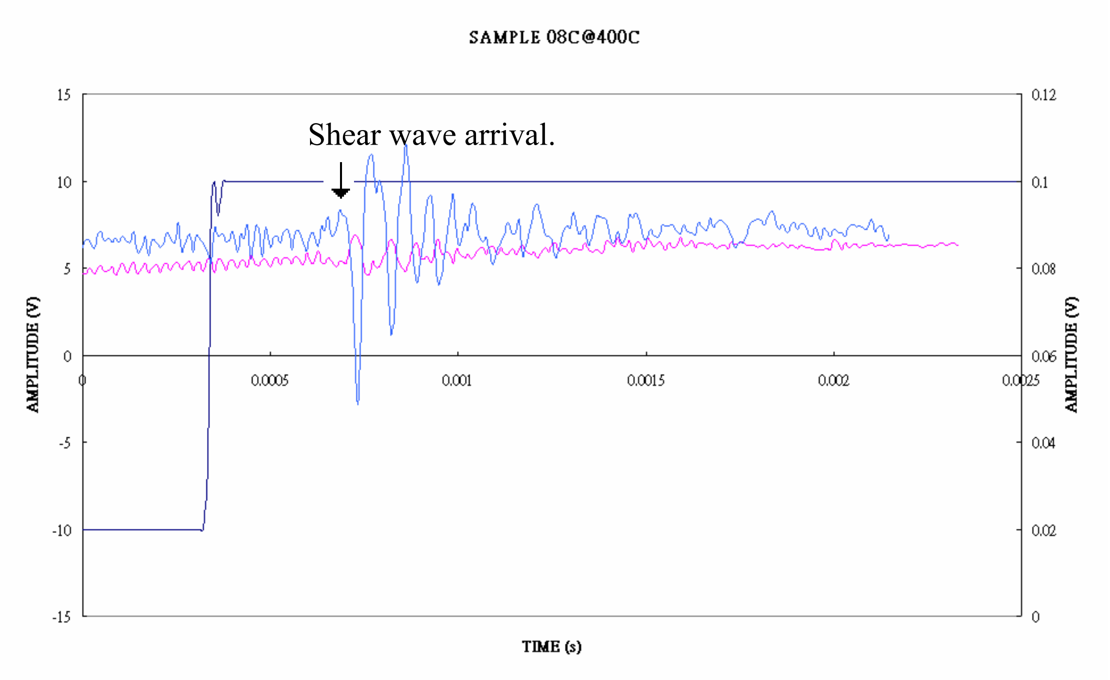
SAMPLE 08C@400C
Shear wave arrival.
15
10
5
0
-5
-10
-15
0.12
0.1
0.08
0.06
0.04
0.02
0
0
0.0005
0.001
0.0015
0.002
0.0025
AMPLITUDE (V)
AMPLITUDE (V)
TIME (s)

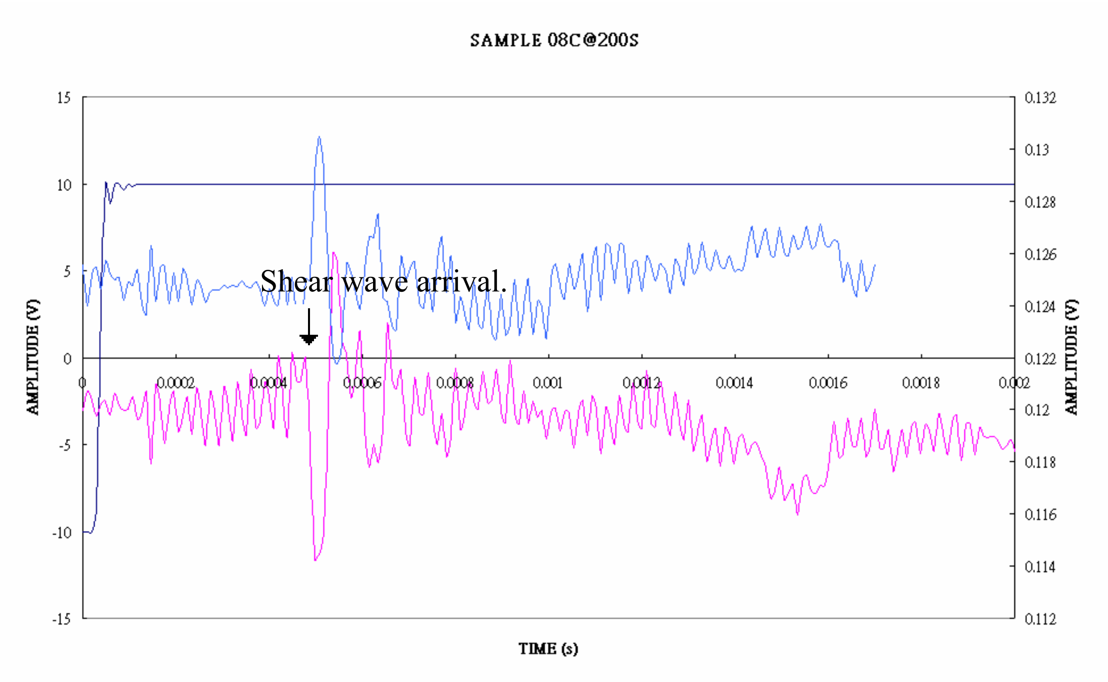
SAMPLE 08C@200S
15
10
5
0
-5
-10
-15
0.132
0.13
0.128
0.126
0.124
0.122
0.12
0.118
0.116
0.114
0.112
0
0.0002
0.0004
0.0006
0.0008
0.001
0.0012
0.0014
0.0016
0.0018
0.002
AMPLITUDE (V)
AMPLITUDE (V)
TIME (s)
Shear wave arrival.

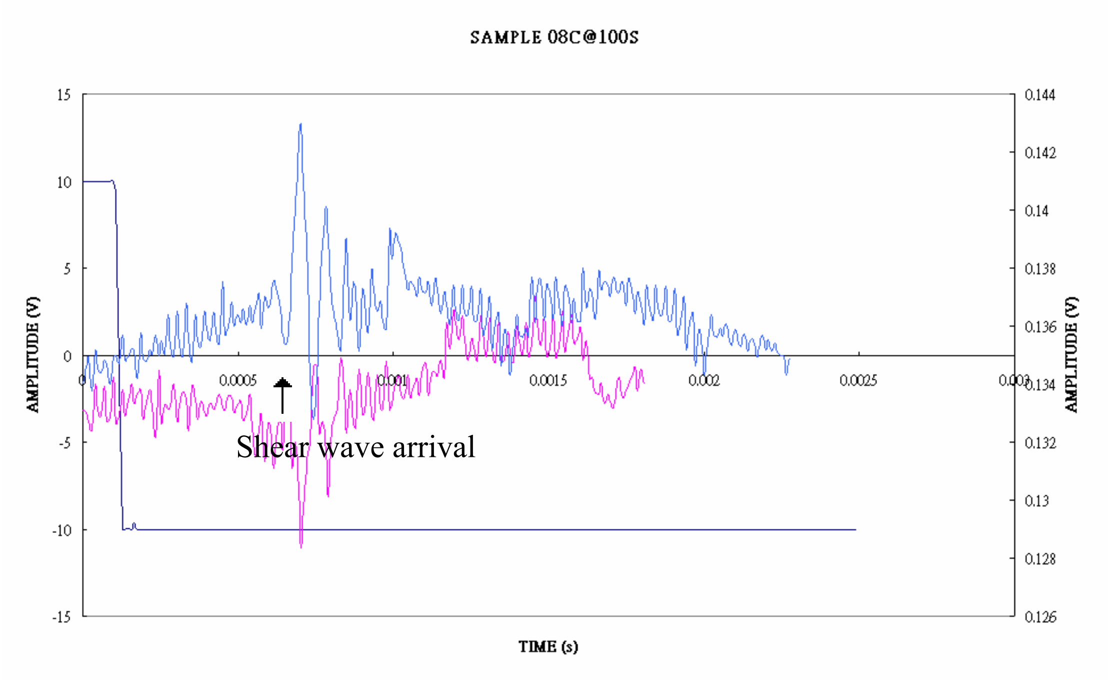
SAMPLE 08C@100S
15
10
5
0
-5
-10
-15
0.144
0.142
0.14
0.138
0.136
0.134
0.132
0.13
0.128
0.126
0
0.0005
0.001
0.0015
0.002
0.0025
0.003
AMPLITUDE (V)
AMPLITUDE (V)
TIME (s)
Shear wave arrival

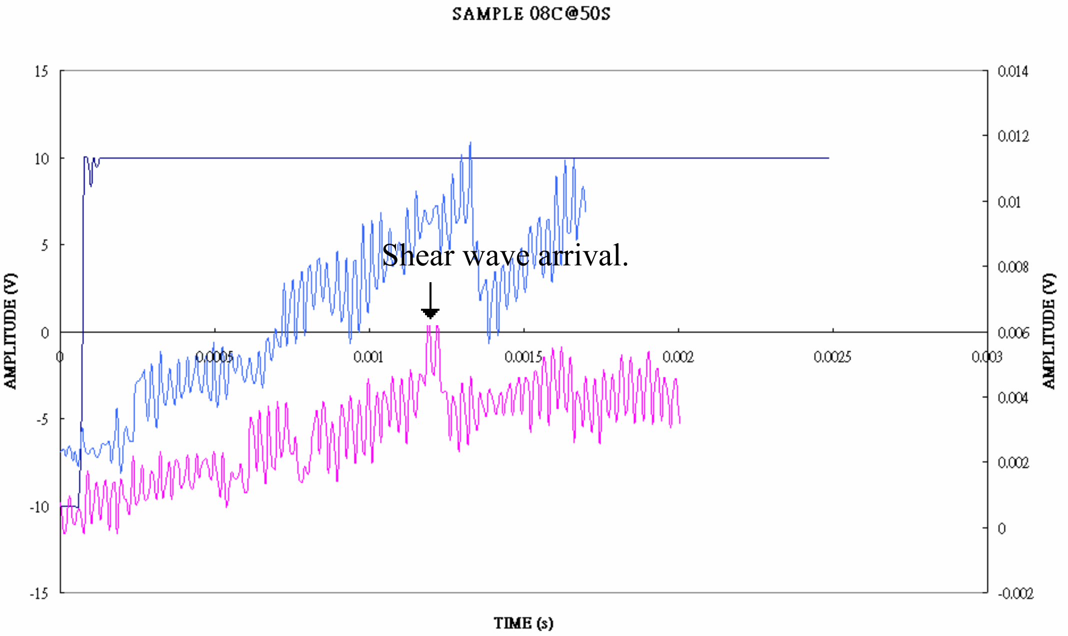
SAMPLE 08C@50S
Shear wave arrival.
AMPLITUDE (V)
15
10
5
0
-5
-10
-15
0
0.0005
0.001
0.0015
0.002
0.0025
0.003
TIME (s)
AMPLITUDE (V)
0.014
0.012
0.01
0.008
0.006
0.004
0.002
0
-0.002

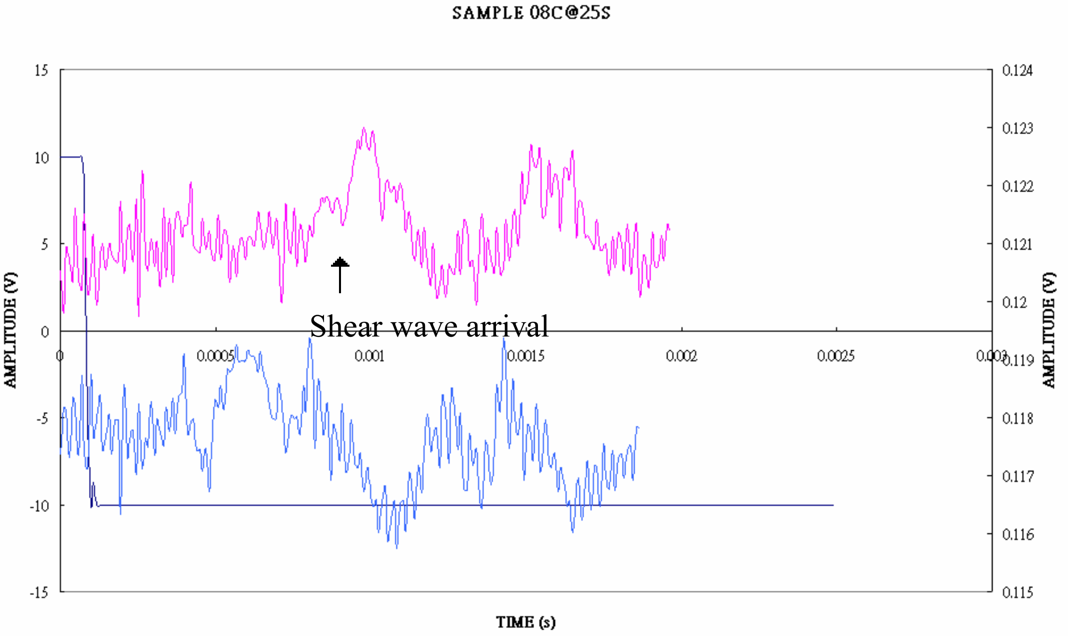
SAMPLE 08C@25S
Shear wave arrival
AMPLITUDE (V)
15
10
5
0
-5
-10
-15
0
0.0005
0.001
0.0015
0.002
0.0025
0.003
TIME (s)
AMPLITUDE (V)
0.124
0.123
0.122
0.121
0.12
0.119
0.118
0.117
0.116
0.115

APPPENDIX E

SHEAR WAVE VELOCITY RESULTS DETERMINED USING PHASE SENSITIVE DETECTION

File	Peak 1	Peak 2	Trough	Frequency (kHz)	Top	Bottom	Amplitude (V)	0	1	2	3	4	5
104	1.82E-03	2.13E-03	1.84E-03	3.23	0.0304	0.0293	0.0011	3780	**229**	118	80	60	48
105	2.05E-03	2.35E-03	2.07E-03	3.33	0.0276	0.0271	0.0005	3780	**236**	122	82	62	50
106	1.97E-03	2.28E-03	1.99E-03	3.23	0.0302	0.0294	0.0008	3780	**229**	118	80	60	48
107													
108	7.32E-04	1.03E-03	7.33E-04	3.36	0.0328	0.0322	0.0006	151200	**253**	127	85	63	51
109	1.31E-03	1.60E-03	1.58E-03	3.45	0.0331	0.0324	0.0007	**280**	135	89	66	53	44
110	1.11E-03	1.40E-03	1.41E-03	3.45	0.0277	0.0273	0.0004	**252**	128	86	65	52	43
111	7.91E-04	1.07E-03	8.11E-04	3.58	0.0272	0.0270	0.0002	3780	**253**	131	88	67	53
112	3.22E-04	6.00E-04	3.52E-04	3.60	0.0309	0.0303	0.0006	2520	**245**	129	88	66	53
113	2.08E-03	2.35E-03	2.12E-03	3.70	0.0327	0.0322	0.0005	1890	**244**	130	89	67	54
114	2.34E-04	5.00E-04	2.64E-04	3.76	0.0327	0.0323	0.0004	2520	**255**	135	91	69	56
115	1.46E-03	1.73E-03	1.47E-03	3.77	0.0277	0.0273	0.0004	7560	**275**	140	94	71	57
116	1.70E-04	4.30E-04	1.86E-04	3.85	0.0304	0.0293	0.0011	4725	**274**	141	95	72	57
117	2.20E-03	2.46E-03	2.23E-03	3.85	0.0281	0.0273	0.0008	2520	**261**	137	93	71	57
118	3.52E-04	6.10E-04	3.91E-04	3.88	0.0329	0.0321	0.0008	1938	**255**	136	93	71	57
119	2.93E-04	5.47E-04	3.52E-04	3.94	0.0328	0.0320	0.0008	1281	**242**	133	92	70	57
120	1.84E-03	2.09E-03	1.96E-03	4.00	0.0334	0.0324	0.0010	630	**204**	122	87	68	55
121	6.84E-04	9.28E-04	7.52E-04	4.10	0.0330	0.0320	0.0010	1112	**242**	136	95	72	59
122	2.30E-04	4.75E-04	3.13E-04	4.08	0.0283	0.0275	0.0008	911	**230**	132	92	71	58
123	1.90E-03	2.14E-03	1.96E-03	4.17	0.0334	0.0324	0.0010	1260	**252**	140	97	74	60

File	Peak 1	Peak 2	Trough	Frequency (kHz)	Top	Bottom	Amplitude (V)	0	1	2	3	4	5
124	1.88E-03	2.12E-03	1.97E-03	4.17	0.0304	0.0293	0.0011	840	**229**	133	93	72	59
125	1.16E-03	1.40E-03	1.49E-03	4.08	0.0332	0.0327	0.0005	**226**	130	92	71	57	48
126	1.27E-03	1.50E-03	1.36E-03	4.35	0.0326	0.0318	0.0008	840	**236**	137	97	75	61
127	1.47E-03	1.71E-03	1.57E-03	4.26	0.0332	0.0325	0.0007	756	**226**	133	94	73	59
128	1.01E-03	1.24E-03	1.10E-03	4.35	0.0331	0.0320	0.0011	840	**236**	137	97	75	61
129	1.16E-03	1.39E-03	1.24E-03	4.35	0.0332	0.0322	0.0010	945	**244**	140	98	76	61
130	3.13E-04	5.27E-04	3.91E-04	4.67	0.0284	0.0276	0.0008	969	**259**	149	105	81	66
131	1.30E-03	1.51E-03	1.39E-03	4.76	0.0304	0.0292	0.0012	840	**252**	148	105	81	66
132	2.44E-04	4.59E-04	3.32E-04	4.65	0.0334	0.0323	0.0011	859	**250**	146	103	80	65
133	5.18E-04	7.32E-04	6.25E-04	4.67	0.0296	0.0277	0.0019	707	**236**	141	101	79	64
134	3.03E-04	5.08E-04	4.00E-04	4.88	0.0315	0.0293	0.0022	779	**250**	149	106	82	67
135	2.12E-03	2.32E-03	2.23E-03	4.88	0.0288	0.0271	0.0017	657	**236**	144	104	81	66
136	2.00E-03	2.21E-03	2.12E-03	4.76	0.0340	0.0323	0.0017	630	**229**	140	101	79	65
137	2.22E-03	2.42E-03	2.34E-03	4.88	0.0288	0.0273	0.0015	605	**229**	141	102	80	66
138	1.56E-04	3.61E-04	2.93E-04	4.88	0.0300	0.0285	0.0015	552	**221**	138	101	79	65
139	1.37E-04	3.37E-04	3.07E-04	5.00	0.0322	0.0305	0.0017	445	**204**	133	98	78	65
140	1.95E-04	3.96E-04	3.42E-04	4.98	0.0337	0.0325	0.0012	514	**217**	138	101	79	66
141	7.42E-04	9.38E-04	8.89E-04	5.10	0.0290	0.0276	0.0014	514	**220**	140	103	81	67
142	1.17E-04	3.13E-04	2.70E-04	5.10	0.0338	0.0328	0.0010	494	**217**	139	102	81	67
143	1.22E-04	3.18E-04	2.73E-04	5.10	0.0293	0.0279	0.0014	501	**218**	139	102	81	67

File	Peak 1	Peak 2	Trough	Frequency (kHz)	Top	Bottom	Amplitude (V)	0	1	2	3	4	5
144	2.05E-03	2.25E-03	2.21E-03	5.00	0.0290	0.0277	0.0013	473	**210**	135	99	79	65
145	7.00E-05	2.64E-04	2.25E-04	5.15	0.0299	0.0284	0.0015	488	**217**	139	103	81	67
146	1.41E-03	1.60E-03	1.56E-03	5.41	0.0289	0.0275	0.0014	504	**226**	145	107	85	70
147	8.20E-05	2.70E-04	2.54E-04	5.32	0.0310	0.0292	0.0018	440	**210**	138	103	82	68
148	1.60E-04	3.46E-04	3.32E-04	5.38	0.0338	0.0326	0.0012	440	**211**	139	104	83	69
149	1.63E-03	1.82E-03	1.80E-03	5.26	0.0337	0.0322	0.0015	458	**213**	139	103	82	68
150	1.61E-03	1.80E-03	1.78E-03	5.26	0.0318	0.0310	0.0008	445	**210**	137	102	81	68
151	1.15E-03	1.33E-03	1.32E-03	5.41	0.0339	0.0325	0.0014	432	**210**	139	104	83	69
152	1.80E-04	3.61E-04	3.52E-04	5.52	0.0342	0.0325	0.0017	440	**214**	142	106	84	70
153	9.77E-05	2.73E-04	2.73E-04	5.70	0.0344	0.0325	0.0019	431	**216**	144	108	86	72
154	1.46E-04	3.22E-04	1.47E-04	5.68	0.0294	0.0276	0.0018	151200	428	**214**	143	107	86
155	2.60E-04	4.30E-04	2.73E-04	5.88	0.0295	0.0276	0.0019	5815	413	**214**	145	109	88
156	1.02E-04	2.73E-04	1.37E-04	5.85	0.0297	0.0279	0.0018	2160	367	**201**	138	105	85
157	1.12E-04	2.83E-04	1.46E-04	5.85	0.0297	0.0282	0.0015	2224	369	**201**	138	105	85
158	2.34E-04	4.02E-04	2.83E-04	5.95	0.0293	0.0279	0.0014	1543	348	**196**	137	105	85
159	1.17E-03	1.34E-03	1.22E-03	5.88	0.0299	0.0280	0.0019	1512	344	**194**	135	104	84
160	1.00E-04	2.64E-04	1.46E-04	6.10	0.0298	0.0282	0.0016	1643	360	**202**	141	108	87
161	2.23E-03	2.39E-03	2.29E-03	6.25	0.0340	0.0327	0.0013	1260	344	**199**	140	108	88
162	2.24E-03	2.39E-03	2.31E-03	6.45	0.0319	0.0306	0.0013	1008	329	**196**	140	109	89
163	2.13E-04	3.74E-04	3.03E-04	6.21	0.0322	0.0311	0.0011	840	301	**183**	132	103	84
164	1.09E-03	1.24E-03	1.18E-03	6.45	0.0311	0.0301	0.0010	796	302	**187**	135	106	87

File	Peak 1	Peak 2	Trough	Frequency (kHz)	Top	Bottom	Amplitude (V)	0	1	2	3	4	5
165	1.16E-03	1.32E-03	1.22E-03	6.25	0.0290	0.0286	0.0004	1260	344	**199**	140	108	88
166	2.16E-03	2.31E-03	2.24E-03	6.67	0.0314	0.0310	0.0004	889	322	**196**	141	110	91
167	1.86E-04	3.42E-04	2.54E-04	6.41	0.0339	0.0333	0.0006	1112	338	**199**	141	109	89
168	1.32E-04	2.85E-04	2.15E-04	6.54	0.0321	0.0313	0.0008	911	320	**194**	139	109	89
169	1.77E-04	3.32E-04	2.73E-04	6.45	0.0291	0.0285	0.0006	788	301	**186**	135	106	87
170	1.82E-04	3.34E-04	3.13E-04	6.58	0.0319	0.0303	0.0016	577	267	**174**	129	102	85
171	1.29E-04	2.80E-04	2.64E-04	6.62	0.0320	0.0303	0.0017	560	264	**173**	129	102	85
172	1.30E-04	2.80E-04	1.31E-04	6.67	0.0324	0.0305	0.0019	75600	501	251	**168**	126	101
173	2.40E-04	3.91E-04	2.54E-04	6.62	0.0344	0.0325	0.0019	5400	458	239	**162**	122	98
174	1.90E-04	3.39E-04	2.34E-04	6.71	0.0319	0.0296	0.0023	1718	392	221	**154**	118	96
175	2.05E-04	3.52E-04	2.44E-04	6.80	0.0323	0.0300	0.0023	1938	406	227	**158**	121	98
176	2.14E-03	2.29E-03	2.19E-03	6.67	0.0345	0.0329	0.0016	1512	378	216	**151**	116	95
177	2.37E-04	3.82E-04	2.93E-04	6.90	0.0347	0.0329	0.0018	1350	376	218	**154**	119	97
178	1.18E-04	2.63E-04	1.79E-04	6.90	0.0324	0.0305	0.0019	1239	367	215	**152**	118	96
179	1.37E-04	2.79E-04	2.03E-04	7.04	0.0346	0.0328	0.0018	1145	363	216	**154**	119	97
180	2.34E-04	3.76E-04	3.03E-04	7.04	0.0325	0.0305	0.0020	1096	358	214	**153**	119	97
181	1.58E-04	2.99E-04	2.25E-04	7.09	0.0313	0.0296	0.0017	1128	363	217	**154**	120	98
182	1.17E-04	2.60E-04	1.86E-04	6.99	0.0311	0.0296	0.0015	1096	357	213	**152**	118	96
183	1.25E-04	2.64E-04	1.90E-04	7.19	0.0308	0.0288	0.0020	1163	371	220	**157**	122	99
184	1.27E-04	2.66E-04	1.95E-04	7.19	0.0334	0.0317	0.0017	1112	365	218	**156**	121	99
185	1.76E-04	3.12E-04	2.40E-04	7.35	0.0348	0.0327	0.0021	1181	378	225	**160**	124	102

File	Peak 1	Peak 2	Trough	Frequency (kHz)	Top	Bottom	Amplitude (V)	0	1	2	3	4	5
186	1.11E-04	2.47E-04	1.86E-04	7.35	0.0352	0.0325	0.0027	1008	358	218	157	122	100
187	1.86E-04	3.20E-04	2.54E-04	7.46	0.0334	0.0303	0.0031	1112	374	225	161	125	102
100	1.22E-04	2.54E-04	1.96E-04	7.58	0.0360	0.0331	0.0029	1022	367	224	161	126	103
101	1.39E-04	2.73E-04	2.15E-04	7.46	0.0371	0.0337	0.0034	995	360	220	158	124	101
102	1.82E-04	3.05E-04	2.15E-04	7.52	0.0322	0.0289	0.0033	2291	485	271	188	144	117
103	2.08E-04	3.40E-04	2.83E-04	7.58	0.0380	0.0349	0.0031	1008	365	223	161	125	103
104	1.81E-04	3.11E-04	2.64E-04	7.69	0.0349	0.0313	0.0036	911	355	220	160	125	103
105	1.97E-04	3.28E-04	2.83E-04	7.63	0.0367	0.0337	0.0030	879	348	217	158	124	102
106	1.29E-04	2.58E-04	2.17E-04	7.75	0.0319	0.0287	0.0032	859	348	218	159	125	103
107	1.84E-04	3.12E-04	2.73E-04	7.81	0.0383	0.0350	0.0033	849	348	219	160	126	104
108	1.27E-04	2.54E-04	2.25E-04	7.87	0.0379	0.0347	0.0032	771	336	215	158	125	103
109	1.95E-04	3.20E-04	2.90E-04	8.00	0.0350	0.0323	0.0027	796	344	219	161	127	105
110	2.13E-04	3.38E-04	3.13E-04	8.00	0.0327	0.0295	0.0032	756	336	216	159	126	104
111	2.03E-04	3.27E-04	3.03E-04	8.06	0.0353	0.0327	0.0026	756	338	217	160	127	105
112	1.82E-04	3.05E-04	2.83E-04	8.13	0.0376	0.0351	0.0025	749	338	218	161	127	106
113	1.66E-04	2.89E-04	2.73E-04	8.13	0.0316	0.0293	0.0023	707	329	214	159	126	105
114	1.08E-04	2.31E-04	2.10E-04	8.13	0.0314	0.0285	0.0029	741	336	217	161	127	105
115	1.25E-04	2.45E-04	2.13E-04	8.33	0.0316	0.0289	0.0027	859	363	230	169	133	110
116	2.03E-04	3.23E-04	3.13E-04	8.33	0.0317	0.0289	0.0028	687	329	216	161	128	106

File	Peak 1	Peak 2	Trough	Frequency (kHz)	Top	Bottom	Amplitude (V)	0	1	2	3	4	5
117	1.76E-04	2.95E-04	2.83E-04	8.40	0.0316	0.0288	0.0028	707	335	219	**163**	130	108
118	2.00E-04	3.20E-04	3.10E-04	8.33	0.0380	0.0348	0.0032	687	329	216	**161**	128	106
119	1.02E-04	2.22E-04	2.10E-04	8.33	0.0379	0.0348	0.0031	700	332	217	**162**	129	107
120	1.88E-04	3.08E-04	3.01E-04	8.33	0.0380	0.0345	0.0035	669	324	214	**160**	127	106
121	1.72E-04	2.89E-04	2.88E-04	8.55	0.0353	0.0311	0.0042	652	324	216	**162**	129	108
122	1.95E-04	3.13E-04	3.13E-04	8.47	0.0370	0.0326	0.0044	641	320	214	**160**	128	107
123	1.86E-04	3.03E-04	3.02E-04	8.55	0.0353	0.0306	0.0047	652	324	216	**162**	129	108
124	1.57E-04	2.73E-04	1.66E-04	8.62	0.0325	0.0277	0.0048	8400	605	314	212	**160**	128
125	1.25E-04	2.40E-04	1.37E-04	8.70	0.0333	0.0283	0.0050	6300	595	312	212	**160**	129
126	1.33E-04	2.46E-04	1.46E-04	8.85	0.0391	0.0341	0.0050	5815	600	316	215	**163**	131
127	1.27E-04	2.39E-04	1.39E-04	8.93	0.0388	0.0340	0.0048	6300	610	320	217	**164**	132
128	1.92E-04	3.05E-04	2.15E-04	8.85	0.0324	0.0273	0.0051	3287	556	304	209	**159**	129
129	1.98E-04	3.11E-04	2.25E-04	8.85	0.0327	0.0282	0.0045	2800	540	299	207	**158**	128
130	1.99E-04	3.11E-04	3.33E-04	8.93	0.0377	0.0327	0.0050	564	307	211	**161**	130	109
131	1.73E-04	2.83E-04	2.05E-04	9.09	0.0341	0.0292	0.0049	2363	532	300	209	**160**	130
132	1.40E-04	2.51E-04	1.76E-04	9.01	0.0370	0.0321	0.0049	2100	514	293	205	**158**	128
133	1.66E-04	2.73E-04	2.05E-04	9.35	0.0376	0.0331	0.0045	1938	518	299	210	**162**	132
134	1.73E-04	2.81E-04	2.10E-04	9.26	0.0337	0.0295	0.0042	2043	521	299	209	**161**	131
135	1.60E-04	2.69E-04	1.95E-04	9.17	0.0385	0.0343	0.0042	2160	525	299	209	**161**	130
136	1.95E-04	3.03E-04	2.34E-04	9.26	0.0344	0.0302	0.0042	1938	514	296	208	**161**	131
137	1.07E-04	2.15E-04	1.46E-04	9.26	0.0320	0.0275	0.0045	1938	514	296	208	**161**	131

File	Peak 1	Peak 2	Trough	Frequency (kHz)	Top	Bottom	Amplitude (V)	0	1	2	3	4	5
138	1.93E-04	3.01E-04	2.38E-04	9.26	0.0351	0.0311	0.0040	1680	494	290	205	158	129
139	1.37E-04	2.43E-04	1.81E-04	9.43	0.0367	0.0327	0.0040	1718	504	295	209	162	132
140	1.37E-04	2.44E-04	1.86E-04	9.35	0.0386	0.0336	0.0050	1543	485	287	204	158	129
141	1.11E-04	2.16E-04	1.61E-04	9.52	0.0361	0.0313	0.0048	1512	488	291	207	161	131
142	1.04E-04	2.06E-04	1.66E-04	9.80	0.0363	0.0325	0.0038	1219	461	284	205	161	132
143	1.96E-04	3.03E-04	2.54E-04	9.35	0.0392	0.0338	0.0054	1303	458	278	199	156	127
144	1.67E-04	2.72E-04	2.25E-04	9.52	0.0326	0.0272	0.0054	1303	464	282	203	158	130
145	1.40E-04	2.44E-04	1.96E-04	9.62	0.0329	0.0274	0.0055	1350	473	286	205	160	131
146	1.51E-04	2.54E-04	2.13E-04	9.71	0.0382	0.0322	0.0060	1219	458	282	204	159	131
147	1.80E-04	2.83E-04	2.42E-04	9.71	0.0381	0.0319	0.0062	1219	458	282	204	159	131
148	1.77E-04	2.79E-04	2.36E-04	9.80	0.0367	0.0305	0.0062	1281	470	287	207	162	133
149	1.37E-04	2.38E-04	2.01E-04	9.90	0.0331	0.0280	0.0051	1181	458	284	206	162	133
150	1.08E-04	2.08E-04	1.76E-04	10.00	0.0324	0.0274	0.0050	1112	450	282	205	162	133
151	1.34E-04	2.34E-04	2.03E-04	10.00	0.0389	0.0338	0.0051	1096	447	281	205	161	133
152	1.66E-04	2.65E-04	2.34E-04	10.10	0.0379	0.0329	0.0050	1112	453	284	207	163	134
153	1.66E-04	2.64E-04	2.36E-04	10.20	0.0381	0.0337	0.0044	1080	450	284	208	164	135
154	1.15E-04	2.14E-04	1.86E-04	10.10	0.0356	0.0309	0.0047	1065	445	281	205	162	134
155	1.48E-04	2.47E-04	2.25E-04	10.10	0.0351	0.0306	0.0045	982	430	275	202	160	132
156	2.04E-04	3.02E-04	2.74E-04	10.20	0.0372	0.0325	0.0047	1080	450	284	208	164	135
157	1.22E-04	2.18E-04	1.97E-04	10.42	0.0344	0.0297	0.0047	1008	442	283	208	165	136
158	1.26E-04	2.23E-04	2.00E-04	10.31	0.0356	0.0313	0.0043	1022	442	282	207	164	135

File	Peak 1	Peak 2	Trough	Frequency (kHz)	Top	Bottom	Amplitude (V)	0	1	2	3	4	5
159	1.49E-04	2.46E-04	2.25E-04	10.31	0.0380	0.0333	0.0047	995	437	280	206	163	135
160	1.78E-04	2.74E-04	2.54E-04	10.42	0.0378	0.0329	0.0049	995	440	282	208	164	136
161	2.44E-04	3.41E-04	3.22E-04	10.31	0.0360	0.0279	0.0081	969	432	278	205	162	134
162	1.90E-04	2.83E-04	2.68E-04	10.75	0.0322	0.0284	0.0038	969	442	286	212	168	139
163	2.26E-04	3.22E-04	3.08E-04	10.42	0.0361	0.0306	0.0055	922	425	276	204	162	135
164	2.01E-04	2.93E-04	2.83E-04	10.87	0.0369	0.0314	0.0055	922	434	284	211	168	139
165	1.09E-04	2.04E-04	1.95E-04	10.53	0.0368	0.0315	0.0053	879	418	274	204	162	135
166	1.47E-04	2.43E-04	2.34E-04	10.42	0.0345	0.0281	0.0064	869	413	271	202	161	133
167	1.37E-04	2.28E-04	2.25E-04	10.99	0.0344	0.0283	0.0061	859	422	280	209	167	139
168	1.37E-04	2.29E-04	2.25E-04	10.87	0.0360	0.0301	0.0059	859	420	278	208	166	138
169	1.44E-04	2.34E-04	2.33E-04	11.11	0.0365	0.0302	0.0063	849	422	281	211	168	140
170	1.63E-04	2.54E-04	2.54E-04	10.99	0.0392	0.0329	0.0063	831	415	277	208	166	138
171	1.27E-04	2.16E-04	1.27E-04	11.24	0.0341	0.0283	0.0058	756000	848	424	283	212	170
172	1.45E-04	2.34E-04	1.51E-04	11.24	0.0366	0.0302	0.0064	12600	796	411	277	209	168
173	1.83E-04	2.73E-04	1.88E-04	11.11	0.0336	0.0270	0.0066	15120	796	409	275	207	166
174	1.57E-04	2.46E-04	1.64E-04	11.24	0.0392	0.0327	0.0065	10800	788	409	276	208	167
175	1.37E-04	2.25E-04	1.38E-04	11.36	0.0377	0.0296	0.0081	151200	854	428	286	214	172
176	1.87E-04	2.74E-04	2.00E-04	11.49	0.0370	0.0314	0.0056	5815	756	404	276	209	169
177	1.56E-04	2.44E-04	1.73E-04	11.36	0.0380	0.0307	0.0073	4447	720	392	269	205	165
178	1.00E-04	1.87E-04	1.18E-04	11.49	0.0352	0.0270	0.0082	4200	720	394	271	207	167
179	1.41E-04	2.29E-04	1.63E-04	11.36	0.0343	0.0266	0.0077	3436	687	382	264	202	164

File	Peak 1	Peak 2	Trough	Frequency (kHz)	Top	Bottom	Amplitude (V)	0	1	2	3	4	5
180	1.84E-04	2.71E-04	2.06E-04	11.49	0.0333	0.0273	0.0060	3436	694	386	267	204	165
181	1.16E-04	2.03E-04	1.37E-04	11.49	0.0381	0.0331	0.0050	3600	700	388	268	205	166
182	1.27E-04	2.13E-04	1.56E-04	11.63	0.0399	0.0312	0.0087	2607	657	376	263	203	165
183	1.45E-04	2.31E-04	1.76E-04	11.63	0.0346	0.0268	0.0078	2439	646	372	262	202	164
184	1.46E-04	2.33E-04	1.81E-04	11.49	0.0374	0.0297	0.0077	2160	620	362	255	197	161
185	1.20E-04	2.05E-04	1.56E-04	11.76	0.0343	0.0265	0.0078	2100	625	367	260	201	164
186	1.74E-04	2.58E-04	2.09E-04	11.90	0.0365	0.0291	0.0074	2160	635	372	263	204	166
187	1.24E-04	2.08E-04	1.66E-04	11.98	0.0342	0.0271	0.0071	1800	602	362	258	201	165
188	1.04E-04	1.87E-04	1.45E-04	12.05	0.0381	0.0311	0.0070	1844	610	365	261	203	166
189	1.27E-04	2.13E-04	1.71E-04	11.63	0.0339	0.0272	0.0067	1718	582	350	250	195	159
190	1.85E-04	2.68E-04	2.30E-04	12.05	0.0343	0.0279	0.0064	1680	591	358	257	201	164
191	1.26E-04	2.08E-04	1.74E-04	12.20	0.0337	0.0275	0.0062	1575	582	357	257	201	165
192	1.35E-04	2.16E-04	1.82E-04	12.35	0.0356	0.0301	0.0055	1609	591	362	261	204	167
193	9.77E-05	1.82E-04	1.48E-04	11.86	0.0334	0.0279	0.0055	1503	562	345	249	195	160
194	1.56E-04	2.37E-04	2.07E-04	12.35	0.0367	0.0323	0.0044	1482	573	355	257	202	166
195	1.21E-04	2.04E-04	1.76E-04	12.05	0.0328	0.0284	0.0044	1375	548	342	249	195	161
196	1.73E-04	2.54E-04	2.26E-04	12.35	0.0331	0.0289	0.0042	1426	564	352	255	201	165
197	1.22E-04	2.04E-04	1.75E-04	12.20	0.0323	0.0283	0.0040	1426	560	348	253	198	163
198	1.78E-04	2.61E-04	2.32E-04	12.05	0.0380	0.0337	0.0043	1400	552	344	250	196	161
199	1.12E-04	1.94E-04	1.64E-04	12.20	0.0335	0.0292	0.0043	1454	564	350	254	199	164
200	1.76E-04	2.55E-04	2.27E-04	12.66	0.0386	0.0341	0.0045	1482	582	362	263	206	170

File	Peak 1	Peak 2	Trough	Frequency (kHz)	Top	Bottom	Amplitude (V)	0	1	2	3	4	5
201	1.55E-04	2.34E-04	2.10E-04	12.66	0.0380	0.0333	0.0047	1375	564	355	259	204	168
202	1.28E-04	2.08E-04	1.85E-04	12.50	0.0385	0.0328	0.0057	1326	552	348	255	201	165
203	1.11E-04	1.92E-04	1.68E-04	12.35	0.0383	0.0321	0.0062	1326	548	345	252	198	164
204	1.27E-04	2.05E-04	1.85E-04	12.82	0.0397	0.0335	0.0062	1303	556	353	259	204	169
205	1.37E-04	2.15E-04	1.96E-04	12.82	0.0395	0.0325	0.0070	1281	552	352	258	204	168
206	1.76E-04	2.54E-04	2.39E-04	12.82	0.0340	0.0272	0.0068	1200	536	345	255	202	167
207	1.31E-04	2.09E-04	1.95E-04	12.82	0.0377	0.0309	0.0068	1181	532	344	254	201	167
208	1.35E-04	2.12E-04	1.98E-04	12.99	0.0344	0.0270	0.0074	1200	540	348	257	204	169
209	1.71E-04	2.47E-04	2.35E-04	13.16	0.0353	0.0275	0.0078	1181	540	350	259	205	170
210	1.54E-04	2.31E-04	2.25E-04	12.99	0.0348	0.0270	0.0078	1065	511	336	250	199	166
211	1.38E-04	2.15E-04	2.10E-04	12.99	0.0347	0.0274	0.0073	1050	507	335	250	199	165
212	1.47E-04	2.25E-04	2.24E-04	12.82	0.0406	0.0320	0.0086	982	488	324	243	194	162
213	1.60E-04	2.35E-04	2.34E-04	13.33	0.0360	0.0283	0.0077	1022	507	338	253	202	168
214	1.70E-04	2.45E-04	2.45E-04	13.33	0.0345	0.0269	0.0076	1008	504	336	252	202	168

APPENDIX F

FULL PAGE SIZE OF GRAPHS SHOWN IN DISCUSSION CHAPTER

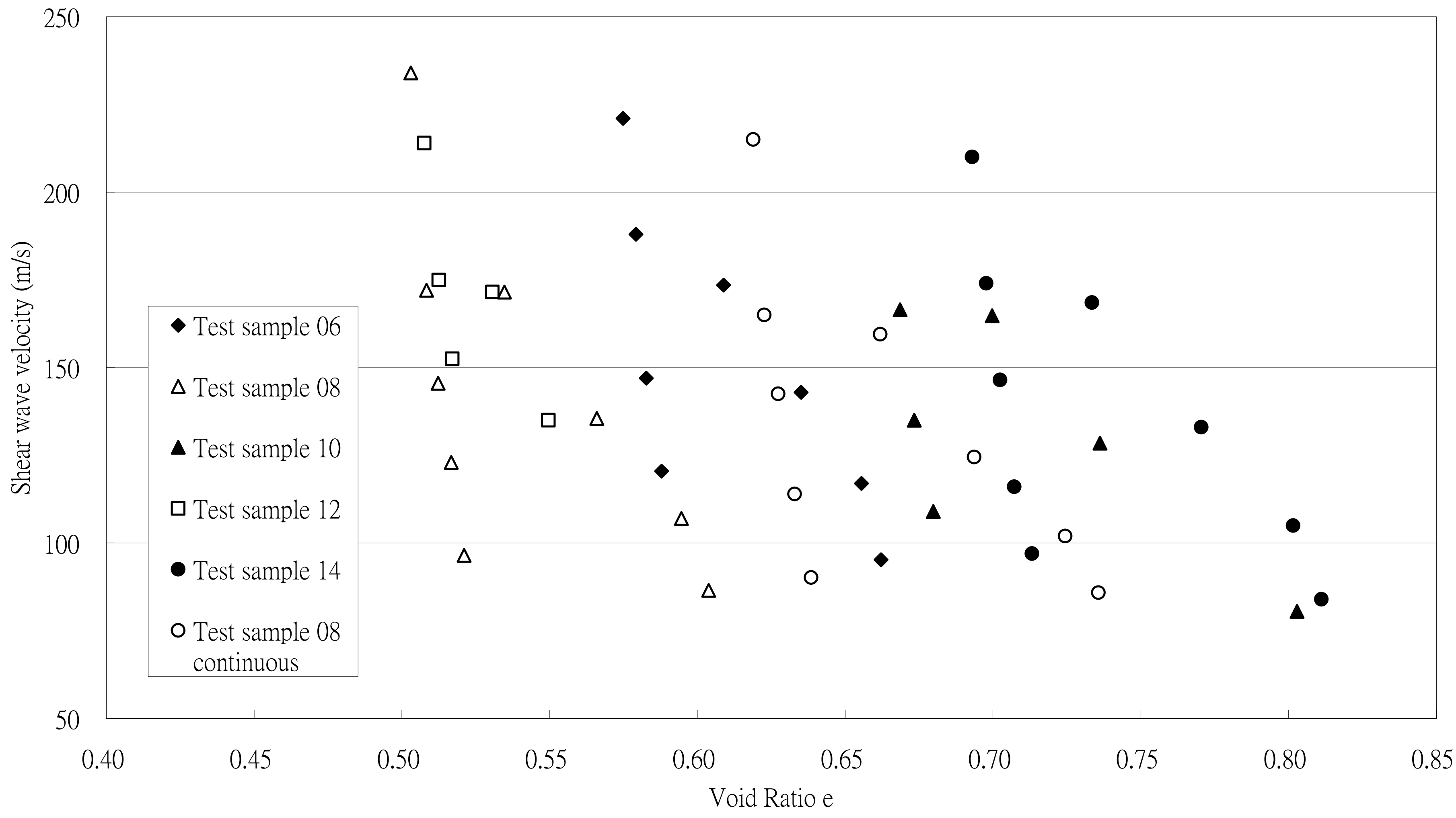

Figure 30. Graph of shear wave velocity against void ratio for various samples.

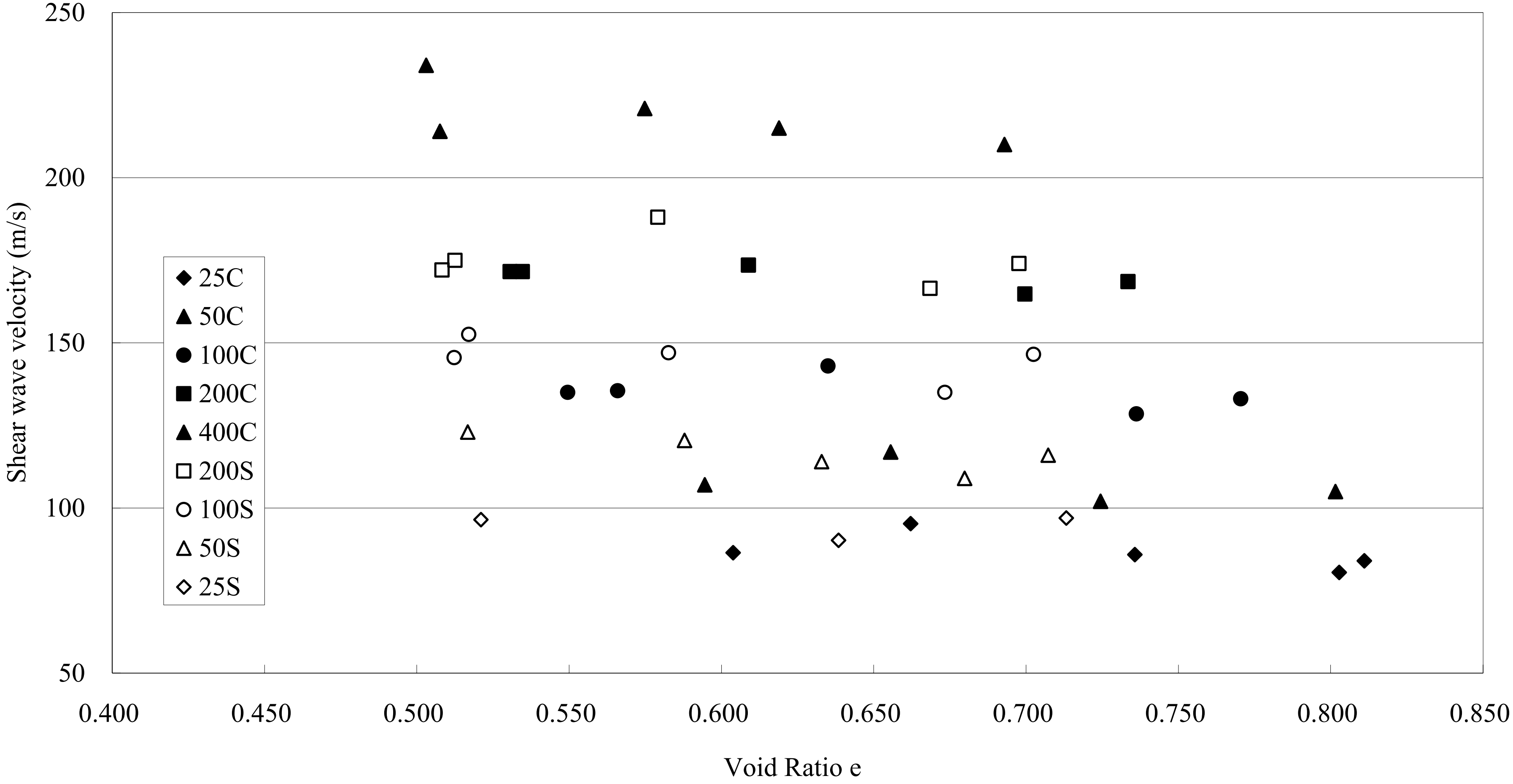

Figure 31. Shear wave velocity vs void ratio plot for various effective stresses.

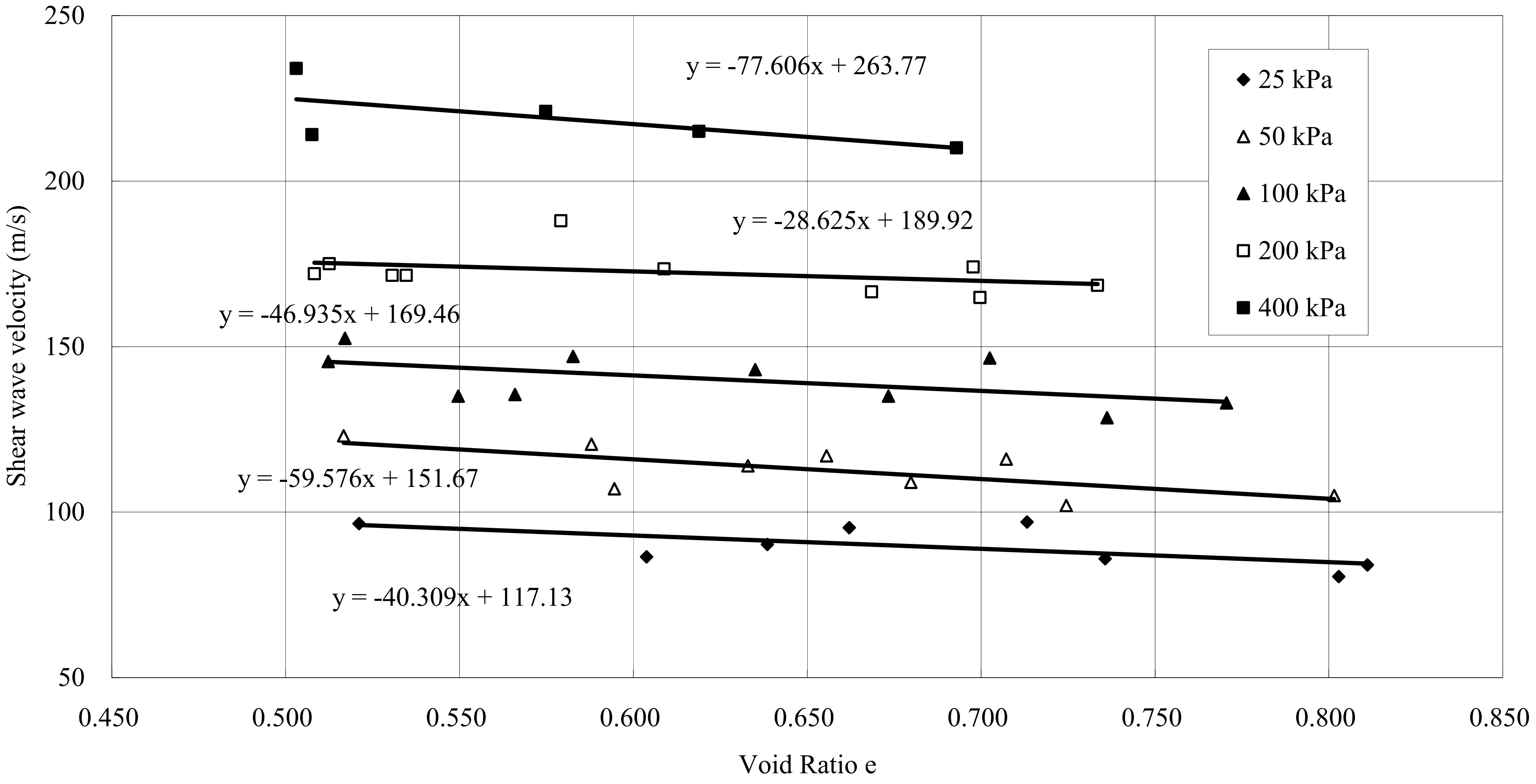
y = -77.606x + 263.77
y = -28.625x + 189.92
y = -46.935x + 169.46
y = -59.576x + 151.67
y = -40.309x + 117.13
◆ 25 kPa
△ 50 kPa
▲ 100 kPa
□ 200 kPa
■ 400 kPa
Shear wave velocity (m/s)
250
200
150
100
50
0.450
0.500
0.550
0.600
0.650
0.700
0.750
0.800
0.850
Void Ratio e

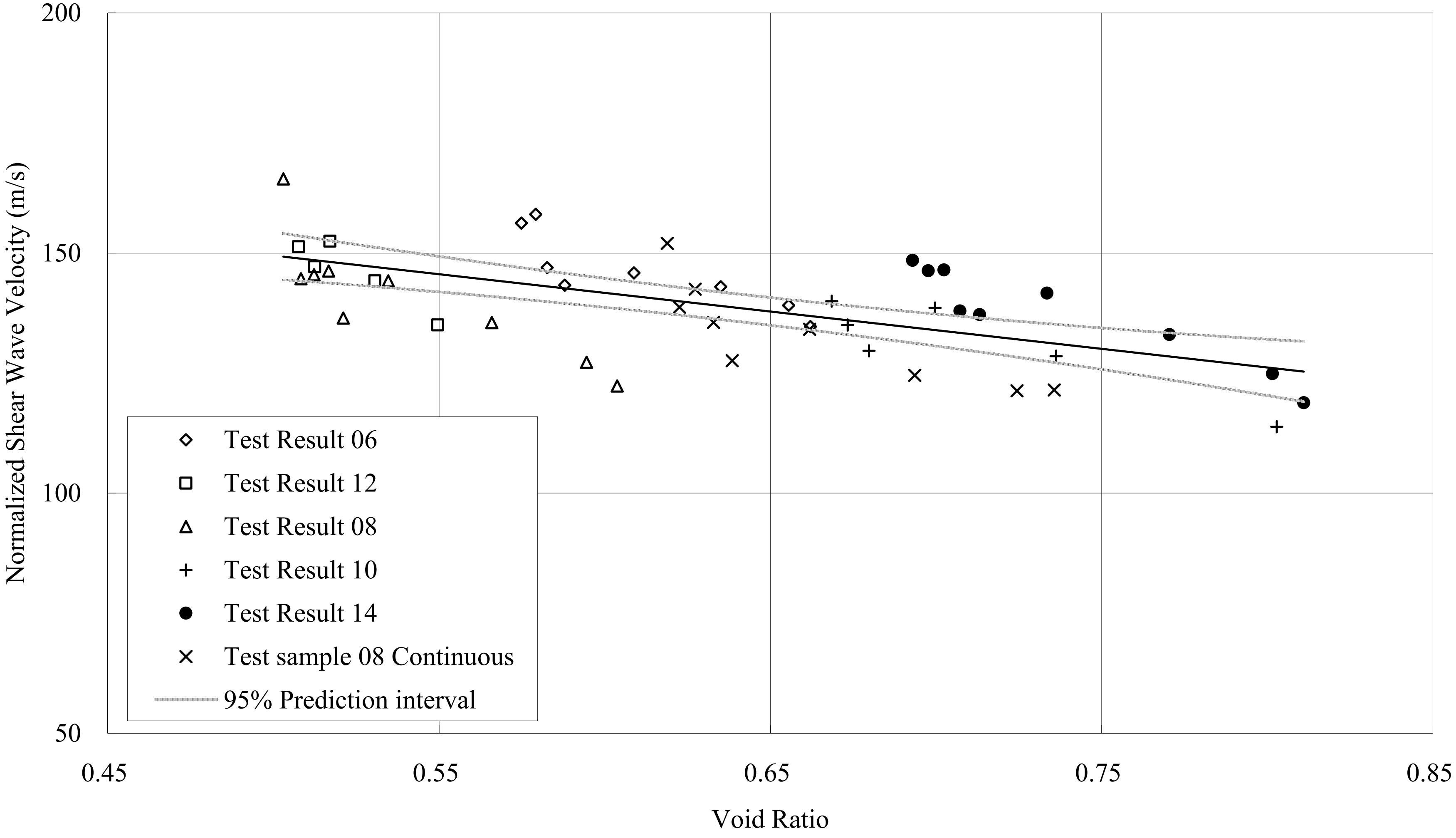
200
150
100
50
0.45
0.55
0.65
0.75
0.85
Normalized Shear Wave Velocity (m/s)
Void Ratio
◇ Test Result 06
□ Test Result 12
△ Test Result 08
+ Test Result 10
● Test Result 14
× Test sample 08 Continuous
95% Prediction interval

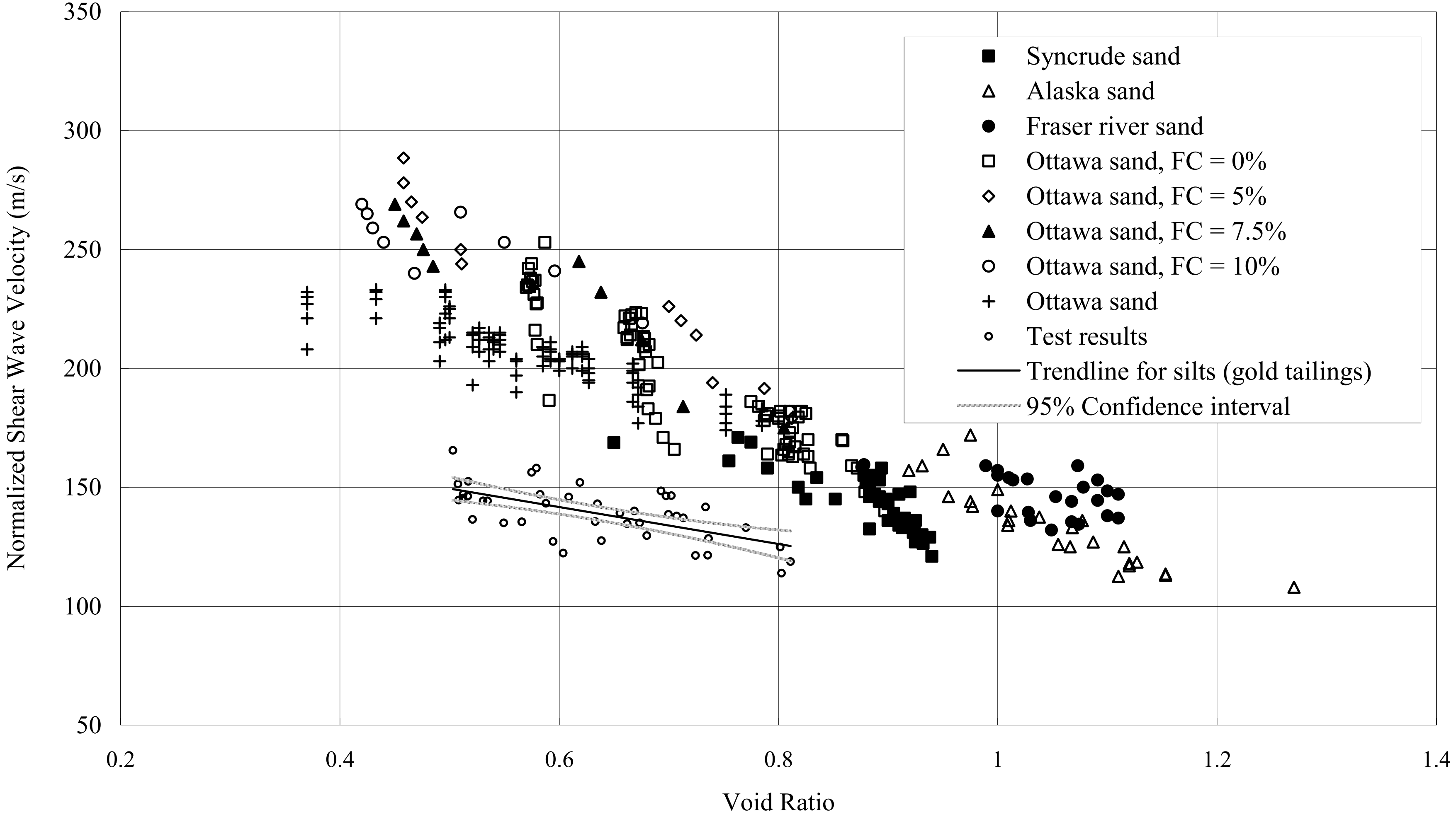

Figure 34. Results obtained in this research imposed on previous results from Robertson and Fear (1995).

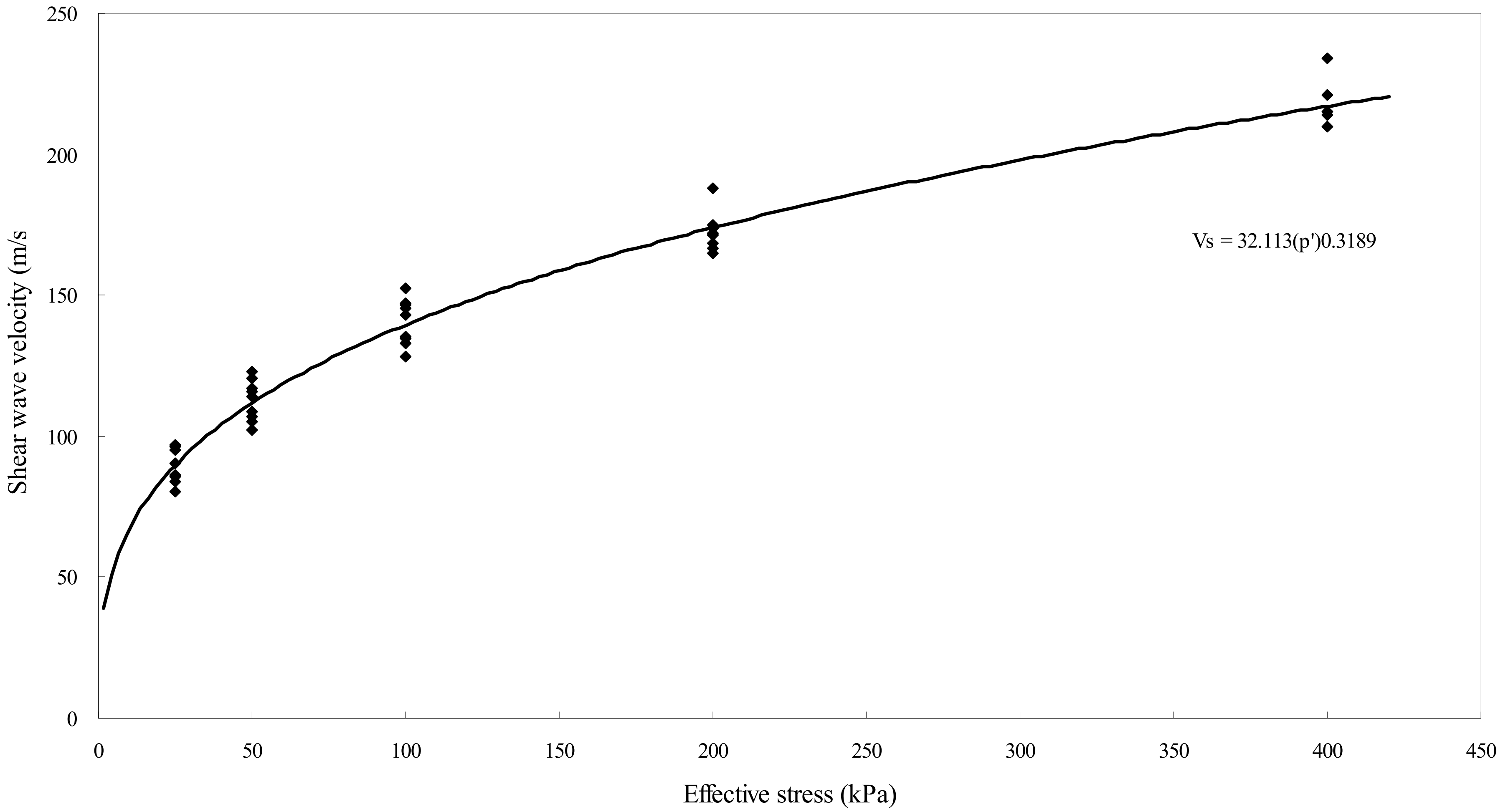

Figure 36. Graph of shear wave velocity against effective stress.

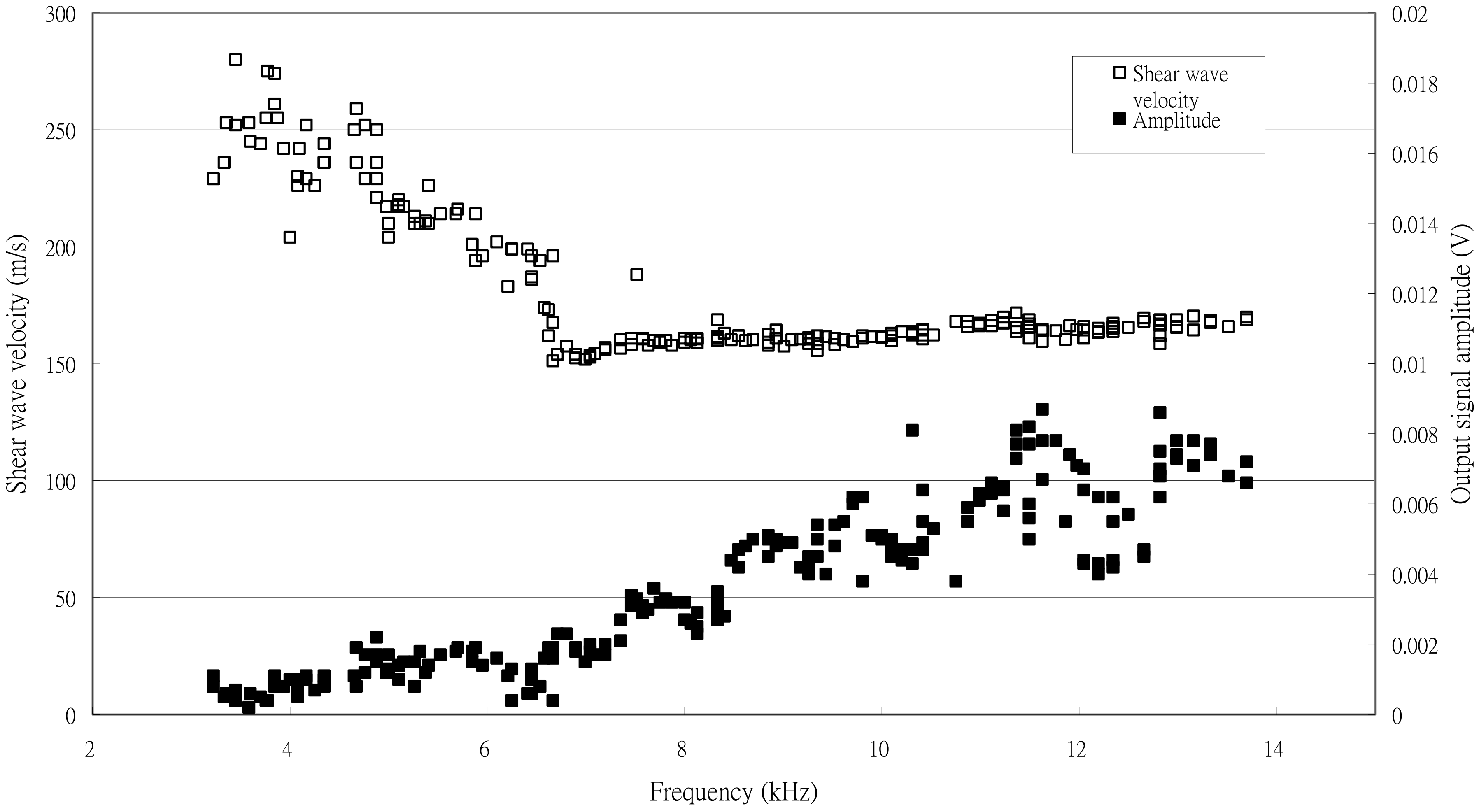

Figure 37. Graph of shear wave velocity and output signal amplitude against frequency.

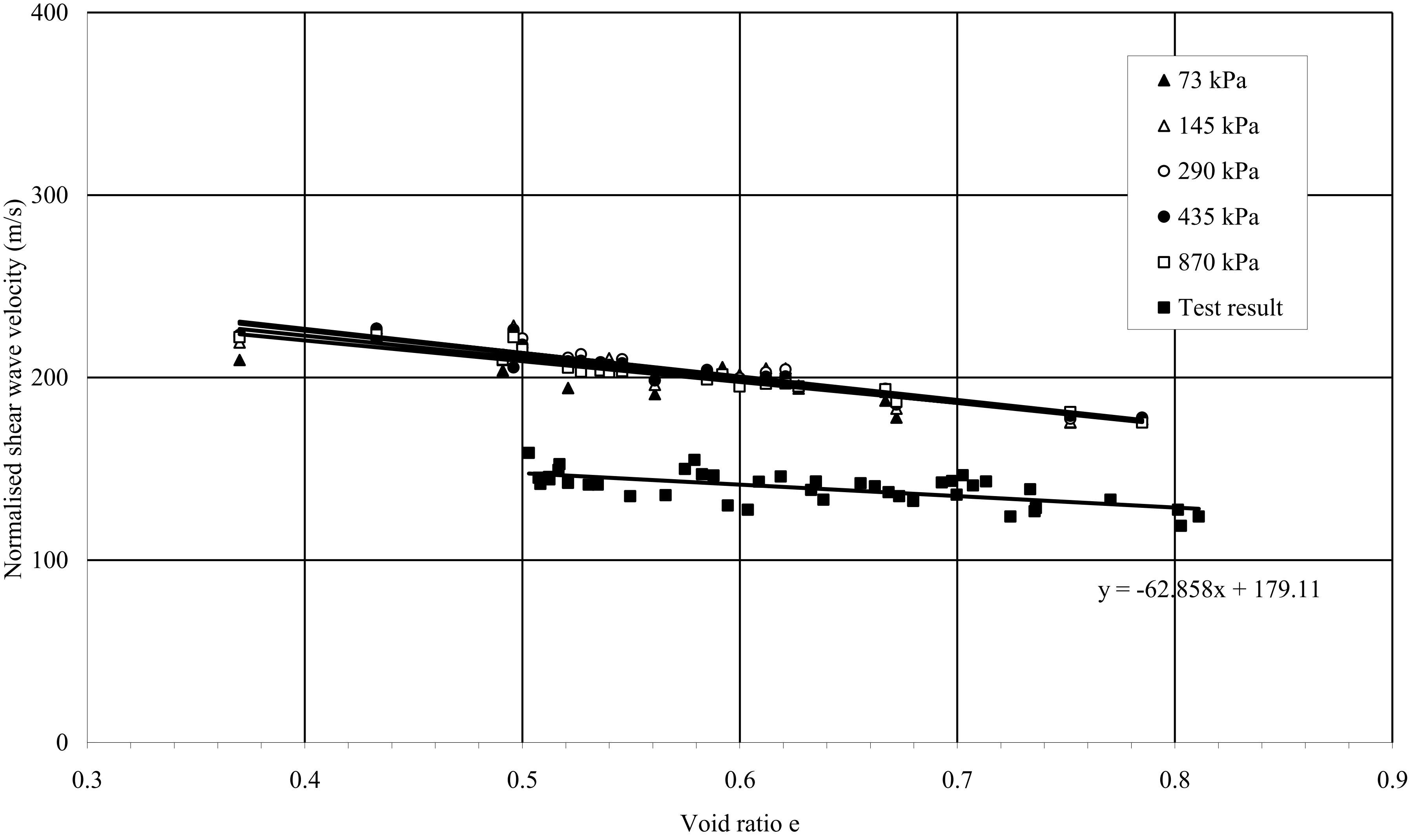

Figure 35. Normalized shear wave velocity imposed on results of Hardin and Richart (1963).